Characterization of UHPFRC Materials for Bridge Construction: An Opportunity to Eliminate the Need for Prestressing in Bridges

Syed A.B. Husain

A Thesis Submitted to the Faculty of Graduate Studies

in Partial Fulfillment of the Requirements

for the Degree of Master of Applied Science

Graduate Program in Civil Engineering

York University

Toronto Ontario

December 2021

Abstract

In the current decade, an increasing number of reinforced concrete bridge structures are deemed to be in need of repair either due to the short durability lifetime of the materials of their original design, or due to climatic extremes that cause the concrete materials to fail (Mermigas 2018). This is especially true for structures such as bridges which are continuously exposed to variations of the environment including temperature, moisture, and road de-icing salts (Carl 1971, L. Spellman 1971, Demich 1975, Steinkamp 2015).

In the present work, a detailed research study of a Canadian UHPFRC material product is undertaken with the objective to investigate the material performance to determine its durability life and identify the limitations and challenges the prequalification process and Code Guidelines present when used to characterize the material. Further, the applicability of the Annex A8.1 was explored of the design procedures using a design benchmark example. The exciting finding of this investigation concluded that by taking advantage of the mechanical properties of this material, it is possible to produce design alternatives for large bridge spans without prestressing (Lee et al. 2017). To quantify the global effects on the response of the structural components comprising UHPFRC materials, design parameters affecting the flexural response of UHPFRC girders were studied.

Acknowledgments

This thesis program would not have been possible without the generous contributions of Dr. Pantazopoulou and Dr. Bashir, who guided me along the way, gave me firsthand knowledge from their experiences from which I learned. Their expertise, understanding, and encouragement motivated me to accomplish the research performed in this thesis. I would like to extend a special thanks to my supervisor Dr. Pantazopoulou who always pushed me to be greater no matter what the circumstances, Dr. Pantazopoulou was always willing to help which I can greatly appreciate as it has allowed me to expand my knowledge and achieve great accomplishments. What I gained is not only knowledge in academia but also a professional and positive attitude towards hardships that often come in life. It has been a great honor for me to be their graduate student that I will cherish throughout my life.

I also want to express my most sincere gratitude to my friends who helped me throughout the experimental program: Zoi Ralli, Konstantinos Tsiotsias, Nicolas Joukhadar, Jordan Santorsola, and Mario Antoun. In addition, I would like to acknowledge our laboratory technician, Riab Rajab, who was always present to answer the million questions I had during the experimental phase of this thesis, without his expertise the full material characterization would not be possible. His extensive knowledge was greatly appreciated.

Moreover, I would like to extend a special thank-you to my family, especially my parents and sisters, for their constant love, support, and encouragement to pursue further studies. I would also like to thank my friends Hashaam, Peter, and Asher who were always present in time of hardship throughout the master's program.

Table of Contents

List of Tables

List of Figures

List of Abbreviations

AASTHO	American Association of State Highway and Transportation Officials
ABC	Accelerated Bridge Construction
AFGC	L'Association des firmes de génie-conseil – Canada
ASTM	American Standard Testing Method
CFRP	Carbon Fiber Reinforced Polymer
CHBDC	Canadian Highway Bridge Design Code
CPCI	Canadian Precast Concrete Institute
CSA	Canadian Standards Association
C.T.E	Coefficient of Thermal Expansion
DL50	Durability life of 50 years achieved
DL100	Durability life of 100 years achieved
DL200	Durability life of 200 years achieved
FHWA	Federal Highway Administration (U.S Department of Transportation)
FLS	Fatigue Limit State
FRC	Fiber Reinforced Concrete
NSC	Normal Strength Concrete
SLS	Service Limit State
THFRC	Tension Hardening Fiber Reinforced Concrete
TN28	Curing the concrete for 28 days with no thermal treatment and under ambient conditions of 23 °C in 95% relative humidity or higher
TSFRC	Tension Softening Fiber Reinforced Concrete
UHPC	Ultra High-Performance Concrete
UHPFRC	Ultra High-Performance Fiber Reinforced Concrete
ULS	Ultimate Limit State

List of Notations

A	Mass of the cylinder after reaching its mass equilibrium after drying
a	Refers to the height of the prism
A'-A	Refers to gauge lines of CTE specimen.
A_c	Area of concrete
b	Width of the beam
b_v	Width for shear calculation.
B	Mass of surface-dried cylinder in air after immersion
B'-B	Refers to gauge lines of CTE specimen.
B1	Refers to batch 1
B2	Refers to batch 2
B3	Refers to batch 3
B4	Refers to batch 4
B5	Refers to batch 5
B6	Refers to batch 6
C	Boiled, surface-dried mass of the cylinder
C1	Refers to Cylinder 1
C2	Refers to Cylinder 2
C3	Refers to Cylinder 3
C4	Refers to Cylinder 4
C'-C	Refers to gauge lines of CTE specimen
D	Mass of the cylinder while suspending in water
D'-D	Refers to gauge lines of CTE specimen
d_v	Effective depth in shear
d_0	Horizontal distance from the center of the span to the tip of the crack width, mm
E_c	Modulus of Elasticity
F	Force in N
F_L	Live load placed as a point load, kN
f_{fu}	Specified ultimate tensile strength at SLS and FLS, MPa
f_{crm}	Average cracking strength of UHPFRC, MPa
f_{cr}	Cracking strength of concrete

f_c' Compressive stress MPa

FC1 Refer to the specimens cured in the freezer at a temperature of -18 °C after a set time of six hours

FC2 Refer to the curing by placing the specimens outside the casting facility where the temperature varied depending on the weather, (during the fall season of 2020, November 2020 – December 2020)

FC3 Refer to the specimens cured in a chamber for 24 hours and then placed in the freezing chamber at - 18°C

G Mass of the cylinder after reaching its mass equilibrium after curing

G_{Fhard} Strain energy corresponding to the area under the curve up until 95% * F_{max}

h Height of the beam

I Mass of the cylinder immediately after demolding

I_e Effective moment of inertia, mm^4

I_{cr} Cracking moment of inertia, mm^4

I_g Gross moment of inertia, mm^4

K Coefficient for displacement

K_1 Inverse analysis coefficient, Annex A8.1

K_2 Inverse analysis coefficient, Annex A8.1

K_3 Inverse analysis coefficient, Annex A8.1

K_4 Inverse analysis coefficient, Annex A8.1

K_5 Inverse analysis coefficient, Annex A8.1

k_0 Factor that links the compressive strength f_c to the modulus E_c

L Length or span of beam

L_x Comparator reading of the specimen at the age of interest.

L_g The gauge length of 295

M_{cr} Cracking Moment, kN-m

M_a Moment occurring at the section of interest with applied loading.

M_{ro} Factored flexural resistance based on reinforcement only.

M_{ru} Ultimate moment resistance of section

M_y Moment resistance at yielding

M_{cr} Cracking moment resistance

P Load measured in four-point flexure prism test, N

P_p Maximum load in four-point flexure prism test for TSFRC inverse analysis, N

P_s Load in four-point flexure prism test corresponding to δ_s for TSFRC inverse analysis, N

P_{cr} Cracking Load in four-point flexure prism test for TSFRC inverse analysis, N

P_m Load in four-point flexure prism test corresponding to δ_m for TSFRC inverse analysis, N

P_1 Load in four-point flexure prism test defined by the intersection of load-deflection curve with a straight line from origin with a slope S_{75} corresponding to 75% of the initial slope S_0, THFRC, N

P_2 Load in four-point flexure prism test defined by the intersection of load-deflection curve with a straight line from origin with a slope S_{40} corresponding to 40% of the initial slope S_0, THFRC, N

P_3 Load in four-point flexure prism test corresponding to 97% of the maximum load P_{max}, N

P_4 Load in four-point flexure prism test corresponding to 80% of P_3, N

P_{max} Maximum Load, FPBT, N

q_o Self-weight of T-beam

S_0 Initial slope of the load-deflection curve used in THFRC inverse analysis, kN/mm, N/mm

S_{75} 75% of the initial slope S_0, THFRC, kN/mm

S_{40} 40% of the initial slope S_0, THFRC, kN/mm

$S_{o,min}$ Initial slope from load-deflection curve for a minimum value

$S_{0,max}$ Initial slope from load-deflection curve for a maximum value

V_r Ultimate shear resistance of section

V_c Shear resistance from concrete

V_s Shear resistance from steel

w_0 Crack width, mm.

X Refers to the heating temperate in Celsius

Y Refers to the cooling temperate in Celsius

ε Strain measured in mm/mm

ε_{ts} Tensile strain at SLS and FLS, design strain

γ_f Fiber efficiency factor

ε_{tu} Ultimate specified strain

ε_{cr} Cracking strain

ε_{c1} Abscissa of the peak stress f_c' first defined without taking into account the favorable effect of confinement provided by the fibers

ε_{c2} The abscissa corresponds to a post-peak stress of $0.7\, f_c$ on the descending branch

$\varepsilon_{c1,f}$ Effect of confinement brought by the fibers

$\varepsilon_{c2,f}$ Effect of confinement brought by the fibers

Δ Displacement

δ_{cr} Displacement corresponding cracking Load in four-point flexure prism test, TSFRC, mm

δ_p Displacement corresponding P_p in four-point flexure prism test, TSFRC, mm

δ_s Displacement corresponding P_s in four-point flexure prism test, TSFRC, mm

δ_m Displacement corresponding to crack width w_m in TSFRC, mm

δ Displacement

ψ_a Curvature at M_a

ψ_s Curvature at factored flexural resistance based on reinforcement only.

ψ_y Curvature at yielding of reinforcement.

ψ_u Curvature at Ultimate moment resistance M_{ru}.

ρ_{bal} Reinforcement ratio of a section at balanced amount of steel.

ρ_{min} Reinforcement ratio of a section with minimum amount of steel

σ_F Maximum bending stress

σ Stress N/mm^2

σ_F Bending stress, N/mm^2

ν Poissons Ratio

Chapter 1. Introduction

1.1 Background

With the emergence of new construction materials and their introduction in codes and design practice, new opportunities for innovative designs, and more durable structures become possible. Of those new materials, the class of reactive concretes known today as Ultra-High-Performance Fiber Reinforced Concrete (UHPFRC) hold promise to change the fundamental concepts of design. This is possible on account of its spectacular compressive strength, tensile resilience, and superior durability, all three properties being their identifying characteristics (Larsen and Thorstensen 2020, Graybeal 2006, Gao et al. 2005). Conventional concrete has an average compressive strength of less than 60 MPa, a post cracking tensile strength of less than 3 MPa which is not considered in design, and a design service life of around 50 years (Tehmina et al. 2014, Alexander 2018). When compared to regular concrete UHPFRC has significantly higher compressive strength (at least 120 MPa), post cracking tensile strength (at least 5 MPa) which is sustained up to very large tensile strain magnitudes, whereas their design service extends or exceeds 150 years (CSA A23.1 Annex U 2019, Azmee 2018, Dong 2018).

Classification of UHPFRC differs among various codes worldwide; in Canada, the above criteria are defined in CSA-A23.1 (2019) - Annex U, which specifies the procedures for quality control and formal characterization of all candidate UHPFRC materials that emerge in the market. UHPFRC comprises of Portland Cement, Supplementary Cementitious Materials, Inert Fillers, Water, Superplasticizer, Fine Aggregates, and Reinforcing Fibers (Azmee 2018): material fineness is designed to be at least 6 times smaller than the fiber length used (Shehab El Din et.al 2016). This is essential for securing deformation capacity in tension, as aggregates in the material microstructure disrupt the homogeneity of the continuum, and cause stress concentrations. Fibers that arrest the crack propagation at the scale of the fine aggregates, prevent the formation of major cracks that participate in the tensile failure. In this manner, several fine cracks may be developed when the material is stressed in tension before the loss of tensile strength, which, after cracking is mainly supported by the fibers that bridge the crack paths (Huang et al. 2018, Huang et al. 2019, Roy et al. 2017). The high compressive strength of UHPFRC is owing to the very low water to cement ratio, and high cementitious material content, which in some cases may be more than 1000

kg/m^3 (Russell, H.G. and Graybeal, B.A 2013). The low amount of water is responsible for several of UHPFRC's attractive characteristics: it leads to low porosity and absence of capillary pores that make the material resistant to adsorption of water and other deleterious agents (e.g. chlorides), therefore leading to prolonged service life (Graybeal 2005). Furthermore, the presence of ample un-hydrated or partially hydrated cement in the material microstructure enables self-healing of cracks after the ingress of water (Granger et al. 2005). Both these aspects contribute to the enhanced durability performance.

The current design practice for conventional concrete ignores the insignificant amount of concrete's resistance to tension on account of its low magnitude, and the immediate loss of tensile strength at very small tensile strain levels (in the order of 0.0001). For this reason, concrete structures are generally designed to contain properly placed reinforcement: longitudinal bars are provided usually for strength, whereas carefully detailed transverse reinforcement is provided for ductility. However, the practice of conventional reinforced concrete, already being prolific in the past 130 years, has shown alarming performance in terms of susceptibility of the embedded steel reinforcement to corrosion, resulting from exposure to inevitable carbonation, and in some cases to chloride attack that can cause premature deterioration to the structure and reduce its service life drastically (Demich 1975, Rodrigues et al. 2020).

The addition of reinforcing fibers improves the tensile strength and ductility of fiber-reinforced material (FRC) (Yoo et al. 2015). However, before the emergence of UHPFRC, localization of cracks would occur immediately after cracking, whereas for UHPFRC, the fibers that crossed the crack openings mobilized the fibers to restrain further crack growth, without being able to supplement the loss of resistance with increasing crack width (Bantia 2012, Hannawi 2016). In the early studies of FRC, larger and thicker fibers were the norm, where aggregates were of standard size. After the effect of the fiber length to diameter aspect ratio became understood, as well as the significance of reducing the maximum aggregate size, the material was optimized into its current technology. Effectiveness of the fibers is dependent on the fiber-matrix, bond strength, and fiber tensile strength (Banthia, 2012). UHPFRC has a high density with limited connected capillary pores which helps in delaying the occurrence of corrosive actions and therefore exhibit excellent durability performance (Mosaberpanah 2016). In the context of bridges, given the high strength to volume ratio of the material, bridge structures can be designed that use less material, have lighter self-weight, extend over longer spans, with reduced life-cycle costs of the entire structure

(Groenveld et al. 2017, Nguyen et al. 2013). Considering all kinds of countermeasures that can be used for prolonging conventional concrete structures, UHPFRC is an outstanding material that can outperform conventional concrete owing to its superior mechanical and durability properties.

1.2 UHPFRC Materials

With the rise of attention and efforts being made in the current decade to develop more sustainable means for construction, Larson et al. (2017) conducted a life cycle inventory analysis in which normal strength concrete (NSC) was compared with a UHPFRC alternative as possible materials of choice for constructing a single bridge with a design life of 100 years. The study illustrated that when opting for NSC more concrete was consumed but with less cement amount per bridge, than the UHPFRC alternative. The lifetime consumption, however considering the necessary repairs and replacements, was found to be 52% greater than in the UHPFRC bridge. According to the Impact assessment included in the study, it was found that the impact to the environment (including the $C0_2$ emissions and the use of energy and natural resources) was 10% less in the UHPFRC than in the NSC bridges. The NSC bridges were estimated to produce 82 tons of CO_2 emissions whereas the UHPFRC alternative was estimated at 68 tons. In light of durability research and current developments in the material technology, UHPFRC materials for bridges are now available that may secure a design service life of up to 200 years as per CSA S6 Annex U 2019.

Thus, the emergence of UHPFRC technology developed in the last 20 years brings new opportunities in designing better performing and more dependable infrastructure. This is why the use of the material in bridge engineering is increasing at an exponential rate as depicted in Figure 1 which shows the number of UHPFRC bridge constructions in the U.S and Canada from 2006 till 2016 as reported by FHWA in 2018.

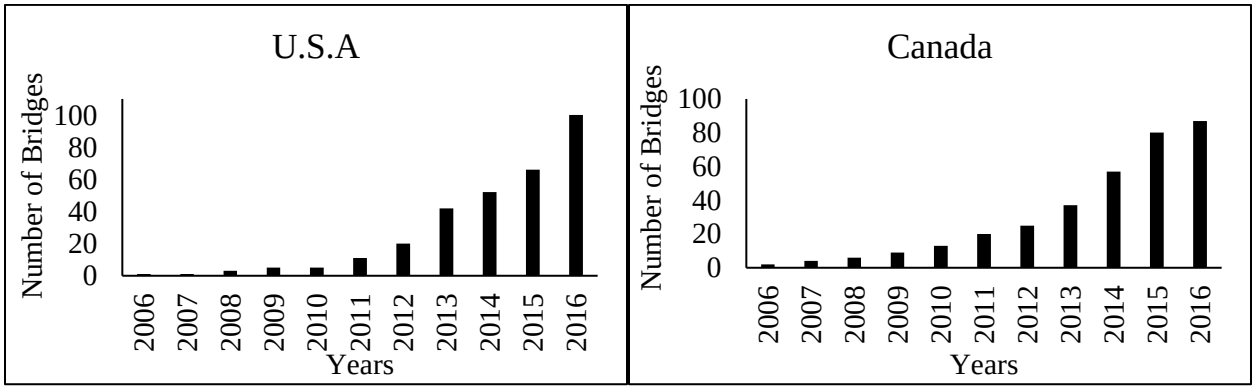

Figure 1: Timeline of UHPC bridge construction in the U.S and Canada from 2006-2016 (FHWA 2018)

UHPFRC may be classified as a composite material comprising the concrete mix and discrete fibers. It was stated before that fibers play an important role once a crack width is opened under load. CSA S6-19 Annex A8.1 describes two types of behaviors that can be observed after cracking, i.e., Tension-Hardening (THFRC) and Tension-Softening (TSFRC) response. Tension- Hardening is a type of behavior that can be observed beyond the first crack, where the concrete demonstrates increasing resistance to increasing tensile strain, over a post-cracking plateau that resembles the behavior of elastic-plastic materials with hardening; this characteristic is enabled by the fiber type and volumetric content of the material. Fibers enable increased tensile strength beyond the cracking limit. In the case of Tension-Softening materials, the post-cracking resistance curve exhibits softening, with the strength degrading significantly after the first localization of a crack. Figures 2 and 3 illustrate the resistance curve of a Tension-Softening and a Tension-Hardening material, respectively.

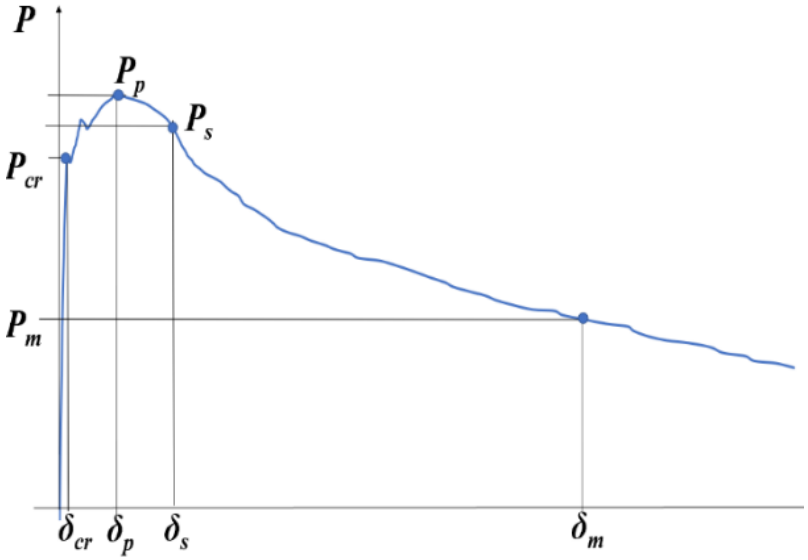

Figure 2:Tension Softening Behavior (CSA S6:19)

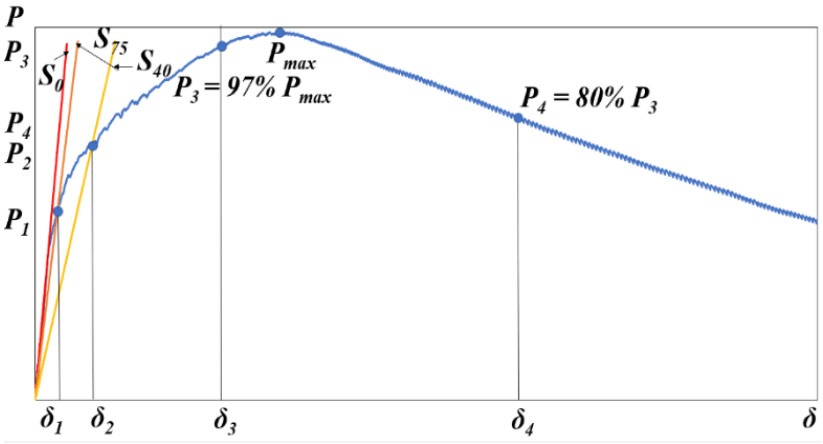

Figure 3: Tension Hardening Behavior (CSA S6:19)

The effect of fiber content and fiber orientation is very critical when considering the post-cracking behavior of UHPFRC. On account of its very fine aggregate content and the reactive powders it contains, in most cases the UHPFRC material is a highly flowable (a flow of around 200mm), self-consolidating material that requires no vibration (Sobuz et al. 2017, Habel et al. 2008). Vibration is often used in conventional concrete to help consolidate the fresh mix so that the hardened concrete has homogeneity and low porosity. Taking advantage of this marked flowability, it is the current practice to pour UHPFRC from one end in the formwork as this mode of casting is believed to help the alignment of the fibers with the direction of the flow (Zhang et al. 2020, Qui et al. 2020). For example, in the formwork of a beam, the mix is poured in a manner to allow the fibers to settle perpendicular to the load direction (Huang et al. 2018). Through pertinent casting, therefore, it is possible to optimize the position of the fibers for as themselves to reduce the crack width growth under tensile load. Figure 4 illustrates the optimal fiber orientation distributed throughout a flexure beam where the fibers are parallel to the direction of tensile stresses.

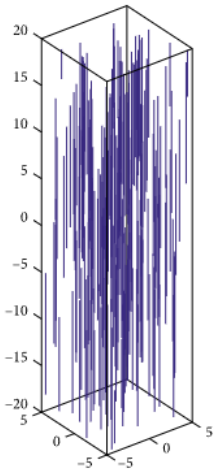

Figure 4: Fiber Orientation (Gu et al. 2018)

The figure above is only for illustration purposes. Generally, when the UHPFRC is poured, not all fibers are oriented vertically. This is the effect of internal friction which happens between the fibers and the concrete (Yoo et al. 2016). Fibers that are oriented parallel to the tensile stresses participate in reducing the crack widths. When fibers are oriented in the intended direction, the material exhibits a higher post-cracking stiffness when compared to random fiber orientation. Furthermore, longitudinal fiber distribution has been shown to give higher values for cracking load, yield load, and peak load (Huang et al. 2019, Roy et al. 2017) on account of the bridging effect which is more effective and robust when the fiber orientation is in the longitudinal direction along with the flow. The bridging behavior is illustrated in Figure 5 which represents a cracked UHPFRC prism that had been previously tested in Lassonde's High Bay Lab. The favorable effect of pouring orientation on the alignment of the fibers is better controlled in precast construction, and in more shallow members. In fact, the deeper and the thicker the member that is being cast, the more difficult it is to control this parameter (Wu 2015, Yoo 2016). In this context, the behavior of the UHPFRC flow direction in field conditions is compromised as compared to that obtained in characterization and quality control tests; this effect is accounted for in practical engineering, through the introduction of an effectiveness coefficient, which may range to as low values as 40%. (CSA Annex A8.1)

Figure 5: Bridging Behavior of Steel Fiber

1.3 Objective and Scope

The UHPFRC materials are rather expensive (about 10 times the price of normal concrete) and require significant expertise in installation, the casting issues mentioned in the preceding being of primary concern. Their favorable properties and durability have made them particularly attractive in Accelerated Bridge Construction (ABC), to eliminate the issues related to corrosion and to provide fast and non-disruptive bridge replacement (Shafieifar 2018, Wang et al. 2020). However, methodologies to design with these materials are still being developed – with the exception of the French supplement to Eurocode 2 (2013) all other countries that use advanced UHPFRC technologies are still in the phase of code developments in the form of preliminary documents and Annexes (e.g., in Canada, bridge design with UHPFRC was first described in Annex 8 to CSA-S6 in 2019, and it was rather preliminary). A major limitation that hinders code development is the uncertainty regarding the documentation of a dependable stress-strain response for the material in tension (FHWA 2019). Until now the established procedures required to qualify the UHPFRC material as THFRC or TSFRC and to obtain the characteristic stress-strain response in tension (Through the prescribed inverse analysis from CSA Annex U for characterization of UHPFRC) are indirect and fraught with several practical and theoretical disputes (Yang 2019). Nevertheless, this is an important limitation for producers of UHPFRC materials, as the result of characterization of their material controls their access to the international market.

In the present study, the performance of pre-qualification procedures adopted for characterization of the tensile response of UHPFRC in Canada is assessed and its limitations and challenges are identified. A Canadian-produced UHPFRC material is used as a case study in order to assess the performance of the 2019 standards (Azmee 2019). To achieve this objective the research study includes both experimental and analytical components. The experimental program consists of practical implementation of the durability, mechanical and physical testing procedures needed in order to characterize the material properties; consistency of the approaches, dispersion, and applicability are investigated. The experiments are focused in a laboratory setting to firstly better understand the materials for a pre-cast environment. Tests which are generally conducted in the field for quality control are not the focus of interest, however some test and curing regimes are explored with the experimental phase.

Along with the material tests, the applicability of the informative version of Annex 8 to CSA-S6 (2019) was explored by participation in a round-robin evaluation of the design procedures using as a design case study a two-span bridge girder under distributed and point loads, designed with a UHPFRC material exhibiting THFRC response. The round-robin procedure involved several other research affiliations including universities as well as industry partners, this procedure was set in the task force committee to discuss the inconsistencies present in the Canadian Annex for UHPFRC (Annex A8.1 – 2019) with regards to a design case study. The round robin evaluation was done by comparing the different results obtained for the same design case study from each research group, the importance of it was to evaluate the readiness of the Annex for publication in design codes.

The evaluation was motivated by the current CSA task force developing the 2025 version of Annex 8, where the performance of the existing procedures, inconsistencies, and open challenges are the focus of interest. An exciting finding of this investigation was that owing to the significant compressive strength of the material, it could be possible to design large bridge spans without prestressing altogether, by taking advantage of the spectacular compressive strength of UHPFRC. An additional finding of this case study investigation was the identification of inconsistencies in the quality control testing method used for the characterization of tensile strength of UHPFRC.

Lopez (2017) proposed a simplified inverse analysis method by which to characterize the tensile strength with analytical equations performed on four-point bending prisms; this method was

adopted in Annex 8.1 (CSA-S6 2019) and has been required to be used in Canada for characterization of all UHPFRCs in the Canadian market. From this method prescribed in the annex, it was found that there exists a range of possible values wherein the prescribed code method may lead to incorrect values for the milestone points of the tensile stress-strain diagram of the material. To quantify the global effects on the response of complete structural components comprising UHPFRC materials, with a particular interest in the precast bridge construction, the last part of this thesis explored the design of a CPCI girder for a variety of possible compressive and tensile strengths of UHPFRC replacement of concrete. Design parameters affecting the flexural response of UHPFRC girders were studied with an emphasis on (a) formulating the design expressions that control ductile performance, (b) cover a range of material properties; and (c) exploring the potential span and weight limits for which prestressing could be mitigated thereby increasing the value of this method of construction by servicing on account of concrete material strength alone, similar roles in bridge design as the established CPCI prestressed girder form.

In summary, the main objectives of this research are defined as follows:

1. To test the applicability, repeatability, and robustness of current material characterization procedures using as a case study a Canadian UHPFRC material product.
2. To validate the proposed method for obtaining UHPFRCs response to tension through direct tension tests as well as the prescribed inverse analysis method and obtain linearized tensile stress-strain and stress crack width openings for UHPFRC. Further to compare the tensile strength results obtained from the different tension tests in the literature and compare with the tensile strength obtained from the inverse analysis of the Code Based methodology.
3. To investigate the applicability and limitations of Annex 8 of CSA-S6 (2019) structural bridge design provisions through application in the case of a T-beam as part of the CSA task force.

1.4 Thesis Outline

This thesis report comprises eight chapters. The chapters are organized according to the following summary:

Chapter 1-Introduction: This chapter introduces UHPFRC and its favorable tensile properties for structural engineering, particularly feasible for the ABC industry by a brief explanation of the constituent performance of the material as a composite, and its spectacular ductility and post-cracking resistance. In addition, the objectives and scope of the research study were presented.

Chapter 2-Literature Review: This chapter focuses on reviewing the historical background of concrete and comparison with UHPFRC material. Further, this chapter explores the classification of a UHPFRC material following CSA and FHWA, the challenges presented to practical material validation and characterization, the limitations induced by the unknown distribution of the fibers, and the experimental evidence regarding the tensile strength of UHPFRC, Flexural strength, and past bridge design applications. The chapter also includes a review of the reported properties of UHPFRC for durability and physical performance.

Chapter 3-Durability Tests: This chapter outlines the procedures and findings of a series of durability tests performed on a proprietary UHPFRC mix which is used as a case study in the thesis. The methods used follow the CSA S6 Annex U for characterization of UHPFRC materials. This enables a first-hand experience for observing the many aspects of the response of a UHPFRC material, illustrating the relationship between different aspects of material assessment.

Chapter 4-Mechanical Tests and Physical Properties: Following are the mechanical and physical tests conducted on the case study material, as outlined in the CSA S6 Annex U. The challenges and observations regarding testing errors and uncertainties are detailed in the chapter.

Chapter 5-Inverse Analysis: This chapter evaluates the tensile response obtained through inverse analysis of flexural tests as is the current quality control methodology adopted by Annex A8.1 to bridge code and identifies and illustrates the challenges to its application as a key characterization methodology in the UHPFRC materials industry.

Chapter 6-T-Beam Investigation: The design clauses of Annex A8.1 are further explored through application to a T-beam example intended to capture the extent to which uncertainties in the material characterization as well as in the actual mechanistic response of UHPFRC structural components propagate in the structural design of the component.

Chapter 7-CPCI 900 Girder Designs: The flexural response of UHPFRC girders is investigated in this chapter, aiming to define the bounds of performance of a precast UHPFRC girder without prestressing as an ABC component in the fast assembly of bridge decks.

Chapter 8-Conclusions/Recommendation: The main findings of this research program and practical recommendations for quality control of UHPFRC and practical design with this material are summarized.

Chapter 2. Literature Review

The scope of this literature review is to provide context for the salient points of the present research. Although the field of UHPFRC is relatively new compared to conventional concrete, the ongoing research in the last few years is vast, covering a wide range of its' applications. However, many of the important questions that form the basis of the design applications of UHPFRC are built on the assumption that material strength and ductility in tension is well understood and given, and that the values reported by the manufacturers are dependable. However, this assumption is under scrutiny and debate: Yang et al. 2021 conducted round robin tests on the same material, in same batch and method of casting, that have illustrated the details of the test setup may affect the results significantly, with a spread more than 30% of the mean value. Apart from the test setup several other causes of uncertainty and dispersion exist, including the orientation of fibers which is affected by the manner of casting and the bias owing to the specimen form being prevalent. The following sections begin with an introduction of those aspects of UHPFRFC behavior that may affect its characterization, followed by experimental results and observations regarding the durability and mechanical properties assessed by other researchers. Additionally, this chapter focuses on the importance and uncertainty still present in measuring the tensile strength of the material.

2.1 FHWA and CSA Classification of UHPFRC

UHPFRC generally consists of Portland cement, fine sands, reinforcing fibers, chemical admixtures, and water. The properties and dosage of each type of ingredient, curing methodology, and casting methodology can result in diverse characteristics of the material. According to FHWA, UHPFRC is a class of material that comprises cementitious based composite with discontinuous fiber reinforcement, compressive strengths of over 150 MPa, above 5 MPa strength in tension, and consists of enhanced durability which is the result of their discontinuous pore structure. The Canadian Standards Association (CSA) defines UHPFRC as a cementitious composite material with enhanced strength, durability, and ductility when compared with high-performance concretes (Annex U). The CSA notes that UHPC can contain fibers for post-cracking ductility where the material may have a specified compressive of at least 120 MPa at 28 days. The Canadian standard

further divides the UHPFRC into two categories based on their compressive strengths at 28 days cured with TN28 curing following testing method CSA A23.2-3C, where TN28 curing is achieved by curing the concrete for 28 days with no thermal treatment and under ambient conditions of 23 °C in 95% relative humidity or higher. Additionally, the CSA prescribes a list of testing methods to obtain the durability properties with specific criteria required to meet the durability life of the material as DL50, DL100, and DL200. DL is referred to the minimum design service life of a structure in terms of years in the range of 50, 100, or 200 years.

The mechanical properties of UHPFRC are enhanced when steam-based curing is used. The steam-based curing treatments tested in the literature include steam, delayed steam, and tempered steam (FHWA 2013, Graybeal 2006). The general trend noticed from steam-based curing concluded that steam treatments increase UHPFRCs compressive strength by 53%, increase in its modulus of elasticity by 23%, decrease the creep coefficient and show little to no length change under long term shrinkage (FHWA 2013). This effect is also seen in the chloride ion penetration (Ahlborn et al. 2008). The tensile strength of UHPFRC before and after cracking is observed to be significantly higher than that of normal concrete. UHPFRC displays durability properties that are significantly beyond those normally associated with concrete, regardless of curing treatment (FHWA, 2013).

2.2 Diverse Effect on Characterization due to Fibers

Huang et al. (2018) report an L-Shape device which controls the flow of the fresh mix showed improvement on fiber orientation which directly showed an improvement effect to the flexural strength of UHPFRC. Huang et al. (2021) reported that fiber alignment can enhance dynamic and quasi-static mechanical properties of the material. Yoo et al. (2016) reported that better fiber alignment in the tensile load direction and higher fiber % per unit area when the mix was placed at one end and allowed the flow of the mix to fill the mold. This further led to higher flexural strength and normalized deflection capacity in beams with better fiber alignment. Ye et al. (2012) reported that UHPFRC mixtures incorporating higher aspect ratio fibers had increased flexural capacity compared to lower aspect ratios which are directly linked due to more fibers with smaller diameters (higher aspect ratios) have increased number of fibers per unit area, leading to more fibers bridging the cracks, thereby resulting in higher flexure capacities. Maca et al. (2012)

reported that during an optimization program for UHPFRC mixes, it was found that fiber content between 2% and 3% reported better workability and superior mechanical properties. Zemei et al. (2015) reported that with the presence of steel fibers the compressive and ultimate flexure strengths of UHPFRC showed increased peak loads compared with mixes without steel fibers. Huang et al. (2019) reported that fiber rotation is restricted by the formwork boundaries which generate inhomogeneous fiber orientation and flexural performance along with the distance from the mold sidewalls. Zhou et. al (2017) reported that a panel that was cast by pouring the material from the center showed a wide scatter of post cracking capacity and that it is not recommended for practical applications.

2.3 Tensile Strength of UHPFRC

Larsen et al. (2020) reviewed the effects of fibers on compressive and tensile strength of UHPFRC from a variety of specimen geometries, sizes, and procedures. The results of these show that steel fibers have the potential to improve the tensile strength of UHPFRC, where the effects on tensile strength depend on fiber content type, and lastly the influence on fibers compressive strength is questionable. Nguyen et al. (2014) investigate the size and geometry concerning the effect on direct tensile stress versus strain response of UHPFRC and conclude that with increasing gauge length, section area, and volume of specimen, there was little reduction in post cracking strength, while strain capacity and energy absorption capacity decreased. Ralli (2019) reported the correlation between results obtained from direct tension tests and bending experiments is not clear due to the strain distribution in direct tension being nonlinear and dependent on the frictional action exerted by the testing grips. Zhou et al. (2019) reported that the fiber bridging behavior plays a major role to resist crack propagation. Graybeal (2019) investigated different direct tension tests to conclude that the uniaxial tensile response of UHPFRC includes four distinct phases, i.e., the linear elastic response, a post-cracking hardening, a plateau, and then a post-peak softening range. UHPFRC tests showed mechanical properties beyond those normally associated with structural concrete with a modulus of elasticity reported for the mix at 54 GPa, tensile cracking of over 7.6 MPa, and maximum tensile strength of 8.3 MPa. Qiu et al. (2020) reported from an investigation conducted experimentally on nine dog-bone specimens that were tested in direct tension, on the effects of reinforcement ratio, fiber orientation, and fiber chemical treatment on the tensile behavior. The

investigation reports that the typical damage done on rebar reinforced UHPFRC members include the rupture of steel rebars, the addition of longitudinal reinforcement effectively improved the post-cracking stiffness, cracking resistance, and a peak load of UHPC members under direct tension.

2.4 Flexural Strength and Bridge Design

Yoo et al. (2015) report that the addition of steel fibers resulted in an increase in the compressive strength, elastic modulus, and a significant improvement in the flexural performance with regards to flexural strength and deflection capacity. The first cracking load and corresponding deflection for reinforced UHPC beams were reduced by the inclusion of steel fibers. Due to the homogeneous fiber dispersion, the post-cracking stiffness, and load-carrying capacity were significantly improved with the addition of steel fibers because of the bridging of steel fibers across the cracks. However, a lower ductility index was obtained for beams with steel fibers than those without. The beams with steel fibers failed by rupture of steel rebars. Mohammadreza et al (2018) proposed a numerical model calibrated by four-point bending tests, based on the assumption of linear strain distribution on rectangular sections. After comparison with the test data it was found that the model converged to the experimental data, showing an error of 12%. Yoo D.Y. (2016) report an investigation where three different fiber lengths having the same diameter were used, the results of which show that enhancements in flexural strength and energy absorption capacity were observed when longer fibers (higher aspect ratios) were used, whereas the insignificant effect of fiber length on first cracking properties was observed. Yang et al. (2010) reported that a one-way pour showed to enhance the flexural capacity for identical cross-sections and rebar ratios when compared with mixes poured at the midspan of the beams. Graybeal (2008) reports an AASTHO type II girder investigation which shows that UHPFRC I-girders developed flexural capacities larger than those of conventional concrete with similar geometries and that flexural design of UHPFRC I girders can be completed rationally through the use of conservative approximation of the stress-strain behavior. Almansour (2008) reports that the use of UHPFRC in precast and prestressed concrete girders enable a significant increase in bridge span of the slab-on-girder bridge design compared with conventional concrete. A comparison between two UHPC examined

sections showed that in order to get the most favorable ratio of girder weight to moment resistance, the optimal section can be developed in the size range between CPCI 900 and CPCI 1200.

2.5 Durability Properties

The material composition of the proprietary mix used for the experimental study conducted for this thesis is called DURA. This was a UHPFRC mix originally introduced in Malaysia in 2006; the technology of the composition was later transferred to Canada by a local proprietor, who embarked on the production of DURA in Canada using Canadian source materials. In fact, this is not a straightforward challenge. On account of the chemical and grain size sensitivity of the material properties, it was found that flowability, setting time and strength could be significantly compromised by the chemical content of Canadian waste powders (Fly Ash and Slag). Optimization of the mix and characterization so that a Canadian made product could be used in Canadian bridges ensued. DURA UHPFRC mix has been used in bridge applications since 2010. The DURA premix consists of Portland cement, Fine sand, Silica Fume, Steel fibers, Super plasticizers, and water (Azmee and Shafiq 2018). The base mix of DURA UHPFRC contains 911 kg/m^3 of Portland cement, 911 kg/m^3 of fine sands, 225 kg/m^3 of silica fume, 173 kg/m^3 of steel fibers, 38 kg/m^3 of superplasticizers and 200 kg/m^3 of water. (Note: the mix used in this thesis is a proprietary mix, the base material quantities are reported here as included in Azmee and Shafiq 2018, the actual mix tested is of a different variation made from the same base mix design). Dura is one producer of this type of material, in the current literature there are many UHPFRC material compositions made by many different producers, but only a few made with locally sourced Canadian materials. The spectacular durability properties of UHPFRC are owing to its porosity and absence of capillary pores which makes the material resistant to absorption of water and other harmful chemicals such as chlorides and sulphates (Graybeal 2005). The following list contains the list of durability parameters and the testing standard prescribed by CSA Annex U for the characterization of UHPFRC used in this thesis,

Chloride Ion Penetration - CSA A23.2-11C / ASTM C1202

Salt Scaling Resistance – CSA A23.2-22C / ASTM C672

Abrasion Resistance – ASTM C944

Sulfate Resistance – CSA A3004-C8 / ASTM C1012

2.5.1 Chloride Ion Penetration/Permeability

UHPFRC has low Chloride Ion Penetration which is a direct result due to the prevalence mostly of fine discontinuous pores in its microstructure. Many researchers have reported low permeability obtained from the ASTM C1202 rapid chloride ion penetration test. According to ASTM C1202 permeability values of less than 100 are considered negligible. Graybeal (2012) reported a chloride ion penetration of fewer than 40 Coulombs at 28 days with steam-cured specimens. Ahlborn et al. (2008) reported a chloride permeability of fewer than 100 Coulombs for both air-cured and heat-treated concretes. Bonneau et al. (1997) reported a value of 6 – 9 Coulombs for two specific mixes. Thomas et al. (2012) also reported a permeability value of 0 – 19 Coulombs at an age of 28 days. For comparison, Pfeifer et al. 1994 reported a chloride ion penetration of a conventional concrete having a water to cement ratio of 0.29 without silica fume to be around 800 coulombs passed. The effects of permeability on cracked beams were also investigated by Graybeal (2008) where beams were subjected to 500,000 cycles of loading over 154 days. The reported penetration showed an ingress of 3mm in the side faces and 5mm on the tensile face of the beam. Moreover, the steel fibers crossing cracks did not show any signs of section loss or failure in tension. Aarup (2004) also tested small beams with reinforcement which were loaded to different loading conditions over 4 years exposed to different levels of salt solutions. The increased loading of the beams caused crack formation at the bottom face of the beams where tension occurs, the salts were poured before each loading stage. They reported no correlation between the loading of beams and chloride ion penetration, the low amount of porosity and capillary pores being the main reason for this result.

2.5.2 Salt Scaling Resistance

The standard method to evaluate the scaling of the concrete due to surfaces exposed to de-icing chemicals is ASTM-C672 or the CSA A23.2-22C. The difference in the two standards in the de-icing agent used were as follows: ASTM C672 uses calcium chloride and CSA A23.2-22C uses sodium chloride. Calcium chloride is an effective de-icer and in comparison, sodium chloride is more effective due to its ability to extract moisture. Graybeal (2012) reported no surface scaling

of UHPC for 215 cycles. Bonneau et al. (1997) also report negligible amounts of scaling for three mixes after 50 cycles. Schmidt et al. (2002) reports a scaling of 100g/m^2 after 56 cycles of freezing and thawing, and also observed that specimens that received no heat treatment showed higher freeze-thaw resistance than specimens that had been heat-treated prior to exposure. The salt scaling reported for conventional concrete tested with ASTM C672 standard was reported at 0.8 kg/m^2 by Bonzoubaa et al. (2008).

2.5.3 Abrasion Resistance

The abrasion resistance reported by the researchers in the field is summed in the following observations. Abrasion resistance of UHPFRC is affected by the curing method, and the condition of the surface being abraded. Graybeal (2012) tested several specimens that had been either steam cured, or, untreated, tempered steamed, and delayed steamed. All specimens tested in abrasion were either sandblasted, finished with steel cast surface, and/or were grounded on the abraded surface. The results show that specimens finished with a steel cast surface showed the least amount of abrasion and the sandblasted surfaces showed the most amount of abrasion. Further, the results show that steam-cured specimens when compared with untreated specimens displayed higher abrasion resistance. Pyo et al. (2019) reported an abrasion loss of 6.8 grams for a conventional concrete mix with a compressive strength of 40 MPa.

2.5.4 Sulfate Resistance

The sulfate resistance was reported by Pierard (2012) after tests on three prisms of 40mm × 40mm × 160mm which were conditioned by immersion in sodium sulfate with the concentration of 16g SO_2^{2-} per liter. It was found that specimens showed no length change over 500 days. However, the testing standards in North America ASTM C1012 and CSA A23.3 A3004-C8A use higher concentrations, of 50g/L Na_2SO_4 and thus results may show larger expansion values. ASTM C1012 reports a length change for a test mix for ASTM C150 Type II concrete to be at 0.04% at 12 months of exposure in the sulphate solution.

2.6 Mechanical Properties

The following list contains the list of mechanical parameters and the testing standard prescribed by CSA Annex U for the characterization of UHPFRC used in this thesis.

Compression Strength – CSA A23.2-9C

Poisson's Ratio and Modulus of Elasticity – ASTM C469/C1856

Linear Shrinkage – CSA A23.2-21C

Coefficient of Thermal Expansion – AASTHO T336

Creep Coefficient – ASTM C512

2.6.1 Compressive Strength

The minimum compressive strength requirement of UHPFRC is 130 MPa according with the AFNOR NF EN1370/CN (2013); the limit is set at 150 MPa in FHWA (2013), and at 120 MPa in Annex A8.1 of CSA-S6 (2018) and Annex U of CSA-A23.1 (2019). Due to the high compressive strengths of the material, SETRA-AFGC (2002) allows UHPFRC materials to be tested under compression with a loading rate ranging 0.24 MPa/s to 1.7 MPa/s. Kazemi and Lubell (2012) as well as Graybeal and Hartmann (2003) recommended that a loading rate up to 1 MPa/s be utilized so that the compressive strength is not affected for UHPFRC material. Moreover, Skazlic et al. (2008) reported a size effect on the compressive strength of UHPFRC specimens obtained from cylinders having 70mm diameter and 140mm height, when compared with 100mm diameter and 200mm high cylinders. The high compressive strength that is achieved by the UHPFRC material is due to its density and compact microstructure which enables its superior response to compressive load. The addition of fibers does not appear to affect the compressive strength before cracking, however, post cracking, the addition of fibers reduces its lateral strain dilatation which indirectly improves its compressive residual strength (Kazemi and Lubell 2012, Ye et.al 2012, Hassan et al. 2012, Orgass and Klug 2004)

2.6.2 Modulus of Elasticity

Equations 2.1 and 2.2 present empirical relationships between compressive strength and modulus of elasticity of UHPFRC. Graybeal (2019) reported a modulus of elasticity for the material tests in tension of up to 54 GPa. The Equation 2.1 was reported by Graybeal (2019) originally proposed by AASHTO (2019) to calculate the modulus of elasticity for f_c' values between 30 – 200 MPa. Ma et al. (2004) developed Equation 2.2 for calculating the elastic modulus of UHPFRC containing no coarse aggregates. Many other researchers have also reported the modulus of elasticity in agreement with Equations 2.1 and 2.2 (Gao et al. 2005, Ichinomiya et al. 2005, and Marijan et al. 2005).

$$E_c = 46200\sqrt{f'_c}\ in\ psi\ units \qquad \text{Equation 2.1}$$

$$E_c = 52500\left(\frac{f'_c}{10}\right)^{\frac{1}{3}}\ in\ psi\ units \qquad \text{Equation 2.2}$$

2.6.3 Poisson's Ratio

It is noted that UHPFRC is generally characterized by low values of the Poisson's ratio. Ozyildirim (2011) and Graybeal (2011) reported a Poisson's ratio of 0.18, whereas Simon (2009) reported a value of 0.2. Joh et al. (2008) reported a Poisson's ratio of 0.16. Ahlborn et al. (2008) reported a Poisson's ratio of 0.21. Lastly, Bonneau et al. (1997) reported a Poisson's ratio of 0.19. CSA A23.2 2019 notes a Poisson's ratio for conventional concrete of around 0.20 – 0.25.

2.6.4 Coefficient of Thermal Expansion

The SETRA-AFGC (2002) reported a coefficient of thermal expansion (CTE) value of 11×10^{-6}/°C. For the same variable, Graybeal (2011) reported a coefficient of thermal expansion of 14.7 to 15.6×10^{-6}/°C. Fehling et al. (2004) reported a CTE value of 12×10^{-6}/°C. Simon (2009) reported a CTE value of 10 to 12 $\times10^{-6}$/°C. Ahlborn et al. (2008) reported a CTE value of 13.6 to 14.8×10^{-6}/°C. Lastly, Behloul et al. (2002) reported a CTE value of 12×10^{-6}/°C. FHWA (2016) reported a range for CTE values for conventional concrete of around 8 $\times10^{-6}$/°C to 12 $\times10^{-6}$/°C.

2.6.5 Creep

The standard test method for creep in North America is the testing method ASTM C512 (2015). In this test, the creep specimens are subjected to axial stress where the length change is measured using a strain measuring device over time. The creep coefficient is calculated as creep strain divided by the initial instantaneous strain response. From several researchers in the field, the following creep coefficients are reported. Graybeal (2011) reported a creep coefficient of 0.29-0.78 having tested 4-inch diameter cylinders loaded at ages 4, 21, and 28 days. Graybeal also reported a creep coefficient of 0.32 to 0.85 which was measured after 30 minutes under sustained loading to indicate the high creep coefficient values during the short loading duration time. Burkart and Muller (2008) reported a creep coefficient of 16-35$\times 10^{-6}$/MPa specific creep values measured from differing ages of loading, specimen size, stress level, and curing conditions on UHPC. They measured a creep coefficient in the range of 0.9-1.3 after 100 days under load. They also reported that the creep coefficient was observed to decrease with age upon first loading and increased with specimen size. Ichinomiya et al. (2005) reported a creep coefficient of 28 to 40 $\times 10^{-6}$/MPa after 150 days under load for specimens loaded at 2 and 4 days, whereas for specimens loaded at 28 days the investigator reported a specific creep of 11×10^{-6}/MPa after 120 days. Nakov (2017) reported a creep coefficient for a conventional concrete mix C30/37 type concrete of 1.501 at 400 days.

Chapter 3. Durability Tests

The protocol prescribed by the Annex U to CSA A23.1 (2019) for evaluation of the durability of UHPFRC materials is meant to classify them in one of three categories that is mapped on the estimated duration of the service life of the resulting structural component, as defined in Table 1. Therefore, this is critical for the material selection and the assumptions made by the bridge designer given the conditions of exposure of the structure.

Table 1: Durability Rating (CSA A23.1:19 Annex U)

Durability limits (DL)					
	Abrasion loss (g)	Salt-scaling (kg/m^2)	Absorption (%)	Chloride Ion Penetration (Coulombs passed)	Sulphate resistance (% expansion maximum at 12 months)
Test Method	ASTM C944	CSA A23.2-22C	CSA A23.2-11C	CSA A23.2-23C	CSA A3004
DL 50	<5.0	<0.4	<3.0	<500	<0.05
DL 100	<1.0	<0.2	<3.0	<300	<0.05
DL 200	<0.5	<0.1	<3.0	<100	<0.05

The design service life of a structure requires a holistic approach and is not only dependent on material properties. At the time of writing this thesis, Annex U is under revision for the 2025 Code, and states that the durability limits for the acceptance of field testing have not yet been established, underscoring the need for more data collection before specific limits may be established.

The following section examines the practical implementation and resulting durability limits of the reference UHPFRC material studied in the present thesis. This material contains Portland cement, Fine sand, Silica Fume, Super plasticizers, water and is reinforced with 2% by volume, brass coated 20 mm long, 0.2mm diameter steel fibers (Azmee 2019).

3.1 Abrasion Testing

The abrasion test is intended to determine the rate of material depletion from a surface that is subjected to repeated mechanical distress. Therefore, the result of the test is measured in grams,

and represents the mass loss from a reference surface subjected to the prescribed load routine. As stated in Annex U, the loss due to abrasion is to be determined on specimens with no thermal treatment cured in 95% relative humidity for 28 days and tested using the ASTM C944 method. The standard requires a drill press with a chuck capable of holding and rotating the abrading cutter at a speed of 200 rotations per minute. A total force of 197 ± 2 N is exerted on a cleaned flat UHPFRC surface. The available drill press which was used during this test rotated at a speed of 260 revolutions per minute at its slowest speed. To obtain comparable data the total rotations was calculated, as specified at 200 r/min for 2 minutes, which corresponds to a total of 400 rotations. Thus, the total time of abrasion was modified to 1.538 minutes at a speed of 260 r/m. A total of three concrete cylinders were used to perform the test, as standard procedure a total of three abrasion tests on the same surface for a total of 2 minutes per abrasion. It is noted that on first running the test, the abraded surface was the finished specimen surface in contact with the mold. The amount of material loss was higher than expected, indicating that the water film that is accumulated on the mold surface causes a thin layer of porous concrete on the contact surface. To examine this hypothesis, cut surfaces were used for this test; cylinders were cut with a concrete saw and were cleaned of all remaining dust with a damp towel. The specimen was then again wiped with a dry towel and dusted with pressurized air to free any particles of dust remaining, and the abrasion test was conducted.

Figure 6: (from Left to right) (a) Abrasion Specimen 100mm × 150mm (Half Cut Specimen); (b) rotating stainless steel wheel; (c) Abrasion Cube Specimen 100mm × 100mm × 150mm)

The test setup included a rotating cutter bearing on the tested surface. The cutter was fabricated in the laboratory using pertinent steel parts (Figure 6b). The cutter comprised the following parts: a threaded rod, plain washers, dressing wheels, nuts, and a special T rod used to connect the

threaded rod with the chuck of the drill press. The dressing wheel was replaced after abrasion of each specimen or after three full cycles of abrasion testing, as it was observed during the abrasion tests that the dressing wheel sustained damage due to the high durability strength of the material as well as the use of double loading on the frictional surfaces of the dressing wheel. The damage on the dressing wheel did not occur in any particular location but rather was random. Where damage occurred on the ends of the threaded rod, it was found that it was due to improper placement of the rod in the drill chuck. To ensure all tests results reflected repeatable observations, the rod was aligned when inserted into the chuck using a right angle made from the chuck to the rod. Then, the rod was rotated at its intended rotating speed to see if the abrasion jig showed signs of bending or damage. It is important to note ASTM C944 does not specify a specific specimen size or abraded surface treatment. The results are shown in Table 2 and Table 3 contains the mass loss after each abrasion of 100mm diameter × 150mm height cylinders.

Table 2: Specimen Weights after each abrasion (100mm × 150mm cylinder)

Specimens	Initial Mass (g)	Before 1st Abrasion (g)	After 1st Abrasion (g)	Before 2nd Abrasion (g)	After 2nd Abrasion (g)	Before 3rd Abrasion (g)	After 3rd Abrasion (g)
1	1606.30	1606.30	1603.96	1603.22	1601.82	1600.94	1599.54
2	1460.62	1430.50	1429.04	1426.44	1424.08	1423.84	1421.94
3	1538.28	1538.14	1535.93	1535.22	1533.98	1533.01	1531.27

Table 3: Abrasion Loss (100mm × 150mm cylinder)

Specimens	Mass Loss 1st abrasion (g)	Mass Loss 2nd abrasion (g)	Mass Loss 3rd abrasion (g)	Average Mass Loss (g)	Average of all 3 Specimens (g)
1	2.34	1.4	1.4	1.71	1.78
2	1.46	2.36	1.9	1.91	
3	2.21	1.24	1.74	1.73	

Additional results are shown in Table 4 obtained from the abrasion test performed on the unfinished and finished surface of a cube specimen of size 100mm × 100mm × 150mm as mentioned in the preceding. (The 1st abrasion was performed on the unfinished surface of the cube where many irregularities in terms of smoothness of the surface existed. Followingly the 2nd and 3rd abrasion tests were performed on the molded surface of the specimen where the wall effect was

observed.) In comparison to the specimens tested in Tables 2 and 3, which were cut surfaces showed less abrasion than with the specimen tested in Table 4.

Table 4: Abrasion Test Results (100mm × 100mm × 150mm)

Abrasion Test Result					
Specimens	Initial Mass	1st Abrasion	2nd Abrasion	3rd Abrasion	Average Loss (g)
1	8466.3	8460.8	8460.4	8459.1	7.2
2	8696.5	8692.9	8692.7	8690.8	5.7
3	8508.4	8506.5	8504.9	8504.7	3.7
				Average	5.5
				Total Time Abraded	6 minutes

3.2 Salt-Scaling Test

The objective of the salt scaling test was to determine the resistance against flaky delaminator of the UHPFRC mix surface when it is exposed to freeze-thaw cycles in the presence of de-icing agents. Three 300 mm × 300 mm × 75mm slab specimens were cast for conducting this test. Of those, two specimens were tested following the testing method listed in Annex U, CSA A23.2-22C, while one specimen was tested following ASTM C672; the difference between the two test protocols is the solution used on the test specimen.

The testing apparatus used to perform the salt scaling test includes a freezing chamber capable of maintaining a steady temperature of -18 ± 3°C, a humidity chamber capable of maintaining a relative humidity of 45 – 55 %, a heat chamber where a temperature of 110 ± 5 °C can be maintained with an average evaporation rate of at least 25 grams per hour, a scale with a minimum capacity of 500g and capable of reading to an accuracy of 0.1g to measure the spalled material from the surface of the concrete, a filter media – 80 µm sieve for the collection of any spalled material, and a thermometer embedded in a control specimen as well as a thermometer to measure the ambient temperature.

Figure 7 (from left-right): (a) Salt Scaling specimen dyke placement. (b) 80µm sieve used to filter the solution. (c) Salt scaling specimens in freezing condition.

Before conducting the salt-scaling test, a control slab specimen of size 150mm × 150mm × 100mm was used with an embedded temperature probe to measure the temperature of the concrete at its core. Upon casting the control specimen special care was given when embedding the probe so that no water or air can travel along with the probe from the open air to the concrete core. The molds used were oiled with a light coating of mineral oil. Both the control specimen and salt scaling specimens were consolidated by tapping 30 times. The salt-scaling specimens are cured following CSA A23.2-3C for 14 days in moist storage and 14 days in air storage. To create ponding of salt solution on the surface of the slab specimens, four dykes were placed on the perimeter of the top surface as shown in Figure 7. The dykes were placed during the air storage period of the specimens' curing. They were made of a 35mm thick plastic board that was non-absorptive and waterproof. The dykes were installed with the use of a silicone sealant, and regularly checked for leaking. During the testing procedure on the 15th cycle, the dykes were re-sealed where leaking was observed. To ensure the freezer used is capable of maintaining the specified temperature, the control specimen was placed into the freezer for five consecutive days, while the temperature monitored over this period was constant at -18 °C. The humidity chamber used is also calibrated to ensure it is capable of maintaining the required humidity. To measure the evaporation rate present in the oven used, three griffin beakers were placed in the chamber, two were placed in opposite corners, and one in the middle. The evaporation rate was calculated after 4 hrs in the oven to be an average of 34.32 g/hr.

It was stated earlier that specimens 1 and 2 were tested according with the method of CSA A23.2-22C whereas specimen 3 was tested in accordance with ASTM C672. The salt scaling test for

specimens 1 and 2 started at an age of 28 days while specimen 3 was started at a mature age >56 days. The test surfaces on the specimens were covered with approximately 6mm of 3% sodium chloride by mass (reagent grade) mixed in distilled water for specimens 1 and 2. Specimen 3 was filled with 6mm of calcium chloride and distilled water with a concentration of 100mL of distilled water containing 4g of anhydrous calcium chloride.

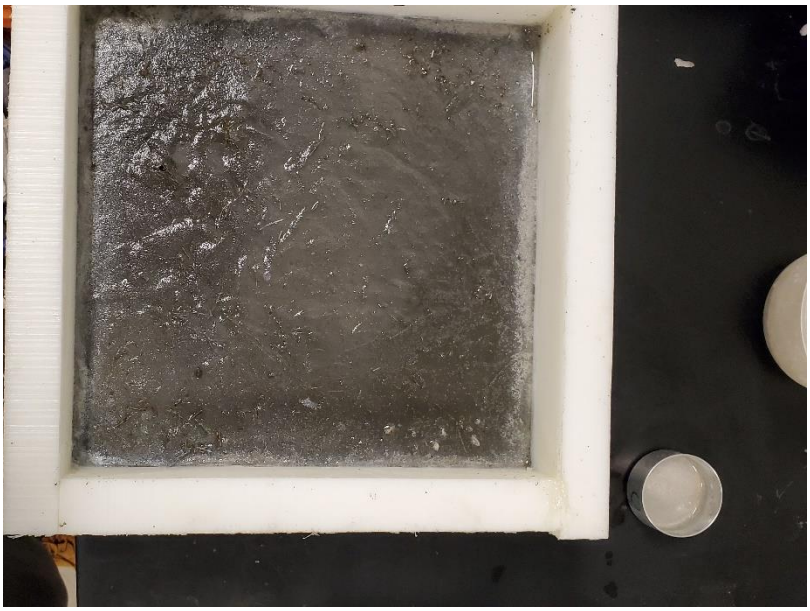

Figure 8: Salt scaling after 40 cycles

The saline solution made for specimens 1 and 2 was added at the end of the 14-day dry storage period for a total of 7 days. These specimens were covered with a plastic sheet to avoid evaporation of the solution. At the end of the 7-day saturation period, all 3 specimens were filled with new solutions and placed in a freezing chamber to begin the first freeze-thaw cycle. The specimens were then placed in the freezer for 17 hours and then placed for thawing in the humidity chamber for 8 hours. At the start of each cycle or before placing it into the freezer, the solution was checked to ensure at least 6mm of the solution was present. If the solution was below 6mm, additional distilled water was added. The scaling residue was measured at 5, 15,30, and 50 cycles. For each cycle measured, a new saline solution was used to rinse off any residue or scaling by tilting the specimen into a funnel and washing out the solution of all the flaked off concrete from the test surface. To ensure only the mass pertaining to the residue of the scaling was measured, the 80 µm filter sieve used was washed and dried by placing it in the oven at 110 °C for 4 hours in advance and left to cool for an additional 1 hour; the sieve was weighed after the cooling period. The saline solution was then strained through the sieve and weighed. The cumulative scaling represented in

terms of scaling measured in kg divided by the surface area exposed to the solution for specimens 1 and 2 were calculated at 0.015 and 0.019 kg/m^2 as shown in Table 5. The visual rating is given as per accordance with CSA A23.2-22C with 0 being no significant scaling observed listed under Table 6.

Table 5: Salt scaling result summary

Number of Cycles	Specimen # 1 (CSA A23.2-22C)	Specimen # 2 (CSA A23.2-22C)	Specimen # 3 (ASTM C672)	Visual Rating
5	0.05	0.08	0.15	0
15	0.19	0.23	0.25	0
30	0.46	0.57	0.59	0
50	0.64	0.79	0.96	0
Total (g)	1.34	1.67	1.95	-
Total (kg/m^2)	0.015	0.019	0.022	-

Table 6: Visual rating Scale for concrete surface (CSA A23.2-14 22C)

Category	Characteristics of Scaling surface (CSA A23.2-14-22C)
0	No significant scaling observed
1	Slight scaling (3 mm depth, maximum, no coarse aggregate visible)
2-A	Slight to moderate scaling of the surface mortar (possibly a few popouts)
2-B	Slight to moderate scaling of the surface mortar, (several popouts)
3	Moderate scaling of the surface mortar (some exposed coarse aggregate)
4	Moderate to severe scaling (significant surface mortar loss with exposed coarse aggregate)
5	Severe scaling (coarse aggregate visible over entire surface)

3.3 Absorption

The absorption test is used as a rapid measure of the capillary porosity of concrete and therefore it may serve as a measure of the compactness of the material microstructure. The test method essentially measures the amount of water absorbed when the material reaches stable weight in fully saturated conditions using as a reference the weight in the fully dried condition. Four cylinders

with a diameter of 75mm and height of 100mm were used to conduct the absorption test following Annex U which specifies a curing condition of 95% relative humidity for 28 days. According to CSA A23.2-11C with regards to the details of the testing procedure in order to obtain indications of water content (%), density (kg/m^3), absorption (%) and void (%). The testing apparatus included a scale sensitive to 0.01 g, an oven capable of maintaining a uniform temperature of 110 ± 5 °C, a humidity chamber capable of maintaining 50% ± 5 % relative humidity at 23 ± 2 °C and a scale which uses a hook to measure the weight from a wire attached to a mesh bowl. The cylinders were cast with a 2-minute flow diameter reading of over 200mm and were consolidated with 30 taps with a mallet. No release agent was used in these cylinder molds as it would affect the flow of air and water through the surface of the cylinder. The molds were filled using a one-way or single layer of concrete; this was done by taking large amounts of UHPFRC in a large trowel and poured until the molds were full. The cylinders were de-molded one day after casting and weighed immediately after demolding.

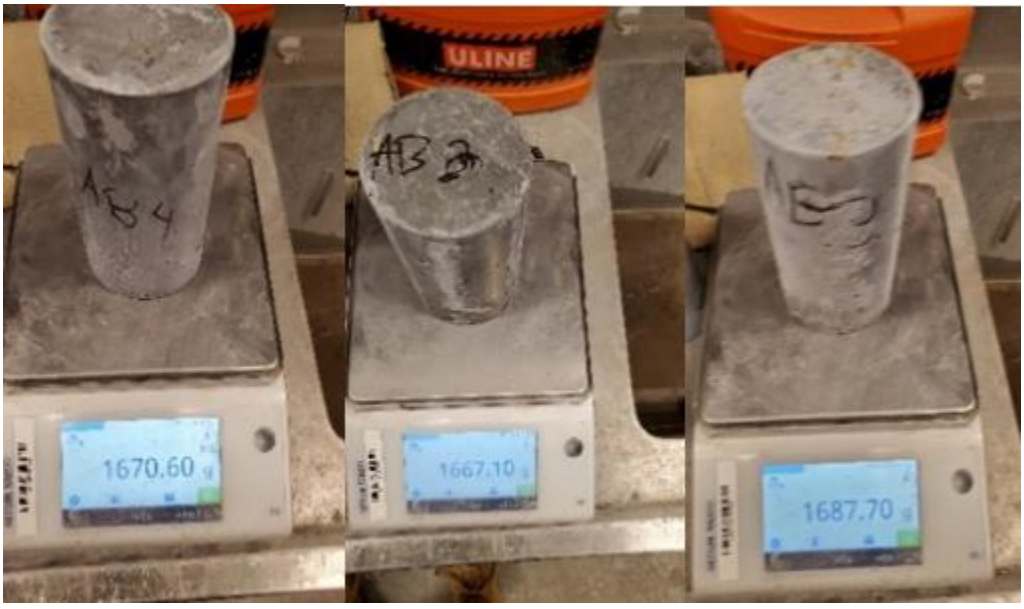

Figure 9: Absorption specimens weighed after demolding on a scale with an accuracy of 0.01g.

The mass measured immediately after demolding is denoted from hereon as Mass I. To measure the air-dry density, the specimens were conditioned in a controlled humidity chamber conforming to ASTM E104, maintained at a relative humidity of 50 % at 23 °C. The specimens were weighted at the age of 35 days and again at 42 and 49 days. On the 49th day, the mass of the specimens showed a difference of 0.192 %, 0.222%, 0.210%, and 0.260% respectively, deeming the change

at 7 days apart of less than 0.5% and therefore the specimens were considered “at equilibrium”. This mass was measured and was averaged at 2596.85 kg/m^3 as shown in Table 8. The specimens were then placed in an oven at 100 °C for 72 hours. After this time period the specimens were placed in a humidity chamber with 50% relative humidity at a temperature of 23 °C for 24 hours to allow the specimens to cool down to ambient temperature. After the specimens were cooled, the mass of the specimens was weighted, and the specimens were then returned to the oven for another two cycles. After completion of two cycles, the weight difference was found to be less than 0.5% compared with the weight values measured after completion of the first cycle; this new mass reading was labeled as mass A. To obtain the water content % the following expression was used:

$$\text{Water content} = \frac{I-A}{A} \qquad \text{Equation 3.1}$$

Furthermore, to determine the mass of the surface-dried cylinder in the air after immersion the cylinders were placed in the water tank at an ambient temperature of 24 °C for one day. The cylinders were taken out after one day of conditioning, wiped with a dry towel, and placed on a dry towel for 30 minutes. After 30 minutes the specimens were weighed and placed again in the water tank for another day and weighed after surface drying at a time of 30 minutes out of the water. This cycle is repeated two times at which point the mass from the first cycle was found to show a difference of less than 0.5%. This mass is noted as B. To obtain the absorption after immersion %, the following expression was used,

$$\text{Absorption after immersion} = \frac{B-A}{A} \qquad \text{Equation 3.2}$$

To determine the absorption after immersion and boiling, the specimens were immersed in a container filled with tap water and placed in an oven at 110 °C for five hours. After completion of the five-hour interval, the specimens were placed in the humidity chamber to cool for one day. The specimens were weighed after completion of the cooling period and returned to the oven with additional tap water added to the container for another 2 cycles. After two additional cycles, the mass difference between the first and last cycle was less than 0.5% and the absorption after immersion and boiling was calculated with the mass denoted as C. Using these readings, the absorption after immersion and boiling % is calculated from the following expression:

$$\text{Absorption after immersion and boiling} = \frac{C-A}{A} \qquad \text{Equation 3.3}$$

Lastly, the cylinders were suspended in water by using a scale with a hook on a wire and mesh bucket. The specimens' weights were measured suspended in a pool of water in a bucket; this mass reading was denoted as mass D. Table 7 lists the different masses obtained for each cylinder under varying procedures performed as discussed above. Table 8 summarizes the results obtained from the absorption test as required by CSA A23.2-11C. The formulas used to determine the Air-dry density, Oven-dried density, Density after immersion, Density after immersion and boiling and Void % are given in Equations 3.4 to 3.8:

$$\text{Air-dry density} = \frac{G}{C-D} * 1000 \qquad \text{Equation 3.4}$$

$$\text{Oven-dried density} = \frac{A}{C-D} * 1000 \qquad \text{Equation 3.5}$$

$$\text{Density after immersion} = \frac{B}{C-D} * 1000 \qquad \text{Equation 3.6}$$

$$\text{Density after immersion and boiling} = \frac{C}{C-D} * 1000 \qquad \text{Equation 3.7}$$

$$\text{Void \%} = \frac{C-A}{C-D} * 1000 \qquad \text{Equation 3.8}$$

Table 7: Mass obtained at each stage of the absorption test.

Cylinder	I (g)	G (g)	A (g)	B (g)	C (g)	D (g)
Specimen 1	1692.6	1689.48	1650.92	1678.27	1673.22	1024.67
Specimen 2	1704.65	1701.5	1662.75	1690.1	1689.98	1036.83
Specimen 3	1696.55	1692.92	1655.15	1683.71	1683.81	1029.61
Specimen 4	1691.1	1688.06	1649.56	1677.96	1682.56	1030.69

Table 8: Results for the absorption test.

Cylinder #	Water Content (%)	Absorption After Immersion (%)	Absorption after Immersion and Boiling (%)	Air-dry Density (kg/m^3)
C1	2.52	1.66	1.35	2605.01
C2	2.52	1.64	1.64	2605.07
C3	2.50	1.73	1.73	2587.77
C4	2.52	1.72	2.00	2589.57
Average	*2.52*	*1.69*	*1.68*	2596.85
Cylinder #	Oven-dried Density (kg/m^3)	Density after immersion (kg/m^3)	Density after immersion and Boiling (kg/m^3)	Void (%)
C1	2545.56	2587.73	2579.94	3.44
C2	2545.74	2587.61	2587.43	4.17

C3	2530.04	2573.69	2573.85	4.38
C4	2530.50	2574.07	2581.13	5.06
Average	2537.96	2580.78	2580.59	4.26

3.4 Chloride Ion Penetration

A total of three specimens were tested for chloride ion penetration. The specimens were cast in a one-way manner in which one large scoop was taken with a trowel to fill the 100mm × 200mm mold. Annex U (2019) requires the chloride ion penetration test to be performed on either molded or cut specimens tested following the testing method of CSA A23.2-23C. The annex also states that the test specimen may be fabricated from the matrix with or without fibers and that the test results could be adversely affected by to the steel fibers spanning across the specimen which can cause a short circuit in the testing apparatus. For the results shown below, no fibers are included. It is important to note that an industrial mixer is used to cast and mix the concrete in which some stray fibers were present. The molds were oiled with a small layer of mineral oil. The test performed consisted of monitoring the amount of electrical current passed through the specimen for 6 hours. A potential difference of 60V DC was maintained across the ends of the specimens with one side immersed in a solution of sodium chloride 3% by mass, and the opposite side in a solution of 0.3 N sodium hydroxide. The total charge passed through measured in coulombs represents the resistance of the specimen to chloride ion penetration. The specimens used to obtain the results were of a nominal size of 100 mm diameter cylinders cut to a length of 50 mm. The apparatus used to perform this test includes the Perma2-ready-made testing apparatus (Giatec Scientific). The Perma2 device used to perform the test included two testing cells, which are shown in Figure 10 (b). Lastly, a vacuum desiccator capable of holding a vacuum with three specimens, a vacuum pump, and reagent grade sodium chloride and sodium hydroxide were used.

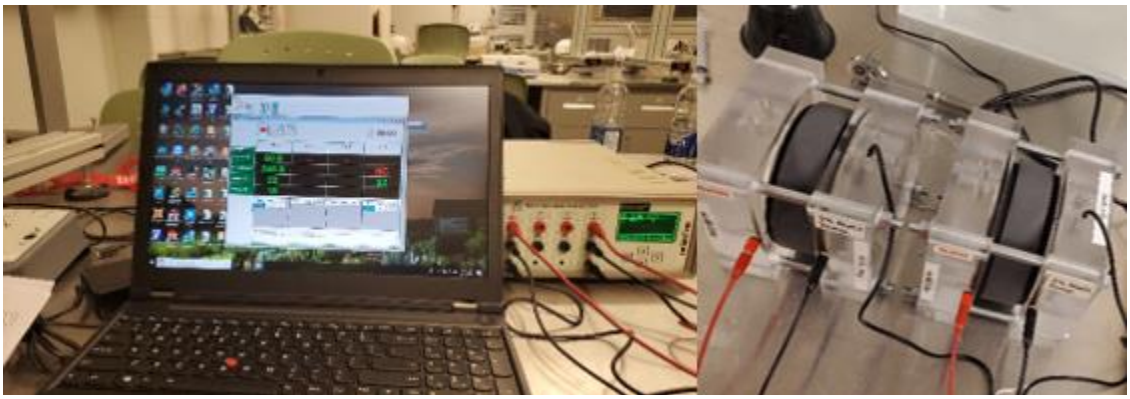

Figure 10: (left to right): (a) User interface of Perma2, (b) Perma2 test cell

The specimens tested were cured in a household cooler capable of maintaining stable humidity level while allowing for a pool of water to form at the bottom. A small humidifier was used to maintain the humidity at 95%. The cooler was modified with the use of a rubber gasket to extract the electrical wire through the cooler and into a wall outlet. The rubber gasket was used to maintain the humidity whilst allowing the humidifier to continuously provide humidity at 95% or higher. A further modification was done to the humidifier used, whereby a hole was made in the water container of the humidifier and the specimens were placed at a raised height in the cooler. The cooler was then filled with water up until the water could enter the humidifier's water container; the intent of this modification was to allow for continuous humidification in the cooler at large intervals of time. Figure 11 illustrates the curing cooler used before conditioning of the specimens.

Figure 11: Specimens in household cooler

Following CSA A23.2-3C, the specimens were cured for an extended period of 56 days. It is important to note that the specimens were transported in their molds to maintain the moisture from the time water was mixed into the dry mix. Before the specimens were prepared for conditioning,

a water-cooled concrete saw was used to slice a 50mm core extracted from the center of the specimen. To condition the core, the test method of CSA A23.2-23C Clause 8.3 was followed in accordance by allowing the specimens to surface dry in air, and then cutting the cores with a concrete saw. After cutting the cores, the specimens were surface dried for 3 hours. While drying the specimens were marked with either a T and B to indicate the top and bottom surface and a concrete sealer was used to coat the lateral surface of each cylinder. It is important to not seal the top and bottom of the surfaces which are to be tested, as they would affect the results of the test. The coating was allowed to dry as specified on the container of the concrete sealer. Next, the specimens were placed in a vacuum desiccator with both end faces of specimens exposed. The desiccator was then sealed with all three specimens and the vacuum was maintained for 3 hours. The desiccator was then filled with distilled water and the vacuum maintained for an additional hour. After one hour, the air was allowed to enter the desiccator. The specimen was then placed in a beaker under distilled water for 19 hours.

The testing procedure was as follows: before the completion of 19 hours, two 1L beakers were used to make the sodium chloride and sodium hydroxide solutions. The beaker was filled with 1L of distilled water and was weighed as an average of 990 grams; to make a solution with 3% sodium chloride, 29.94 grams of reagent was used to ensure 3% concentration by mass. Similarly, the sodium hydroxide solution was made with 1L of distilled water with a 0.3N concentration. Twelve grams of sodium hydroxide pellets were used to dilute the 1L distilled water into 0.3N sodium hydroxide solution. Figure 12 is shown for illustration of the chemicals weighed before making of the solution.

Figure 12: (a) Sodium Hydroxide used for RCPT (b) Sodium Chloride used for RCPT

To prepare the test cells, a stainless-steel wire mesh was placed inside each test cell's cup and hand tightened to ensure a firm electrical connection. After 19 hours, one specimen was taken out,

removed of excess water, and placed back into the cooler wrapped with a plastic bag with 95% humidity still present in the cooler. The other two specimens were fitted with a plastic spacer and rubber gaskets on the ends to ensure a tight sealed fit into the test specimen as is illustrated in Figure 13. The test cell is then filled with the NaOH and NaCl solution. Note that the specimens' top surface was placed alongside the NaOH and bottom surface with the NaCl solutions. Lastly, a temperature probe was inserted in the NaCl test cell which was also marked with 'Temp'. Before the test can be run the test cells were checked for any leaks. If leaks were present the specimens were taken out and adjusted until no leaking was present in a 10-minute time interval. The test cells were then attached to their corresponding terminals into the Perma2 measuring device. The testing device was then set to the testing standard of ASTM C1202 in its user interface and the test was conducted for 6 hours at which point the program was terminated automatically. No temperature spike was observed and were stable around 20 °C to 25 °C. The results obtained from the 3 cylinders are listed in Table 9. All specimens passed less than 100 coulombs which are considered negligible chloride ion penetration.

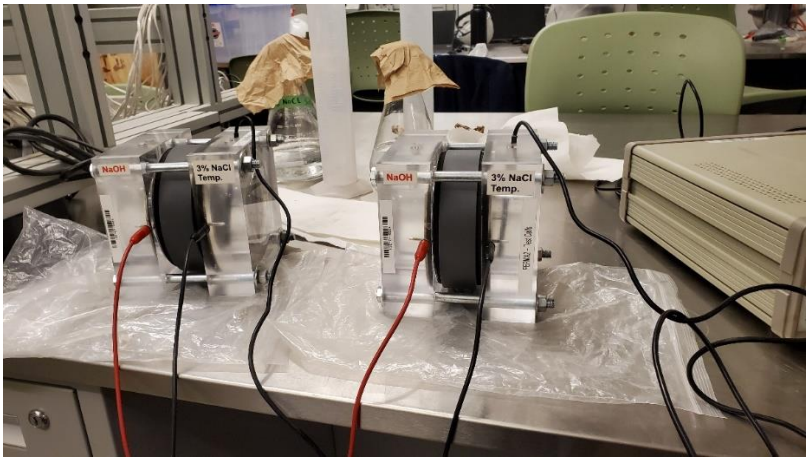

Figure 13: Specimens fitted in Perma2 test cells

Table 9: Results for RCPT

Chloride Ion Penetration	Age (Days)	Length (mm)	Diameter (mm)	Charge Passed (Coulombs)
Specimen 1	56	50.1	100.12	32
Specimen 2	56	51.4	101.5	37
Specimen 3	56	50.5	99.87	33
Average	56	50.66	100.50	34
Result	Charge < 100 Negligible as per Table 1			

3.5 Sulfate Resistance

Six bars with the size of 25mm × 25mm × 285mm were cast to conduct the sulfate resistance test following CSA Annex U and testing method CSA A3004-C8A. The prisms were cast as one-way prisms and were consolidated by tapping 30 times due to the flow reading of over 200mm. The testing method included in CSA A3004-C8A is used to determine the sulfate resistance of mortar bars by measuring length change from exposure to a sulfate solution. Twenty cubes were also cast along with the six bars. Immediately after the bars were molded, the molds were kept in a sealed container at a temperature of 35 ± 3°C as shown in Figure 14. After 24 hours the molds are removed from the curing tank and were transported to the laboratory.

Figure 14: Sulfate bars in the heated chamber after casting

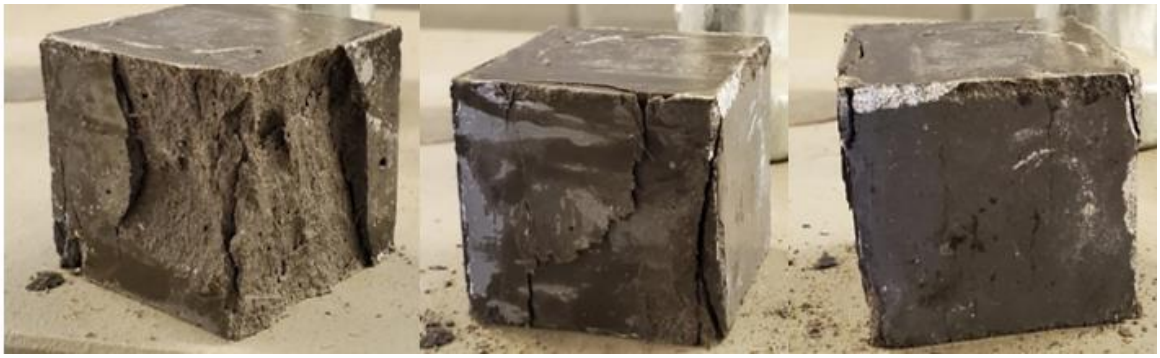

Figure 15: Cubes tested for Sulfate test and their failure mode

Upon the arrival of the specimens, the cubes were tested in compression and showed a strength greater than 20 MPa at an age > 24 hours (at around 98 MPa). At this point, the initial bar measurement was taken, herein noted as I. Before every reading of the test prisms were taken, the

reference invar bar was inserted, and the gauge was zeroed on the reference bar. The invar bar was then taken out and the prisms to be measured were wiped surface dry. Special care was given to the ends of the bars on the gauge studs and their seating caps on the length comparator as dust can accumulate and give poor readings. Before noting the length of the bar, each bar was rotated while inserted in the length comparator to ensure no prisms showed signs of bending. Bars that showed a change in length whilst rotating in the length comparator were taken out and the seating cups were inspected for dust or particles which may affect the results. These bars were then re-inserted into the length comparator. In the case the bars showed a difference in reading whilst rotating, the smaller reading was whilst the bar was rotating was noted. A difference of less than 0.006mm was noted as an average length change whilst rotating the bar in the length comparator. Figure 16 is shows the 6 bars being measure in the length comparator.

Figure 16: Sulfate bars in length comparator.

After all bars were measured, the invar reference bar was measured, and its reading was recorded again. This was done to note any changes in the zero-reference used by the gauge whilst measuring the individual lengths of each bar. The lengths of the bars were recorded at 1, 3, 4, 14, and 15 weeks, and at 4, 6, 9, 12, and 13 months. The sulfate solution was made using sodium sulfate at a concentration of 50g/L of solution. The total solution made was four volumes of solution to one

volume of mortar bar. Each bar consisted of a volume of 0.178L, to make enough solution for one bar 4 x 0.178L = 0.7125 L. For a total of 6 bars the total volume of sulfate solution needed was 4.275L. The total volume of the solution made after every reading was taken, was 4.3L of sulfate solution. To ensure the solution was conforming with ASTM C1012, the pH reading of the distilled water before the addition of sulfate solution, and the pH reading of the solution after the addition of the sodium sulfate were recorded. The distilled water used varied within a range of 6.7-7.2 pH, and a range of 7.2-7.6 pH respectively, as shown in Figure 18. The bars were placed in a container and the lid was closed so that the solution would not evaporate. The container used for storage is shown in Figure 17. The results are summarized in Table 10.

Figure 17: Sealed storage container used for sulfate bars.

Figure 18: (a) PH reading of distilled water, (b) PH reading of sulfate solution with specimen's bars

Table 10: Sulfate bar test results for up to 12 months

Sample ID	1	2	3	4	5	6	Average
Age	Length Change %						
Initial	-	-	-	-	-	-	-
3 weeks	-0.004	0.001	0.001	0.004	0.004	-0.001	0.00

4 weeks	0.058	0.060	0.062	0.063	0.064	0.059	0.06
13 weeks	0.091	0.067	0.073	0.067	0.068	0.061	0.07
15 weeks	0.081	0.083	0.086	0.084	0.087	0.082	0.08
4 months	0.106	0.106	0.112	0.109	0.110	0.104	0.11
6 months	0.109	0.112	0.116	0.116	0.114	0.109	0.11
9 months	0.108	0.106	0.109	0.112	0.110	0.112	0.11
12 months	0.108	0.109	0.112	0.111	0.111	0.139	0.11

The expansion due to exposure of sulfate solution done by Pierard (2012) showed no length change over 500 days, whereas the length change reported in the test conducted at York University show a length change in % of 0.11, as shown in Table 10. This is possibly due to the higher amount of sulfate concentration specified in the North American testing standards. Another possibility is the corrosion of the mortar as observed in Figure 19. It is not clear at the current time of reporting this thesis as to why the length change observed in the tests conducted was high when compared with the length change reported from the literature, therefore more investigation is recommended for sulfate attack of the UHPC mortars. Note: no steel fibers were used in the mortars tested for sulfate resistance.

Figure 19: Sulfate bars exposed to the solution after 3 months.

3.6 Summary of results

Table 11 summarises the durability property tested, the test method, mean and the durability category which it falls under following Table 1. Though Annex U provides the durability limits, these limits for the acceptance of field testing have not yet been established due to insufficient data collection, therefore these durability limits provided as service design life should include a holistic approach not dependent on material properties (CSA Annex U 2019).

Table 11: Durability tests and limits of Dura UHPFRC.

Property	Test Method	Test Results	Applicable Category/ Durability Limit (DL)
		Mean	
Abrasion	ASTM C944 /C1856	1.78 g	DL 100
Salt Scaling	CSA A23.2-22C	0.017 kg/m^2	DL 200
Salt Scaling	ASTM C672	0.022 kg/m^2	DL 200
Absorption	CSA A23.2-11C	1.68%	DL 200
Chloride Ion Penetration	CSA A23.2-23C	34 coulombs	DL 200
Sulfate Resistance	CSA A3004-C8A	0.11 %	Inconclusive

Chapter 4. Mechanical Tests

4.1 Introduction

This chapter presents results of an extensive experimental campaign conducted in order to develop a full material identity characterization of the UHPFRC material under study. The effects of the material characteristics and casting methodology on the mechanical and physical response of the material are explored. The full characterization of the material's mechanical response was based on the following suite of tests:

1) Compression Test in order to evaluate the stress strain response and peak strength,

2) Four-Point Bending Test in order to obtain data needed for extracting the tensile properties of the UHPFRC material through inverse analysis,

3) Modulus of Elasticity and Poisson's Ratio,

4) Creep Coefficient,

5) Linear Shrinkage, and

6) Coefficient of Thermal Expansion.

Along with these tests, further experimentation was done on larger size beams under FPBT so as to assess the effect of size on the results of inverse analysis for the tensile response of the material. The inverse analysis methodology and results are included in chapter 5.

4.2 Materials and Casting Methodology

Six mix batches of ultra-high-performance fiber-reinforced concrete (UHPFRC), were prepared. The batch identification is formally referred to as B1, the numeral corresponding to the sequence of the batch. All mixes were cast at Facca Inc. located in Ruscom station, Windsor, Ontario. The specific mix tested for the experimental phase of the thesis contains 0.2mm diameter, 20mm long, brass-coated steel fibers mixed at 2% by unit volume. Annex U from CSA A23.1:19 was referred to for the consistency properties listed under clause U.4.1.4. The flow of UHPC was determined following ASTM C1437, which states a brass flow table and brass flow mold conforming to specification C230 be used. The flow was determined by carefully wiping the flow table clean and

with a damp cloth, and then the flow mold was placed at the center of the flow mold. The UHPFRC mix was then transported into a trowel from which the flow mold was filled in a one-way action filling the mold. Before lifting the flow mold, the flow table was wiped of any UHPFRC residue with a damp cloth. Following Annex U, the UHPFRC mix was not tampered, nor the table dropped to encourage flow; instead, the flow mold was lifted within 1 minute after being discharged from the mixer, and the flow was allowed to elapse over the flow table at a time of 2 minutes ± 5 seconds. The diameter of the UHPFRC flow was measured along the lines of maximum and minimum diameter with each recording done to the nearest millimeter from which the average was calculated as the flow achieved for that specific mix. Figure 20 shows the pictures of molds, flow and filled molds during cast of batch one.

Figure 20: (a) Pictures of molds, (b) Flow, and (c) filled sulfate molds.

For mixes with a flow greater than 200mm, specimens were consolidated by tapping the sides of the mold 30 times with a mallet. For the UHPFRC mixes with a flow of less than 200mm the specimens were consolidated by dropping the filled molds at least 30 times, followed by tapping the sides of the mold 30 times with a mallet. The temperatures recorded in degrees Celsius and flow in mm are listed in Table 12 for all mixes. Immediately after all specimens were cast into their molds, the top surfaces of the molds were protected from dehydration from moisture loss to the atmosphere by covering the specimens in a polyethylene sheet as shown in Figure 21 below.

Table 12: Flow and Temperature of batches 1-6.

Properties	Batch 1	Batch 2	Batch 3	Batch 4	Batch 5	Batch 6
Temperature °C	25	25.5	24.5	25.8	22.9	25
Flowability (mm)	213	196	198	220.6	213	205

Figure 21: Filled mold covered with plastic to prevent moisture from evaporation.

It is worth noting that during batch 4 mixing, due to the clogging of fibers in the mixer, additional admixtures were added to extend the curing time. The history of each batch cast and received is summarized in Table 13. All specimens were de-molded upon taking delivery within 24 hours of casting. Specimens were inspected to ensure the results to be obtained are not affected. In the case of specimens failing inspection, those specimens were cast again to ensure the consistency and repeatability of the test were also not affected.

Table 13: Casting history of all batches.

Casting History	Batch 1	Batch 2	Batch 3	Batch 4	Batch 5	Batch 6
Casting Date	January 27th, 2020	June 23rd, 2020	August 18th, 2020	September 10th, 2020	November 11th, 2020	February 2nd, 2021
Delivery Date	January 28th, 2020	June 24th, 2020	August 19th, 2020	September 11th, 2020	November 12th, 2020	February 3rd, 2021

4.3 Mechanical Tests

4.3.1 Compressive Strength

Forty-eight cylinders with a size of 75mm × 150mm were cast over a total of 6 batches, as follows: ten cylinders were cast in batches 1-3, 3 cylinders in batches 4-6, and an additional nine cast in batch 5 which were cured differently from all the others. All cylinders were cast in a one-way pour by using a large trowel. The cylinders in batches #2 and #3 were consolidated by dropping the filled molds onto a hard leveled surface and then tapped 30 times on the sides with a mallet, whereas batches 1, 4, 5, and 6 were consolidated by tapping the sides of the molds 30 times with a mallet. All cylinder molds prepared for the compression test were lightly coated with mineral oil. CSA Annex U and testing method CSA A23.2-9C were used to conduct the compression test. Annex U was used to determine the testing rate which was used in the controls pilot testing machine to carry out the tests at a rate of 1 MPa per second. Before compression testing, the cylinders were ground using a concrete grinder as shown in Figure 22, until the surface of the cross-section was perfectly level. Note: some cylinders when ground showed large voids after the grinding was done, where the voids were large enough to cause a disruption in the results. In that case, back up cylinders were used; if the backup cylinders also showed the same large voids, then the best from among the cylinders were used and filled with small amounts of plaster to ensure improved distribution of the loading stress being applied. Before testing in the Pilot Testing Frame, the diameters of the top and bottom end surfaces were measured using a digital caliper. The average diameters were calculated based on the minimum and maximum diameters measured from the digital caliper. The average diameter and height were then input in the testing equipment when the test was conducted. The failure modes observed included a combination of Type 1 and Type 2 failures where, these are defined as follows:

Type 1 failure: Concrete Cylinder with reasonably well-formed cones on both ends.

Type 2 failure: Concrete Cylinder with well-formed cone on one end, vertical cracks running through caps, no well-defined cone on other end.

From each test, the failure mode and crack patterns were recorded. The majority of the specimens developed large cracks running horizontally rather than diagonal, whereas vertical cracks extended from the horizontal cracks. Illustration examples are depicted in Figure 23. The average values

obtained for the compressive strength for the six batches are included in Table 14 for all batches. The detailed test reports are given in Appendix 1.

Figure 22: Concrete cylinder grinder

Figure 23: Picture of the commonly observed failure mode.

Table 14: Compressive tests results of 6 batches

Results: Compression Test			
Batch #	Mean (MPa)	Standard Deviation	Characteristic Values (MPa)
1	146.7	7.7	135.9
2	137.5	4.1	131.8
3	138.3	4.1	132.6
4	135.5	2.6	131.8
5	137.2	4.7	130.6
6	144.2	6.2	135.5
Average	139.9	4.9	133.0

4.3.2 Compressive Strength: The Effect of Freeze Curing

Additional testing was done to determine the effect on compressive strength resulting from four different curing conditions. This mix of material was tested in batch 5 where the flow was recorded over 200mm and was consolidated with 30 taps with a mallet on the sides of the molds. These cylinders' molds were oiled with a light coating of mineral oil. The testing method used was the same as the one used for all compression tests as discussed above. The labels for the specimens in Table 15 FC1, FC2 and FC3 are used to distinguish the three different curing regimes, and the following last digit separated with a dash is for the specimen ID, for a total of 3 specimens tested per curing regime. The specimens labeled FC1 refer to the specimens cured in the freezer at a temperature of -18 °C after a set time of six hours, specimens labeled FC2 refer to the curing by placing the specimens outside the casting facility where the temperature varied depending on the weather, (during the fall season of 2020, November 2020 – December 2020), whereas , specimens labeled FC3 refer to the specimens cured in a chamber for 24 hours and then placed in the freezing chamber at - 18°C. All specimens were tested at an age of 28 days. The results of this study are summarized in Table 15. The failure mode for these cylinders was Type 1 and Type 2 failure modes. Failure mode pictures are included in Appendix 2.

Table 15: Freeze Curing effect on Compressive Strength

Batch 5: Compression Test-Freeze Curing				
Specimens	Average Diameter (mm)	Average Length (mm)	Compressive Strength (MPa)	Average Strength (MPa)
FC1-1	76.62	147.31	42.26	41
FC1-2	76.39	147.49	41.37	
FC1-3	76.62	147.85	38.68	
FC2-1	76.36	147.47	103.45	107
FC2-2	76.62	145.41	108.21	
FC2-3	76.10	145.45	109.15	
FC3-1	76.58	147.56	88.13	92
FC3-2	76.53	145.92	94.32	
FC3-3	76.71	147.19	93.08	

4.3.3 Poisson's Ratio and Static Modulus of Elasticity

Thirty cylinders with a size of 75mm × 150mm were used to test the Poisson's ratio and the static modulus of Elasticity. The cylinder molds were lightly coated with mineral oil. The filled molds

from batch 2 and 3 were consolidated by tapping the sides of the molds 30 times as well as dropped on a hard level surface 30 times, the filled molds from batch 1 were consolidated by tapping the side 30 times with a mallet. The specimens were de-molded 24 hours after casting and placed in a curing tank for 27 days until they were ready to be instrumented. On the 27^{th} day, the cylinders were instrumented with foil strain gauges. Before applying the strain gauges, the cylinders were ground until both ends of the specimen were leveled. A bubble level was used to ensure the ends were perfectly leveled and normal to the longitudinal axis of the cylinder. Some cylinders showed large voids present at the top after grinding; these voids were filled with plaster to stop failure from stress concentration where the large void was present. The plaster was only used to fill the voids. The foil strain gauges were of a gauge length of 10mm. The area on which the strain gauge was to be placed was first sanded lightly with fine sandpaper, wiped with a damp towel to clear off any loose particles, and then wiped with a dry towel.

The strain gauges were then applied onto the specimens at mid-height, with four gauges placed at diametrically opposing sides. Each side of the cylinder was instrumented with two strain gauges one placed horizontally and one vertically to measure the horizontal and vertical strains for each opposing side of the cylinder. A small drop of super glue was used to adhere to the strain gauge; then, the strain gauge was firmly pressed down with the use of the special non-adhering clear plastic sheet provided with each gauge. Once the gauge was applied, a protective white rubber tape was applied on the top of the gauge to protect it from damage during the transportation of the specimens around the laboratory. Once the strain gauges were applied, their respective electrical terminals were glued on the specimen and a lead wire was soldered onto them. Wires were then connected into the Data Acquisition System (DAQ) which was used to record the strain readings during the loading stage on the Universal Testing Frame (MTS). The testing method prescribed by ASTM C469 was used to conduct the experiment. Figure 24 illustrates the test setup as it was used in the study.

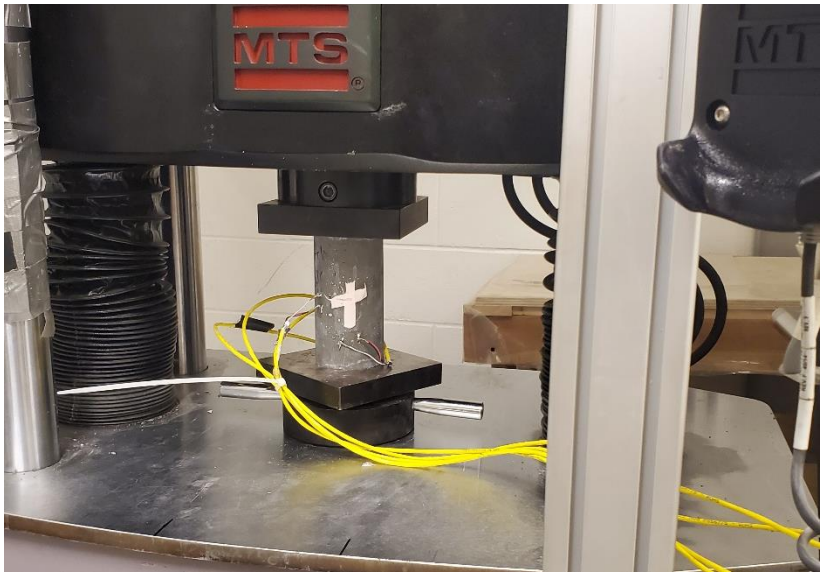

Figure 24: Poisson's ratio specimen in the MTS being tested

After placing the specimen on the lower bearing block of the MTS, the lower block was levelled. The MTS loading arm was then lowered just above the top of the specimen. Before the test was run, an average of at least five cylinders was taken for compressive strength obtained from the Pilot Testing Frame, where 40% of this load was used to load the specimens. The summary of the results is shown in Table 16.

Table 16: Poisson's ratio test and Modulus of elasticity.

Results Summary: E, ν		
Batch #	E (GPa)	ν
1	45.89	0.21
2	45.87	0.20
3	48.04	0.21
Average	46.60	0.21

4.3.4 Flexural Strength Tests

This type of test was conducted so as to provide evidence and data for the flexural response of the UHPFRC material, from which then the uniaxial stress strain response of the material in tension could be extracted using an inverse analysis approach. Thirty prismatic beams with a size of 100mm × 100mm × 350mm were cast in 3 batches. These prisms were cast in batch numbers 1, 2, and 3. All molds were lightly coated with mineral oil. All prisms were filled with fresh material with a one-way pour, due to the large volume of the prisms, multiple scoops and buckets were

used to fill the molds. The mold was filled × holding the scoop or bucket at one designated end of the molds, and the flow of the mix was used to fill the entire mold. Figure 25 is shown for illustration.

Figure 25: One-way pour of mix.

The molds filled in batch 1 were consolidated × tapping the sides of the molds 30 times, whereas batches 2 and 3 were consolidated additionally by dropping the molds 30 times onto a level ground surface. After each prism mold was filled, a wood strike off-board was used to level the top surface. Each prism for all three batches was covered with a plastic sheet to maintain the moisture present until they were transported for delivery to the laboratory. Batches 2 and 3 were additionally covered with plexiglass to better form the top surfaces of the molds. Figure 26 shows the molds being covered in the mixing facility.

Figure 26: Flexure prism molds covered with plexiglass and empty molds to help level the finish surface.

The prisms were cured in a water storage tank at a constant temperature of 22 °C. Figure 27 shows the beams from batch 1 stored in the water storage tank. All specimens stored in the tank were placed on top of a plastic mesh to allow free water all around the specimens.

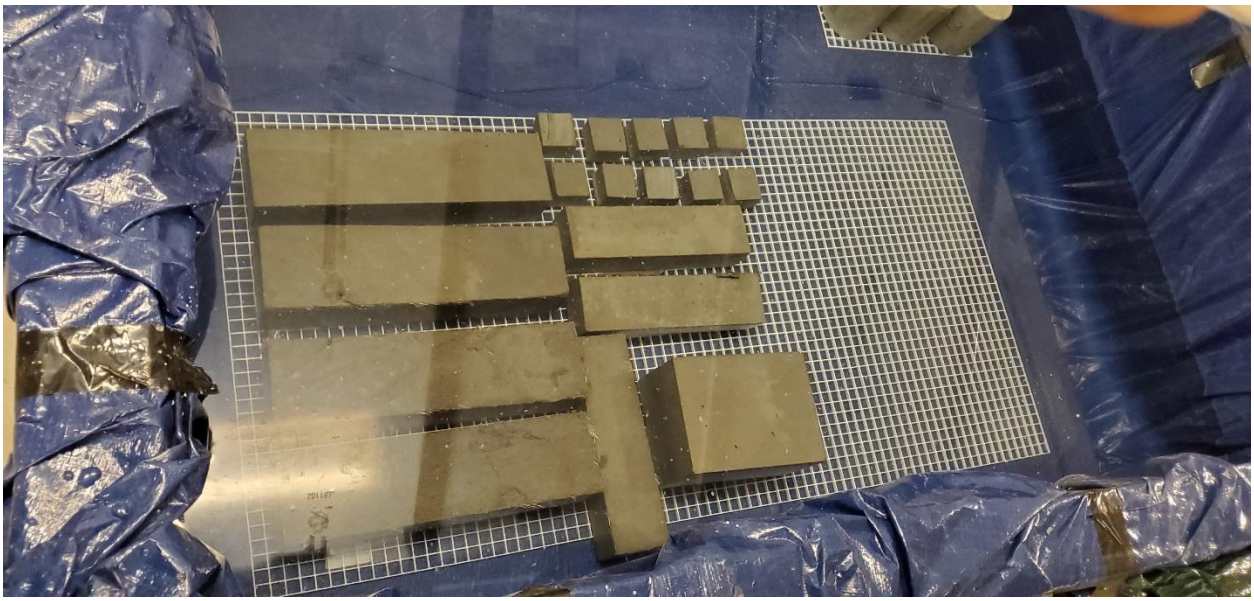

Figure 27: Water tank used to cure specimens

Testing of the prisms was done at 27, 28, and 29th days from the time of mixing, due to the loading rate used and a minimum of ten prims tested per batch. Note that each prism required an average time of testing of 1.5-2.5 hours from the time of instrumentation till the completion of the test.

Annex U prescribes the four-point bending test following ASTM C1609/C1609M, from which a testing machine capable of servo-controlled operation where the net deflection of the center of the beam was measured and used to control the rate of increase of deflection. This standard also prescribes a deflection measuring device such as a linear variable displacement transducer (LVDT) to be placed in such a manner as to capture the prisms' true deflection. Figure 28 (b) shows the testing setup used to conduct the flexure tests.

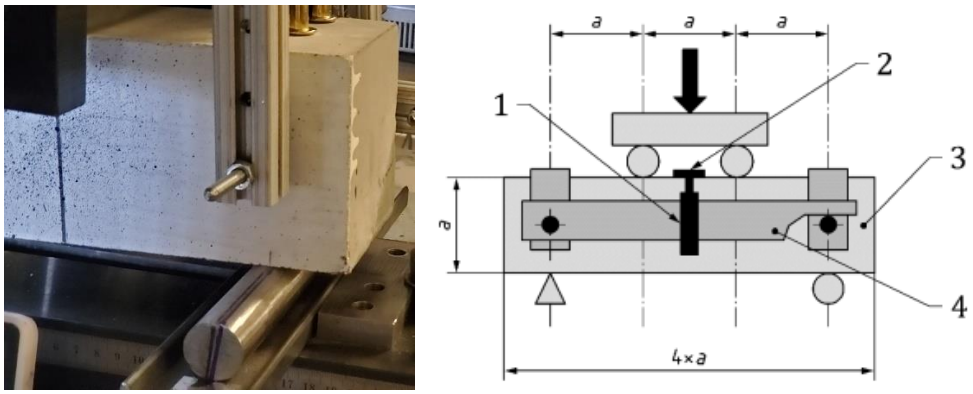

Figure 28 (Left to right): (a) Placement of instrumentation frame on prism specimens. (b) Third point loading illustration.

In illustration 28, ‘a’ refers to the height of the prism. The loading rollers were spaced at a distance ‘a’ from each other and the support rollers were spaced at a clear span of ‘3a’. For the beams tested and discussed the distance ‘a’ was 100mm. With reference to Figure 28 (b), if axis y is the span of the beam, axis z is the height of the beam and axis x is the out-of-plane width of the beam, the loading rollers were allowed to rotate about axis x and y. This rotation was allowed to ensure no eccentricity or torque effects are being considered and only flexural loading was applied. The support rollers were allowed to move along the span of the beam and rotate about the x axis.

The true deflection of the prism tested is the mid-height distance of the deformed members’ elastica from the chord which is defined between the end points over the supports, in order to exclude the effects of seating or twisting of the specimen on its supports. The instrumentation jig used to obtain the true deflection for all tests was arranged as a rectangular cage surrounding the prism and clamped at mid-height directly over the supports as shown in Figure 29. The LVDT was held in place on the threaded rods at mid-height over the support rollers with nuts. The aluminum beam as shown in Figure 30, had a pin connection on the left and a roller connection on the right side.

Figure 29: Instrumentation frame side and top view

The total travel of the LVDTs used was 10.550mm. For instrumentation purposes and to observe any torsional effects that may be observed during testing, the LVDTs were compressed to a travel of 8mm-9mm and tightened. Note: a thick rubber tape was placed around the LDVT, so the clamp used to tighten would not cause damage.

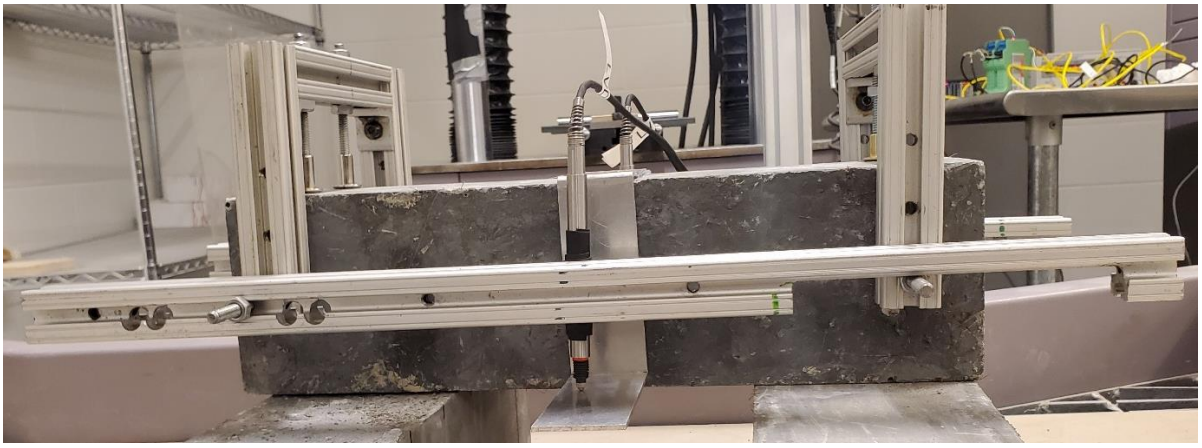

Figure 30: Placement of LVDTs and instrumentation frame

The threaded rods at the top of the beams were then lowered down and tightened so that the frame does not move or bend during testing. Next, the plate angles used to bear on the LVDTs were glued with hot glue directly at the mid-span of the beam. The plates were stiff and were bent at 90-degree angle. Lastly, of all the specimens tested only prisms with failure modes that represented flexure or flexure/shear were used. All specimens showing the behavior of torsion or pure shear failures

were not included in the results shown in the thesis. Due to the nature of the test and its sensitivity to shear and torsional failures approximately 20% of prisms tested were excluded. The majority of the specimens consisted of pure flexure failure or a combination of flexure and shear failure.

To align the beam onto the Universal Testing Frame, whilst allowing rotations and displacement along multiple axes of the loading jig, the following methodology was used. Once the instrumentation was fixed onto the prism, the beam was lifted and placed onto the support rollers with the LVDT's attached. The support rollers which were placed inside a transverse C channel were marked along their centerlines, to align the prism with a constant 300mm span. Note: it was critical to align both sides of the prism; if one side was not aligned, the beams would be prone to shear failure. Lastly, additional marks were drawn on the top of the prisms where the loading rollers were located at a relative distance of 100mm, to ensure their alignment (Figure 31). The four-point bending test was conducted using the MTS where a stepwise loading rate was used. A loading rate of 0.15mm/min was applied to the prisms before reaching 70% of the post-peak load. A loading rate of 0.05mm/min was applied to the post-peak softening branch. All prisms were tested until the post-peak residual strength had reached 20% of the peak load. The summary of the results obtained from the three batches is included in Table 17. The maximum bending stress σ_f was calculated from the following Equation 4.1 where P peak load, L is the total span, b is the width, and h is the height.

$$\sigma_f = PL/bh^2 \qquad \text{Equation 4.1}$$

Figure 31: Marks used to align the prism perfectly perpendicular.

Table 17: Summary of Bending stress for batches 1-3.

Results Summary: P_{max}, σ_f		
Batch #	P_{max} (kN)	σ_f (MPa)
1	84.79	24.89
2	103.27	30.01
3	99.73	29.08
Average	95.9	28.0

To determine if the failure modes are purely flexural, or contain shear or torsional contributions, the crack path was taken into account as well as the location where the crack occurred. For cracks that propagated within the distance "a" between the loading rollers and support rollers, the failure mode was classified as torsional or shear, whereas for cracks that were observed in the region of constant moment (the length between the intermediate loading rollers) the failure mode was classified as flexure. Photos included in Figures 32 (a) and (b) show examples of shear and flexural failures. Additional photos and failure modes are shown in Appendix A2.

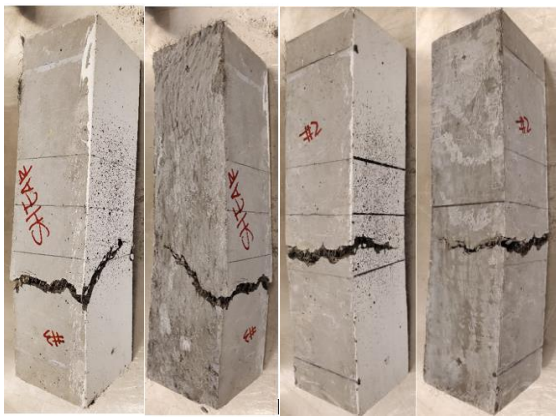

Figure 32: Failure Modes (from left to right) (a) Shear failure (b) Flexure Failure

4.3.5 Tensile Strength

There are currently a few different ways to test the tensile strength of UHPFRC either indirectly or directly; these include the standard Splitting Test, flexural beams under 4-point loads combined with Inverse Analysis, and direct tension tests on Dog Bone shaped specimens. The Splitting Tests are done in a manner where a concrete cylinder is placed on its side and load is applied through a diametric plane on the cylinder. The figure below shows a splitting test cross-section view. The tensile strength from this test is taken directly from the load at which the failure occurs divided by the cross-sectional area of the diametric plane of the cylinder, multiplied by $2/\pi$.

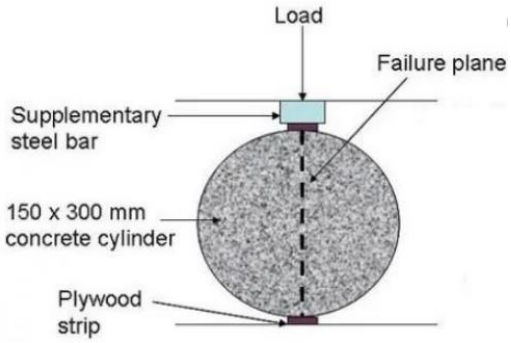

Figure 33: A splitting test of Cylinders

The problems with the splitting test depicted in Figure 33 when conducted on UHPFRC are that (1) fibers can be oriented randomly during pouring on account of the gravity effects and the pour happening in a tight space (i.e., the cylinder diameter), therefore leading to great variability in the splitting test results; and (2) after splitting the mode of load transfer reverts to that of compression in a direction parallel to the vertical crack, so that the result obtained is not representative of tensile response in tension, but rather of compressive response in the direction of the applied load. For this reason, the splitting test has been abandoned in the case of these strain resilient materials. Searching for palatable alternatives, the flexural modulus test which has been used in normal weight concrete was adopted for evaluating the tensile response of UHPFRC. However, after cracking, uncertainties in the interpretation of the results obtained from this test also arise. These are owing to the inherent material nonlinearity which prevent the confident evaluation of the milestone points of the tensile stress-strain response. To this end much debate has existed in the research community focussing on the tensile response characterization of UHPFRC and much of it is reflected by the discord among different codes (Yang 2019). In Canada, Annex 8 (2019) uses an approach originally developed in Spain by Lopez et al. (2017), whereas different procedures

developed in France and Switzerland are recommended in Annex U (2019). Here, the former approach has been used for consistency with Annex 8 (2019) to CSA-S6 since the intended application of the materials is mostly bridge construction.

The inverse analysis is performed on the results obtained from a 4-point bending test conducted on a plain UHPFRC concrete beam; the method is intended for THFRC materials. This method is an indirect way of getting the tensile strength and corresponding strain values particularly in the range beyond cracking. To apply it, 4 characteristic points are selected from the Load-Deflection graph from which a set of parameters are obtained, and the stress-strain or stress vs crack width plots are developed. Based on previous testing of the approach (Yang 2020), concerns have been raised regarding the bounds of its applicability on account of the many empirical coefficients that have been calibrated by the developer on a limited database; for this reason, more experimental validation is needed.

As an alternative to inverse analysis of flexural prism tests, direct tension tests have been proposed. This type of test is done on specimens having either prismatic form or with widened ends resembling a dog bone to facilitate gripping. In this type of test, instrumentation is usually installed in the mid-point of the specimen. In this setup uniform tension is applied without other stress combinations, and it is considered ideal for characterization of the tensile material properties of strain ductile materials. In the absence of eccentricities and other unaccountable effects, the concrete specimen develops cracks normal to its longitudinal axis. The figure below shows the apparatus for this test as well as the so-called dog bone specimen.

Figure 34: Dog Bone Direct Tension Test

(Graybeal, Benjamin & Baby, Florent (2019). Tension Testing of Ultra-High-Performance Concrete.)

In the present study, the tensile strength of the UHPFRC material was obtained from direct and indirect tensile tests, including the four-point bending test, and direct tensile test with various specimen geometries. The nominal dimensions of the specimens tested under direct tension are illustrated in Figure 35. All specimen molds were lightly coated with mineral oil. The specimen molds were filled with a one-way pour. Upon the arrival of the specimens after de-molding, the specimens were left for curing in a water curing tank for 28 days. At the age of 28 days, the specimens were stored in a refrigerator until testing to stop further hydration beyond the reference age. All specimens were tested with a loading rate of 0.00254mm/s. Longitudinal Carbon Fiber Reinforced Polymer (CFRP) strips were epoxied at the ends and outside the gauge lengths. This was done to promote failure within the gauge length. AASHTO (2013) and SIA (2014) type specimens were tested by gripping them in the ends with bearing action which transfers the load through friction between the MTS grips and the CFRP strips. A double -T dog-bone specimen form was also considered (Georgiou and Pantazopoulou, 2016) were loaded with bearing action applied at the armpits of the specimen through a specially designed steel frame as shown in Figure 36. The steel frame was pulled in opposing directions, causing direct tensile stresses in the central part of the specimen. A summary of the results is shown in Table 19.

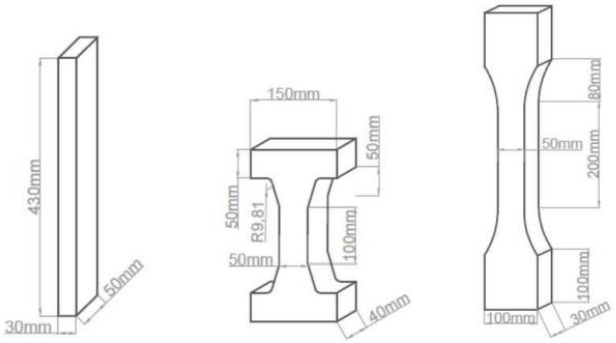

Figure 35: Nominal dimensions of direct tension specimens: from left to right: AASHTO (FHWA 2013), Georgiou and Pantazopoulou 2016, SIA2052 2014.

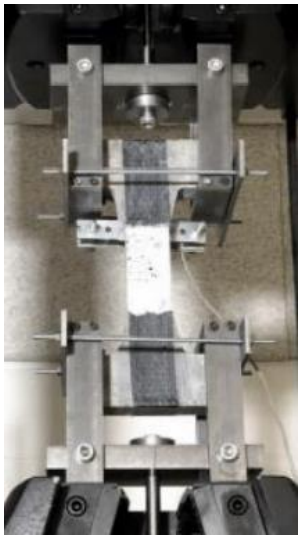

Figure 36: Georgiou and Pantazopoulou (2016) type specimen loading frame.

Table 18: Tensile strength from varying specimen geometries

Specimen	Tensile Strength (MPa)	Average Tensile Strength (MPa)
B4-SIA-2	8.15	9.8
B4-SIA-3	11.54	
B5-SIA-1	14.78	13.1
B5-SIA-2	13.30	
B5-SIA-3	11.37	
G-P-1	5.74	5.4
G-P-2	5.15	
GB-1	12.74	13.3
GB-2	13.47	
GB-3	13.67	

The tensile strength as reported in the table above is calculated from the Equation 4.2.

$$\sigma = F/A \qquad \text{Equation 4.2}$$

where F is the peak force, and A is the area of the cross-section within the gauge length. The specimens which relied on the bearing action of the MTS grips showed signs of slip until the crack had fully opened the cross-section. This was observed with DIC analysis done on select specimens from each test. The variance of the tension test results reported above indicate a further need for investigation for direct tension tests conducted as for setups with shear and bearing action to create a tension failure in the specimen. This variance could be as a result of inconsistent specimen

geometry which is evident when using wood molds. Splitting tests were conducted on six cylindrical specimens having 100mm diameter and 200mm length. These cylinders were cut in half with a water-cooled concrete saw and tested as two separate specimens. Of the six, three were tested with a wood strip placed at the top and bottom contact surface of the testing setup and three without, in direct contact with the loading plates. The tests conducted without the wood inserts gave more conservative results as depicted in Figures 37 and 38.

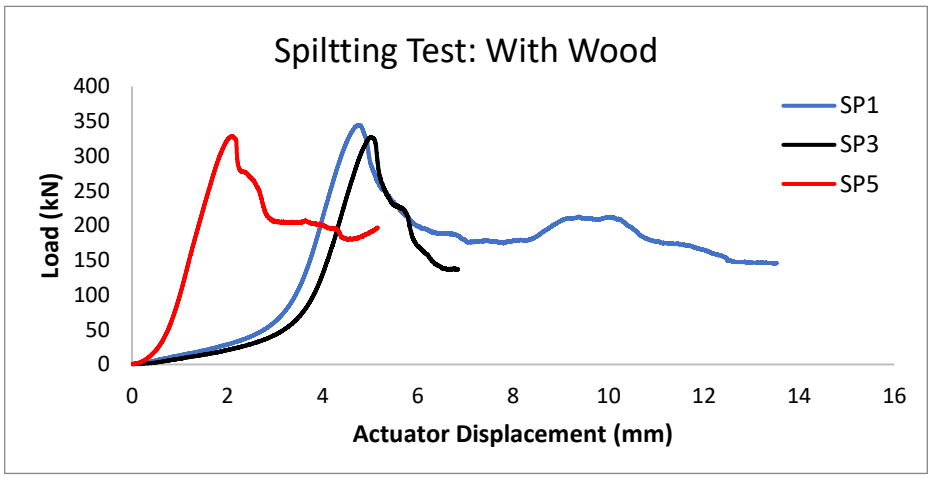

Figure 37: Splitting tests with wood strip placed between the cylinder and the loading plate

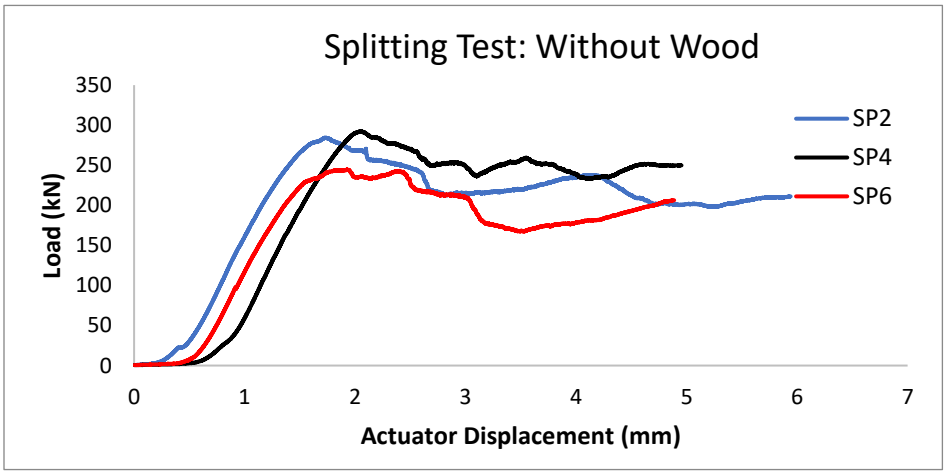

Figure 38: Splitting tests with direct bearing of the loading plates on the cylinder.

The average tensile strength calculated from the splitting test with wood strips was calculated as 16.6 MPa, whereas the average tensile strength calculated from splitting tests without the strips was 15.9 MPa.

4.4 Physical properties of the UHPFRC

These are properties that concern the length change of UHPFRC with time or in response to external exposure to natural phenomena. These include the linear shrinkage, creep and coefficient of thermal expansion. The following sections describe the procedures followed to measure these properties.

4.4.1 Linear Shrinkage

Five prism specimens with the size of 75mm × 75mm × 295mm were cast to test the linear shrinkage following Annex U (2019) and testing method CSA A23.2-21C. This test procedure was used to determine the length change under controlled conditions of temperature and moisture. The apparatus used for this test are as follows; a refrigerator that was unplugged and was used as a humidity chamber capable of maintaining a relative humidity of 50% ± 4%, with the door propped open enough to allow an evaporation rate of 15mL/24 hours ± 3mL. The evaporation rate was measured by placing a 1L griffin beaker filled to 500mL. After 7 days the beaker had dropped to 410mL which indicated an evaporation rate of 12.85 mL/day. Additionally, the length comparator was also used to determine the length change. The specimens were consolidated by tapping the sides of the molds 30 times. A light coating of mineral oil was used on the molds. The specimens were de-molded at an age of 24 hours and placed in saturated lime water solution for 30 minutes. The specimens were measured for their initial length. The specimens were additionally cured in lime water until the 7d age. The specimens were measured at the age of 7d which was noted as its 0-day drying age. After the specimens' lengths were recorded, they were placed in the humidity chamber at 50% relative humidity. The specimens' lengths were recorded at 1, 4, 7, 14, 21, 28, 56, and 90 days.

Figure 39: Linear shrinkage specimens in length comparator.

The length change was calculated as shown in Equation 4.3 where L_x is the comparator reading of the specimen at the age of interest, L_b is the initial or base comparator reading, and L_g is the gauge length of 295. The results of the linear shrinkage test are shown in Table 20. Length change (%):

$$L = \frac{(L_x - L_b)}{L_g} * 100 \qquad \text{Equation 4.3}$$

Table 19: Length change due to shrinkage.

Age of Specimen (D)	Drying Time (D)		Linear shrinkage (%)			
		Prism 1	Prism 2	Prism 3	Prism 4	Average
7	1	0	0	0	0	0
11	4	0	0	0	0	0
14	7	0.006	0.004	0.006	0.004	0.005
21	14	0.007	0.005	0.009	0.004	0.006
28	21	0.009	0.008	0.008	0.005	0.006
35	28	0.011	0.012	0.011	0.009	0.011
63	56	0.012	0.014	0.011	0.009	0.012
97	90	0.011	0.015	0.012	0.009	0.012

4.4.2 Coefficient of Thermal Expansion

A total of four cylinders with a size of 75mm × 150mm are used to test the coefficient of thermal expansion following Annex U (2019) and the testing method of AASHTO – T 336-15. The testing

method used determines the coefficient of thermal expansion (CTE) of cylindrical specimens maintained in a saturated condition. The testing method determines the CTE of the UHPFRC by measuring the length change of the specimen due to a specified temperature change. The CTE was calculated by dividing the length change by the temperature change and then by the specimen length. The testing apparatus is shown in Figure 40; it includes two sous-vides, a water tank, 1 control specimen, a digital demec gauge, and demec gauge studs. For the tests discussed in this thesis, pieces of wood were used to cover the top to allow the water to maintain its temperature throughout the height of the water.

Figure 40: Test setup for C.T.E

The specimens were cast in a one-way pour. The flow measured for this batch of materials had a flow of greater than 200mm and was consolidated by tapping the sides of the molds 30 times. The specimens were conditioned by submersion in limewater in a storage container maintaining a temperature of 23 °C. The specimens are weighted at an age of 38 days and were 1709.15 g, 1679.9 g, 1686.25 g, 1703.6g respectively. The specimens were weighed again at 39 days in 1711.45g, 1682.6g, 1689.1g, and 1705.6g, and the difference in weight was calculated at 0.134%, 0.160%, 0.169%,0.117% respectively. Before the specimens were weighed, they were surface dried with a dry towel. Since the difference of weights was less than 0.5% the CTE test was ready to commence. The specimens were then instrumented using a digital demec gauge. A total of four demec gauge

lines were used in the test. Each set of demec gauge lines were placed at diametrically opposing sides.

To ensure the gauge studs were perfectly diametrically opposite, the cylinders' diameters of the top and bottom surfaces were measured. Two lines were then drawn at right angles to each other. Since the cylinder was of a small diameter of 75mm, it was deemed important to consider the offset that the writing utensil may have. After two lines were drawn at the top and bottom of the cross-section area, a bobber was hung with a string and a straight vertical line was drawn. The surface on which the bobber was placed was checked for its level with a bubble leveler, and the bottom surfaces of the cylinders were also ground to a perfect horizontal level. This end of the cylinder was then placed on a leveled surface and the bobber was then used to draw perfectly vertical lines. The gauge studs were glued first with a very high strength adhesive capable of maintaining its strength under high temperatures. The gauge studs were then secured with hot glue to minimize any displacements that might take place when placed in the hot water.

The gauge studs were spaced using the reference bar included in the digital demec gauge testing apparatus, this bar was used to space the gauge at 100mm. The specimens were left to rest for 3 hours to allow the glue to adhere to the UHPFRC surface. (The areas where the studs were to be placed were lightly sanded and wiped clean to allow the glue to adhere effectively.) Figure 41 is shown to illustrate the gauge lines drawn and measured using a digital gauge length reader.

Figure 41: Demec gauge and gauge readings on C.T.E specimens.

The testing procedure as prescribed by AASTHO uses a temperature range of 10°C to 50°C, which was difficult to conduct because it requires immersion of the specimen in a water bath and

measuring the expansion as the temperature of the water grows within the prescribed range. The test done in this thesis was conducted in a temperature regime of 15°C to 55°C. This temperature range was used because the tap water available for use enters the testing facility at a steady temperature of 13 ± 2 °C at the time of testing. Before the water in the tank was filled, all four specimens were placed in the center of the tank along with the control specimen which contained a temperature probe embedded in its core. This specimen was used to measure the equilibrium of the temperature from the water present to the core of the concrete specimens. It was recommended by the testing method to start the test at warmer temperatures; the test was therefore conducted with the first cycle starting at 55°C. The sous-vides were set to a temperature of 55 °C, and the water was filled as high as the top surface of the temperature control specimen. After the temperature in the tank and the temperature reading taken of the control specimen indicated equilibrium, the gauge readings were recorded at intervals of 10-mins over a ½ hour period, until two successive measurements showed a difference of less than or equal to 0.00025 mm. In the case of two consecutive readings not showing a difference of less than or equal to 0.00025mm, additional readings at 10-min are taken until 4 consecutive readings showed a difference of less than 0.00025mm. When one successful reading was taken, the temperature was also recorded to 0.1 °C precision. Next, the water from the tank was emptied and the tank was refilled with water entering at a temperature of 13 ± 2 °C. The water in the tank was emptied and refilled until the control specimen read a core temperature of 15 degrees at a time interval of 15 mins or more. Once equilibrium was reached, the measurements were taken similarly as described above. The test was concluded when the results of two CTE values were obtained from two test segments that varied not more than 0.7 micro strains. Note: a segment was the measured length change for a given heating (15°C to 55°C) or cooling (55°C to 15°C), and a cycle comprised two consecutive segments. The CTE for the cooling interval is reported in micro strains calculated from Equations 4.4 to 4.7. The CTE for the heating interval was reported in micro strains calculated from Equations 4.8 to 4.11. Note: the subscripts used for Equations 4.4-4.7 indicate cooling and the subscript used in Equations 4.8-4.11 indicate heating. The gauge line A-A was diametrically opposite to gauge lines C-C, similarly, gauge lines B-B were diametrically opposite to gauge line D-D. The variable A’ refers to gauge lines A-A under cooling, the same was done for gauge lines B-B →B’, C-C→C’, D-D→D’. Lastly variables X, Y and Z are temperatures in °C.

$$CTE1_c = \left(\frac{\frac{A'-A}{100}}{Y-X}\right) * 10^6 \quad \text{Equation 4.4}$$

$$CTE2_c = \left(\frac{\frac{B'-B}{100}}{Y-X}\right) * 10^6 \quad \text{Equation 4.5}$$

$$CTE3_c = \left(\frac{\frac{C'-C}{100}}{Y-X}\right) * 10^6 \quad \text{Equation 4.6}$$

$$CTE4_c = \left(\frac{\frac{D'-D}{100}}{Y-X}\right) * 10^6 \quad \text{Equation 4.7}$$

$$CTE1_h = \left(\frac{\frac{A'-A}{100}}{Z-Y}\right) * 10^6 \quad \text{Equation 4.8}$$

$$CTE2_h = \left(\frac{\frac{B'-B}{100}}{Z-Y}\right) * 10^6 \quad \text{Equation 4.9}$$

$$CTE3_h = \left(\frac{\frac{C'-C}{100}}{Z-Y}\right) * 10^6 \quad \text{Equation 4.10}$$

$$CTE4_h = \left(\frac{\frac{D'-D}{100}}{Z-Y}\right) * 10^6 \quad \text{Equation 4.11}$$

The summary of the results is shown in Table 21. An additional study was done to obtain the CTE values under less harsh temperatures included in Table 22. The temperatures used here were, on one end the ambient laboratory temperature of 21°C - 22°C and then on the other end, placed in a refrigerator to cool to 3°C. This test was performed using the same methodology as used in the CTE values obtained from temperature ranges of 15°C – 55°C. The CTE values measured under 21°C - 3°C were similar to the harsher temperatures of 15°C – 55°C. Note: The readings provided in Tables 21 and 22 in the rows with gauge line readings A-A, B-B etc. and A'-A', B'-B' refer to the length change from its reference value, with positive values showing expansion and negative values indicating shrinking. The rows with contain "-" indicate the gauge lines destroyed due to the harsh temperatures used. The average C.T.E values are reported also in the table as these were the values which determined if each consecutive segment of cooling or heating displayed a difference of less than 0.5%.

Table 20: C.T.E values (Temperature of 55°C -15°C)

Cylinder	C1			C2			C3			C4		
Test #	1	2	3	1	2	3	1	2	3	1	2	3
X °C	54.2	54.2	54.2	54.2	54.2	54.2	54.2	54.2	54.2	54.2	54.2	54.2
A-A (mm)	0.048	0.05	0.048	0.043	-	-	0.035	0.037	0.036	0.038	0.049	0.04
B-B (mm)	0.043	0.046	0.042	0.037	0.041	0.039	0.036	-	-	0.042	0.046	0.043
C-C (mm)	0.036	0.043	0.044	0.035	0.04	0.037	0.038	-	-	0.048	0.057	0.051
D-D (mm)	0.036	0.038	0.035	0.035	0.039	0.036	0.046	0.045	0.045	0.031	0.034	0.034
Y °C	15.4	15.4	15.5	15.4	15.4	15.4	15.4	15.4	15.4	15.4	15.4	15.4
A'-A' (mm)	-0.015	-0.012	-0.013	-0.016	-	-	-0.035	-0.028	-0.027	-0.018	-0.015	-0.016
B'-B' (mm)	-0.02	-0.018	-0.019	-0.028	-0.028	-0.028	-0.026	-	-	-0.024	-0.018	-0.02
C'-C' (mm)	-0.024	-0.02	-0.024	-0.029	-0.025	-0.028	-0.03	-	-	-0.018	-0.014	-0.015
D'-D' (mm)	-0.026	-0.023	-0.026	-0.031	-0.026	-0.026	-0.025	-0.018	-0.022	-0.032	-0.031	-0.031
CTE1	16.237	15.979	15.722	15.206	-	-	18.041	16.753	16.237	14.433	16.495	14.433
CTE2	16.237	16.495	15.722	16.753	17.784	17.268	15.979	-	-	17.010	16.495	16.237
CTE3	15.464	16.237	17.526	16.495	16.753	16.753	17.526	-	-	17.010	18.299	17.010
CTE4	15.979	15.722	15.722	17.010	16.753	15.979	18.299	16.237	17.268	16.237	16.753	16.753
Average	15.979	16.108	16.173	16.366	17.096	16.667	17.461	16.495	16.753	16.173	17.010	16.108
Z °C	54.2	54.2	54.1	54.2	54.2	54.2	54.2	54.2	54.2	54.2	54.2	54.2
A-A (mm)	0.05	0.04	0.05	-	-	-	0.037	0.037	0.0377	0.049	0.048	0.048
B-B (mm)	0.046	0.042	0.047	0.041	0.042	0.041	-	-	-	0.046	0.045	0.046
C-C (mm)	0.043	0.044	0.042	0.04	0.044	0.042	-	-	-	0.057	0.055	0.056
D-D (mm)	0.038	0.035	0.037	0.039	0.035	0.035	0.045	0.046	0.045	0.034	0.033	0.033
CTE1	16.753	13.402	16.321	-	-	-	18.557	16.753	16.675	17.268	16.237	16.495
CTE2	17.010	15.464	17.098	17.784	18.041	17.784	-	-	-	18.041	16.237	17.010
CTE3	17.268	16.495	17.098	17.784	17.784	18.041	-	-	-	19.330	17.784	18.299
CTE4	16.495	14.948	16.321	18.041	15.722	15.722	18.041	16.495	17.268	17.010	16.495	16.495
Average	16.881	15.077	16.710	17.869	17.182	17.182	18.299	16.624	16.972	17.912	16.688	17.075

Note: Gauge lines marked with "- "are the gauges that had been destroyed due to the harsh temperatures used.

Table 21: C.T.E values (Temperature of 20°C -3°C)

Cylinder	C1			C2			C3			C4		
Test #	*1*	*2*	*3*	*1*	*2*	*3*	*1*	*2*	*3*	*1*	*2*	*3*
X °C	21.2	21.2	21.2	21.2	21.2	21.2	21.2	21.2	21.2	21.2	21.2	21.2
A-A (mm)	-0.002	-0.001	-0.003	-0.013	-0.012	-0.012	-0.01	-0.011	-0.012	-0.005	-0.006	-0.007
B-B (mm)	-0.006	-0.006	-0.005	-0.013	-0.013	-0.013	-0.013	-0.014	-0.013	-0.005	-0.007	-0.006
C-C (mm)	-0.01	-0.011	-0.01	-0.011	-0.011	-0.012	-0.014	-0.013	-0.014	-0.004	-0.005	-0.008
D-D (mm)	-0.013	-0.012	-0.013	-0.015	-0.015	-0.016	-0.023	-0.021	-0.022	-0.022	-0.021	-0.019
Y °C	3.2	3.2	3.2	3.2	3.2	3.2	3.2	3.2	3.2	3.2	3.2	3.2
A'-A' (mm)	-0.031	-0.033	-0.032	-0.041	-0.042	-0.041	-0.043	-0.044	-0.044	-0.034	-0.035	-0.036
B'-B' (mm)	-0.037	-0.036	-0.036	-0.043	-0.044	-0.044	-0.046	-0.044	-0.045	-0.038	-0.041	-0.039
C'-C'(mm)	-0.041	-0.04	-0.041	-0.045	-0.045	-0.046	-0.044	-0.045	-0.044	-0.036	-0.038	-0.039
D'-D'(mm)	-0.047	-0.044	-0.045	-0.049	-0.05	-0.049	-0.053	-0.051	-0.052	-0.05	-0.052	-0.049
CTE1	16.111	17.778	16.111	15.556	16.667	16.111	18.333	18.333	17.778	16.111	16.111	16.111
CTE2	17.222	16.667	17.222	16.667	17.222	17.222	18.333	16.667	17.778	18.333	18.889	18.333
CTE3	17.222	16.111	17.222	18.889	18.889	18.889	16.667	17.778	16.667	17.778	18.333	17.222
CTE4	18.889	17.778	17.778	18.889	19.444	18.333	16.667	16.667	16.667	15.556	17.222	16.667
Average	17.361	17.083	17.083	17.500	18.056	17.639	17.500	17.361	17.222	16.944	17.639	17.083
Z °C	21.2	21.2	21.2	21.2	21.2	21.2	21.2	21.2	21.2	21.2	21.2	21.2
A-A (mm)	-0.001	-0.003	-0.002	-0.012	-0.011	-0.012	-0.011	-0.012	-0.012	-0.006	-0.005	-0.006
B-B (mm)	-0.005	-0.004	-0.006	-0.011	-0.011	-0.013	-0.014	-0.013	-0.014	-0.005	-0.005	-0.007
C-C (mm)	-0.011	-0.009	-0.009	-0.009	-0.012	-0.012	-0.014	-0.013	-0.014	-0.005	-0.006	-0.008
D-D (mm)	-0.015	-0.014	-0.011	-0.014	-0.015	-0.016	-0.02	-0.021	-0.02	-0.02	-0.021	-0.02
CTE1	16.667	16.667	16.667	16.111	17.222	16.111	17.778	17.778	17.778	15.556	16.667	16.667
CTE2	17.778	17.778	16.667	17.778	18.333	17.222	17.778	17.222	17.222	18.333	20.000	17.778
CTE3	16.667	17.222	17.778	20.000	18.333	18.889	16.667	17.778	16.667	17.222	17.778	17.222
CTE4	17.778	16.667	18.889	19.444	19.444	18.333	18.333	16.667	17.778	16.667	17.222	16.111
Average	17.222	17.083	17.500	18.333	18.333	17.639	17.639	17.361	17.361	16.944	17.917	16.944

4.4.3 Creep

Six-cylinder specimens with a size of 75mm × 150mm were cast in order to test the long-term length change of the specimens under sustained load. The molds were filled using a one-way pour, this was done by taking a large scoop of the fresh mix in a trowel where the mold was filled to the top. The molds were consolidated with 30 taps due to the flow of the mix being over 200mm. As per CSA-A23.1 Annex U (2019), the creep was tested following the testing method of ASTM C512, with testing conducted at a sustained load of 40% of the specified strength of UHPFRC (i.e., a constant pressure of 35 MPa). Upon the arrival of the specimens at the age of 24 hours, the specimens were in a moist condition at a relative humidity of 95% until the age of 33 days. The specimens designated to test the creep were examined to ensure large amounts of voids were not present on the exterior surfaces of the specimens. Once selected, these specimens were coated with a concrete sealer to prevent evaporation until completion of the test.

To read creep strains, a digital demec gauge was used. It was standard practice to use two-gauge lines diametrically opposite to measure one cylinder, however, due to the sensitivity of the strains for UHPFRC, four-gauge lines were used placed at equal quarter lines of the cylinder. A total of 4-gauge lines were used so that if one gauge stud falls off, the other two diametrically opposite gauge lines can be used. To ensure all four lines are placed at equal lengths and are diametrically opposite, the specimens are ground until the top and bottom ends of the cylinders were perfectly horizontal. To test this, the surface on which the gauge studs are placed was measured using a bubble level to ensure the surface on which the specimen was placed for instrumentation was perfectly level as well. To ensure the gauge lines were vertical, a bobber and string were used to align the studs onto the cylinder. The demec gauge reference bar was then used to space and glue the gauge studs onto the specimens. Two cylinders were tested in compression at the age of 34 days and showed a compressive strength of 149 MPa and 148 MPa. The 40% load at which the creep specimens are to be loaded was calculated at 262 kN or 26.7 Tons. The testing frame used an analog gauge that reads the force applied from the hydraulic system which was loaded with a lever. The frames' loading piston was inserted into a custom spring assembly which uses a total of 7 springs placed in parallel. These springs are designed to take a stress of 26 MPa at its ultimate capacity. The charts pertaining to the manufacturer spring force and spring assembly are included in Appendix 2.

Disc Springs in Parallel.

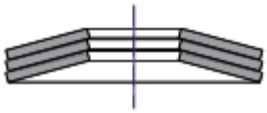

Figure 42: Spring assembly in parallel

The creep frame was self-reacting with the loaded cylinders. Therefore, as the cylinders experience shortening due to creep, the springs and the creep frame worked together to ensure the force applied stays consistent between intervals of maintenance checks. The frames' load was checked once a week for three months and monthly after that. Table 23 shows the summary of creep for 201 days. Figure 43 is the creep strain per unit stress plotted against time in days. The creep coefficient reported was measured by calculating the difference of the creep strain from the instant of loading to time *t*, divided by the instantaneous strain of 651 micro strain (Figure 43). Figures 44 and 45 presents the creep frame and the spring assembly used for performing the creep test.

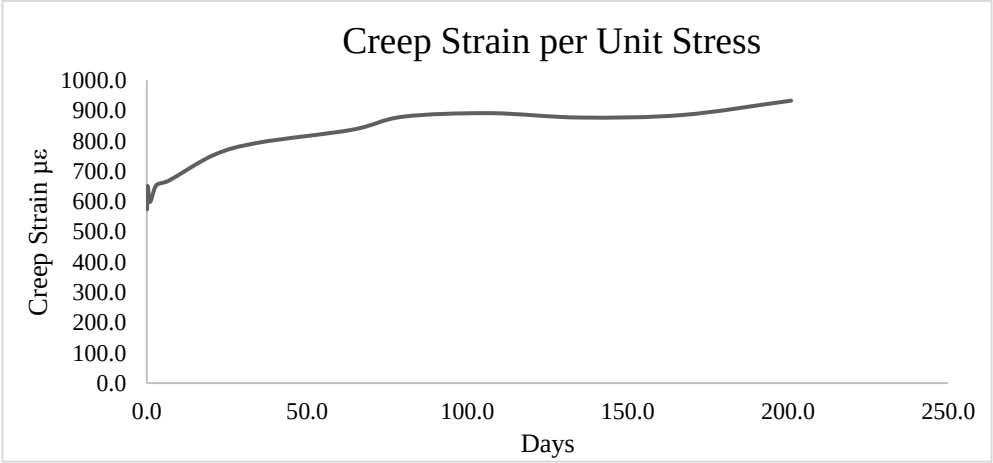

Figure 43: Creep strain per unit stress over 200 days.

Table 22: Creep Coefficient

Time (Days)	Creep Strain per unit stress, με	Creep Coefficient
0.1	574.0	-
0.3	651.0	-
1.0	598.1	-
3.0	653.8	-
7.0	669.2	0.03
21.0	753.8	0.16

35.0	794.2	0.22
64.0	836.5	0.29
80.0	879.8	0.35
107.0	891.3	0.37
135.0	877.0	0.35
167.0	885.3	0.36
201.0	932.7	0.43

Figure 44: Spring assembly

Figure 45: Creep Frame

4.5 Summary of results

The mechanical and physical properties studied in this chapter are summarized in Table 25. The testing method used, and its mean and standard deviation are also provided. Where applicable, the characteristic value is also calculated. In the present state of the annex (Annex 8.1, 2019) the characteristic values for compression tests are calculated as the mean minus 1.4 * standard deviation, which corresponds to a 7% – 8% probability of overestimation of the lowest bound. The characteristic value is another area where the annex needs to be further developed.

Table 23: Summary of Mechanical test and its Applicable Category

Property		Test Method	Test Results			Applicable Category/ Durability Limit (DL)
			Mean	Standard Deviation	Characteristic Value	
Compression Test		CSA A23.2-9C	141 MPa	5.09 MPa	134 MPa	Category 120
Poisson's Ratio		ASTM C469/C1856	0.21	0.006	-	
Static Modulus of Elasticity			46.6 GPa	1.016	-	
Flexural Strength (Peak Strength)		ASTM C1609/C1856 with analysis in accordance to AFNOR NFP18-470, Appendix D	28 MPa	2.227	-	
Tensile Strength (via Flexure) f_{cr}			8.79 MPa	0.6 MPa	7.95 MPa	
Tensile Hardening Strength (via Flexure) f_{fu}/f_{cr}			1.25 MPa	0.14 MPa	1.05MPa	
Tensile Post-Cracking Strength (via Flexure) f_{ti}			2.41 MPa	0.91 MPa	1.13 MPa	
Tensile Strain (via Flexure)	w_i		3.31 MPa	0.88Mpa	2.07 MPa	
	ε_{cr}		1.93E-4	2.846E-5	1.592E-4	
	ε_{fu}		0.0123	0.003	0.008	
Linear Shrinkage		CSA A23.2-21C	0.012 %	0.002 %	-	-
Coefficient of Thermal Expansion		AASHTO T336	17.117 μ ε	0.651 μ ε	-	-
Creep Coefficient (at 200 days)		ASTM C512	0.43	-	-	-

Note: Category 120 in the table above refers to the material obtaining a minimum compressive strength in MPa of at least 120. “-” refers to Not Applicable.

Chapter 5. Inverse Analysis

5.1 Introduction

The following section entails work done in collaboration with the CSA Task Force for revision of Annex A8.1. The objective of this group was to revise the provisions and commentary for the next version of the CHBDC with the intent that Annex A8.1 will become mandatory in the 2025 S6 code cycle. Material Characterization was identified as an essential need that requires the review of tests in tension and updating/improving the existing methods of testing and performing analysis. Specifically, reducing the uncertainty in the characterization of the testing and inverse analysis methods to extract the tensile response not only in material characterization of UHPFRC but also in quality control was identified as the most pressing priority for the introduction of design provisions with this material in the design code. Therefore, the need for development of standardized direct tension tests, and quality control tests to ensure the material delivered in field in construction projects matches the characteristics of the approved material and round-robin testing for proofing and verification are key to further progress in the field. To better define the need, and to proof-test the applicability and voids of the existing approaches of Annex A8.1, two design examples were subjected to round robin evaluation by different research groups so as to compare the results and any possible differences in the output of the analysis. The round robin evaluation for the material characterization in the CSA Task Force was done with three research groups specifically dedicated for material characterization, two of which were from York University and one from Ecole Polytechnique Montreal. The purpose of it was to compare data and discuss the variance if any.

The first example is explored in the present chapter, and it concerns a systematic examination of the inverse analysis procedure of Annex 8, which is used to extract the tensile stress - strain response of sample in THFRC materials from the prism flexural tests depicted in Figure 46. Upon completion of this investigation the method was applied to the collection of the thirty beam tests conducted in the present thesis, as presented in Chapter 4, with the objective to extract the tensile stress – strain response of the UHPFRC material studied. The second example is the subject of the follow-up chapter; it concerns the performance of the design provisions when applied to a complete bridge girder. The load – deflection response in the figure below was provided in the design example in the round robin evaluation from the CSA task force group being discussed.

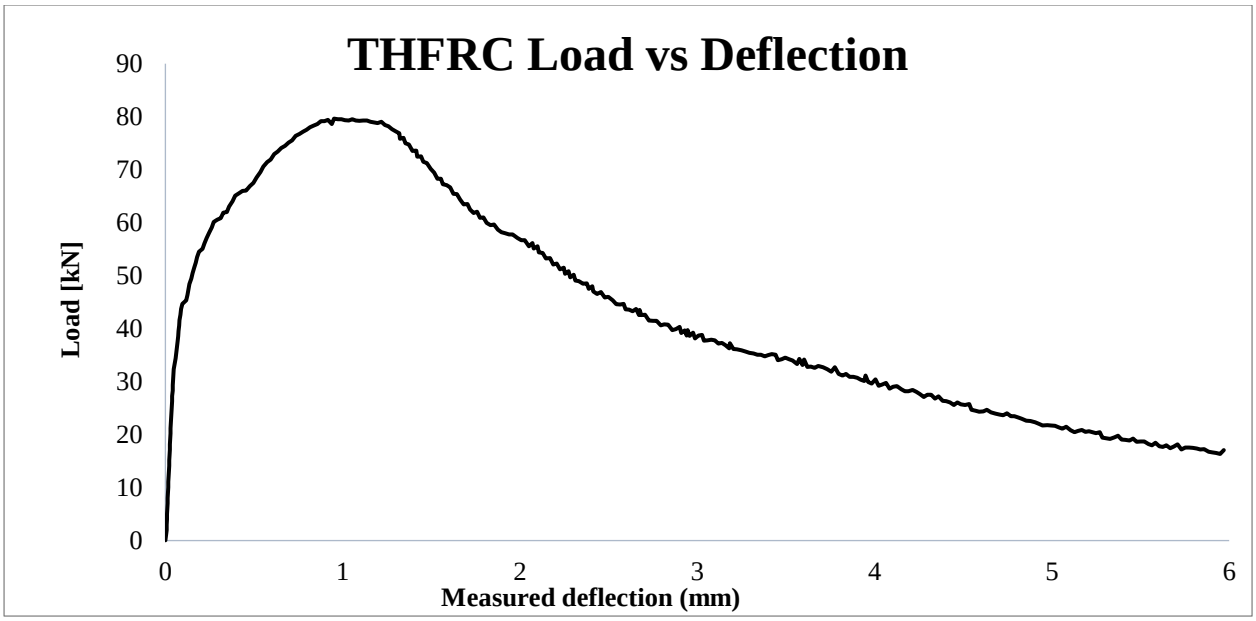

Figure 46: Load vs Deflection curve under investigation (THFRC)

The inverse analysis methodology summarized in the next section was applied on a suite of data from beams tested in the laboratory, having various sizes. To illustrate the user-dependent variability in the results obtained from the inverse analysis as specified by CSA-S6 Annex A8.1, the data from the specimens tested in the present work, having size of 100mm × 100mm × 300mm are discussed in the methodology section below. To further investigate the effect of size on the derived tensile properties obtained from the inverse analysis, additional larger beams of nominal sizes of 150mm × 150mm × 450mm and smaller beams of sizes of 100mm × 50mm × 400mm made according to the AFNOR NF EN 13670 (2013) Code were also analyzed. Note: the fibers lengths used in the large beams of size 150mm × 150mm × 450mm were 13mm steel fibers.

The fibers in the mix used for the 100mm × 100mm × 300m were 20mm long with 0.2mm diameter at a 2% mixture ratio (per volume). Additional parameters needed to conduct the analysis included the compressive strength and the horizontal distance from the center of the span to the tip of the crack width. An example case illustrating this distance is shown in Figure 47 below.

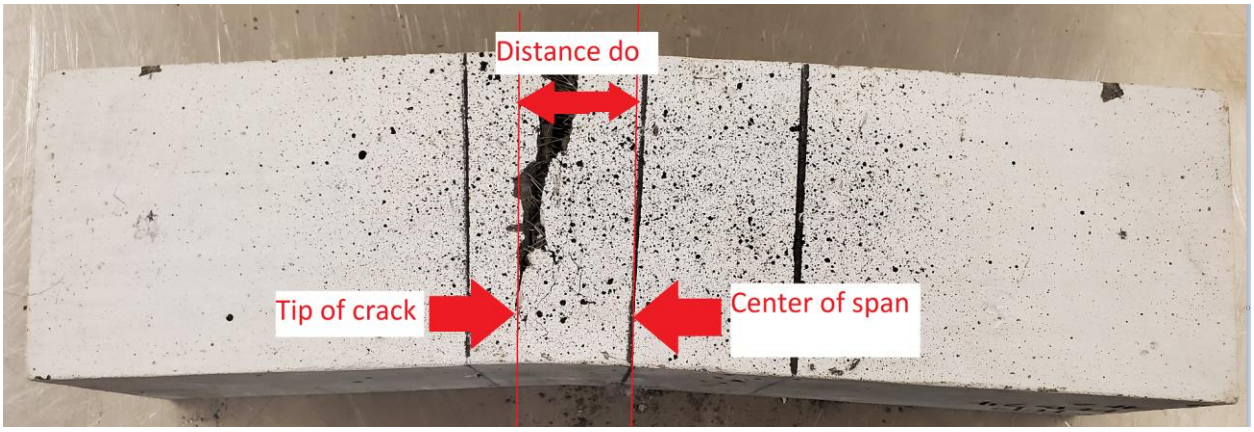

Figure 47: Distance d_o (measured from center span to tip of the crack)

5.2 Inverse Analysis Methodology - CSA Annex A8.1

In order to perform the inverse analysis, the UHPFRC material must first satisfy two limits. These limits are shown in Equations 5.1 and 5.2. The limits were set by Annex A8.1 in order to characterize the material as a THFRC. Along with these limits, the inverse analysis proposed by the Annex requires the compressive strength of the material to be tested in accordance with Annex U, which proposed testing method CSA A23.2-9C be used to test cylinders in axial compression. Lastly the fiber lengths are also required in order to perform the inverse analysis.

$$f_{fu} \geq 1.1 f_{crm} \qquad \text{Equation 5.1}$$

$$\varepsilon_{tu} \geq 0.001 \qquad \text{Equation 5.2}$$

Further, Annex A8.1 classifies the cracking strength f_{crm} from Equation 5.3, or the value obtained from the inverse analysis performed on prismatic beams of specified dimensions as shown in Table 26 to be used.

$$f_{crm} = 0.6\sqrt{f'c} \leq 7.35 \text{ MPa} \qquad \text{Equation 5.3}$$

The simplified direct tensile model for THFRC is defined by f_{crm}, ε_{cr}, and the specified post-cracking properties f_{fu} and ε_{tu}. Figure 48 is a visual representation of the simplified direct tensile model for THFRC. The goal of the analysis is to obtain this tension model for the material for characterization.

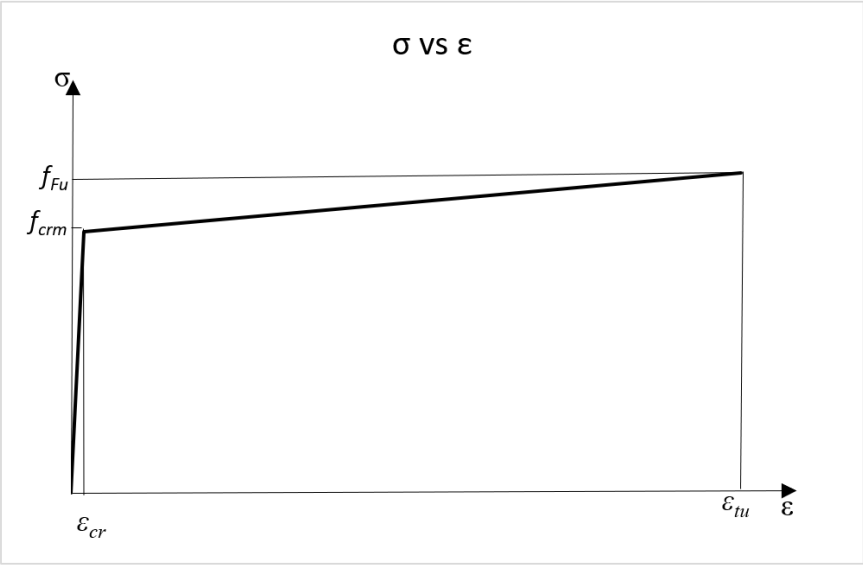

Figure 48: Simplified direct tensile model for THFRC, (CSA Annex A8.1)

To perform the inverse analysis after the preliminary data is obtained as discussed above, a load-deflection resistance curve is generated from a flexural test conducted using symmetric loads at the third points of the beam span under displacement control. To this end, at the coordinates of four characteristic points are selected from the resistance curve, as illustrated in Figure 49. Using P for the total applied force, and δ for the deflection at midspan, the slopes *S* of secant lines drawn from zero the four selected points are defined as follows: Therefore, S_0 is the ascending linear elastic slope of the resistance curve before the occurrence of the first crack; S_{75} and S_{40} represent lines with slopes equal to 75% and 40% of S_0 respectively; when drawn from the origin the straight lines with these slopes intersect the envelope at two points with coordinates (P_1, δ_1) and (P_2, δ_2). Lastly, two additional points, P_3 and P_4 were obtained: in the case of P_3 by finding the corresponding P_{max} from which, the coordinates of the point with strength equal to 97% of P_{max} before the peak was defined as (P_3, δ_3). Point P_4 corresponded to 80% of P_3, in the post-peak is defined as the characteristic coordinates (P_4, δ_4).

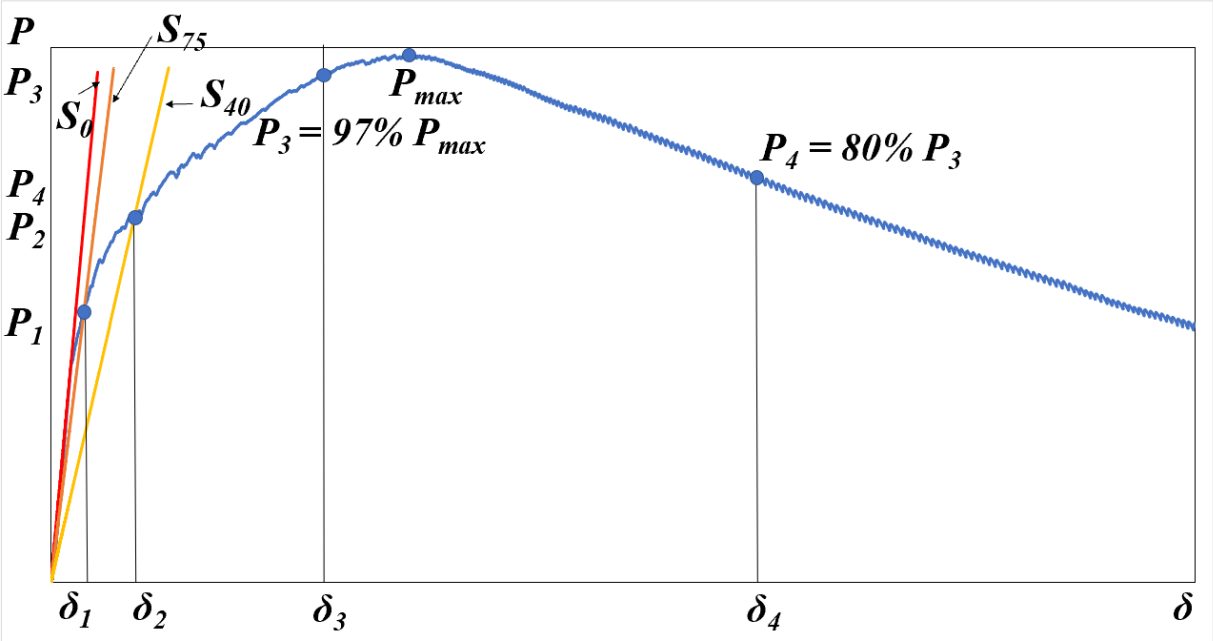

Figure 49: Characteristic points for Inverse analysis (CSA Annex A8.1)

Once the coordinates of the 4 characteristic points were obtained, they are input to the equations of Table 26, leading to a linearized tensile stress vs strain diagram. In fact, the material law is defined as comprising two parts; one representing the ascending part including the hardening component, where the coordinate in the horizontal axis is tensile strain; and one representing the response beyond the onset of crack localization, comprising the post peak descending relationship between stress and increasing crack width. The average plots obtained as a result conducted from this analysis are shown in Figures 50 and 51. This procedure is both calculation intensive, requires high accuracy instrumentation, and experienced personnel to conduct the tests apart from the need of a displacement-controlled testing facility. In the table below L refers to the shear span length, and h refers to the height of the specimen.

Table 24: Tensile Properties of THFRC using inverse analysis

Property	L=3h	Normalized Parameters
E_{co}	$\frac{7.2}{b}S_0$	
f_{crm}	$K_1\frac{P_1 L}{bh^2}$	$K_1 = \frac{(\frac{P_1}{P_2})^{0.19}}{1.63}$
ε_{cr}	$\frac{f_{crm}}{E_{c0}}$	-

ε_{tu}	$K_2\varepsilon_{cr}$	$K_2 = (7.65\frac{\delta_3}{\delta_1} - 10.53)$
f_{fu}	$K_3 f_{crm}$	$K_3 = {K_2}^{-0.18}(2.46\frac{P_3}{P_1} - 1.76)$
ε_{t0}	$K_4\varepsilon_{cr}$	$K_4 = {K_3}^{-0.37}{K_2}^{0.88}(3.00\frac{{\delta_4}^*}{\delta_3} - 1.80)$
w_0	$\left(\varepsilon_{t0} - \varepsilon_{tu} + \frac{10 f_{Fu}}{3E_{c0}}\right)\frac{3h}{2}$	-
$\delta_4^* = K_5\delta_4 \; where \; K_5 = 1 + \frac{0.6}{L}d_0$		

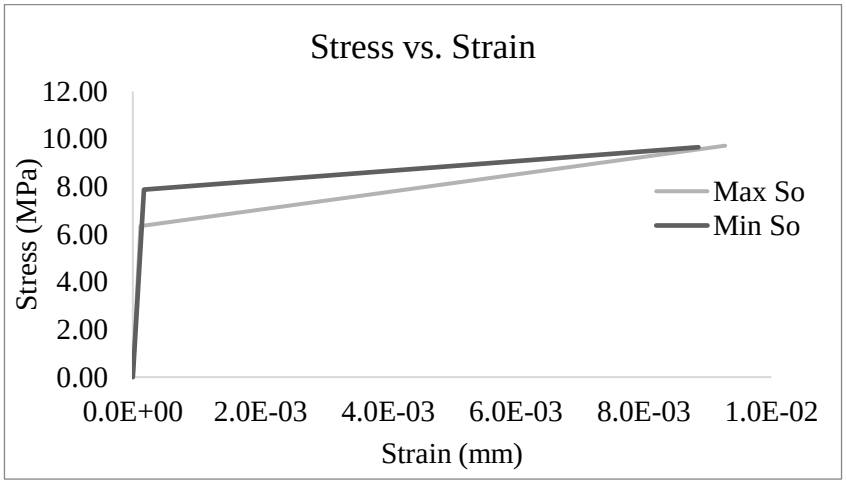

Figure 50: Stress vs Strain for Maximum So and Minimum So

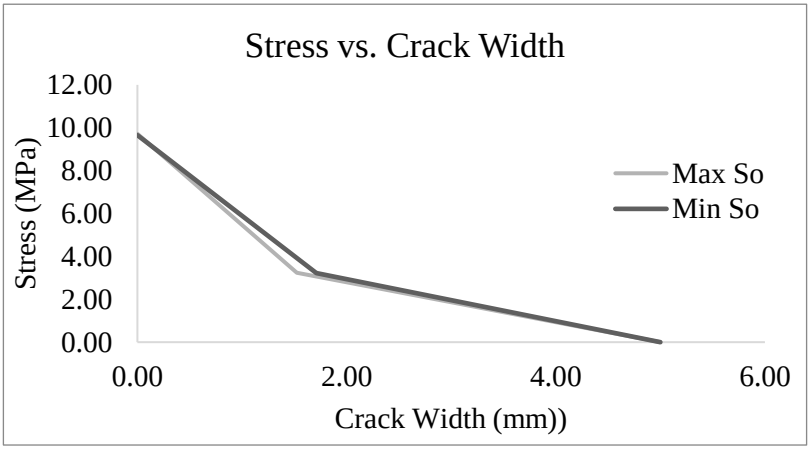

Figure 51: Stress vs Crack width for maximum So and minimum So

5.3 Results/Discussion

This section consists of the results of the prisms tested in three batches, with ten beams cast per batch as presented in Chapter 4. Along with beams, ten 75mm diameter cylinders were also cast in every batch, in order to obtain the compressive strength for each mix. The summary of the resistance curves and cylinder tests are given in Tables 27 and Figure 52 below. Using the same methodology as in the preceding section, inverse analysis results were obtained for thirty beams in total. For each beam two inverse analyses were performed, with the maximum and minimum estimates of $S_{0.}$ When selecting an appropriate slope from the raw data of the beam tests, it was observed that during the loading stage of the beam, prior to cracking, the slope of the resistance curve starts to decrease as microcracks form allowing the beam to bend. This bending compensates for the load being applied and therefore the resistance curve slope decreases as the specimen becomes more compliant. The upper limit range of allowable slopes was therefore associated to the point just before any apparent deviation from linearity occurs.

These slopes were selected from a range of loads with the lower limit set to 10 kN for all beams, while the upper limit of the range was kept dependent on the linearity of the load-deflection curve. In the rare circumstance of a beam's behavior under loading in which a large slope of more than 1000 kN/mm was calculated, although the inverse analysis could still be performed, it was often the case of user error in its testing setup. In fact, these beams have been shown to fail under torsion. These beams are not reported in the present analysis as they are outliers in the overall assessment of the material over the three batches.

Table 25: Summary of compressive strength for batches 1-3.

Batch #	Mean (MPa)	Standard Deviation	Characteristic Value (MPa)
1	146.68	7.68	135.93
2	137.54	4.11	131.79
3	138.25	4.06	132.57

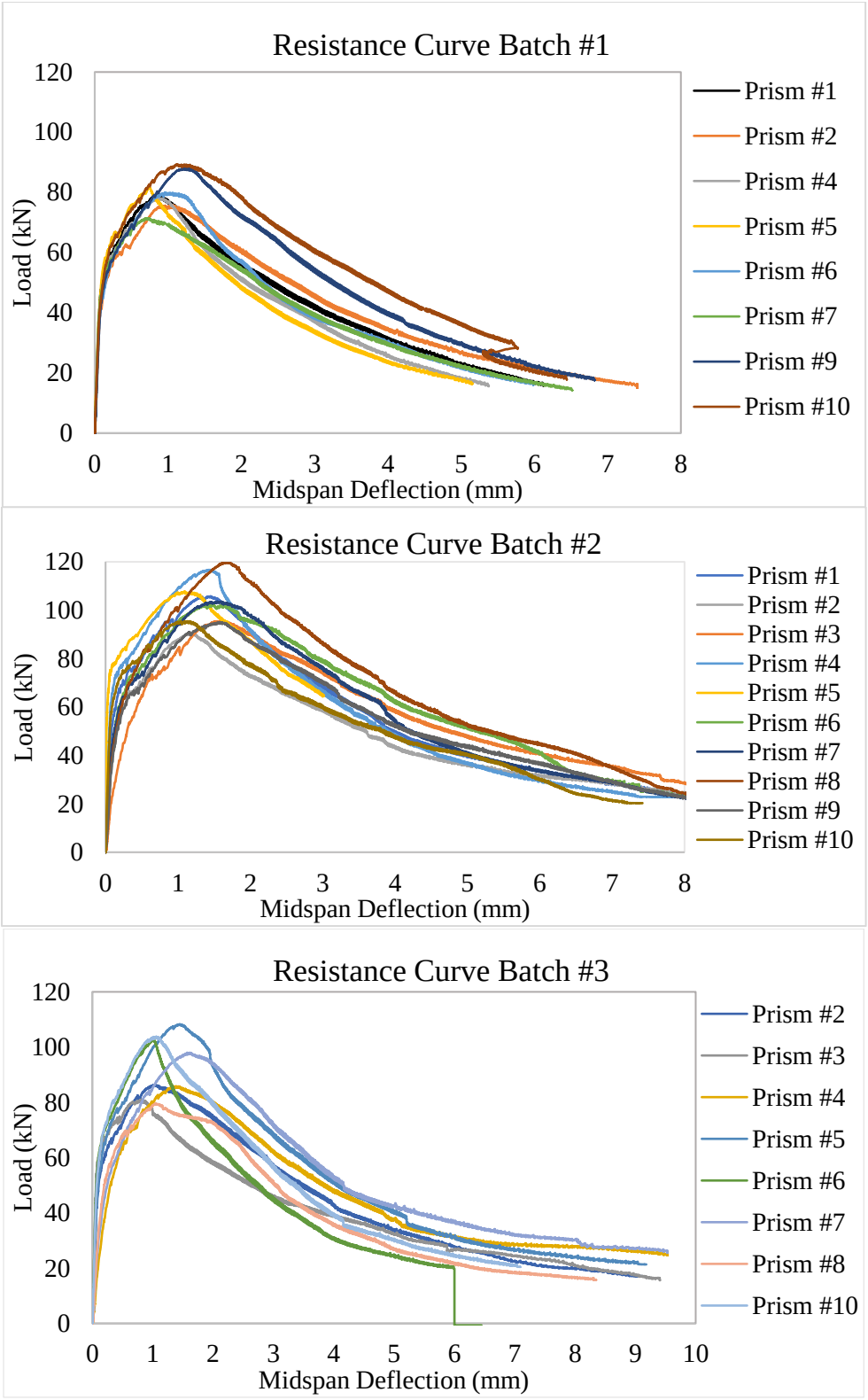

Figure 52: Summary of resistance curves for batches 1-3.

The difference in the values of the initial slopes S_0 that can vary for a single design mix of UHPFRC material averaged over thirty beams tested calculated in the inverse analysis was in the range of 9% to 43%. The minimum S_0 was on average equal to 559 kN/mm, which yielded an ultimate tensile stress f_{Fu} of 11.37 MPa, and a corresponding ultimate tensile strain ε_{tu} of 0.012 mm/mm at the peak. Furthermore, the average cracking stress, f_{crm}, and strain ε_{cr} were estimated at 9.410 MPa and 0.000248 mm/mm. Similarly, the maximum S_0 was 686.6 kN/mm on average, and the cracking stress f_{crm} and strain ε_{cr} were evaluated at 8.3MPa and 0.000178 mm/mm, respectively. The ultimate stress f_{Fu} and ultimate strain ε_{tu} evaluated at the mean were 11.3MPa and 0.011165 mm/mm. These mean values of the stress-strain profile are depicted in Figure 53 below as characterization curves for the studied material.

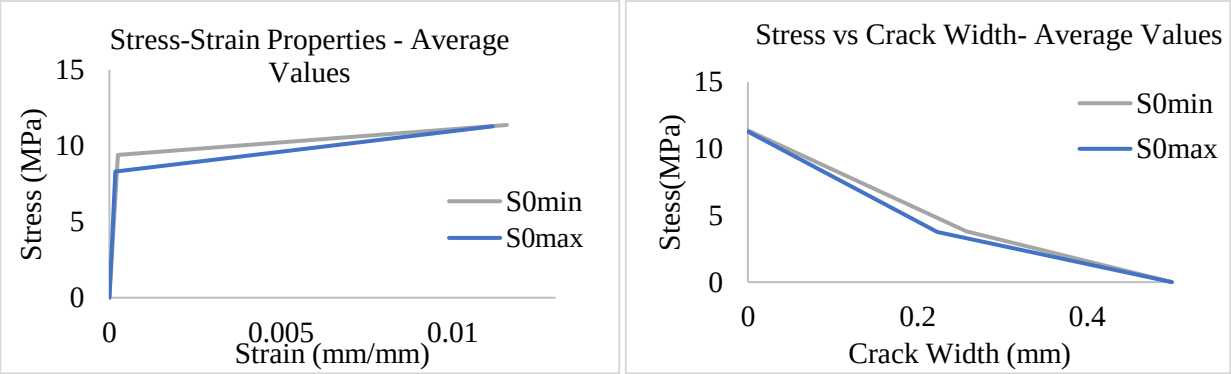

Figure 53: Mean tensile stress vs strain and stress vs crack width plots for maximum and minimum So (result of 30 tests)

To investigate the variability in the inverse analysis from a maximum and minimum value of S_o, a compilation of the results is plotted in Figures 54 which present the relationship between the initial slope S_0 and the calculated material parameters such as w_0, f_{fu}, f_{crm}, ε_{tu}, $E_{co,}$ and ε_{cr}. In the case of S_0 vs w_0, the cluster of results ranges from crack widths w_0 of 2mm to 5mm. In the plot of S_0 vs f_{Fu}, the grouping of results was dense in the range for f_{fu} equal to 8MPa – 13MPa, the same was observed in the plot for S_0 vs f_{crm} where the grouping of results was observed from 7MPa-11MPa. The strain plots with the ultimate specified strain ε_{tu} and the average cracking strain ε_{cr}, show a cluster of strains ranging from 0.0065-0.0156 and 0.0001 – 0.0003 respectively. Lastly, in the plot of S_0 vs E_{c0}, there is a linear range in which it is observed that the slope S_0 is linearly related to the modulus of elasticity in tension which falls in a range of 31 GPa – 52 GPa. The standard deviation is summarized in Table 28.

Table 26: Standard Deviation of Inverse analysis results, 100mm × 100mm × 350mm.

Standard Deviation $S_{0,min}$ & $S_{0,max}$						
$S_{0,min}$						
S_0	ε_{cr}	f_{crm}	ε_{tu}	f_{fu}	w_0	E_{co}
103.80	8.01E-05	1.53	3.92E-03	2.16	1.06	10.24
$S_{0,max}$						
S_0	ε_{cr}	f_{crm}	ε_{tu}	f_{fu}	w_0	E_{co}
126.83	5.30E-05	1.95	3.57E-03	1.97	1.12	8.39

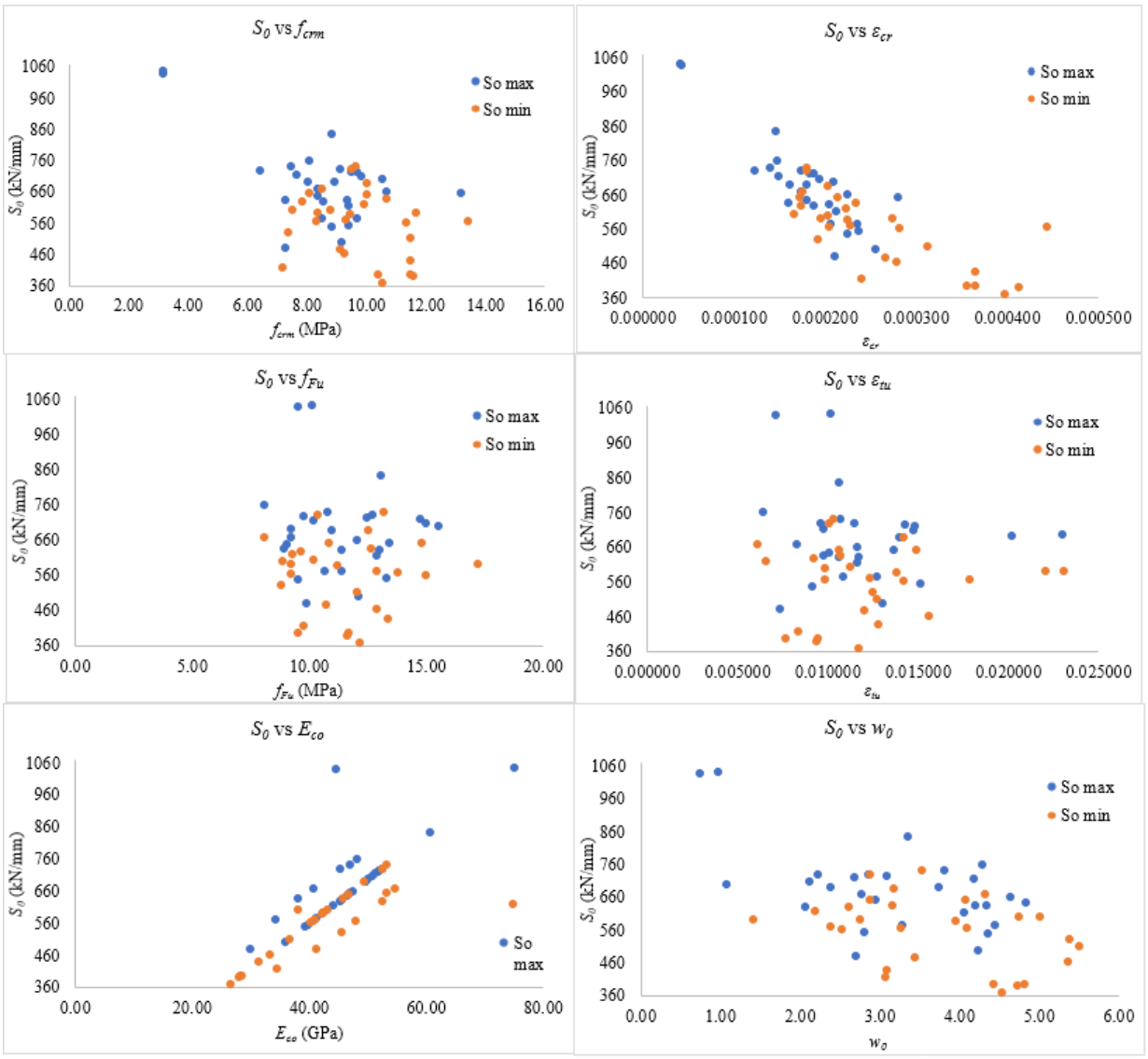

Figure 54: Scatter plot for maximum and minimum estimates of S_0 on prism sizes 100mm×100mm×350mm

In the compilation of Figures 54, the distribution of the results obtained from the thirty beams was plotted including the results from eight additional beams tested as per ASTM C1609 / C1856. These beams having nominal dimensions of 100mm × 100mm × 350mm, with fiber lengths of 20mm. The beams were made with the same mix of material and obtained a mean compressive strength of 155MPa tested on standard 75mm diameter cylinders cast and tested as per CSA A23.2-9C, ASTM C39/ C1856. In Figure 55 the triangle and cross refer to the maximum and minimum slopes for the 150mm × 150mm × 500mm beams, 13mm long fibers. The blue points and orange points are the maximum and minimum slopes achieved for the smaller 100mm × 100mm × 350mm beams. From these plots, the results are examined to show the larger beams obtaining higher stresses and modulus of elasticity at cracking, but lower hardening capacity in terms of ultimate strain.

Table 27: Standard Deviation for beams 150mm × 150mm × 500mm.

Standard Deviation $S_{0,min}$ & $S_{0,max}$						
$S_{0,min}$						
S_0	ε_{cr}	f_{crm}	ε_{tu}	f_{fu}	w_0	E_{co}
63.92	2.09E-05	0.92	2.29E-03	2.11	1.11	3.07
$S_{0,max}$						
S_0	ε_{cr}	f_{crm}	ε_{tu}	f_{fu}	w_0	E_{co}
102.37	2.76E-05	1.28	2.25E-03	2.02	1.13	4.91

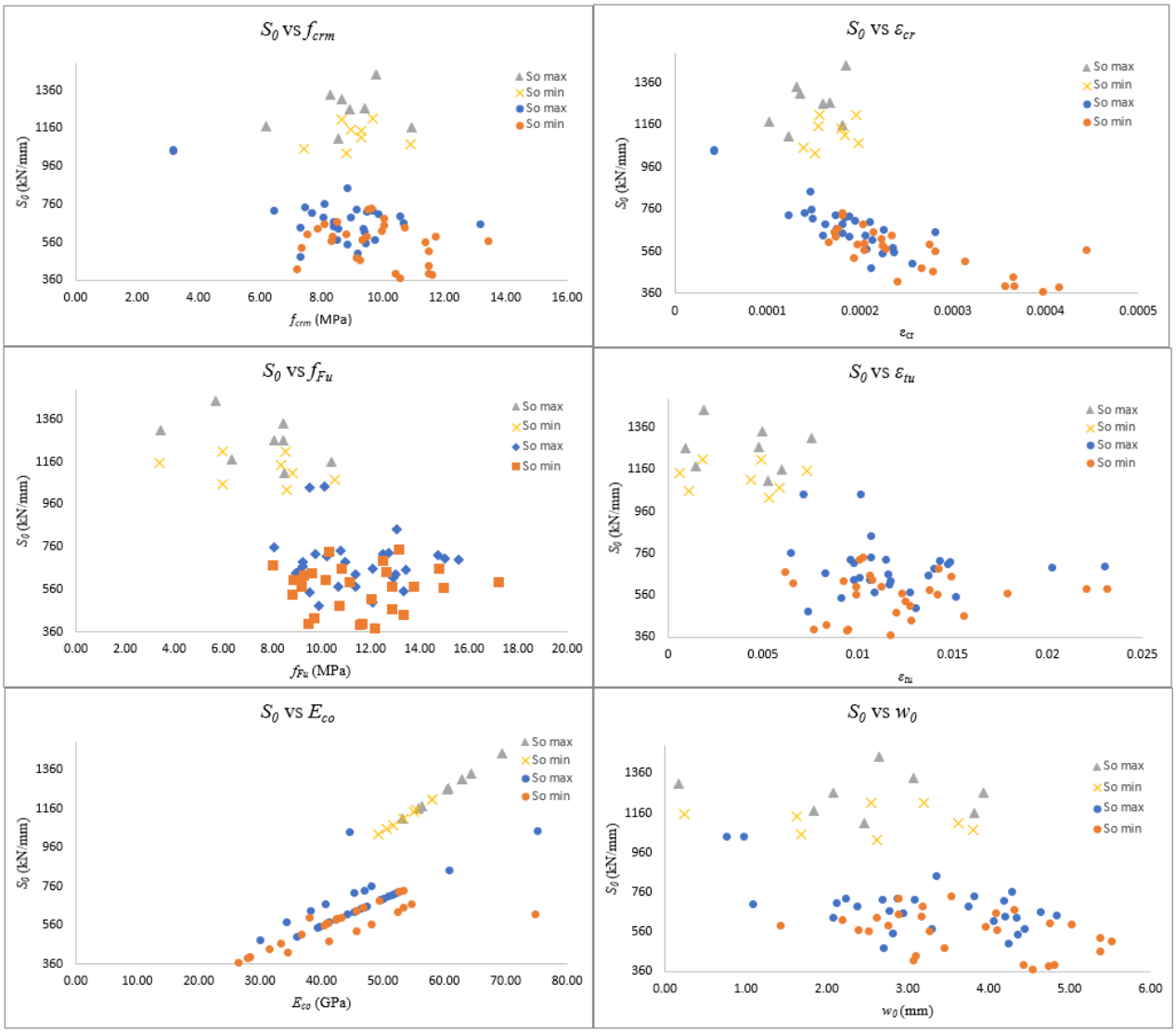

Figure 55: Compilation of scatter plots comparing 100mm × 100mm × 350mm (20mm long fibers) prisms with 150mm × 150mm × 500mm (13mm long fibers).

Figure 56 displays the inverse analysis performed on prisms having the AFNOR-type (2013) geometry with the size of 100mm × 50 mm × 400mm (50 mm was the beam height in this test setup, whereas the shear span and distance between intermediate loads at 100 mm was 2 times the beam depth, i.e., more flexure-dominated specimens). In comparison to Figure 54, the results clearly display a size effect observed where smaller depth prism experience a lower initial S_0 slope and consequently demonstrate lower tensile properties.

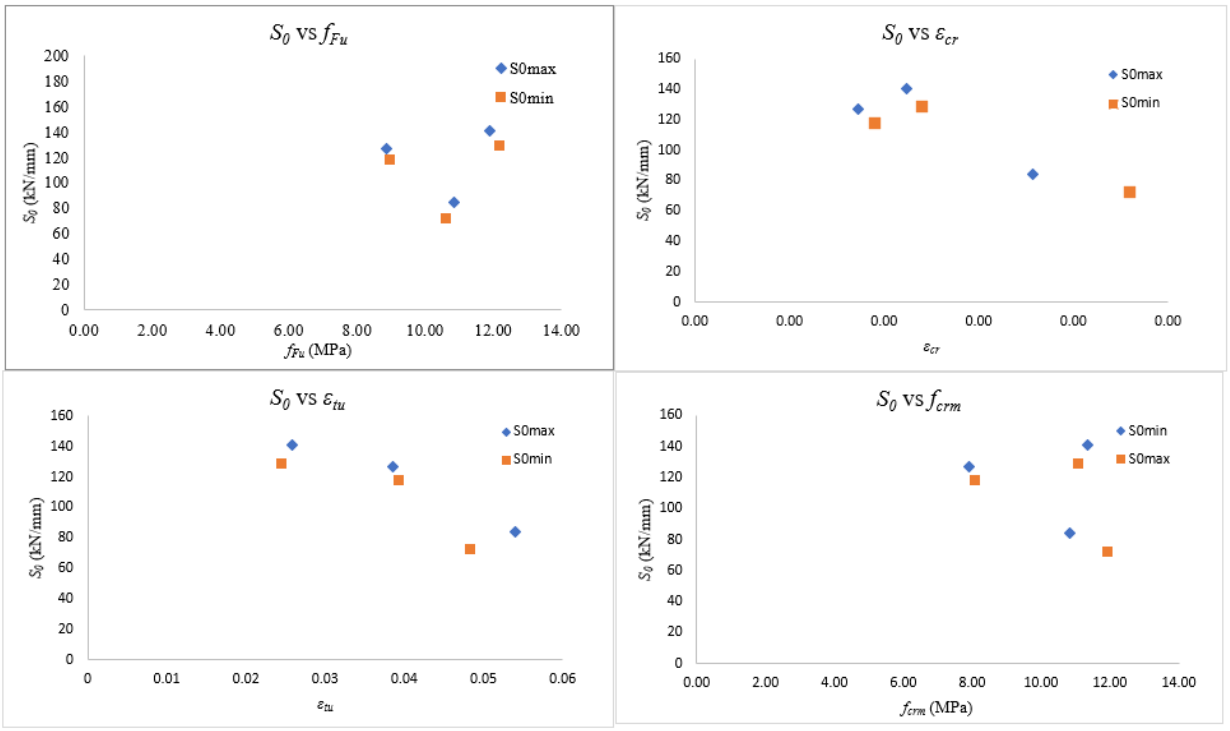

Figure 56: Scatter plot of AFNOR beams size (100mm × 50mm × 300mm)

Figure 57 and 58 present the summary of results achieved by taking a maximum and minimum S_0 value for inverse analysis from beams tested in batches 1-3 for prism sizes of 100mm × 100mm × 300mm.

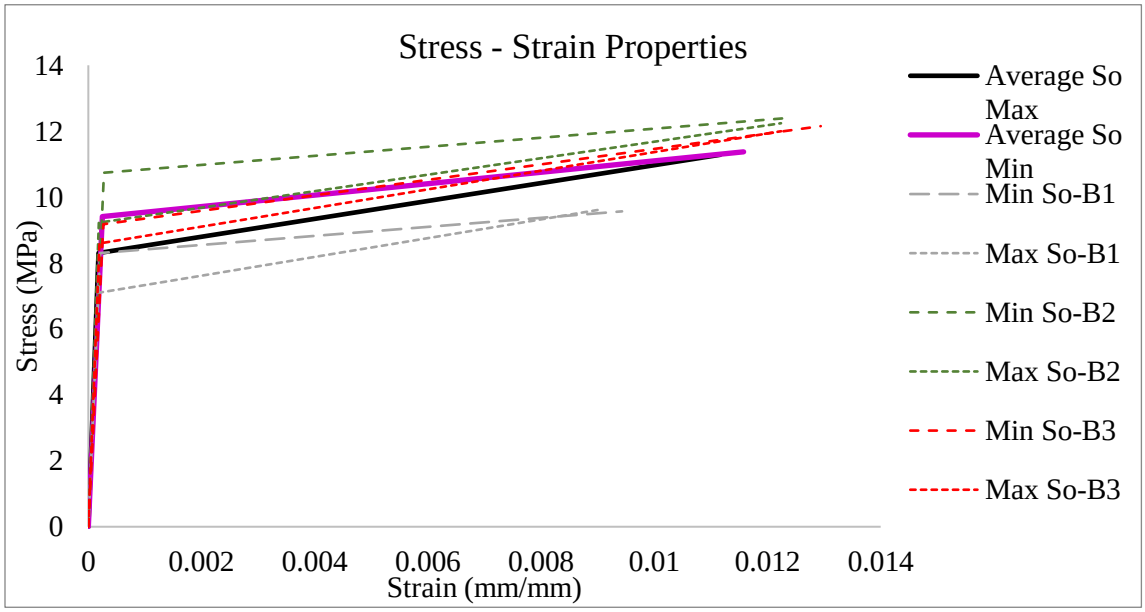

Figure 57: Variability of Stress vs Strain results achievable by S_o minimum and maximum.

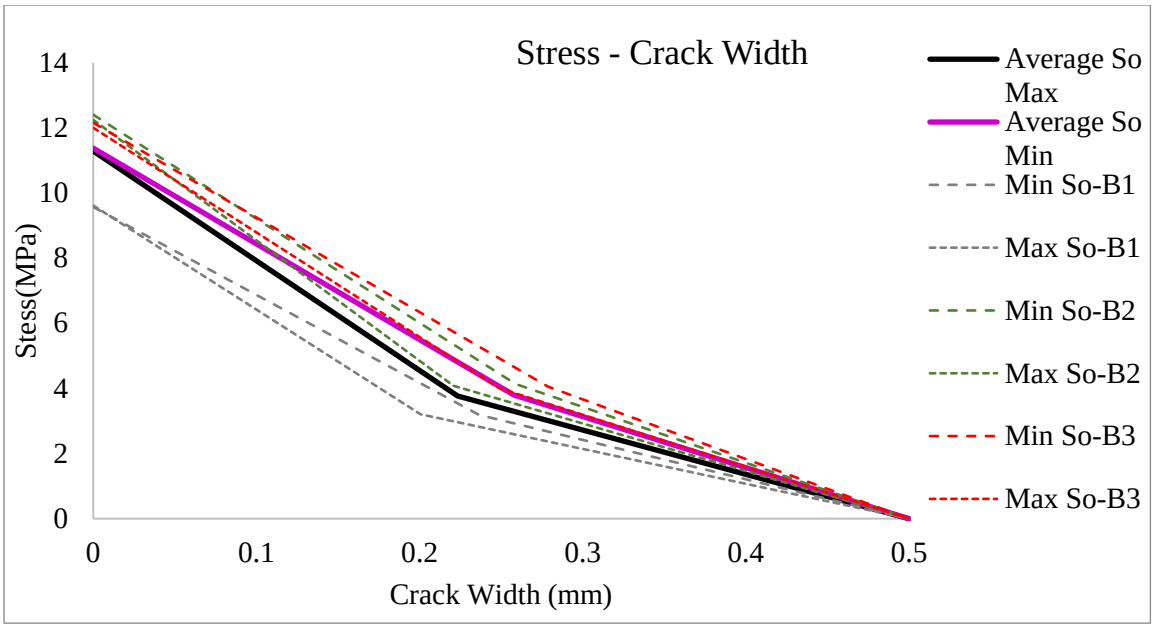

Figure 58: Variability of Stress vs Crack width results achievable by S_o minimum and maximum

5.4 Conclusions, Findings and Recommendations

From the inverse analysis performed following the CSA Annex A8.1, there exists a range of possible tensile properties that can be calculated for a single design mix. In the chapter above a total of forty-two beams were tested, having different cross-section dimensions and span lengths, however all subjected to the same load sequence. All prisms were tested using the same loading rates, test setups, and mix design. As a standard, the CSA prescribed inverse analysis was not found to be adequately robust in obtaining the tensile properties of UHPFRC. The results plotted in Figures 54 and 56 were expected to converge, however the results obtained show a variability that could be a result of lack of calibration needed for the inverse analysis method, by considering different prism sizes. This calibration was not yet mentioned in the CSA Annex 8.1, which however causes high values of standard deviation for the tensile properties. In light of its importance for the UHPFRC Materials Industry the standard prescribed to characterize the material in tension, additional testing should be required where direct tension tests would be used to characterize the material. Overall, however, the current state of the art and best practices for direct tension tests also show high variance and low confidence in the results needed to classify UHPFRC in tension. It is then recommended to warn users of the annex of this variability and to add additional methods by which UHPFRC can be classified in tension.

The results obtained by the inverse analysis are highly dependent on the selection of the initial slope S_0. This is a measure of the elastic stiffness and should lead to results for the cracking tensile strength of the material that is independent of the specimen size and the rate at which the beam sustains bending load. Nevertheless, as seen in Figure 56, there is evidence of size effect in the inverse analysis method required to obtain the tensile properties.

In the current development of the annex, the alternative method is under discussion which brings about a quality control measure for the material in tension. The new approach quantifies the strain energy absorbed by the beam under flexure and throughout the range of the elastic and the hardening part of the response. The new approach is being sought to add in a minimum performance criterion for quality control for THFRC materials under flexure. The strain energy is calculated as the area under the load-deflection curve, this area is proposed to be summed up until the 95% post peak load, this area is referred to as G_{Fhard} as shown in Figure 59.

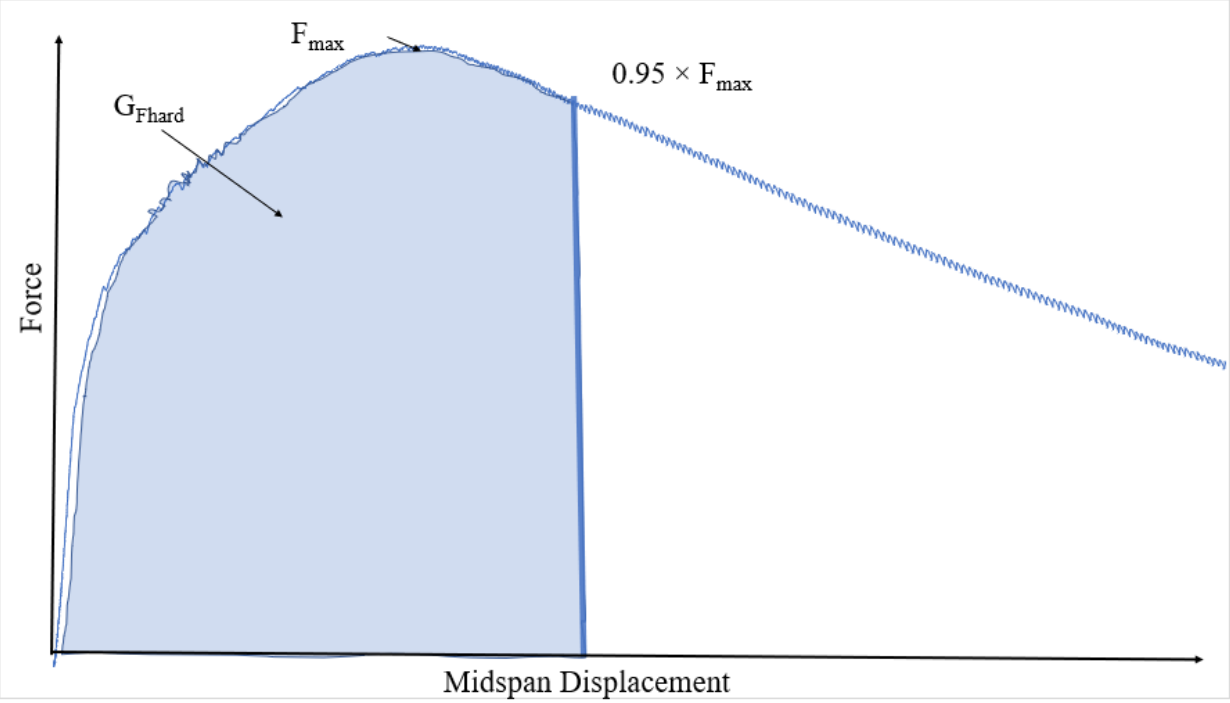

Figure 59: Strain Energy (95% F_{max})

For the case of the experimental data collected, this area was approximated using the method of equivalent rectangles at the displacement steps along the load deflection plot. The calculated strain energy values up to the onset of the post peak branch are shown in Figures 60 to 62 for the beams reported in the preceding. From these plots, it can be seen that different energy values are

calculated for the same design mix, with the same nominal specimen dimensions, loaded with the same rate. The dispersion underscores the need for further research needed for the development of alternative quality control criteria for high-strength UHPFRC mixes with steel fibers. Apparently, the fibers are oriented randomly even under a one-way pour cast methodology. It is recommended to further develop a direct method to test tensile strength for this type of material for use in practical design. The summary of strain energies from batches 1-3 are shown in Figure 63. Lastly, its also recommended to use the strain energy approach to quantify a quality control measure so that the results used for characterization can be shown in full transparency with respect to the consistency of the test results. Factors which are intended for calibration for such variance are not recommended as a future option as the current method for testing and obtaining results is already calculation intensive, rather a simple direct tension test would rather help with characterization of this material in tension.

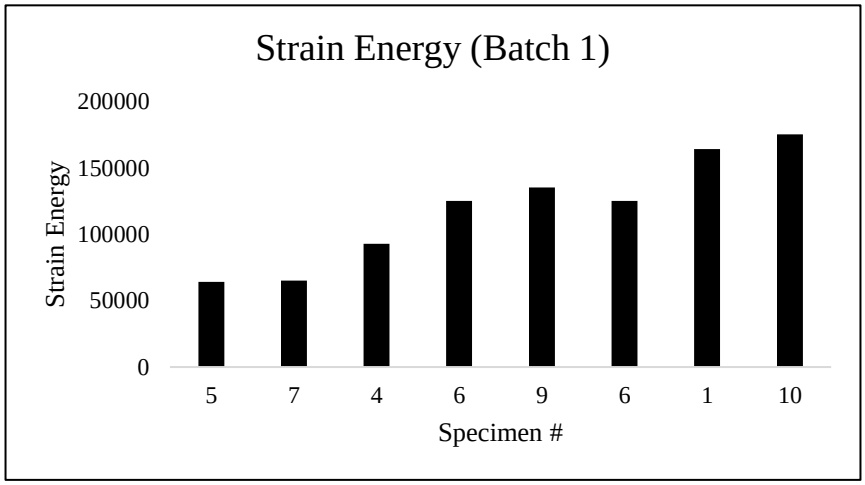

Figure 60: Strain energy for batch 1.

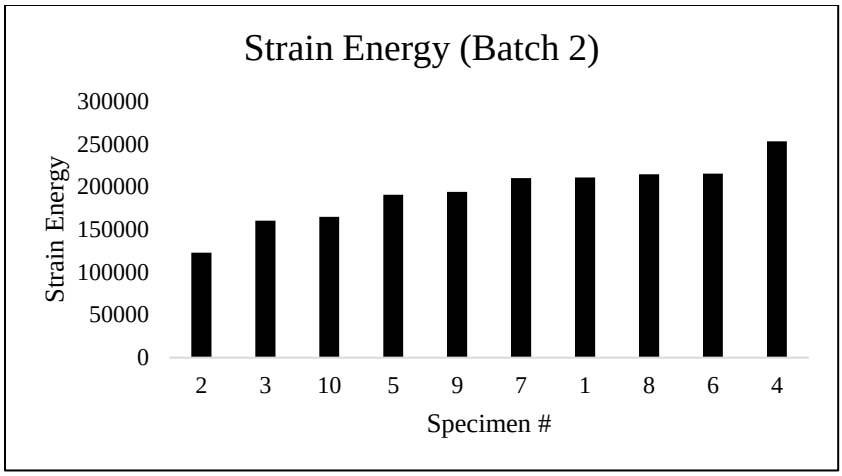

Figure 61: Strain energy for batch 2.

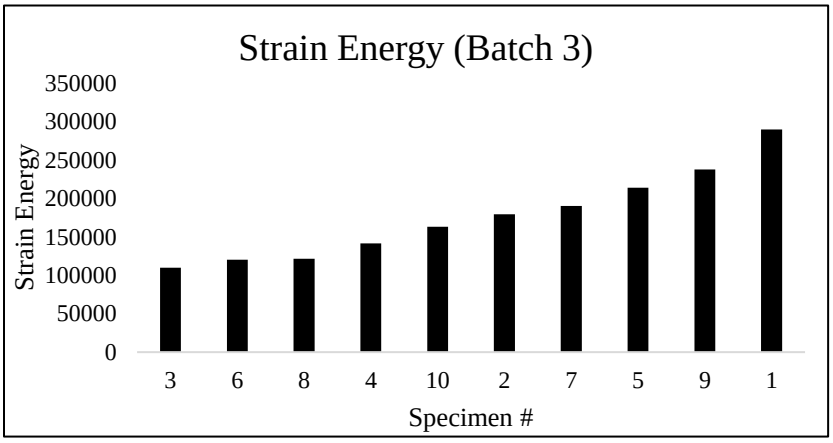

Figure 62: Strain energy for batch 3.

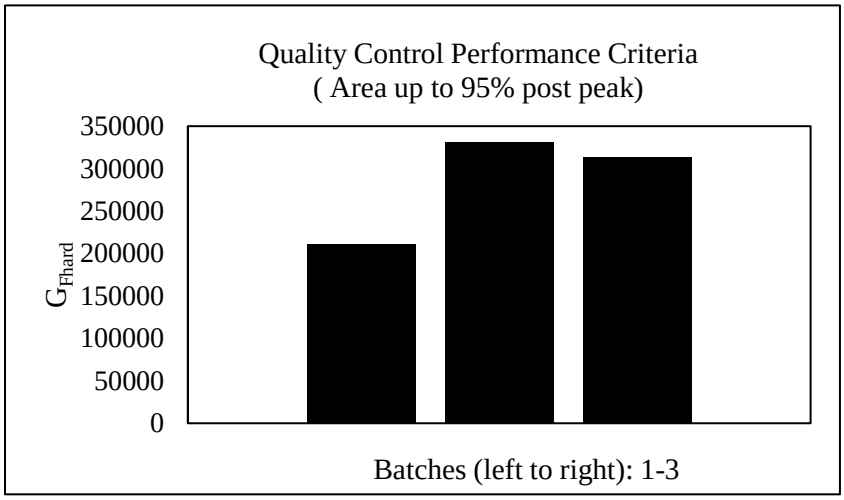

Figure 63: Comparison of G_{Fhard} for batches 1-3.

Chapter 6. T-Beam Bridge Example

6.1 Introduction

The second benchmark case study used for round robin evaluation by the task group of Annex 8.1 of CSA-S6 (2025) was a bridge-type girder having a T-shaped cross section which was analyzed to the current provisions of the Annex 8 CSA -S6 (2019) for UHPFRC bridges. This chapter takes an in-depth look into the prescribed method for the design of UHPFRC elements with regards to flexural analysis, and shear strength estimation and serviceability criteria.

6.2 Objective

The following section describes the solution developed at York for the round robin comparison, aimed at proof-testing the applicability and consistency of the provisions of Annex 8.1, as input for the improvement of the annex in the next round of the CHBDC revision[1]. The annex specifies the requirements for the design of structural elements that are made with precast or cast in place UHPFRC containing prestressed or non-prestressed steel. The method in the annex does not exclude prestressed elements with pre-tensioned steel or grout post-tension steel.

The annex defines the behavior of the UHPFRC as either tension hardening (THFRC) or tension softening (TSFRC). It is important to note that this classification rides on the results of pre-qualification testing of each commercial pre-packaged UHPFRC product using the procedures tested in Chapter 5; pre-qualification is the essential ticket for the material producers to access the market of UHPFRC construction, however it is recognized that in the field, preferential fiber orientation aimed at by unidirectional casting may not be achievable (Huang 2019, Huang 2012). Random fiber orientation is likely to prevail in members having greater depths where casting is unavoidably going to lead the fibers to bulk, random orientation (Yoo et al. 2016, Zhang 2020). To account for this uncertainty the design provisions introduce a significant reduction factor, γ_F which depends on the conditions of casting and member size and once selected, it attenuates the tensile material strength that is obtained from prequalification testing. The fiber efficiency factor

[1] CHBDC stands for the Canadian Highway Bridge Design Code also referred to as CSA-S6 Standard

γ_F can be determined from design assumptions or calculated from extracted samples of cast members. For design assumptions include the following:

i) For elements cast horizontally, where the fibers are mostly two-dimensional such as decks and slabs, $\gamma_F = 0.8$ for flexure and beam shear, $\gamma_F = 0.6$ for two-way shear action.

ii) For elements cast vertically, where the fibers are mostly two-dimensional such as walls $\gamma_F = 0.5$ for flexure and beam shear, $\gamma_F = 0.5$ for two-way shear action.

iii) For bond and development length of reinforcements, $\gamma_F = 0.5$.

iv) For large structural components and elements in which three-dimensional fibre dispersion is expected, such as beams, girders, and footings $\gamma_F = 0.4$.

v) For local effects, such as anchors $\gamma_F = 0.3$.

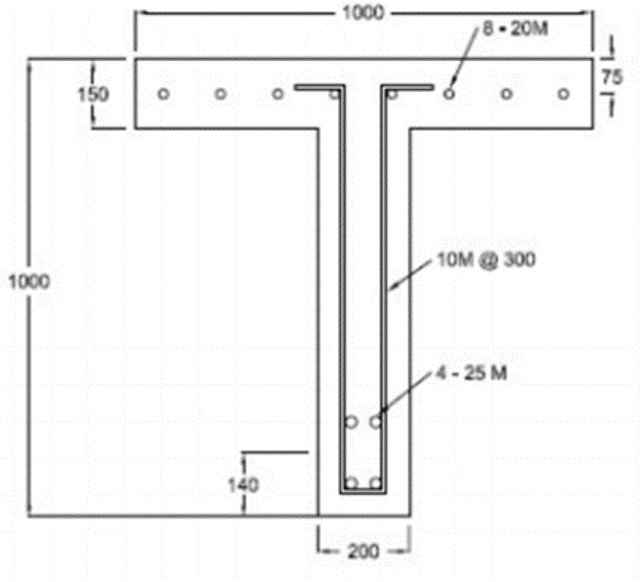

Figure 64: T-beam cross-section provided.

6.3 Description of the case study

The T-section bridge girder considered in the present chapter as a benchmark example consists of a 1000mm × 150mm top flange as depicted in Figure 64; the web is 850mm × 200mm. The member is reinforced longitudinally with 4-25M S400 bars in the web, such that the tension reinforcement centroid is at 140 mm from the soffit; the flange is reinforced with 8-20M bars placed at 75mm from the extreme compression fiber. Transverse reinforcement in the form of open, U-shaped links

are placed in the web of the member, spaced at 300mm. Links are made of 10M bars having a nominal yield strength of 400 MPa. The clear cover given for the analysis is 50mm typical.

The bridge consists of a total of 2 spans simply supported by rollers at the ends and fixed over the central support of the bridge. Each span is 10m between support axes, for a total length of the bridge equal to 20m as shown in Figure 65. The loading condition consists of 2 loads, i.e., the self-weight uniformly distributed over the entire span and 2-point loads acting at the center spans which are assumed to occur simultaneously. The unit density of the girder is given as 24 kN/m^3 supporting a live load of 190 kN. Since there is symmetry present in the support conditions as well as in the loading condition provided, for the needs of the benchmark example half the total bridge length was analyzed for a span of 10m where one end was fixed against rotation whereas the other end was simply supported. A single point load acted at midspan together with the uniformly distributed self-weight of the beam. Figure 65 summarizes the bridge span and the loading condition described above.

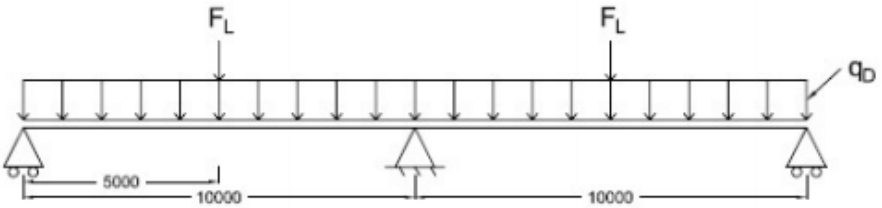

q_o	γ_o = 24 kN/m^3
F_L	190 kN

Figure 65 (from left to right): (a)Bridge span. (b) Loading

The material properties of the T-beam were analyzed as THFRC - UHPFRC. As per the annex, the THFRC classification requires a hardened ultimate tensile strength that exceeds by 10% the cracking limit and a strain capacity at the onset of localization that exceeds 0.001. The material properties for the THFRC were given in terms of mean cracking stress, $f_{crm} = 6.84\ MPa$, mean strain at cracking, $\varepsilon_{cr} = 0.00011$, mean ultimate tensile stress $f_{Fu} = 8.3\ MPa$, and mean strain at ultimate tensile stress $\varepsilon_{tu} = 0.0018$, as depicted in the tensile stress strain law of Figure 66. The compressive strength of the UHPFRC was also given as 130 MPa. Figure 66 shows the provided data in a visual graph which was provided by the CSA Task Force.

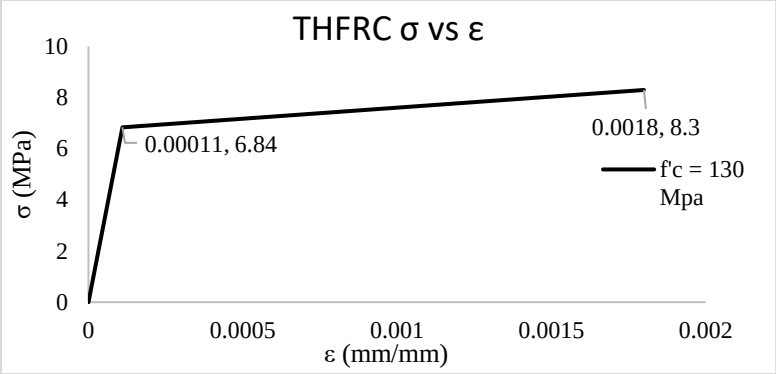

Figure 66: Stress-Strain tensile behavior for THFRC. (Given for design example)

Using this input, the T-section girder was analyzed to calculate crack widths and deflections at the serviceability limit state under both positive and negative bending. The amplification factors used to calculate the factored loads following the prescribed loading combinations from CSA S6 are summarized in Table 30. For the serviceability limit state the factored dead load due to self-weight and factored live loads are calculated as 7.68 kN/m and 171 kNs. The factored dead load and live load at fatigue limit state are calculated at 7.68 kN/m and 190 kNs. Lastly, the factored ultimate limit state loads are calculated at 9.60 kN/m and 323 kNs. A structural analysis software LinPro is used to place these factored loads to obtain the moments, and shears demanded from the T-beam. A summary of these results is shown in Table 32.

The flexural resistance at the ultimate limit state under in negative and positive bending was calculated following the ULS combination 1 (Table 30). The factored shear resistance was calculated at ULS to support flexural action whereas the fatigue limit state was verified with reference to the FLS combination 1 in CSA S6 Table 30.

Table 28: Calculation of Factored Loads

Calculation of Factored Loads		
F_L	190	kN
q_o	7.68	kN/m
Load-Factors	Dead Load	Live Load
SLS (Comb. 1)	1.0	0.9
FLS (Comb. 1)	1.0	1.0
ULS (Comb. 1)	1.25	1.7
Factored Loads	Dead Load (kN/m)	Live Load (kN)
SLS (Comb. 1)	7.68	171.0
FLS (Comb. 1)	7.68	190.0
ULS (Comb. 1)	9.60	323.0

6.4 Analysis of the Geometric Properties of the T-Section

The centroid of the section shown in Figure 64 is calculated in Table 31. In Table 31, where b_1 is width, t_1 is the height and y_1 is the distance from the extreme compression fiber to the centroid of the area being calculated. The THFRC modulus is calculated by dividing the cracking stress 6.84 MPa with the cracking strain, 0.00011 at 62181 MPa. (The modulus of the reinforcement is set at 200 GPa). The properties and areas of the constituent components of the cross section are calculated in the adjacent cells. The centroid of the girder cross section measured from the extreme compression is calculated as, y_{CG}= 344 mm.

Table 29: Calculation of centroid.

Calculation of centroid of the cross-section							
	b_1	t_1	y_1	Modulus	Area	Moment of Area	Area * Modulus
Flange	1000	150	75	62181.82	150000	6.99545E+11	9327272727
Web	200	850	575	62181.82	170000	6.07827E+12	1.0571E+10
Rebar							
Compression Steel	8	300	75	200000	2400	36000000000	480000000
Tension Steel	2	500	792.5	200000	1000	1.585E+11	200000000
Tension Steel	2	500	927.5	200000	1000	1.855E+11	200000000
				Sum		7.15782E+12	2.0778E+10
						y_c	**344.48**

Table 30: LinPro results for SLS, ULS, and FLS moment and shears. (kN, kN-m)

SLS (Combination 1)	FLS (Combination 1)
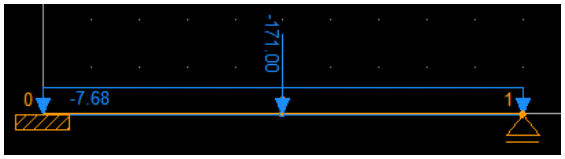	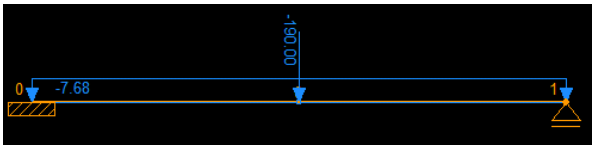
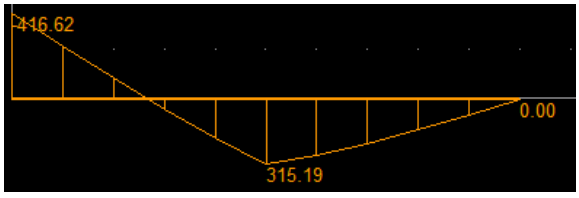	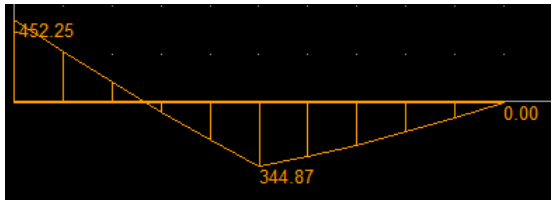

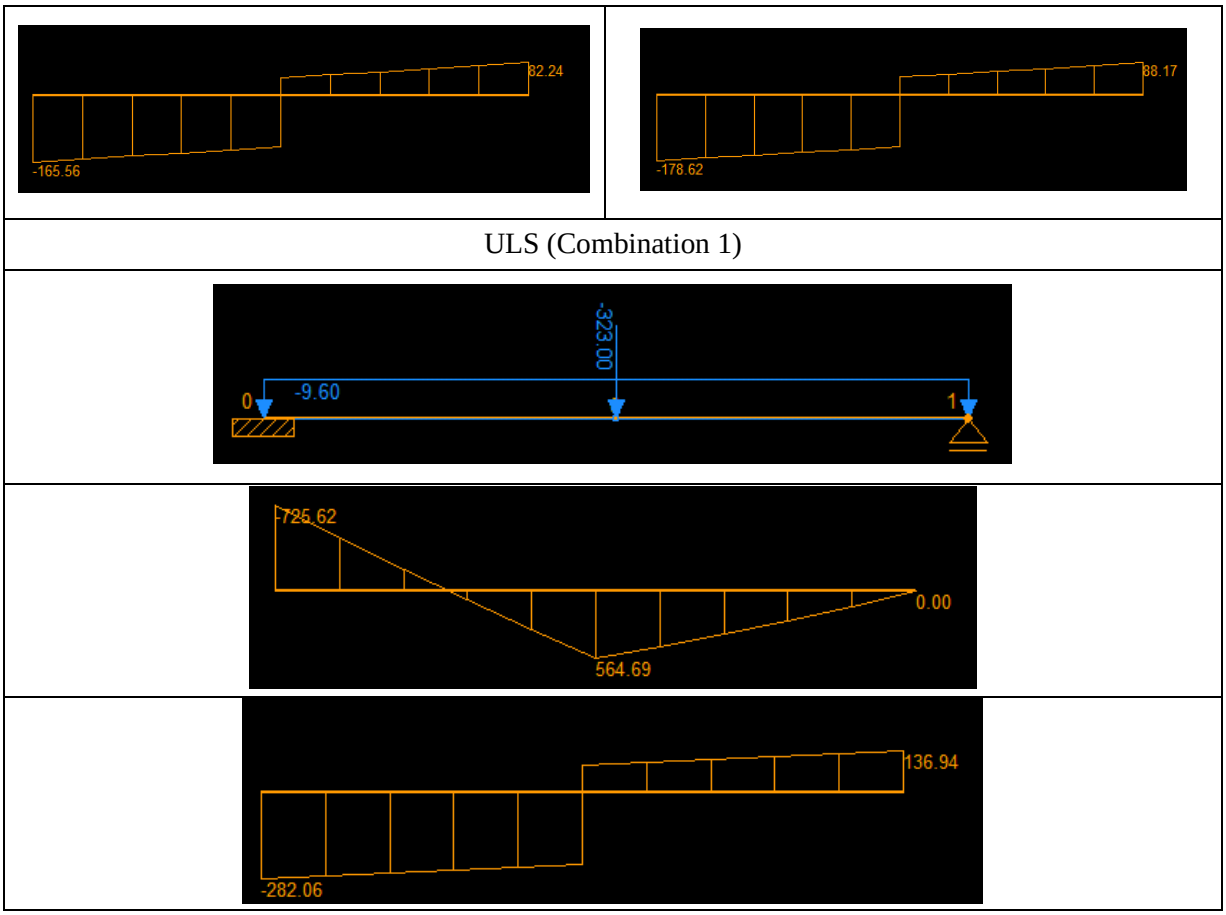

6.5 Crack Width Estimation and Deflection Calculation

To compute the crack width for tension hardening UHPFRC, Clause A8.1.12.1 and the commentary CA8.1.12.1 state that the annex limits the use of THFRC to linear-elastic and strain hardening zones under SLS and FLS. The annex suggests that the cracking of the UHPFRC is controlled by assuring that the material does not exceed the design strain demands under service conditions. This is done so that the concrete remains in the strain hardening zone and cracks do not localize, and therefore crack control is secured. For the needs of the design calculations a conservative estimate of the tensile stress strain response of THFRC was considered, as depicted in Figure 67. Clause A8.1.8.2.3 only allows a maximum design strain of $\varepsilon_{ts} = 0.5\ \gamma_f \varepsilon_{tu}$ for SLS and FLS, whereas the corresponding stress limit is equal to the min $\{f_{crm},\ \gamma_f \cdot f_{fu}\}$. The strain at ULS is limited to $\gamma_f \varepsilon_{tu}$, with the same stress limit as for SLS and FLS.

The fiber efficiency factor for the girder studied was assigned the value of 0.4 based on Clause A8.1.4.6b) iv) specified for large structural elements in which three-dimensional fiber dispersion

is expected. This limit for SLS, FLS, and ULS is estimated as 3.3 MPa. The design strain for SLS, FLS was calculated to be 0.00036 and 0.00072 for ULS.

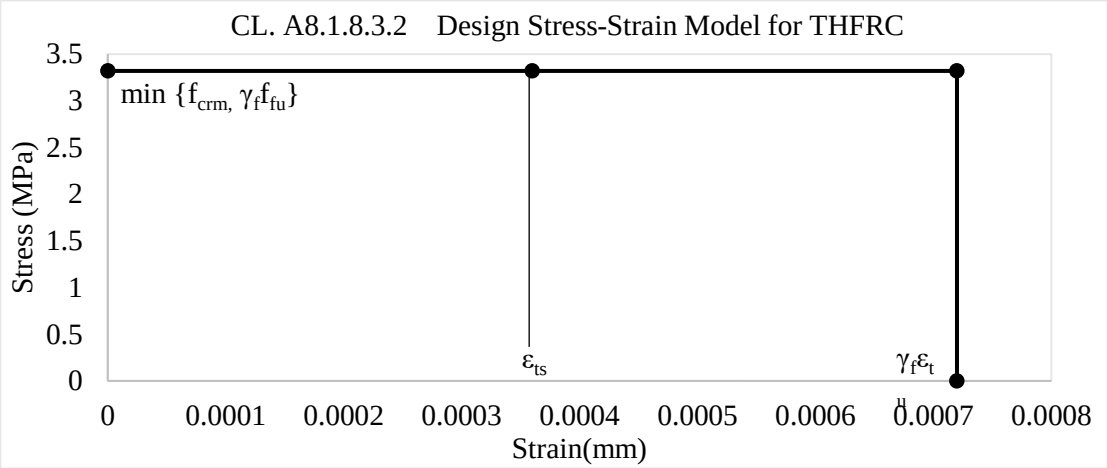

Figure 67: Adopted design tensile stress-strain model for THFRC

A sectional analysis program using layered analysis was used for strength calculations: here the UHPFRC behavior in compression was idealized using a stress-strain model following Hognestad's parabola as is shown in Figure 68. Table 33 is shown to summarize the setup of the layered analysis performed.

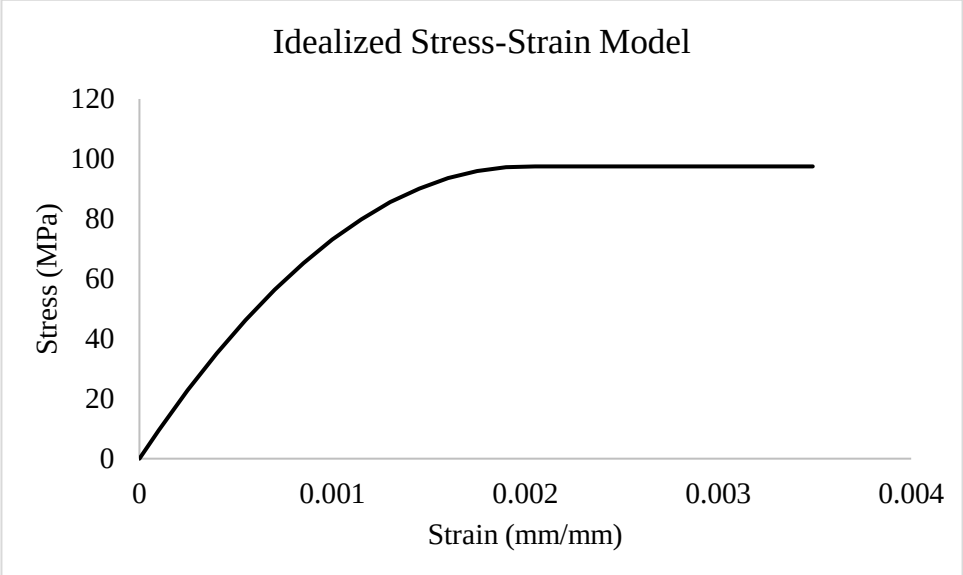

Figure 68: Idealized stress-strain model for concrete in compression.

Table 31: Sectional analysis program.

Concrete	Layer w	Ac(mm^2)	y-Top(mm)	Layer strain	Stress(Mpa)	Layer Force	Layer Moment
layer #1	25	25000	12.5	2.990E-05	3.0861	77.1520	25.6135
layer #2	25	25000	37.5	2.866E-05	2.9590	73.9738	22.7090
layer #3	25	25000	62.5	2.742E-05	2.8317	70.7935	19.9629
layer #4	25	25000	87.5	2.618E-05	2.7045	67.6113	17.3752
layer #5	25	25000	112.5	2.494E-05	2.5771	64.4271	14.9463
layer #6	25	25000	137.5	2.369E-05	2.4496	61.2409	12.6761

From this sectional analysis, the program's algorithm is iterated for constant strains at the extreme compression fiber where through equilibrium of axial forces the neutral depth is calculated, until the program shows the tension steel strain set at the onset of yielding, to find the flexural strength at SLS; for M_y= 314.33 kN-m, the strain in the extreme tension fiber was estimated as 0.00002, which is less than the strain ε_{ts} and therefore no cracking would occur in the section under service loads.

Next, to compute the deflections of the T-beam under positive bending, LinPro and the simplified method to compute deflections in clause 8.13.3.3 (CSA S6 - 2019) were used. The deflection calculation according with the clause A8.1.13.1 refers to CSA S6 Clause 8.13 which requires deflections that occur immediately under the presence of load should be based on elastic methods where the modulus E_c at the time of loading and effects of cracking and reinforcement be considered. Section 8 of the S6 code gives a simplified method to calculate the effective moment of inertia as shown in Equation 6.1 and Annex A8.1 further specifies that the moment of a cracked section I_{cr} used to compute the effective moment of inertia I_e at the critical section for service load M_a be calculated as shown in Equation 6.2 where ψ_a is the curvature of the section at service load moment M_a.

$$I_e = I_{cr} + \left(I_g - I_{cr}\right)\left[\frac{M_{cr}}{M_a}\right]^3 \leq I_g \qquad \text{Equation 6.1}$$

$$I_{cr} = M_a / E_C \psi_a \leq I_g \qquad \text{Equation 6.2}$$

$$\Delta = K\left(\frac{5}{48}\right)\frac{M l_n}{E_c I_e} \qquad \text{Equation 6.3}$$

The deflections are calculated from Equation 6.3 where K is 0.8 for beams fixed at one end and simply supported at the other, M is the moment due to service loads, E_c is the modulus of elasticity as previously calculated to be 62181 MPa, and I_e is the effective moment of inertia. Table 34 summarizes the calculation of deflection done from both LinPro and the excel program.

Table 32: Calculation of immediate deflection.

Immediate Deflection only		
I_{cr}	2.703E+10	mm^4
I_g	3.203E+10	mm^4
l_e	2.771E+10	mm^4
M_{cr}	161.524	kN-m
M_a	315.190	kN-m
f_r	6.841	N/mm^2
E_c	62181.818	N/mm^2
N	3.216	-
y_t	655.513	mm
K	0.8	-
ψ_a	1.875E-07	1/mm
$\Delta_{calculated}$	1.849	mm
$\Delta_{Live\ Load}$	1.789	mm
$\Delta_{Dead\ Load}$	0.50212	mm
$\Delta_{DL + LL}$	2.291	mm

6.6 Factored Flexural Resistance

To determine the factored flexural resistance at ULS for the T-beam the layered analysis of the section was used to obtain the moment-curvature relationship. Figure 69 is shown as a summary of the moment-curvature relationship obtained when the tensile response is defined as a constant stress from 0 strain to a design strain of 0.00036.

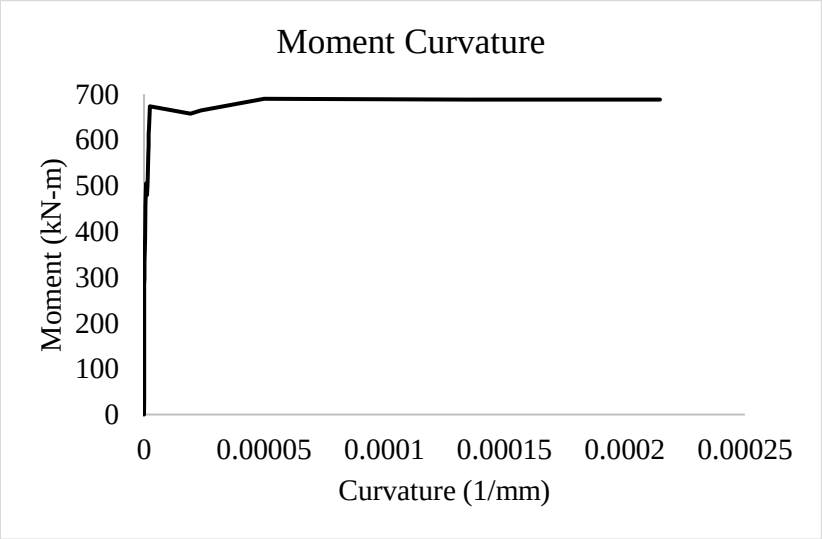

Figure 69: Moment curvature obtained from plastic tensile model.

Clause A8.1.8.4.3.1 which enlists the method to determine the flexural resistance using a curvature ductility ratio μ which is calculated as a ratio of curvature ψ_1 and $\psi_{y,}$ where ψ_1 is the curvature at the maximum calculated flexural resistance and ψ_y is the curvature of the section at yielding. The annex specifies the minimum curvature ductility ratio μ_{min} to be 2 for members designed with elastic analysis without any redistribution of forces.

For members with a curvature ductility ratio of greater than 2, the annex states that the moment resistance at yielding of the reinforcement to be set equal to the factored flexural resistance. For members with a curvature ductility ratio of less than 2.0 the moment resistance is calculated as 0.5 times the maximum calculated flexural resistance from the program, or the flexural resistance of the section calculated based on the resistance provided by the reinforcement only, without considering the tensile contribution of the fibers. The maximum of either is flexural resistance is taken in this case. The flexural resistance for the T-beam in question, by the method included in the annex, is 688 kN-m which is based on the resistance provided by the reinforcement without considering the tensile contribution of the fibers (i.e., the curvature ductility ratio was less than 2.0)

6.7 Factored Shear Resistance

To calculate the shear resistance of the T-beam, Annex A8 refers to the CSA S6-19 shear resistance clauses set for conventional concrete from Equations 6.4 to 6.6. Additionally, the annex limits the compressive strength of the UHPFRC for shear calculations to 85 MPa. The shear calculation shown in Table 35 does not include the contribution of the fibers for the tension hardening behavior of UHPFRC. The shear resistance of the concrete and transverse steel is computed in the table from Equations 6.5 to 6.6.

$$V_r = V_c + V_s \leq 0.25\Phi_c f'_c b_v d_v \qquad \text{Equation 6.4}$$

$$V_c = 2.5\beta\Phi_c f_{cr} b_v d_v \leq 3.2\ MPa \qquad \text{Equation 6.5}$$

$$V_s = \frac{\Phi_s f_y A_v d_v \cot\theta}{s} \qquad \text{Equation 6.6}$$

Table 33: Summary of shear resistance at ULS.

Shear Resistance at ULS			
V_r	570.38	kN	CL. 8.9.3.3
$V_{r,\,max}$	2631.60	kN	CL 8.9.3.3
V_c	178.33	kN	CL. 8.9.3.4
$V_{c,\,max}$	222.91	kN	Cl. 8.9.3.3
V_s	392.05	kN	CL. 8.9.3.5
B	0.18	-	CL. 8.9.3.6
f_{cr}	3.2	MPa	CL 8.4.1.8.1
b_v	200	mm	CL. 8.9.1.6
d_v	774	mm	CL 8.9.1.5
f_y	400	MPa	-
A_v	200	mm^2	taken as 2-10M bars
Θ	35	°	CL. 8.9.3.6
s	300	mm	-

6.8 Verifying Fatigue

To verify the FLS of the T-beam, CSA Annex A8.1 limits the stress of straight reinforcing bars as shown in Equation 6.7, where f_{sf} is the minimum stress in reinforcement due to FLS combination 1 (where the sign convention for the equation is; Tension +, Compression -).

$$\sigma_{FLS} < 165 - 138\, f_{sf}/f_y \qquad \text{Equation 6.7}$$

The annex allows the contribution of steel fibers when verifying the FLS of the section as long as the total strain in tension reinforcement does not exceed the design strain ε_{ts} = 0.00036. The program used for this section analysis considers the fibers to function throughout its design life. To determine the stress in the reinforcement at FLS, the loading analysis calculated a mid-span moment of 54 kN-m.

From a moment-curvature plot done by iteration of the strain and depth of neutral axis through the equilibrium of axial forces, the stress in the most extreme reinforcement layer in tension at FLS was f_{sf} = 0.0146 MPa. The limit from Equation 6.7 calculates the stress limit to 165 MPa.

The strain in the reinforcement is calculated as 7.28E-08 which is less than the design strain $\varepsilon_{ts,}$ and therefore the section is determined to be sufficient under FLS at mid-span.

6.9 Results and Discussion

The CSA Annex A8.1 for the design of UHPFRC structural elements is not organized in a manner to allow new designers to implement the clauses listed effectively. The annex contains clauses for THFRC and TSFRC together, which can be dangerous as new users are prone to use the incorrect equations and design methodologies suggested. The calculation of crack widths for example is stated as not necessary for THFRC on the assumption that the design of the structural elements is kept in the hardening range of the material. The use of a hardening range where rectangular tension stress blocks are used for a sectional analysis performed in layers can drastically underestimate the true capacity of the material in tension. Moreover, the calculation of the deflections for these structural elements is based on sectional analysis in which the curvature ψ_a is needed for a moment of M_a occurring on the section. The annex does not provide a more efficient method to compute these deflections which are also based on the assumption of an equivalent rigid-plastic stress-strain response in tension, which as previously discussed underestimates the moment resistance, and proportionally underestimates the immediate deflections.

The method by which the flexural resistance is calculated for UHPFRC is discussed in more detail below. In the commentary provided for the annex, the authors of the annex describe 3 key values to determine the flexural resistance of the material, where the three key values include the yielding of the reinforcement, strain at the extreme compression fiber of the member equal to $\gamma_f \varepsilon_{tu}$, and strain at the extreme compression fiber of the member equal to the ultimate compression strain ε_{cu} equal to 0.0035. Figure 70 is shown to summarize the milestone points on which the annex determines the flexural resistance of the T-beam comprising UHPFRC.

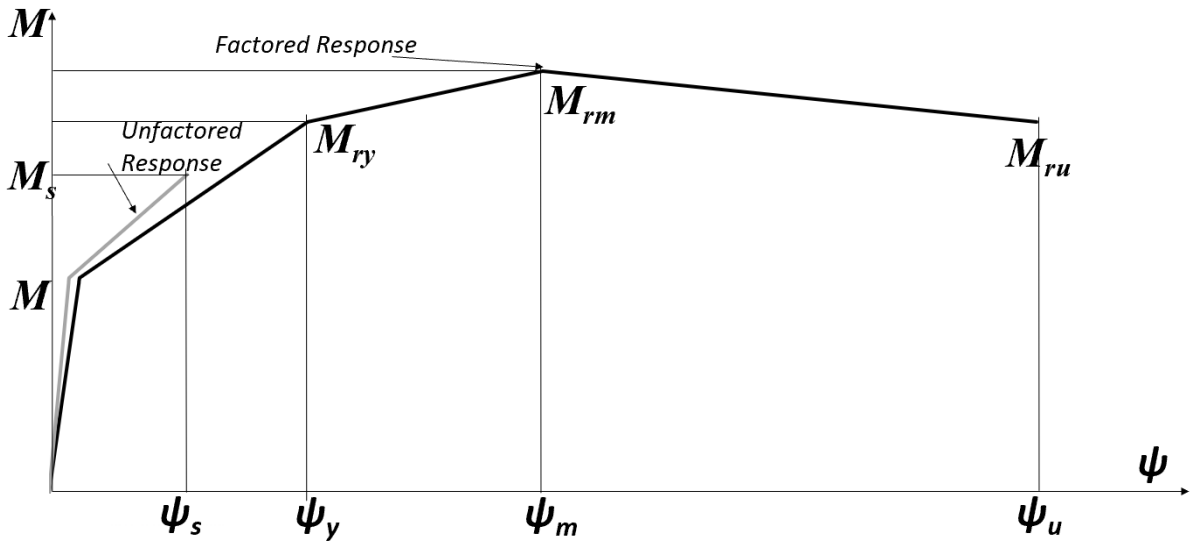

Figure 70: Summary of milestones points.

The suggested approach to determine the flexural resistance curve by calculating the coordinates of three milestone points, namely, (a) Yielding of steel reinforcement, (b) Extreme compression strain equal to 0.0035 and (c) Extreme tension strain equal to $\gamma_f \cdot \varepsilon_{tu}$.

The ductility curvature ratios ψ_1 are assessed at the factored moment resistance from the maximum moment of any of the three $M_{ry,}$ $M_{rm,}$ *or* M_{ru}. The factored design moment resistance M_r is the maximum from among M_{ry} or M_{ro}, where M_{ro} is the moment resistance calculated based on only the reinforcement without considering the contribution of the fibers for the case when the ductility ratio is greater than 2. For the case where the ductility ratio is less than 2, the moment resistance is taken as the maximum of the two values, 0.5 * M_1, or M_{ro}, where M_1 corresponds to the moment resistance at the curvature ductility ratio ψ_1. For the purpose of design the current method included in the annex underestimates UHPFRCs capability for larger ductility at higher moment resistances by severely reducing the design strains the material may take (the design strains being limited to 0.001, where the material from chapter 4 and 5 display a capability of maintain tensile strain up to 0.01, the difference being almost 10 times). In the current state of the annex, where equations from conventional concrete are used, more testing data is needed so that separate equations may be developed for such a high strength material.

6.10 Conclusion

The analysis performed on a benchmark bridge girder comprising tension hardening UHPFRC material according with the CSA annex A8.1 proved that the standard design and analysis procedures for normal concrete may be extended to this new class of concrete materials with tension resistance, with further need for calibration of the conventional equations.

An important finding from the analysis performed was the ductility calculated significantly surpassed the required values by the design code, indicating the need for further calibration of the design methods when applied to UHPFRC materials. Assuming a constant value for the tensile stress regardless of the magnitude of tension strain but neglecting the post-peak softening stress-strain branch overestimates the contribution of layers near the neutral axis causing significant calculated overstrength in the region beyond the onset of cracking strain up to bar yielding. This has an adverse effect on the curvature values associated with relatively small moment resistances. This issue can be mitigated by calculating the stresses in the ascending branch of the stress-strain diagram using Hooke's law rather than the Code assumed rigid plastic stress-strain diagram, thereby avoiding the overestimation of stress in individual layers. Lastly, it is highly recommended to separate the annex into two distinct parts that would refer to the THFRC and TSFRC materials, respectively.

Chapter 7. An opportunity in bridge design

7.1 Introduction

The discussion in the preceding chapter is focused on the benefits of UHPFRC material with strain hardening response in tension and how it may affect the flexural response of a structural member. It was noted that the UHPFRC in the tension zone contributes to the resistance even at large tensile strains, whereas in the case of normal concrete the established practice is to ignore the contribution of concrete in the tension zone.

However, in the discussion so far very little use has been made to the exceptional compressive strength of this class of materials – compressive stresses in the range of 120 MPa or more are in the same range as that which can be supported by some qualities of structural iron and steel, underscoring the fact that this new class of materials provides a new opportunity in concrete design, that reaches beyond the limits of an active tensile concrete zone. It is noted that for a given cross section geometry (height and width) the maximum amount of steel reinforcement that can be provided in the tension zone is limited by the strength of the compression zone. This is because reinforcement yielding is used as the fuse by which a ductile failure is controlled to occur prior to concrete compression crushing (a brittle mode). The maximum area of longitudinal tension reinforcement, A_s, divided by the area of the cross section ($b \times h$), is the reinforcement percentage at balanced failure, ρ_{bal}, where simultaneous concrete compression crushing occurs along with tension reinforcement yielding. Therefore, it may be said, that the peak flexural strength of the cross section which is obtained through ρ_{bal}, is effectively controlled by the compressive strength of the cross section, f_c'.

The prospect of a three-fold increase of the value of f_c' which is offered by the replacement of normal concrete with UHPFRC opens up the possibility of introducing significantly larger amounts of reinforcement in the tension zone of the member – to such an extent that the embedded amounts may only be limited by geometric and detailing considerations once the risk of premature concrete crushing is mitigated.

In the case of normal concrete, reaching to orders of magnitude higher flexural strength than the balanced reinforcement amount could support for a given cross section, is possible with the

introduction of prestressing. This is a common method to counteract the need for bulkier members in order to support higher loads - (larger members combine the disadvantage of leading to higher static moment demands therefore doing away with much of the benefit they bring due to size). Prestressing is used primarily in bridge girders in order to (a) maintain elastic response (below cracking) under serviceability conditions, (b) support significant dead and live loads, and (c) engages additional flexural strength by means of an eccentric compressive force that acts in the familiar tension zone and counteracts mainly the moment resulting from dead loads.

The objective of the present section is to explore other alternatives to prestressing, that could achieve comparable strength increase in a girder of fixed dimensions by the mere strength increase that is provided by the compression zone of UHPFRC and the tension stresses in the concrete tension zone. For this reason, comparisons are made with the flexural resistances of standard CPCI girders of a known external geometry, which are off-the shelf products used in bridge deck construction in Canada.

7.2 Stress-Strain models

To enable the intended comparison, stress-strain models representing the response of UHPFRC in compression and tension are needed. The current codes including the CSA A23.3-14 and CSA S6-19 do not provide methods that can model the behavior of UHPFRC under compression or tension for preliminary designs of structural elements that can represent the post-peak behavior with some relevance to the experimental evidence. To model the behavior of the material under compression, the recommendations provided by the French Association Française de Genie Civil (AFGC) (2013) in Annex 2 were used. The AFGC model provides an analytical stress-strain law that approximates the entire range of compression response. This model extends a stress-strain law that was originally proposed by Popovic's for regular concrete.

Before the model could be assembled, three parameters are needed. These include the modulus of elasticity of concrete under compression, the compressive strength, f_c', and ultimate tensile strength, f_{tu}. The model developed in the annex is based on tested cylindrical specimens with the size of 110mm × 220mm instrumented with three strain gauges placed symmetrically (vertically and horizontally).

For a conservative design and given the several uncertainties which still exist in classifying this material under tension, the plastic model included in the CSA S6-19 Annex A8.1 was used in the present study. This model is illustrated as a constant strength starting at 0 tensile strain, which stays constant up till a strain of at least $\varepsilon_{tu} \geq 0.001$ as shown in Equation A8.1.4.3 from the annex. The ultimate tensile stress is taken as the lowest of the two parameters, i.e., the average cracking stress $f_{crm,}$ and the specified ultimate tensile stress f_{Fu}. Figure 67 illustrated the rigid-plastic model as it is used to model the tensile behavior of UHPFRC following CSA S6-19 Annex A8.1 clause A8.1.8.3.2.

The annex classifies tension hardening behavior based on compressive strength f_c', ultimate tensile strength $f_{Fu,}$ ultimate tensile strain $\varepsilon_{tu,}$ and cracking strength, f_{crm}. The design of the UHPFRC girders in the present investigation is based on the assumption of the material to be THFRC on account of its favorable characteristic of sustaining the same or higher loads after cracking supported by bridging of fibers across the cracks.

As previously mentioned, the AFGC model requires the input of a known modulus of elasticity E_c, compressive strength f_c', and ultimate tensile strength f_t. To develop a preliminary design methodology the modulus of elasticity of UHPFRC may be calculated from Equation 7.1. (See the U.S Department of Transportation Federal Highway Administrations' State of the Art Report, 2013), which correlates the modulus of elasticity E_c to the compressive strength f_c'.

$$E_c = 46200\sqrt{f_c'} \text{ (psi) or } 3800\sqrt{f_c'} \text{ (MPa)} \qquad \text{Equation 7.1}$$

This equation can be used on a range of compressive strengths of 30 – 200 MPa (Graybeal, 2018). The model prescribed by AFGC is developed with the abscissa ε_{c1} of the peak stress f_c' first defined without taking into account the favorable effect of confinement provided by the fibers as,

$$\varepsilon_{c1} = \left[1 + 0.016\frac{k_0}{{f_c}^2+800}\right] * \frac{{f_c}^{2/3}}{k_0} \qquad \text{Equation 7.2}$$

Where f_c is in MPa and k_0 is the factor that links the compressive strength f_c to the modulus E_c by the relationship shown in Equation 7.3, this equation is used to obtain the factor k_0:

$$E_c = k_0 {f_c}^{1/3} \qquad \text{Equation 7.3}$$

The abscissa ε_{c2} corresponds to a post-peak stress of $0.7\ f_c$ on the descending branch according with Equation 7.4:

$$\varepsilon_{c2} = \left[1 + \frac{20}{f_c}\right] \varepsilon_{c1}$$ Equation 7.4

To take the effect of confinement brought by the fibers these equations become

$$\varepsilon_{c1,f} = \left[1 + 4\frac{f_{tu}}{f_c'}\right] \varepsilon_{c1}$$ Equation 7.5a

$$\varepsilon_{c2,f} = \left[1 + 15\frac{f_{tu}}{f_c'}\right] \varepsilon_{c2}$$ Equation 7.5b

The model for the post-peak compressive behavior is then obtained using Popovic's curve as follows,

$$x = \varepsilon/\varepsilon_{c1,f}$$

$$y = \sigma/f_c$$

$$X = \varepsilon_{c2,f}/\varepsilon_{c1,f}$$

$$Y = \frac{\eta x}{\eta - 1 + x^{\phi\eta}}$$

Where,

$$\eta = k/(k-1)$$

$$k = E_c\varepsilon_{c1,f}/f_c$$

$$\phi = 1 \; in \; the \; ascending \; branch$$

$$\phi = \frac{\ln\left(1 - \eta + \frac{X}{0.7}\right)}{\eta \cdot lnX} \; in \; the \; decending \; branch$$

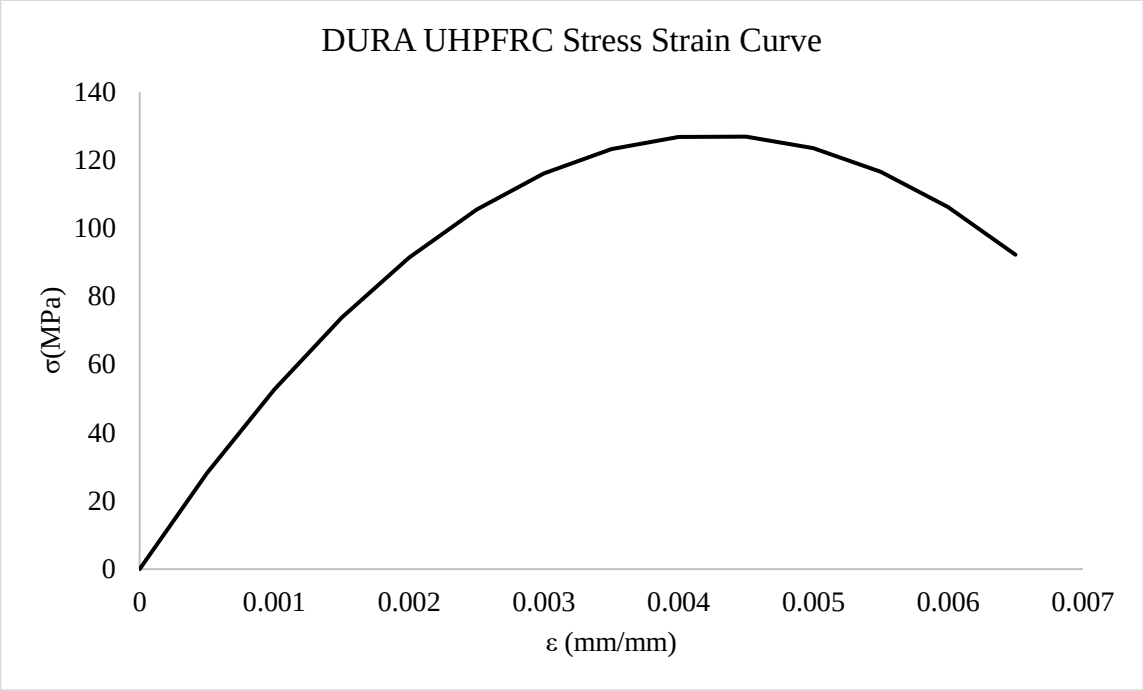

Figure 71: Tested mix stress-strain curve in uniaxial compression.

Using this analytical law to model the stress-strain relationship of UHPRFC various compressive strengths ranging from 30MPa – 200MPa can be illustrated with the complete uniaxial compressive a stress-strain diagram that includes the post-peak response of the material. The calculated stress-strain response relationship for the UHPFRC mix studied in the present thesis (Chapters 3 and 4) is plotted in Figure 71. Similarly, the compressive constitutive law of compressive strengths ranging from 100 MPa to 200MPa are modeled and summarized in Figures 72 to 76. In all, five models are presented, staggered at peak compressive strength intervals of 25MPa. Each model that corresponds to a different value of strength f_c', is further analyzed for different ultimate tensile strengths, f_{tu}. Here the f_{tu} is taken to be equal to a fixed a fraction of f_c' by varying a range from 5%-20%, with 5% intervals (i.e., $f_{tu}=\lambda \cdot f_c')$.

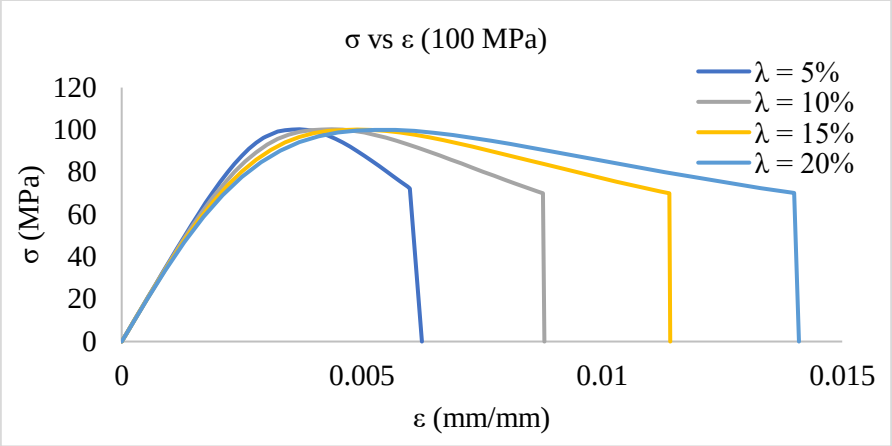

Figure 72: Stress-strain models including post-peak for f_c' = 100 MPa.

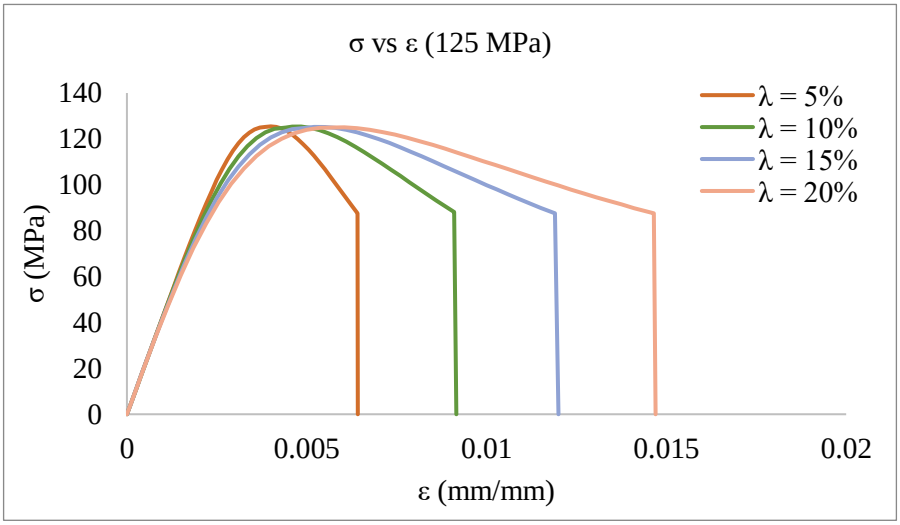

Figure 73: Stress-strain models including post-peak for f_c' = 125 MPa.

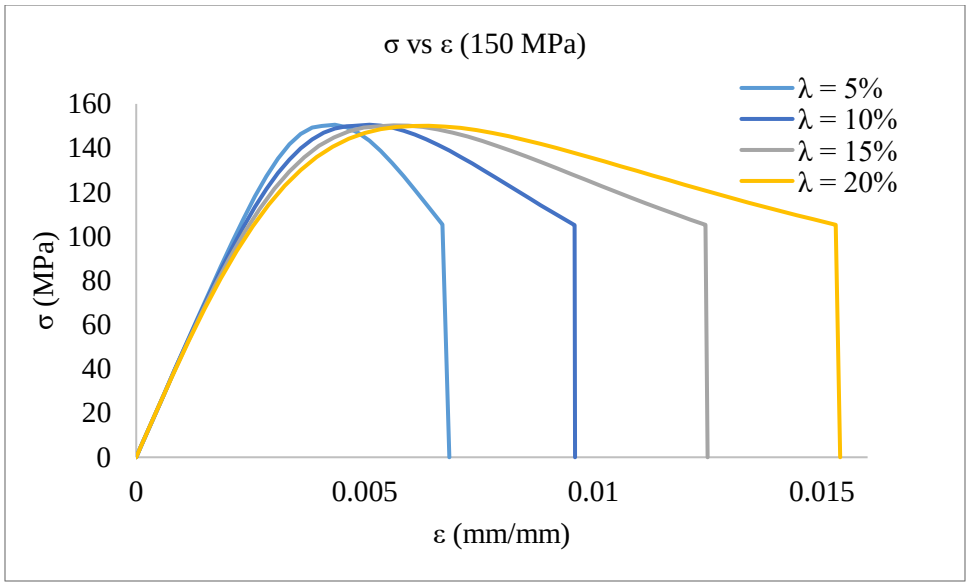

Figure 74: Stress-strain models including post-peak for $f_c^{'}$ = 150 MPa.

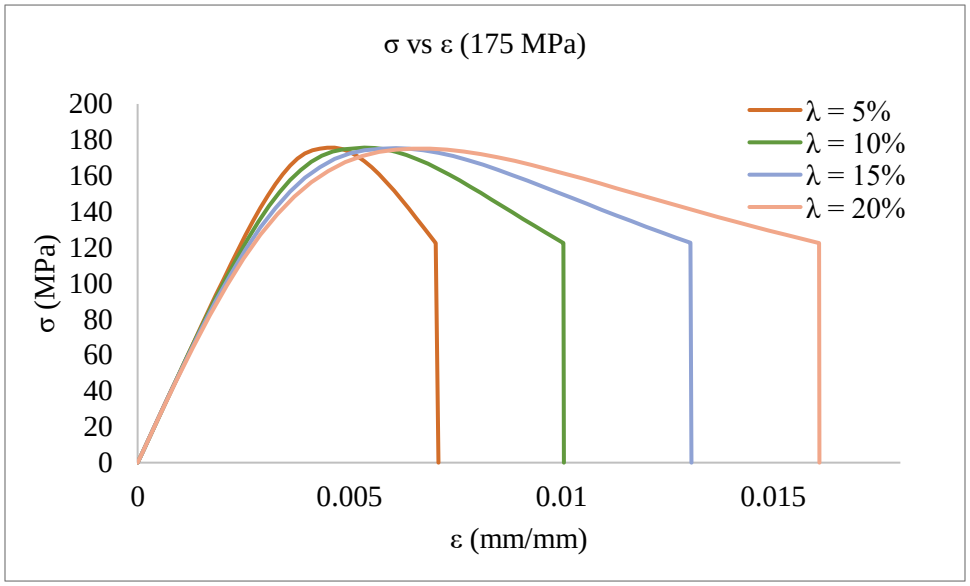

Figure 75: Stress-strain models including post-peak for $f_c^{'}$ = 175 MPa.

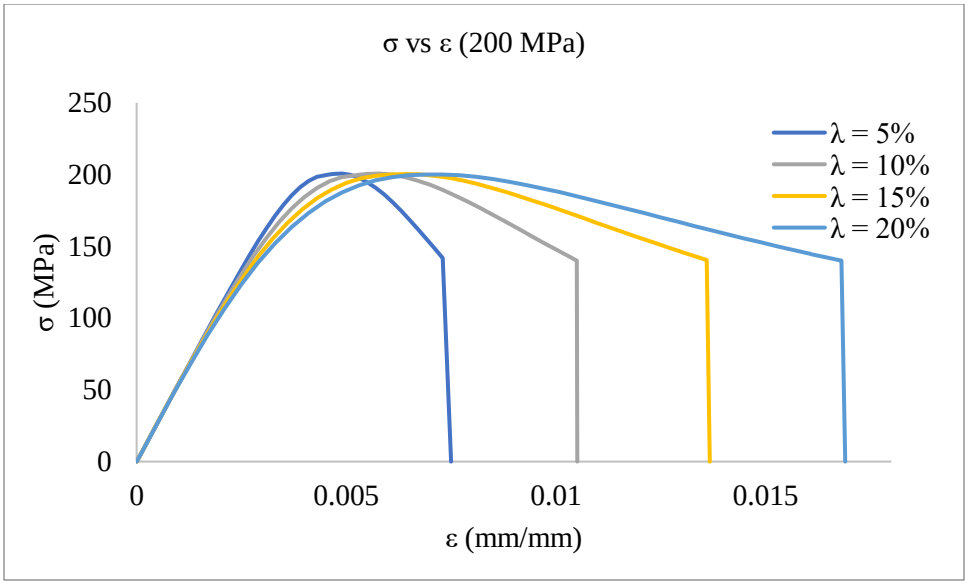

Figure 76: Stress-strain models including post-peak for $f_c' = 200$ MPa.

In the parametric investigation that follows, the ultimate tensile strength f_{tu} was compared with the compressive strength of the UHPFRC by being represented as the product of $\lambda \cdot f_c'$. By relating the ultimate tensile strength of the material as a fraction of its compressive strength various girder cases could be modeled, so as to illustrate the amount of tensile resistance required in order to achieve the ultimate capacity of a given section with a range of compressive strengths. The tensile model used consists of plastic behavior where the resistance under tensile strains is constant until the ultimate tensile strain of at least $\varepsilon_{tu} \geq 0.001$ as shown in Equation A8.1.4.3 from Annex A8.1 (Figure 77).

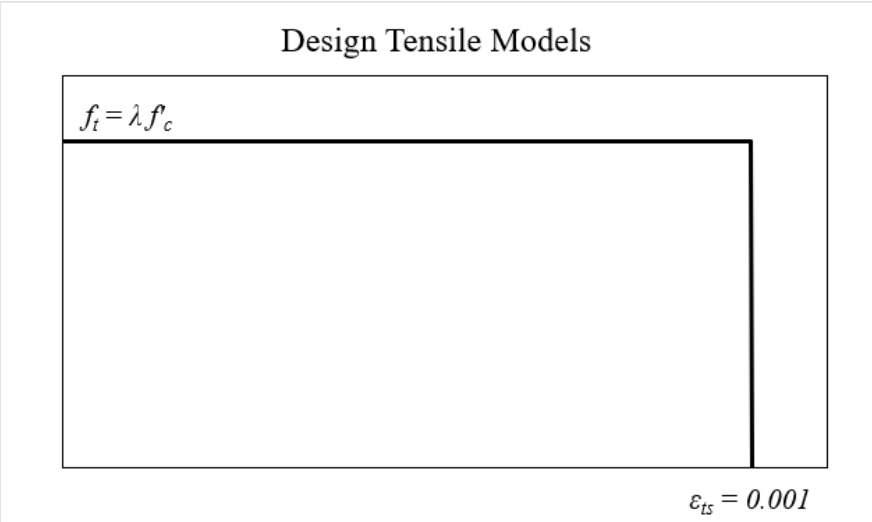

Figure 77: Design Tensile Model for UHPFRC

7.3 Analytical Model

The compressive behavior of UHPFRC was modeled with the recommendations of the AFGC. Further, the tensile behavior was modeled to reflect a constant stress until the peak strain of $\varepsilon_{tu} \geq 0.001$ was reached. The two models were used to analyze as a benchmark case the CPCI 900 girder (CPCI 2017). Parameter of the investigation was the compressive strength of the UHPFRC material used in the girder. To develop a sectional analysis program, the following assumptions were made for the ultimate limit state:

1) The normal strain in concrete was assumed to vary linearly over the height of the cross section (i.e., plane sections remaining plane),

2) bonded reinforcement is assumed to be fully compatible with the surrounding concrete (i.e. equal strain assumption)

7.3.1 Sectional Analysis in Pure Flexure

In this manner, the following compressive strengths with corresponding reinforcement ratios, and λ values can be analyzed together to observe the trends to best design a bridge girder. For this thesis, a CPCI 900 girder is selected as a reference size for which the models are made. Table 36 summarizes the model parameters used to develop preliminary design charts.

Table 34: Summary of all model parameters for varying f_c' and reinforcement ratios.

Model Parameters	
f_c' = 100 MPa	f_c' = 125 MPa
➢ ρ_{min} • λ = 5% • λ = 10% • λ = 15% • λ = 20% ➢ ρ_{bal} • λ = 5% • λ = 10% • λ = 15% • λ = 20%	➢ ρ_{min} • λ = 5% • λ = 10% • λ = 15% • λ = 20% ➢ ρ_{bal} • λ = 5% • λ = 10% • λ = 15% • λ = 20%
f_c' = 150 MPa	f_c' = 175 MPa

➢ ρ_{min} • λ = 5% • λ = 10% • λ = 15% • λ = 20% ➢ ρ_{bal} • λ = 5% • λ = 10% • λ = 15% • λ = 20%	➢ ρ_{min} • λ = 5% • λ = 10% • λ = 15% • λ = 20% ➢ ρ_{bal} • λ = 5% • λ = 10% • λ = 15% • λ = 20%
f_c' = 200 MPa	
➢ ρ_{min} • λ = 5% • λ = 10% • λ = 15% • λ = 20% ➢ ρ_{bal} • λ = 5% • λ = 10% • λ = 15% • λ = 20%	

For each design compressive strength, two limiting reinforcement ratios were considered, i.e., ρ_{min} and ρ_{bal} which correspond to the minimum required tension reinforcement ratio and the balanced tension reinforcement ratio, respectively. The minimum amount is defined by the requirement that the flexural strength of the cross section after cracking is at least equal to the cracking strength so that there is no loss of resistance in the structural component if it cracks; the balanced ratio is the maximum reinforcement ratio that can be placed in the cross section without the addition of compression reinforcement so as to avoid premature crushing failure of concrete in the compression zone when the tension reinforcement reaches yielding.

For each ratio of reinforcement, the λ values are incremented by 5% from 5% - 20%. To calculate the minimum reinforcement ratio and balanced reinforcement ratio of the CPCI 900 section the following methodology was used. In Figure 78, b_t is the width of the top flange, b_b is the width of the bottom flange, h_t is the height of the top flange, h_b is the height of the bottom flange, h is the total height of the section, c is the depth of the compression zone, A_t is the area of the top flange shown as the hatched area, A_b is the area of the hatched area at the bottom flange, b_w is the width

of the web, A_s' is the compression steel reinforcement, and A_s is the tension steel reinforcement. From these variables, the total area of the section can be summed as

$$A_{tot} = hb_w + A_b + A_t$$

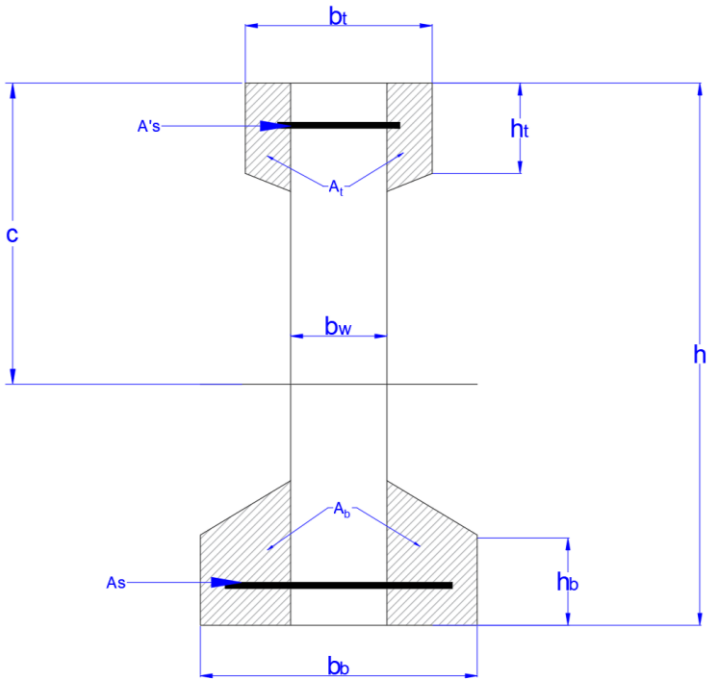

Figure 78: CPCI girder section geometric parameters.

To calculate the reinforcement ratios of the section, equilibrium of forces is established from the following illustration of forces acting on the non-prestressed section; the section is considered at the onset of concrete crushing, which is taken conservatively as occurring at a maximum compressive strain of 0.0035. (In fact, this is a conservative assumption, because UHPFRC is known to reach higher strains before post-peak response in compression. However, as it is still relatively difficult to collect adequate data regarding the ultimate strain capacity of the material in compression on account of the relatively flexible testing frames used for this test in comparison to the UHPFRC, the limit of 0.0035 is used). Factors β_1 and α_1 are calculated following CSA S6-19 as shown in the Equations 7.6 and 7.7.

$$\alpha_1 = 0.85 - 0.0015f'_c \geq 0.67 \qquad \text{Equation 7.6}$$

$$\beta_1 = 0.97 - 0.0025f'_c \geq 0.67 \qquad \text{Equation 7.7}$$

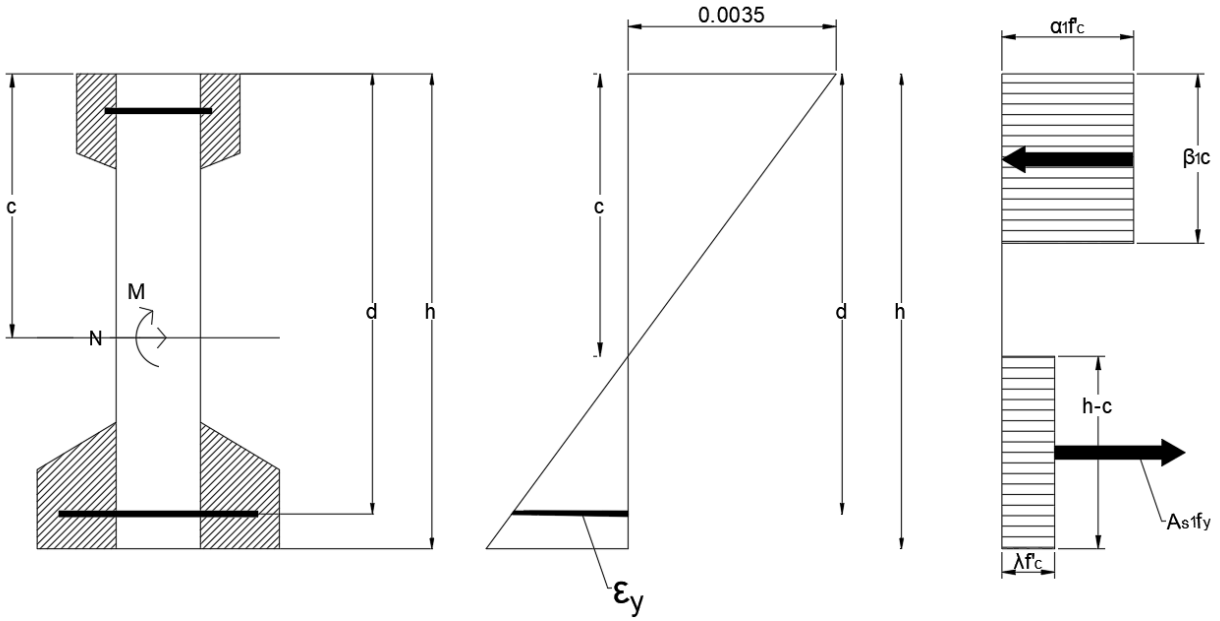

Figure 79: Definition of terms for sectional equilibrium

By summation of axial stress resultants on the cross section the following expression was derived,

$$\sum \mathrm{F} = 0$$

$$0 = \alpha_1 f'_c b \beta_1 c - N - A_{s1} f_y - (\lambda f'_c)(h - c)b \qquad \text{Equation 7.8}$$

Where N = 0 (no axial load for the girder). Equation 7.8 is simplified by dividing with the product b×d, where d is the effective depth of the cross section (measured from the extreme compression fiber to the centroid of the tension reinforcement). Using the definition of $\rho_s = A_s/(b \cdot d)$, Equation 7.9 is obtained, where the depth of compression zone is calculated from the reinforcement fraction of tension steel. By setting the depth of compression zone to that of balanced failure, c_{bal} (Eqn. 7.10), the balanced reinforcement ratio $\rho_{s1,bal}$ is derived in Eqn. 7.11.

$$\rho_s = \left[\alpha_1 \beta_1 \frac{c}{d} - \lambda\left(\frac{h}{d} - \frac{c}{d}\right)\right] \frac{f'_c}{f_y} \qquad \text{Equation 7.9}$$

$$\rho_{s1,bal} = \left[\alpha_1\beta_1\frac{c_{bal}}{d} - \lambda\left(\frac{h}{d} - \frac{c_{bal}}{d}\right)\right]\frac{f'_c}{f_y} \quad \text{Equation 7.10}$$

$$c_{bal} = \frac{f_{su}}{f_{su}+f_y} * d \quad \text{Equation 7.11}$$

The minimum reinforcement, $\rho_{s,bal}$ may be calculated from the requirement that $M_{min}>M_{cr}$:

$$\rho_{min} = {A_s}/{A_{tot}} \quad \text{Equation 7.12}$$

The tension force in the member is obtained from the stress resultants in the tension zone as shown in Equation 7.13, considering the force of the concrete tension zone, before post-peak degradation of tensile strength of the UHPFRC.

$$f_t * (A_b + (h-c)b_w) + A_s f_y = T \quad \text{Equation 7.13}$$

Here, it is assumed that steel has also developed yielding for conservatism. Once the member has cracked, and as the cracks propagate through the tension zone, the tension force will be resisted by the reinforcement in the tension zone; the maximum available capacity is given by Equation 7.14:

$$T_{su} = A_s f_u \quad \text{Equation 7.14}$$

From the CSA Annex A8.1, the tension hardening characteristic represents the materials' ultimate tension resistance; by requiring this to be greater than the cracking strength, the girder need be provided by a minimum amount of reinforcement as shown below:

$$T < T_{su}$$

$$f_t * (A_b + (h-c)b_w) + A_{s,min} f_y < A_{s,min} f_u$$

$$f_c\lambda * (A_b + (h-c)b_w) < A_{s,min}(f_u - f_y)$$

$$\mathrm{A_{s,min}} > \frac{\mathrm{f_c}\lambda}{\mathrm{f_u} - \mathrm{f_y}} * (\mathrm{A_b} + (\mathrm{h} - \mathrm{c})\mathrm{b_w})$$

$$\rho_{min} > \frac{f_c\lambda}{f_u - f_y} * \frac{(A_b + (h-c)b_w)}{A_{tot}} \quad \text{Equation 7.15}$$

To apply the above relations for calculating ρ_{bal} and ρ_{min}, a cover of 30mm was used for the CPCI 900 cross section. Annex A8.1 specifies a minimum cover of 25mm for precast structural elements, additionally, the new annex proposed that the contribution of the external 5mm of concrete cover be neglected on account of the plausible corrosion of fibers (Draft version of Annex 8.1, 2025),

and therefore a total of 30mm cover is considered. Reinforcement layers that can be present in the CPCI 900 girder are dependent on the diameter of the bar on account of the spacing requirements, as specified in clause A8.1.14.2.2.3. Therefore, each layer is initially assumed to consist of 25M bars which would allow for a total of five reinforcement layers fitting in the lower flange of the section depicted in Figure 79 for a CPCI 900 girder section.

7.3.2 SAP2000 Model

To verify the results from the sectional analysis performed using a layered type analysis and following first principles (algorithm written in excel) the same analysis was conducted using SAP2000. This model was used to compare the moment curvatures of each girder section. To create the material models for the UHPFRC stress-strain behaviors in compression and tension, a multi-linear segment plot was defined using uniaxial nonlinear stress-strain data. Table 35 summarizes the multi-linear plots used for compression and tension for the different compressive strengths analyzed. The linear plots are defined as stress-strain relationships with corresponding point IDs. SAP2000 uses point IDs to define the behavior of the material at various stages of loading, where point A is defined at the origin which is equal to 0 for both stress and strain, point B is the stress and strain after cracking, point C is the peak stress and corresponding strain, point D is the residual stress-strain in the post-peak branch, and point E is the failure stress-strain coordinates where the material is considered to lose its resistance degrading linearly to zero stress. In the table shown summarizing the coordinates of the milestone points defining the multilinear stress-strain behavior, the corresponding model calculated from the AFGC recommendation is shown in black and the corresponding linear model used in SAP2000 is shown in red.

Table 35: Compression models used in SAP2000 plotted against AFGC models.

Compression Models: SAP2000 vs AFGC

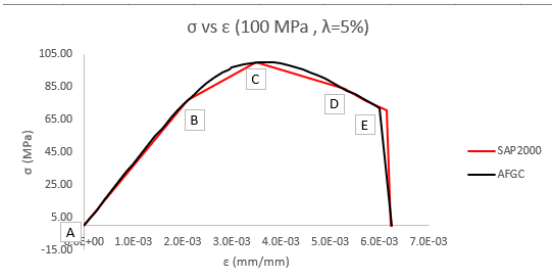
σ vs ε (100 MPa , λ=5%)
σ (MPa)
ε (mm/mm)
A
B
C
D
E
SAP2000
AFGC

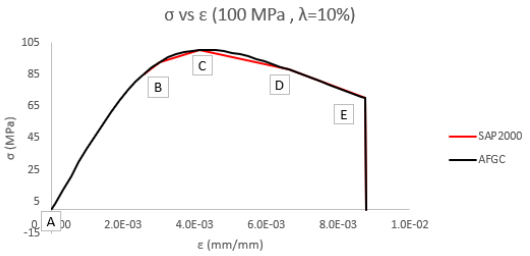
σ vs ε (100 MPa , λ=10%)
σ (MPa)
ε (mm/mm)
A
B
C
D
E
SAP2000
AFGC

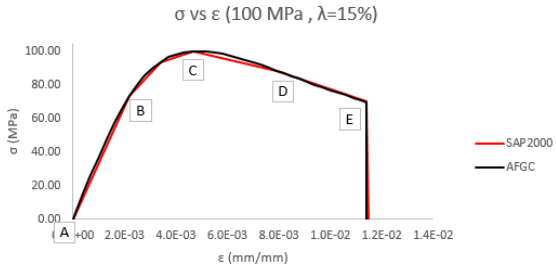
σ vs ε (100 MPa , λ=15%)
σ (MPa)
ε (mm/mm)
A
B
C
D
E
SAP2000
AFGC

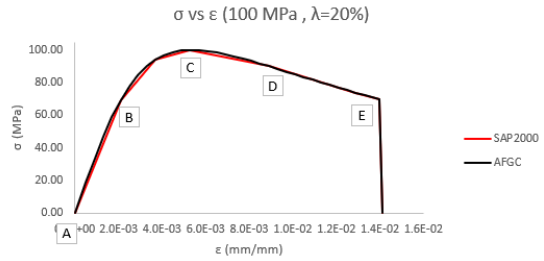
σ vs ε (100 MPa , λ=20%)
σ (MPa)
ε (mm/mm)
A
B
C
D
E
SAP2000
AFGC

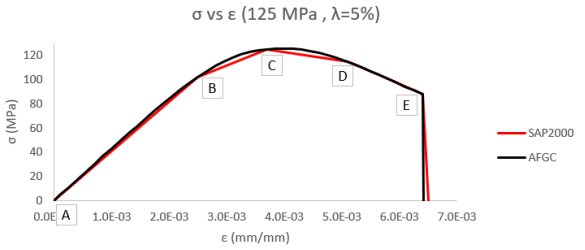
σ vs ε (125 MPa , λ=5%)
σ (MPa)
ε (mm/mm)
A
B
C
D
E
SAP2000
AFGC

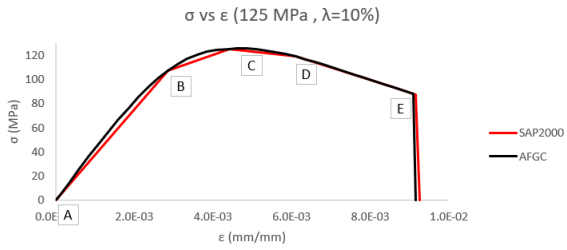
σ vs ε (125 MPa , λ=10%)
σ (MPa)
ε (mm/mm)
A
B
C
D
E
SAP2000
AFGC

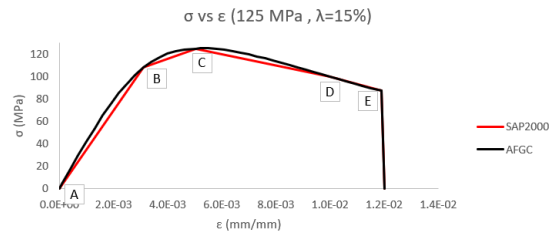
σ vs ε (125 MPa , λ=15%)
σ (MPa)
ε (mm/mm)
A
B
C
D
E
SAP2000
AFGC

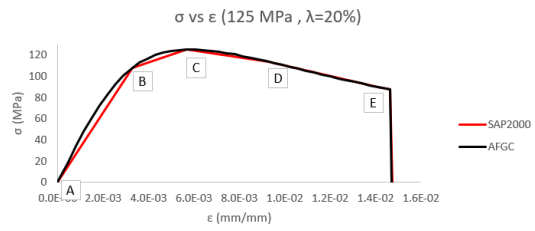
σ vs ε (125 MPa , λ=20%)
σ (MPa)
ε (mm/mm)
A
B
C
D
E
SAP2000
AFGC

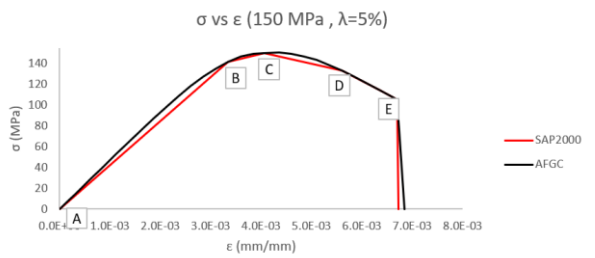
σ vs ε (150 MPa , λ=5%)
σ (MPa)
ε (mm/mm)
A
B
C
D
E
SAP2000
AFGC

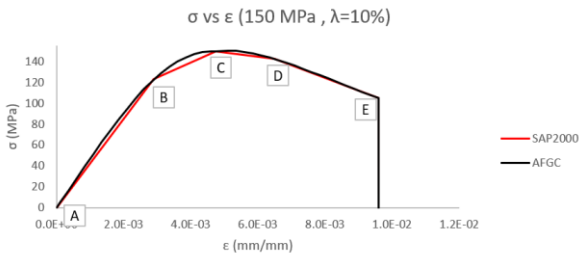
σ vs ε (150 MPa , λ=10%)
σ (MPa)
ε (mm/mm)
A
B
C
D
E
SAP2000
AFGC

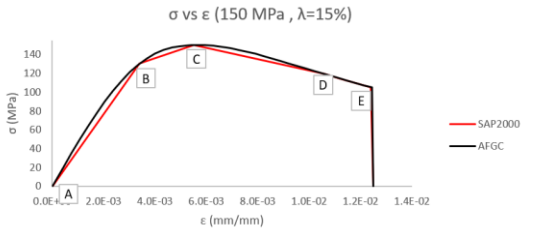
σ vs ε (150 MPa , λ=15%)
σ (MPa)
ε (mm/mm)
A
B
C
D
E
SAP2000
AFGC

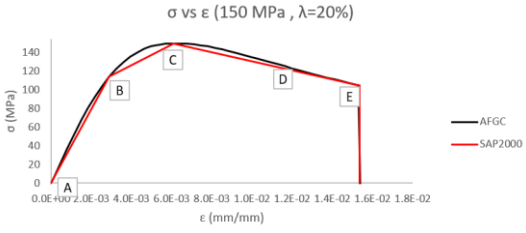
σ vs ε (150 MPa , λ=20%)
σ (MPa)
ε (mm/mm)
A
B
C
D
E
AFGC
SAP2000

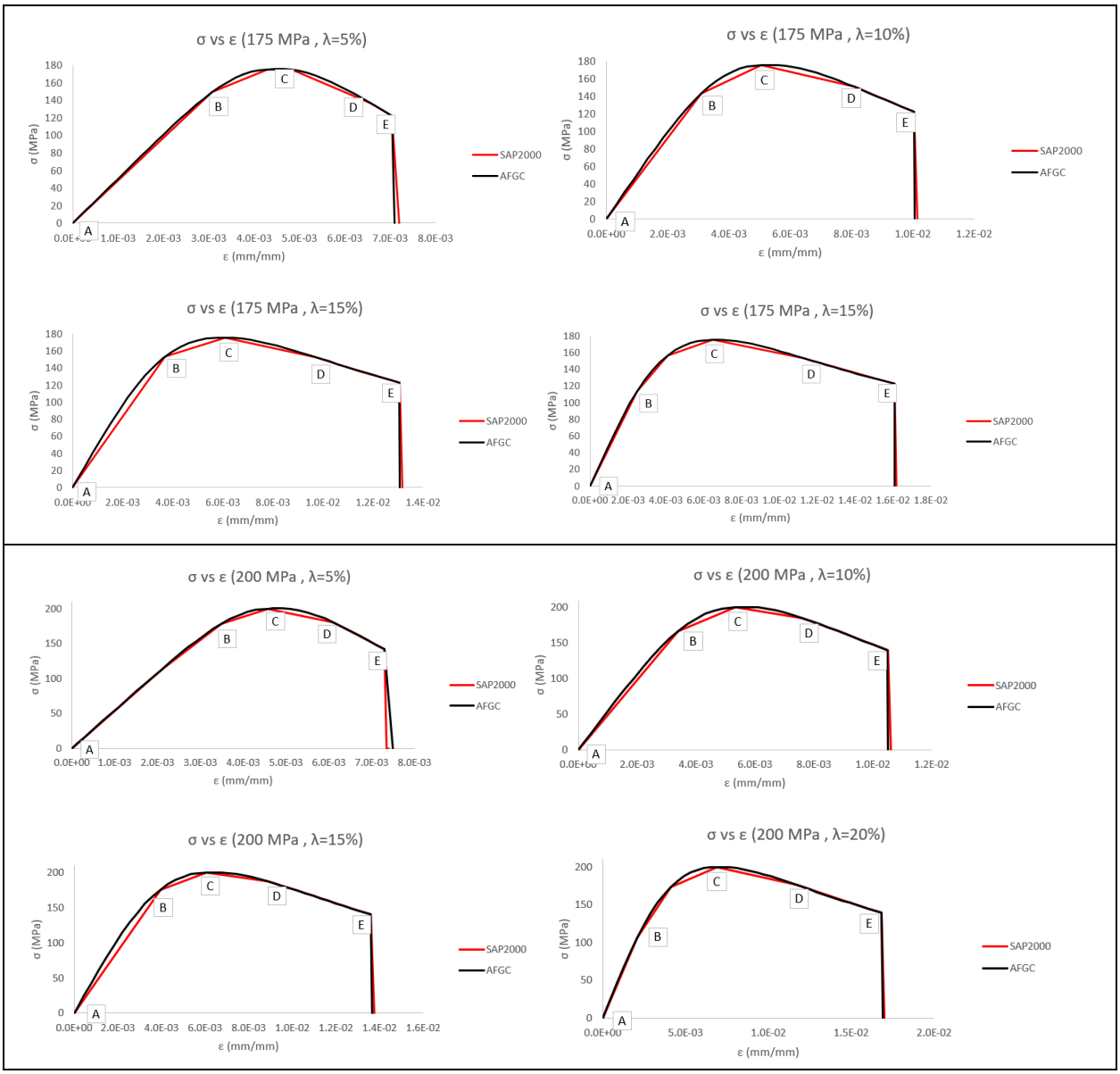

7.4 Analytical Model vs SAP2000 Model

To verify the results obtained from the excel program and the SAP2000 2-D model, Figures 80 - 84 summarize the plots obtained by varying the compressive and tensile strengths while the reinforcement ratio is kept at a balanced amount for the section. In the figures two groups of resistance curve are shown for each girder, from the layered analysis and from the SAP2000 respectively. Here, the red line corresponds to the layered analysis using the true compressive stress-strain curve while the moment resistance curve shown in black is obtained from SAP2000. The two resistances are observed to be comparable with the difference seen to be predominantly

due to the underestimation of the compressive behavior of UHPFRC in the SAP2000 model. Considering this, the SAP2000 model is assumed to be viable to perform further analysis for the girder sections.

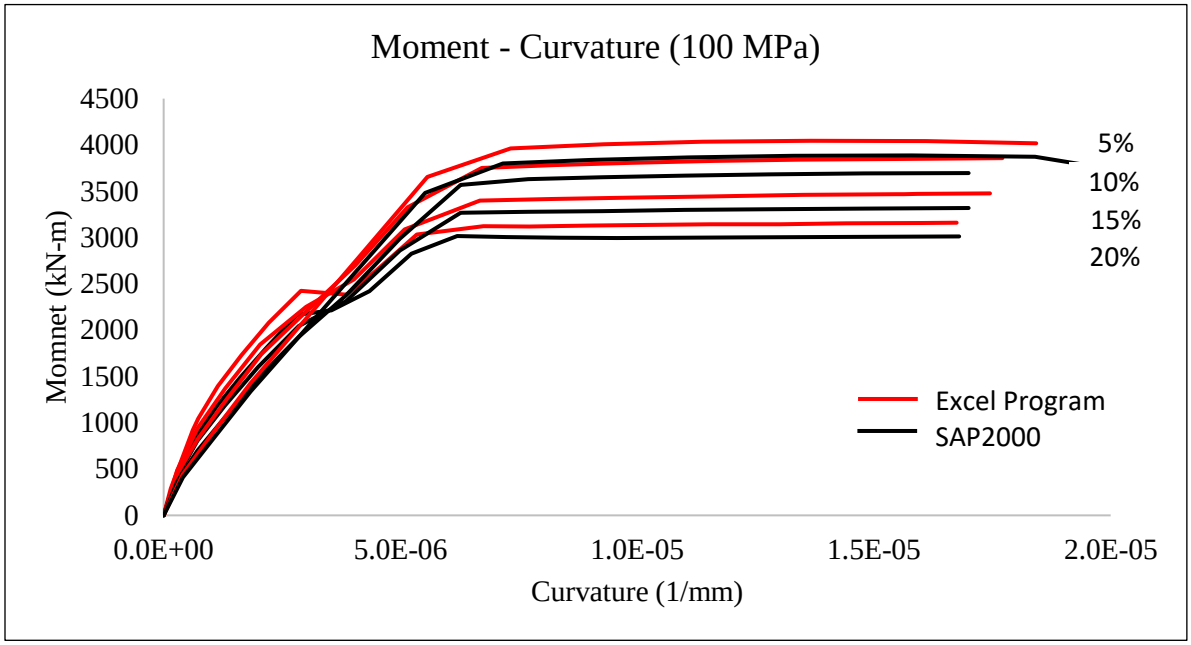

Figure 80: Moment-Curvature, f_c' = 100 MPa (SAP2000 vs Excel Program)

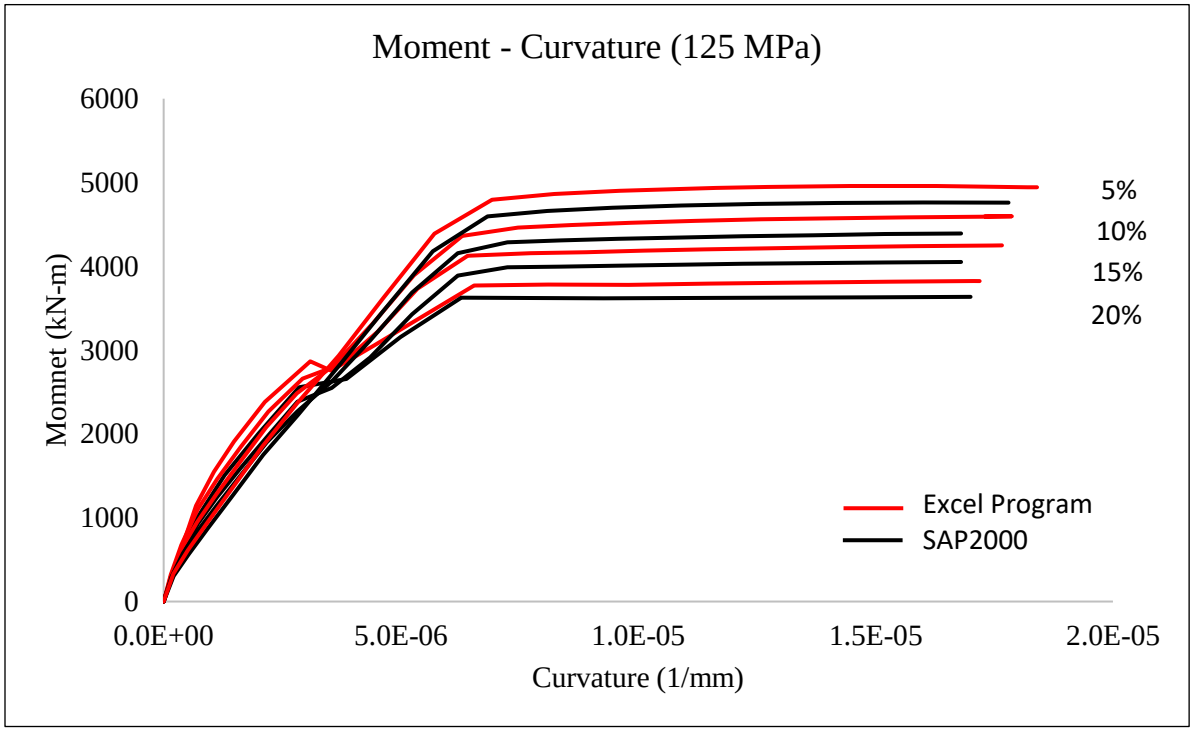

Figure 81:Moment-Curvature, f_c' = 125 MPa (SAP2000 vs Excel Program)

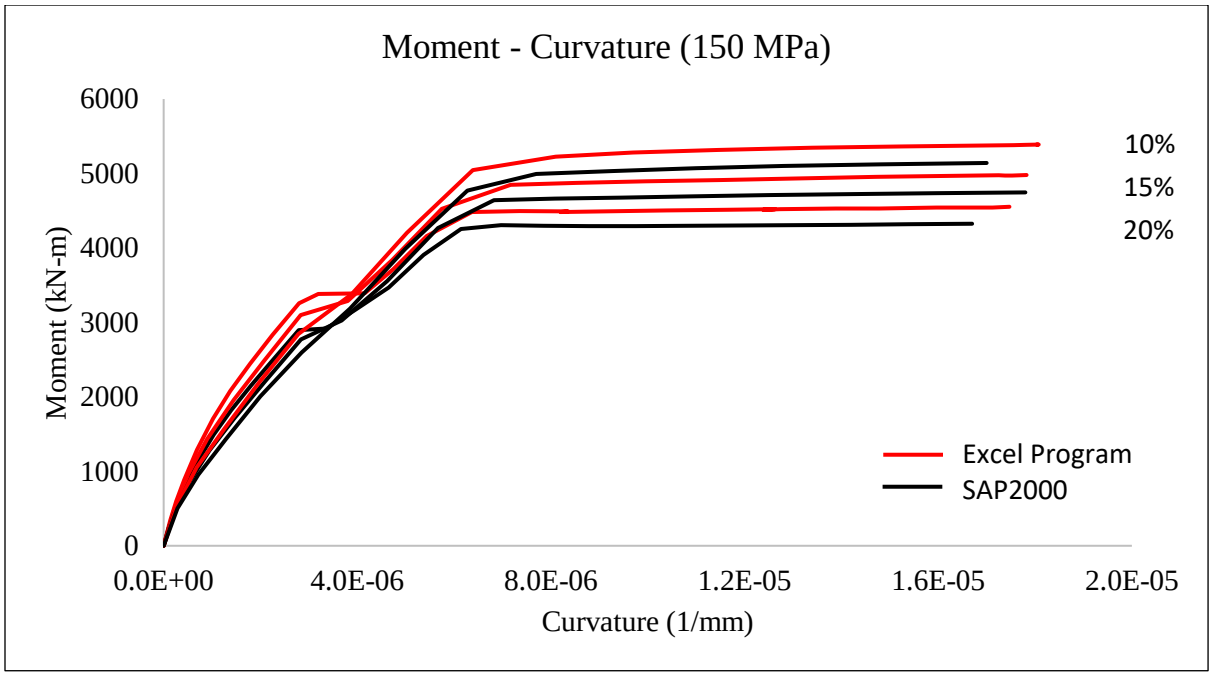

Figure 82: Moment-Curvature, f_c' = 150 MPa (SAP2000 vs Excel Program)

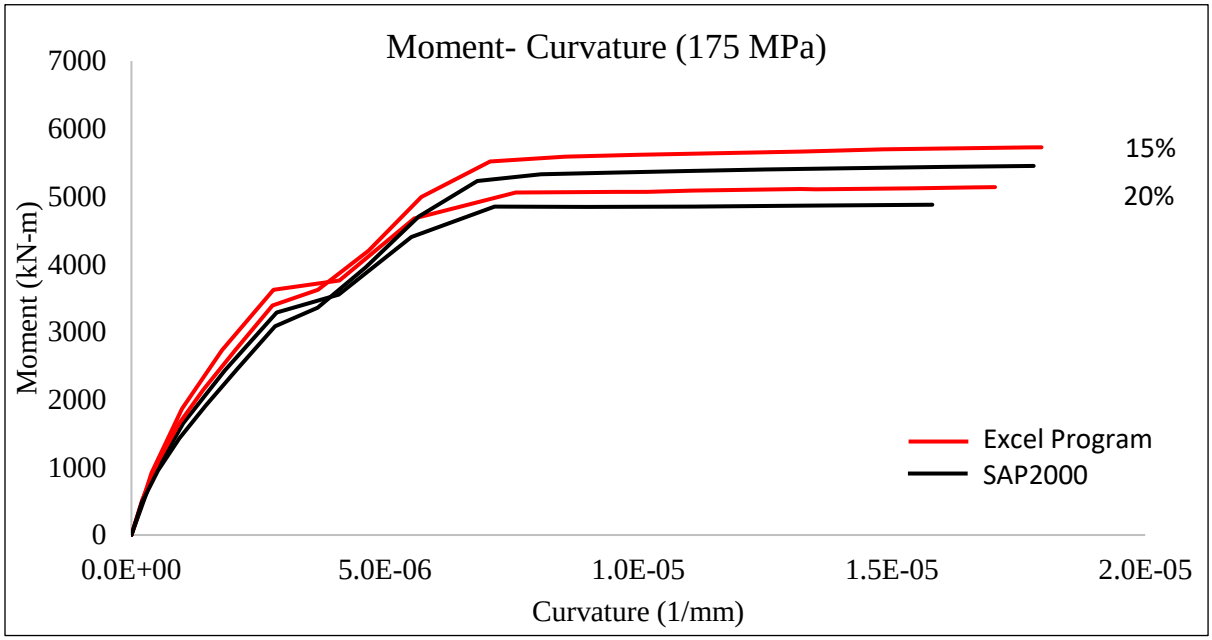

Figure 83: Moment-Curvature, f_c' = 175 MPa (SAP2000 vs Excel Program)

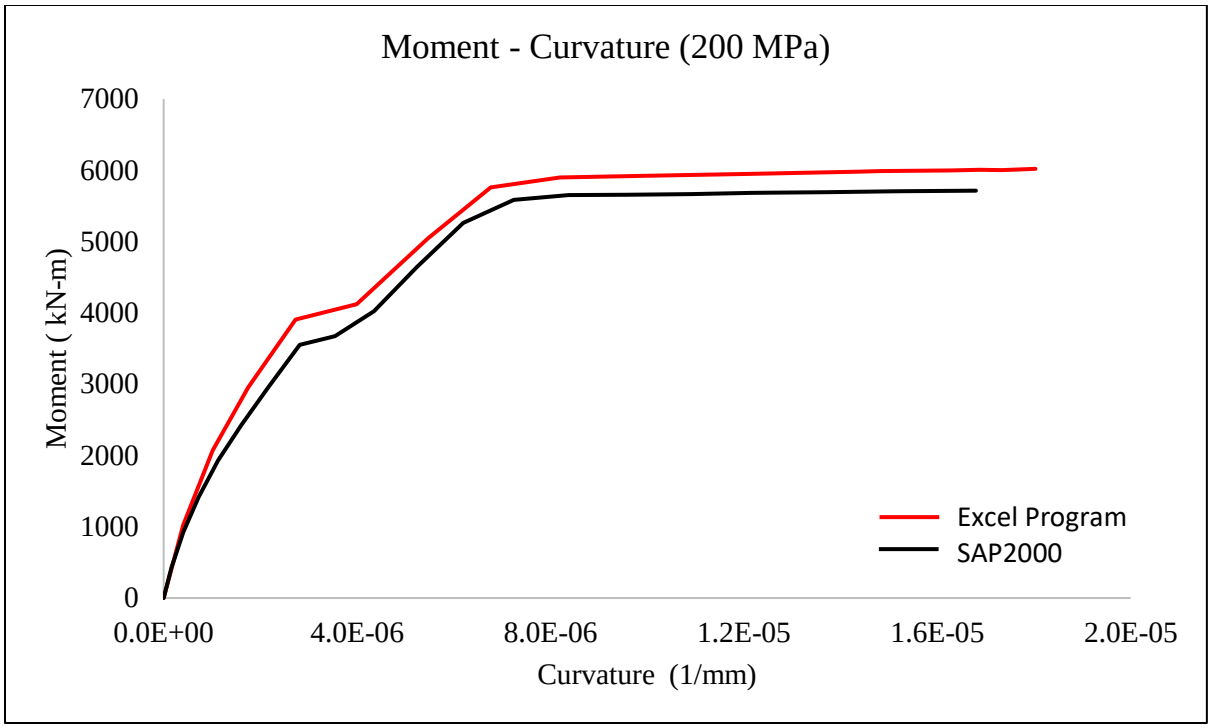

Figure 84: Moment-Curvature, f_c' = 200 MPa (SAP2000 vs Excel Program)

The moment resistance plots obtained from the SAP2000 model are shown in Figures 84 - 88 in order to compare the peak moments attainable with varying compressive strengths. In these figures, girder sections with minimum amount of reinforcement are presented. Figure 77 which is made for preliminary design calculations is developed using Equation 7.15 where the reinforcement ratios are plotted against the ultimate tensile strength by varying the UHPFRC compressive strengths.

Furthermore, in Figures 92 - 96 the moment - curvature relationships for the same girder sections are obtained, with a reinforcement ratio equal to the balanced section amount. As the compressive and tensile strengths are increased for a minimum amount of reinforcement required, the area of required steel also increases proportionally. Figures 85 and Figures 84 - 96 were obtained assuming the yield stress of the reinforcing steel equal to 400 MPa. (Calculations were carried out using E_s=200 GPa and steel plateau up to peak strain of ε =0.01).

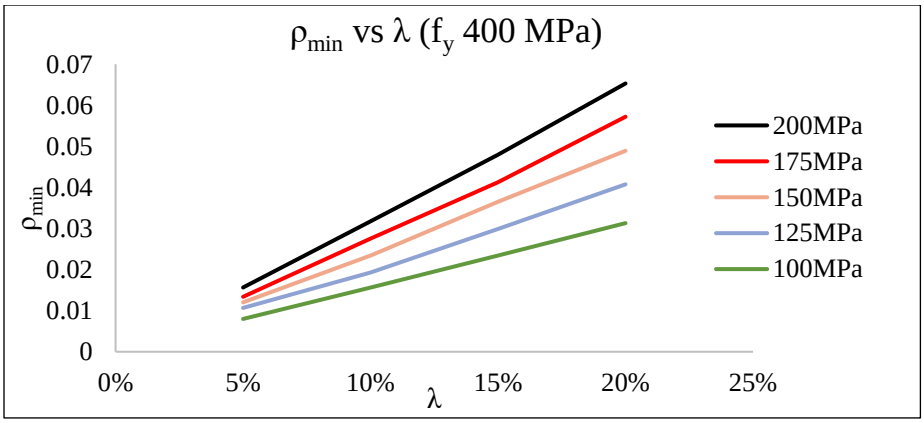

Figure 85: Design charts for minimum reinforcement ratios for CPCI 900 girder section.

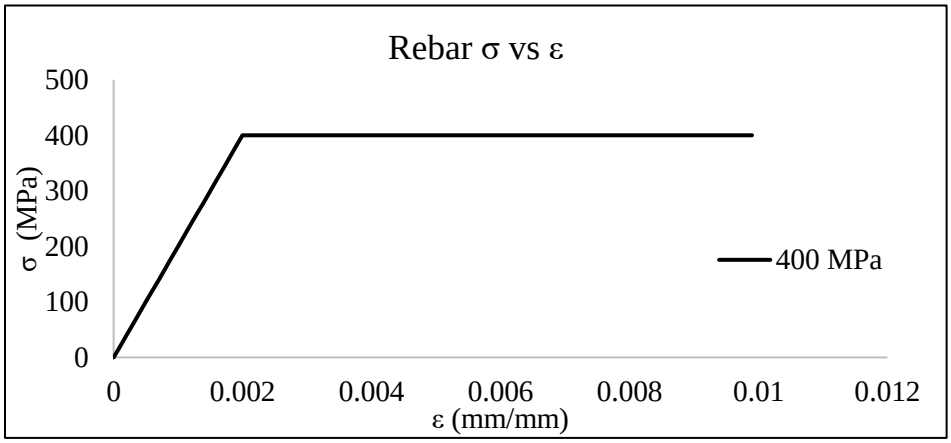

Figure 86: Stress-Strain response used for 400MPa steel rebar.

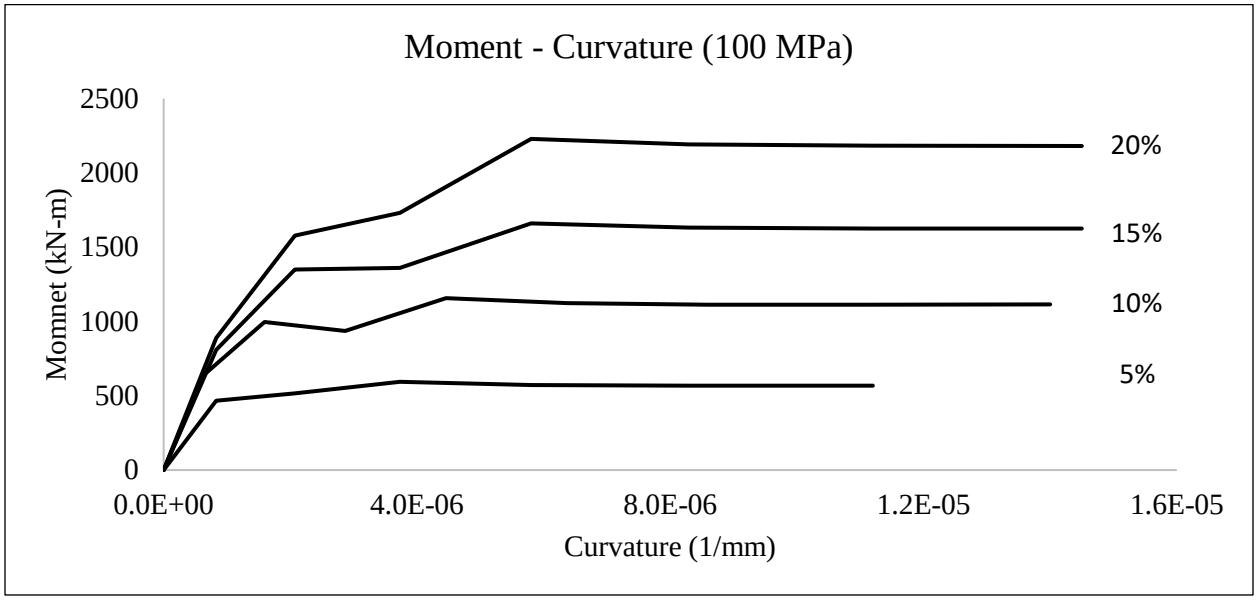

Figure 87:Moment-Curvature, ρ_{min} reinforcement, f_c' = 100 MPa, SAP2000

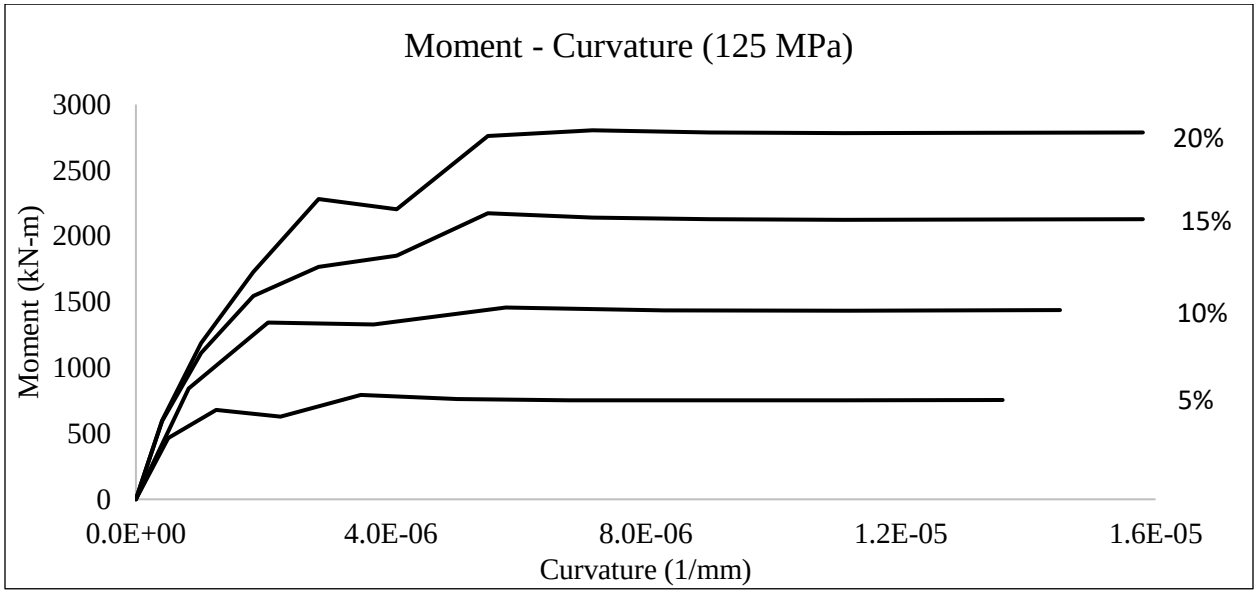

Figure 88: Moment-Curvature, ρ_{min} reinforcement, f_c' = 125 MPa, SAP2000

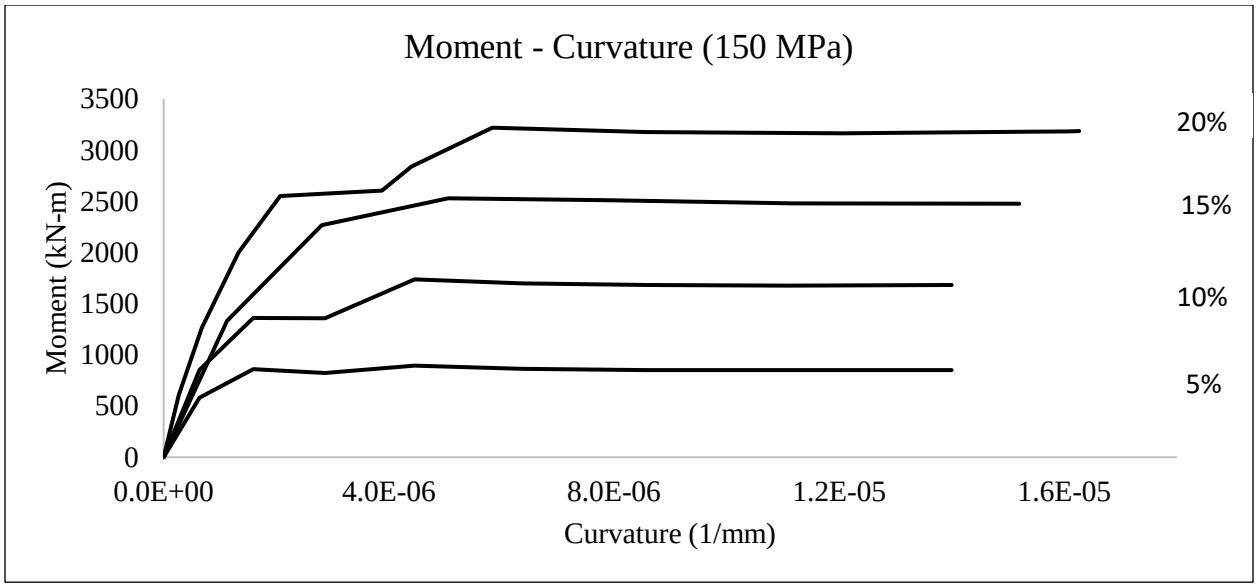

Figure 89: Moment-Curvature, ρ_{min} reinforcement, $f_c' = 150$ MPa, SAP2000

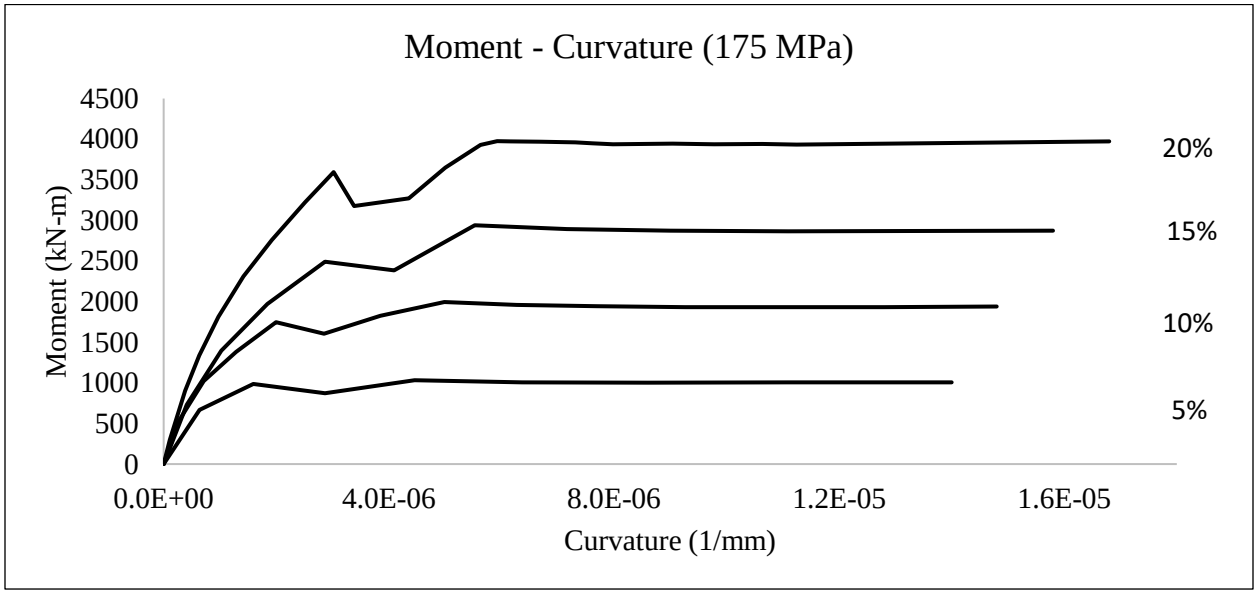

Figure 90:Moment-Curvature, ρ_{min} reinforcement, $f_c' = 175$ MPa, SAP2000

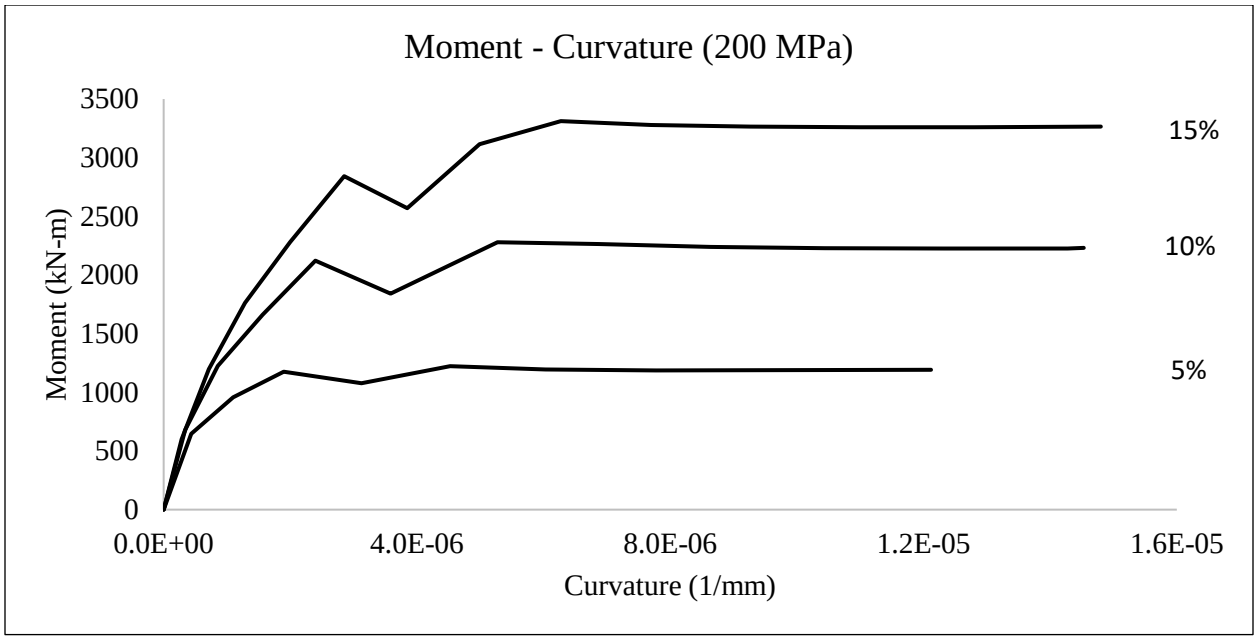

Figure 91: Moment-Curvature, ρ_{min} reinforcement, f_c' = 200 MPa, SAP2000

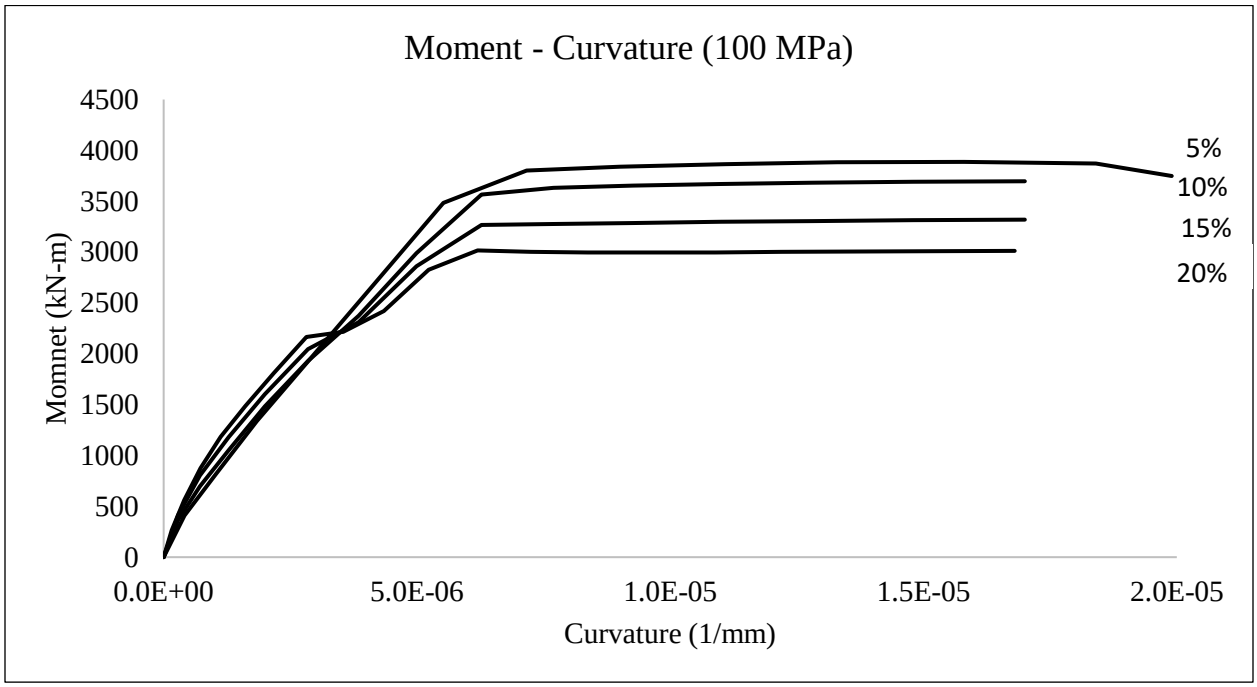

Figure 92:Moment-Curvature, ρ_{bal} reinforcement, f_c' = 100 MPa, SAP2000

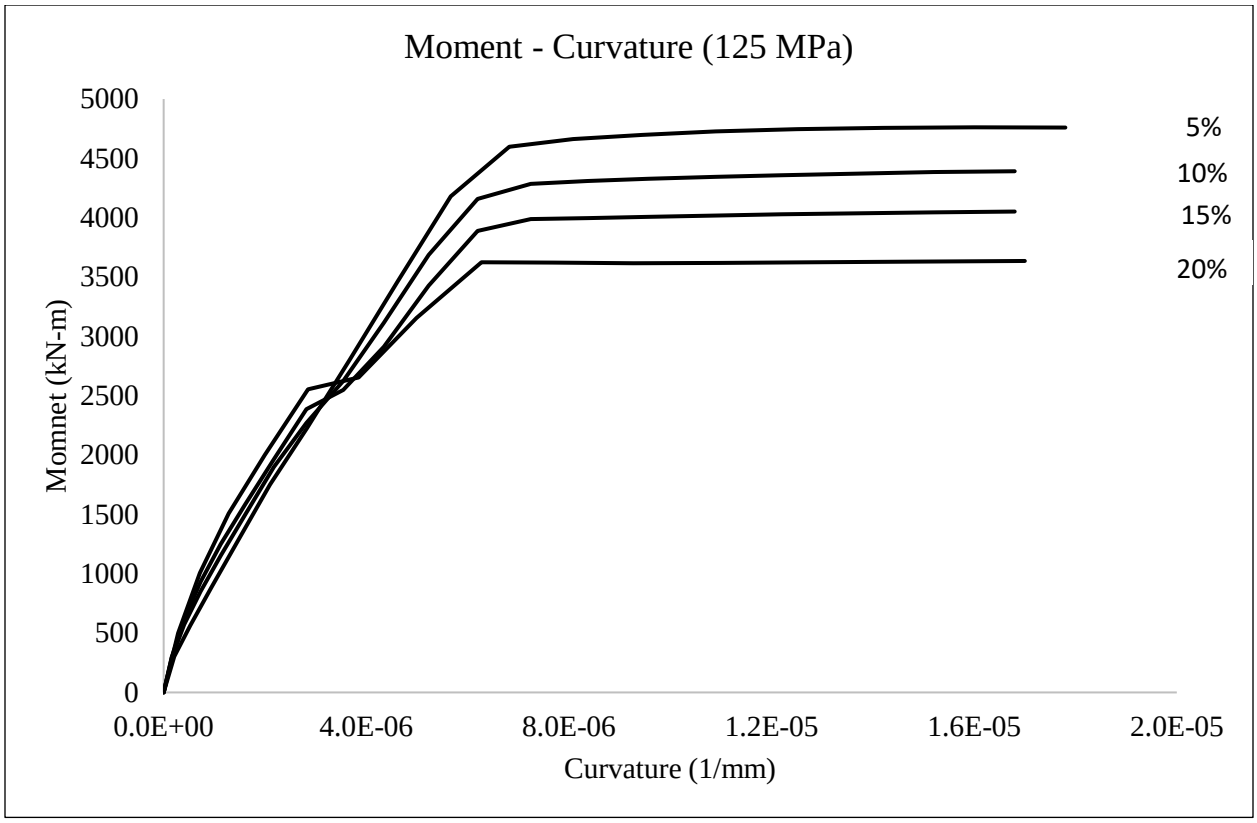

Figure 93: Moment-Curvature, ρ_{bal} reinforcement, f_c' = 125 MPa, SAP2000

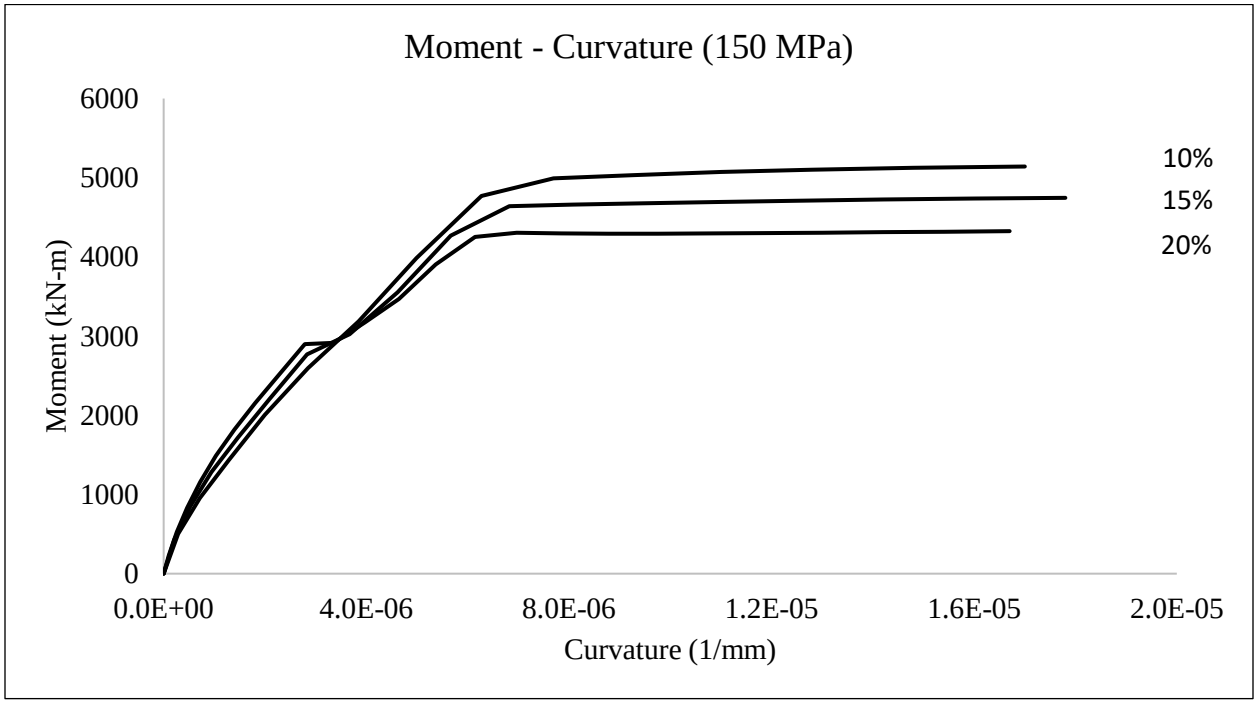

Figure 94:Moment-Curvature, ρ_{bal} reinforcement, f_c' = 150 MPa, SAP2000

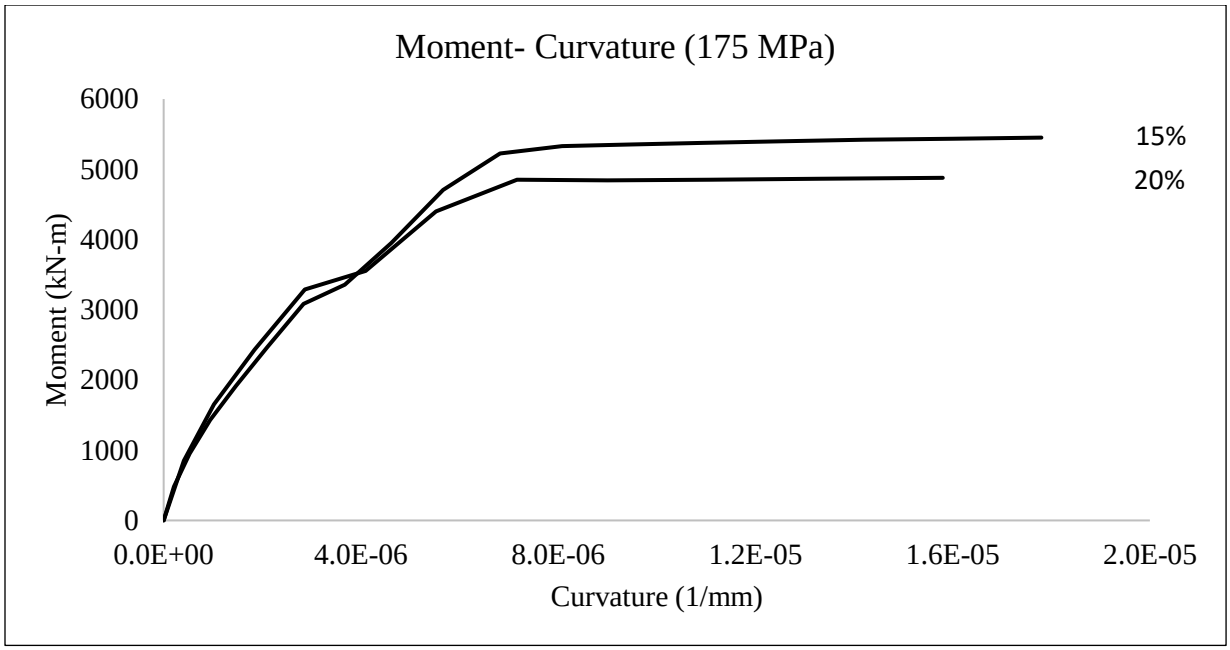

Figure 95:Moment-Curvature, ρ_{bal} reinforcement, f_c' = 175 MPa, SAP2000

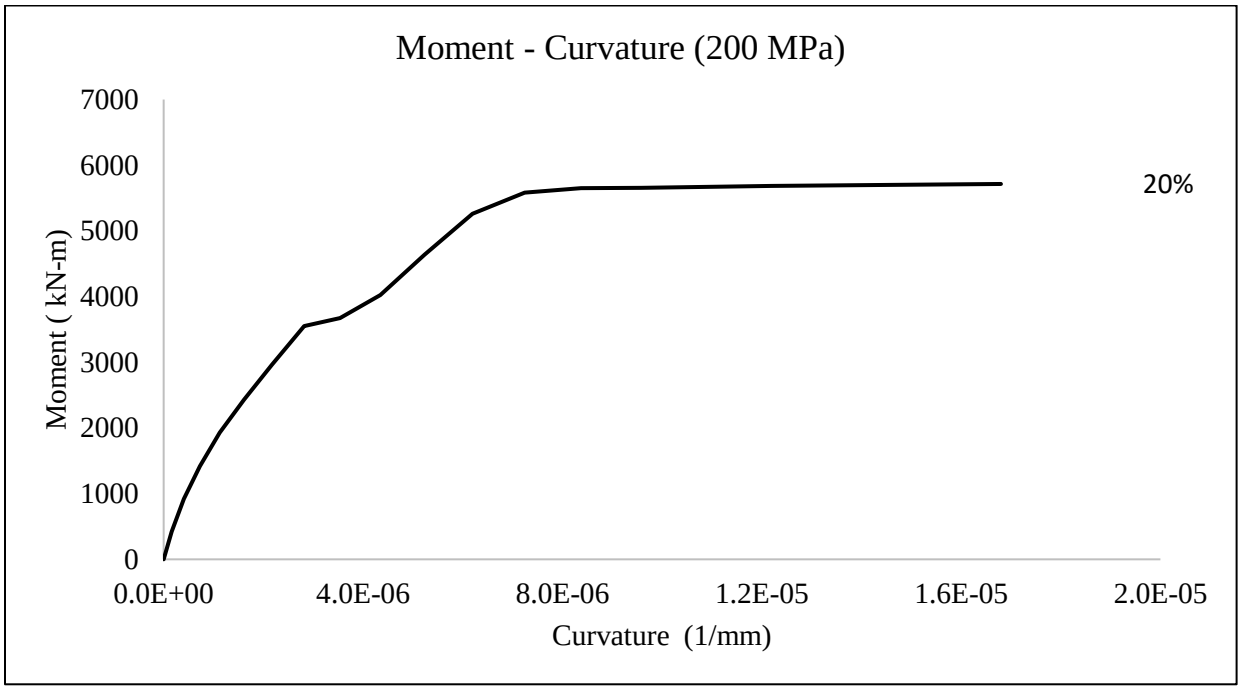

Figure 96:Moment-Curvature, ρ_{bal} reinforcement, f_c' = 200 MPa, SAP2000

Due to the spacing limitations, it was calculated that the maximum amount of reinforcement that can fit the bottom flange of a CPCI 900 girder is approximately 9.7%. Therefore, as the compressive strengths are increased and the section dimensions are kept constant, the girders'

resistance plateaus to a maximum reinforcement ratio of 9.7%. For compressive strengths of greater than 150 MPa and λ >15%, it was observed that the minimum reinforcement ratio calculated could not fit in the bottom flange of the girder. For all the moment resistances shown in Figures 87-96, no material safety factor was used. This was done because calculations used mean values for material strengths. It is noted that there are significant safety margins here. For example, the available hardening behavior of the UHPFRC after cracking was neglected, whereas the design strain under tensile stresses as specified by the CSA Annex A.81 for UHPFRC is at least 0.001, whereas in Chapter 3, the mix of UHPFRC tested at York University shows that the UHPFRC tested with a compressive strength of 130 MPa reached an ultimate tensile strength of 8.33 MPa and was capable of sustaining peak strains of 0.01 under bending as calculated from the inverse analysis. This calculated strain is considerably larger than the one used per the Code provisions. By using a design strain value of 0.001 the girder design can be very conservative and underestimates the materials' true capability.

Additionally, to study the effect of increasing the girder section, the CPCI 1200 girder was also analyzed using the same methodology as used for the CPCI 900. The results of this analysis, obtained for CPCI 1200, and for compressive strengths f_c' of 100 MPa, 125 MPa, and 200 MPa for a minimum amount of reinforcement ratio are depicted in the plots shown in Figures 97 - 100; similarly, Figure 102 summarizes the results for the balanced reinforcement ratio respectively.

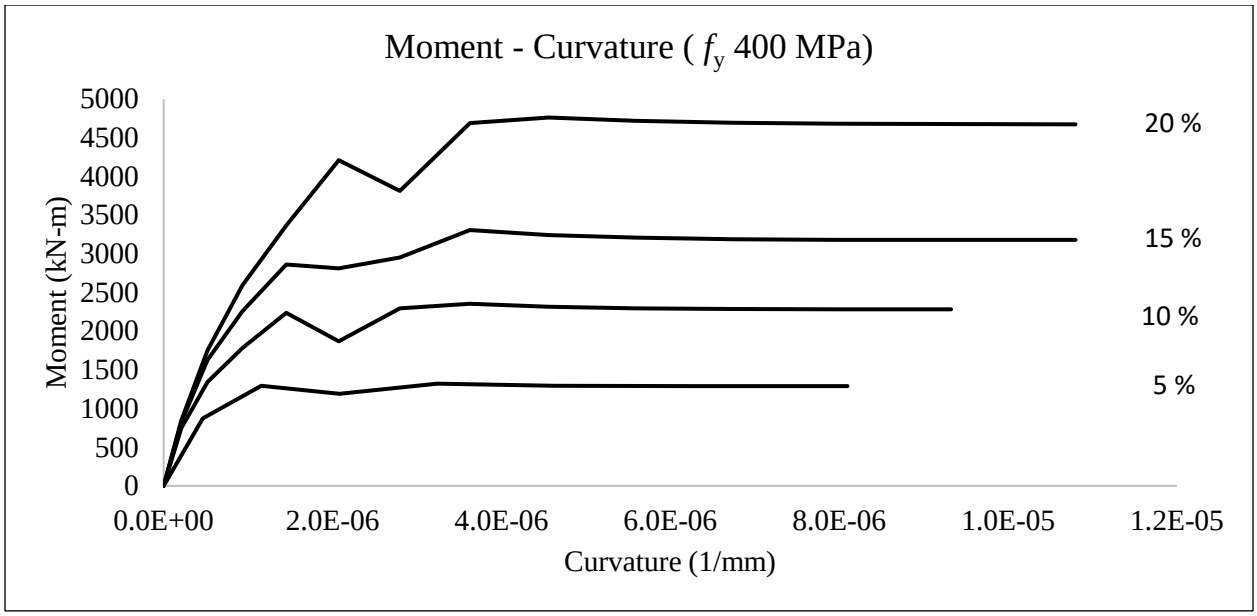

Figure 97: CPCI 1200 Moment - Curvature relationships, ρ_{min}, f_c' = 100 MPa, SAP2000

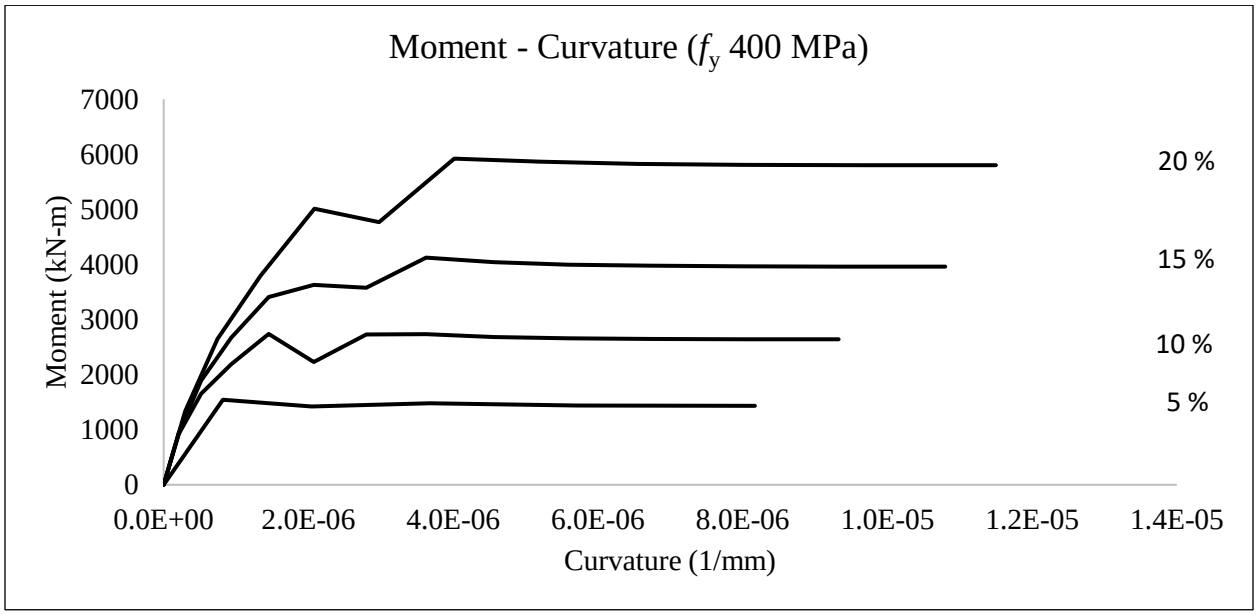

Figure 98: CPCI 1200 Moment - Curvature relationships, ρ_{min}, f_c' = 125 MPa, SAP2000

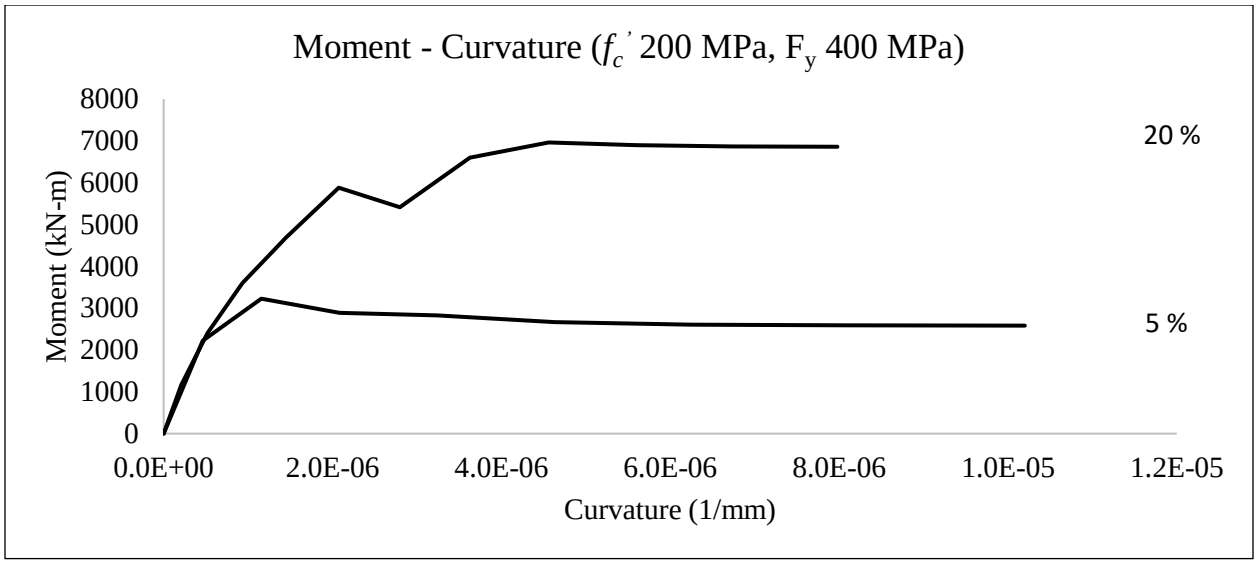

Figure 99: CPCI 1200 Moment - Curvature relationships, ρ_{min}, f_c' = 200 MPa, SAP2000

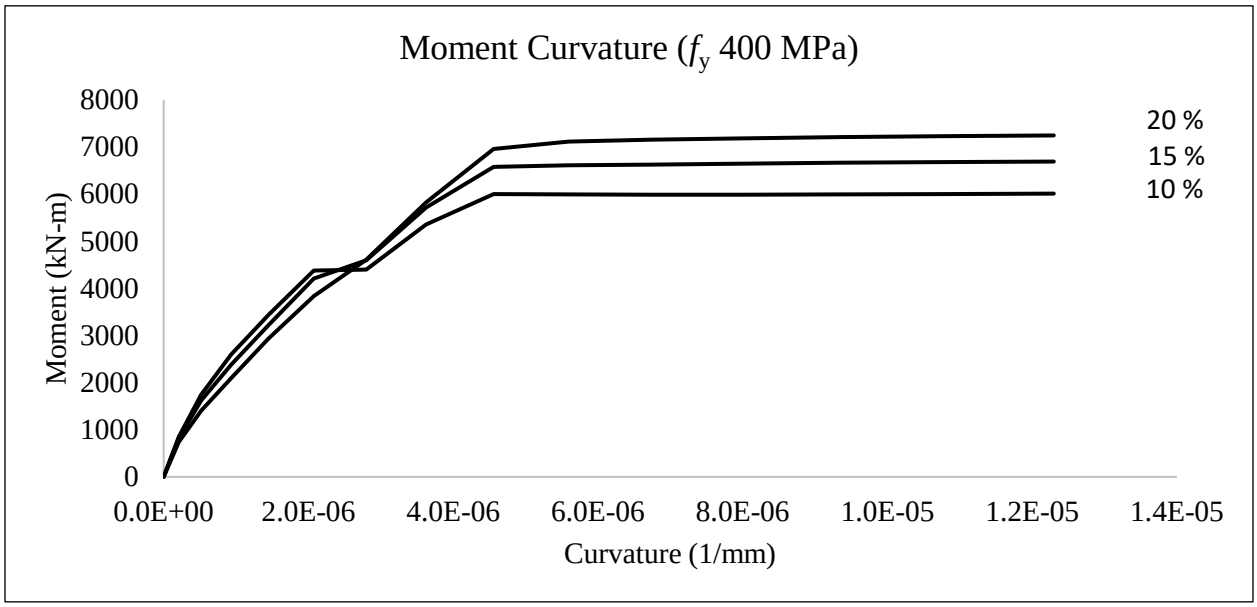

Figure 100: CPCI 1200 Moment - Curvature relationship, ρ_{bal} , f_c' 100 MPa, SAP2000

7.5 Development of Design Charts

From the analysis performed on the alternative material strengths for compression and tension, with different reinforcing ratios design charts were developed for the CPCI girders comprising of UHPFRC materials with dimensionless units. The design charts made are directly calculated from the moment resistances obtained from the plots above. To create a dimensionless chart not

dependent on section area or strength of the material used, the peak moments are divided by the girders' cross-section area and multiplied by the concrete's compressive strength. In this manner, it is possible to create design charts for various loading conditions that are valid for a range of compressive strength values.

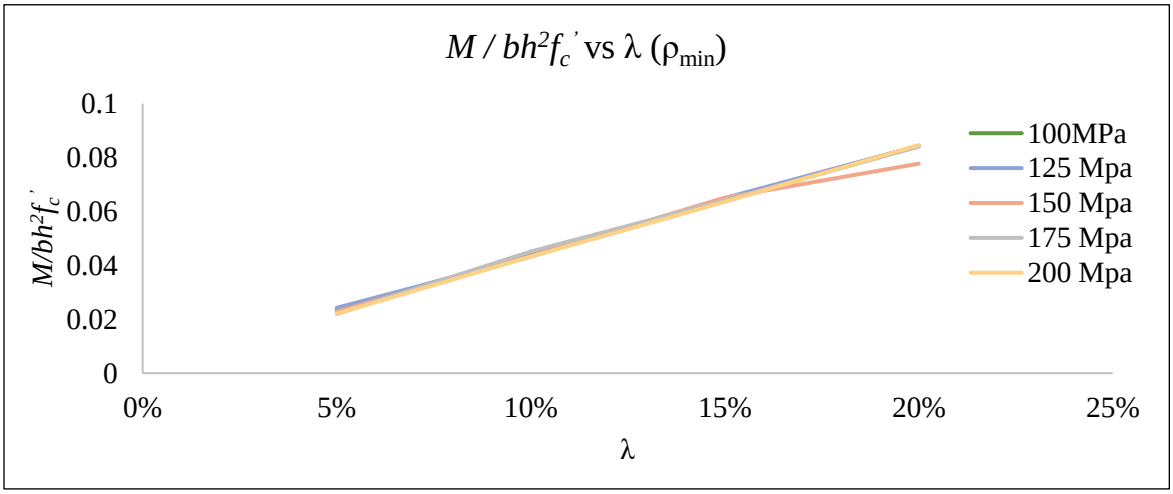

Figure 101: Design chart for minimum reinforcement for CPCI 900 or 1200 girders for minimum reinforcement.

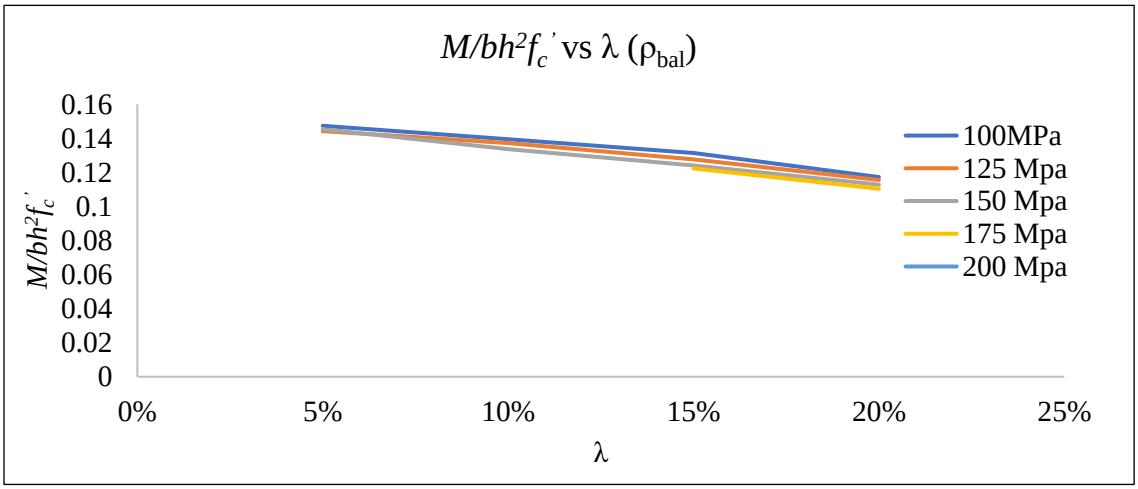

Figure 102: Design chart for minimum reinforcement for CPCI 900 or 1200 girders for balanced reinforcement.

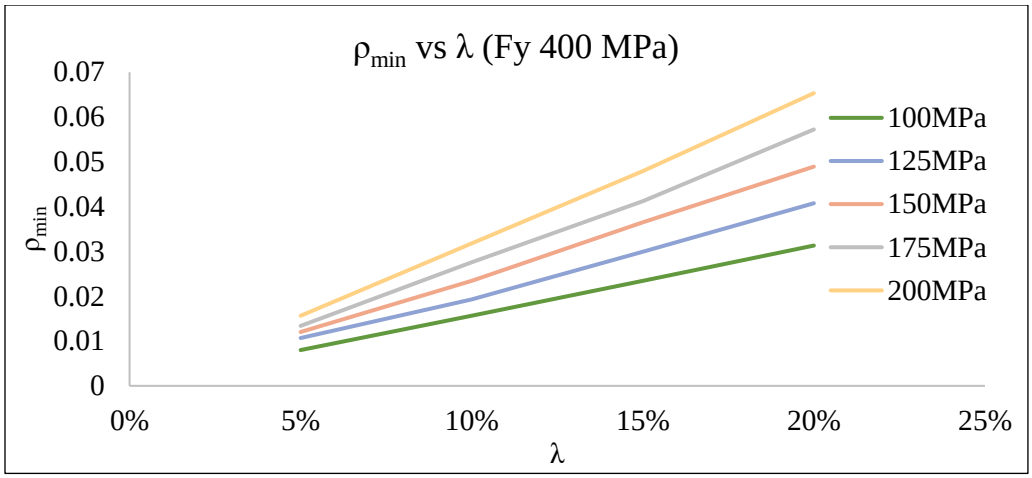

Figure 103: Design chart to obtain p_{min}

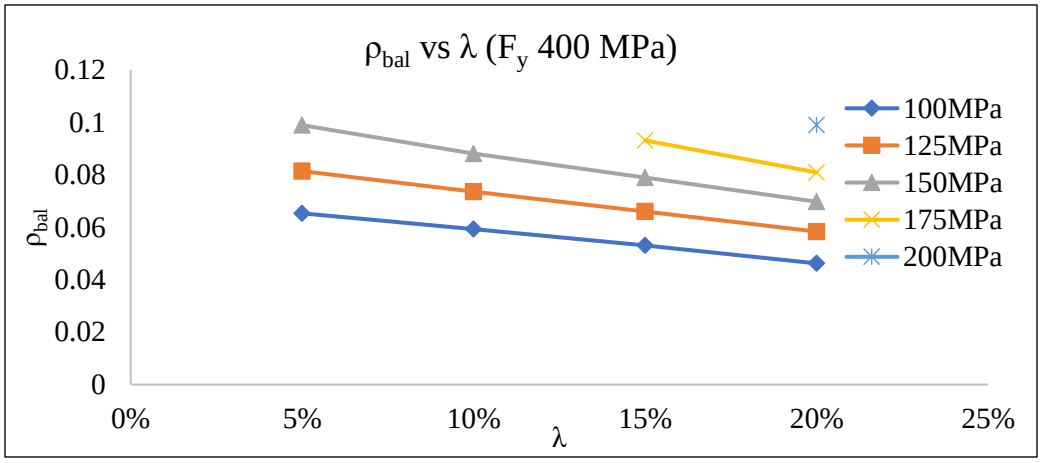

Figure 104: Design chart to obtain p_{bal}

To ensure the design charts can be used for CPCI 900 and CPCI 1200 girders, Figure 105 is shown for illustration of the normalized design chart made for the CPCI 900 and CPCI 1200. Note that results are defined as a straight line – the normalized moment, $m = 0.02+\alpha\cdot\lambda$, where $\alpha=1/3$.

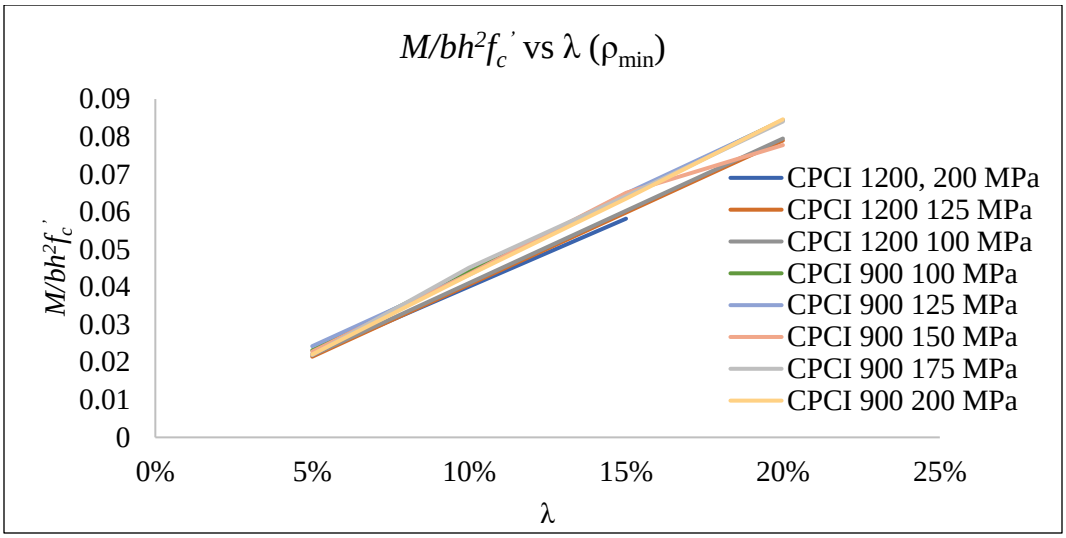

Figure 105: Comparison of design chart for convergence of results.

7.6 Conclusion / Recommendations / Future Development

In the chapter above a design methodology was developed for a CPCI 900 girder to enable detailing of longitudinal reinforcement ratio for a given design moment, and for a range of values of compressive and tensile strengths of the UHPRC material. The material stress-strain response under tension was represented using the prescribed stress block by CSA S6 Annex A8.1, where all tensile stresses are constant until an ultimate design strain. The stress-strain under compression was evaluated from AFGCs (2013) recommendation for UHPFRC compression post-peak response considering confinement provided by the fibers. The design charts are developed for CPCI 900 and CPCI 1200 sections for users to be able to provide the use of UHPFRC as an alternative to conventional prestressed concrete girders since the attained flexural strengths are comparable.

7.7 Recommendations/Future Development

The design charts made in this chapter ignored the strain hardening of the reinforcing steel, assumed a linear tensile stress-strain model and did not use material factors. To further this development, it is recommended to include these parameters to see how much resistance the section will provide at in-situ conditions vs the design resistance. Moreover, this methodology can be used to model the CPCI 900 girder with UHPFRC to evaluate the span limitations. Lastly, the

tensile model used was following CSA S6 Annex A8.1, where the stress in the girder was assumed to be a constant from 0 strain up until the design strain. In order to calculate a better model the tensile stress-strain law should be represented by a bi-linearized curve in order to account for the initial elastic response, cracking tensile stress and tension hardening.

Chapter 8. Conclusion

8.1 Introduction

UHPFRC is a new type of cement-based material which is still being researched and investigated with regards to its performance in mechanical aspects as well as its spectacular durability life. The research spans along multiple areas focusing on the type of fibers used, volumetric ratios, orientation of the fibers, curing regimes, testing practices and many more. The research done in this thesis provides the data set of a UHPFRC materials for both durability and mechanical aspects, which is non-existent for a single mix design produced in Canada in the current literature. Further, the current state of the art for this material in terms of tension tests to obtain the tension behavior uses an indirect method for material characterization, the works presented in this thesis compares both, indirect and direct tension tests conducted to bring light to the inconsistencies in the results achieved. Moreover, this thesis fills the gaps in the literature with regards to the applicability of the prescribed code in Canada for design provisions for this material.

The work presented in this thesis was concerned with the evaluation procedures of CSA-S6 Annex 8.1 (2019), applied for complete material characterization of a Canadian UHPFRC product made by using strictly Canadian source materials and waste powders. Both mechanical and durability performance were studied following CSA A23.1-Annex U (2019). The most attractive aspect of the development of this material is its behavior in tension, particularly the tensile strength it can reach at cracking and ultimate limit states, and its resilience to large, post-cracking tensile deformations. The flow-aligned distribution of the steel fibers used with a specific volumetric ratio of 2% enabled a resilient and ductile response in tension. This was possible due to the materials capability to delay the crack localization and its ability to sustain large levels of deformation owing to the fact that UHPFRC fails under tension when the steel fibers pullout due to gradual slip (Yoo et al. 2014). In the work presented, this behavior for a tension-hardening behavior of the UHPFRC was experimentally confirmed. This material was also tested for its durability aspects which yield at least a durability life of 100 years as per CSA A23.3 Annex U. In addition, a detailed study was done on the inverse analysis method prescribed by Annex U for characterizing this class of material in tension. Moreover, a T-Beam was analyzed with a CSA Taskforce made to proof test the CSA

S6 Annex A8.1 with prescribed design clauses. Further, a detailed CPCI 900 girder was analyzed with varying compressive strength, tensile strength, and steel yield strength to develop a design chart that will enable designers to easily check whether this material can be used quickly and effectively as an alternative material to current best practices.

8.2 Conclusions

To conclude the experimental program, the UHPFRC material tested in the laboratory displayed durability life of around 200 years, a compressive strength of 133 MPa, and ultimate tensile strength of 8.3 MPa. The testing methods prescribed for the material characterization by CSA Annex U can be conducted in a certified laboratory setting, though field tests may require further research. The lack of field data to assess how these tests in the lab perform in the field include flowability, cylinder tests with different curing regimes, and quality control measures for tension such as the strain energy approach.

8.2.1 Durability Tests

Three cylinders of size 100mm × 150mm were tested for abrasion. The load applied was 200 kNs for a total of 3 cycles consisting of 2 min abrasions. The drill used was set to its lowest speed of 260 r/m, to keep consistent with the testing standard ASTM C944, the testing method requires a rotation of 200 r/m therefore to compensate for an equivalent amount of abrasion, the time of abrasion per cycle was 1.538 minutes at a speed of 260 r/m. The average mass loss due to abrasion was 1.78 g for the 3 specimens. CSA annex U notes an abrasion of less than < 5.0 g for a durability life of 50 years.

Three salt-scaling specimens were tested for resistance of the UHPFRC surface exposed to freeze-thaw cycles in presence of de-icing agents. Two specimens were tested following CSA A23.2-22C which uses 3% sodium chloride, and 1 specimen was tested following ASTM C672 which uses 4g of anhydrous calcium chloride per 100ml of distilled water. The specimens tested as per CSA A23.3-22C showed a scaling of 0.015 and 0.019 kg/m^2 whereas the specimen tested following ASTM C672 showed a scaling of 0.022 kg/m^2. As per CSA Annex U, all three specimens showed a scaling of < 0.1 kg/m^2 as are classified for 200-year durability life.

Three-cylinder specimens of size 75mm by 150mm were tested for absorption tested following CSA A23.2-11C. The average water content %, density kg/m^3, absorption %, and void % were 2.52 %, 2596.85 kg/m^3, 1.68%, and 4.26%. CSA A23.1 - Annex U (2019) gives a durability life of 200 years for absorption less than 3 %.

A total of three specimens were tested for chloride ion penetration. These specimens were cut from a molded size of 100mm by 200mm. The test was conducted following CSA A23.2-23C which displayed a charge passed of less than 40 coulombs. As per CSA A23.1 - Annex U (2019), a charge of less than 100 is considered negligible.

Six bars of size 25mm by 25mm by 285mm were tested for resistance to sulfate attack. These bars were tested following CSA A3004-C8A. This standard uses a sulfate solution concentration of 50g/L of solution. The results obtained from the length comparator show a length change from emersion in the sulfate solution of 0.11%.

8.2.2 Mechanical Tests

The flow for each batch was tested from the fresh mix of UHPFRC mortar with fibers included. The flow mold was filled in one layer. The flow mold was then lifted and after an elapsed time of 2 minutes, the flow was measured by taking the maximum and minimum lengths. Batches 1, 4, 5, 6 showed a flow of over 200mm and batches 2 and 3 showed a flow less than 200mm. The average flow for a total of 6 batches was 207.6 mm, indicating that the material met the flowability requirements established for UHPFRC.

A total of 48 cylinders were cast over a total of 6 batches. Each cylinder was of size 75mm by 150mm cast in a one-way pour. The average compressive strength achieved from all 6 batches was 133 MPa (Characteristic Value). Additional testing for compressive strength was performed to see how the curing conditions may affect the high compressive strength of the material. Three different curing regimes were used where specimens were cured in a freezer at -18°C, under local weather conditions at Windsor ON in the month of November – December of 2020, and lastly, specimens were cured in a chamber for 24 hours and then placed in the freezer at -18°C. The compression tests show that specimens cured in the freezer had a compressive strength of 40.8 MPa at 28 days, specimens cured in local weather had a compressive strength of 107 MPa, and

specimens cured in a chamber for 24 hours then placed in a freezer had a compressive strength of 92 MPa.

Thirty-cylinder specimens of size 75mm by 150mm were tested for Poisson's ratio and modulus of Elasticity. All specimens tested were instrumented with vertically and horizontally with 4 strain gauges. A minimum of 5 control specimens was tested under compression, from which a load of 40% was calculated to place on the instrumented cylinders. Over 3 batches the average modulus of elasticity was obtained at 46.6 GPa and a Poisson's ratio of 0.21.

Over 30 prism beams were tested with a size of 100mm by 100mm by 350mm. All prism molds were cast with a one-way pour and consolidated with respect to flow. All prisms were loaded at a rate of 0.05 mm/min. The deflection of the prisms was measured from the neutral cord along the beam. The average flexural stress over 3 batches was averaged to 28 MPa.

Five SIA2052 2014 Direct tension dog bone specimens, two Double-T (Georgiou and Pantazopoulou 2016), and three FHWA-type specimens (Graybeal 2013) were tested under axial tension at a loading rate of 0.00254mm/s. SIA specimens had an average tensile strength of 11.8 MPa, Double-T specimens showed a tensile strength of 5.4 MPa, and lastly, the FHWA-Type specimens showed an average of 13 MPa tensile strength. Splitting tests performed on three cylinders of diameter 100mm and 100mm length with wood fillets under the loading platen reached a tensile strength of 16.6 MPa, whereas the same splitting test done on three specimens without wood-fillets showed an average tensile strength of 15.9 MPa. The ultimate tensile strength calculated from the inverse analysis was 8.33 MPa (Characteristic value).

Five prism specimens with a size of 75mm by 75mm by 295mm were cast to test linear shrinkage following the CSA A23.2-21C testing method. The specimens were cured at a relative humidity of 50%. The average length change reported for the 5 prisms was 0.012 % measured with a length comparator.

Three cylinders with a diameter of 75mm and a height of 150mm were tested for C.T.E following the AASHTO-T 336-15 testing method. A control specimen with the dimensions of 100mm by 100mm by 150mm was used to measure the concrete core temperature with a probe that was embedded using the cast. These cylinders were instrumented with demec gauges along 4 diametrically opposing sides. The average C.T.E value reported for these cylinders was 16 μ-strain

/^{o}C under a testing temperature range of 55 ° - 15°C. Additional C.T.E testing was done with a temperature range of 20°C - 3°C for which the reported C.T.E value was 17 µ-strain /^{o}C.

Two cylindrical specimens are tested for creep under an axial stress equal to 40%f_c'. This load was determined with five specimens set aside for testing the compressive strength on the day of loading. Lastly, an additional two specimens were kept near the loaded specimens to measure the length change occurring due to ambient temperature. A demec gauge and demec points were used to measure the strains of the specimens under load and due to ambient temperature effects. A total of 4-gauge lines were used placed diametrically opposing to measure the strains. The creep coefficient at 28 days was reported to be 0.22, and 0.43 at 201 days.

8.2.3 Tension Tests and Inverse Analysis

From the inverse analysis performed on over 30 prism beams tested in flexure, it was found that there exists a range of possible user-defined slopes at the initial step of the analysis for which the prescribed inverse analysis of Annex A8.1 is used in order to characterize the tensile properties of UHPFRC and therefore provide the ticket for the material to enter the market. This range was dependent on the rate at which the prism can sustain flexure loads. The results showed that the analysis was highly user-biased as the results are dependent on the initial slope S_0. It was also found that this analysis gives different results for varying sizes of prims tested, that were cast from the same type of material. As a material property, it should not be dependent on specimen size as this can lead to non-conservative values for characterization under tension, but it can also be used by manufacturers and users alike to tamper with the intentions of quality control in the field. In terms of the validity of this type of analysis for a means to characterize the material, this method delivers poor results in terms of consistency and other forms of tests should be performed to test the tensile properties for material in this class. Similarly as done in this thesis, direct tension tests should be conducted on specimens provided in the literature such as dog bone or double-T specimens.

However, even the direct tension tests give uncertainty as is shown in Chapter 4 of this thesis. This variance exists as a result of the two different mechanisms at play when testing tension. The first being friction which occurs when the specimen in placed in the universal testing frame and held by friction, this friction force is used to then pull apart the specimen so as to cause tension at the

center and result in tension failure. The other method is by bearing action on the double-T specimen, which uses a steel frame cage which pulls apart the specimen from the underside of the T shape on each end of the specimen. It is inconclusive as to why the two different methods result in such different tensile stresses. Though currently in the development of the code and annex for this material, the new testing setup which considers aluminum strips placed at the sides to alleviate slip and a separate instrumentation frame placed at mid-height of the dog bone specimen shows promise for better and more consistent results.

8.2.4 T-Beam Analysis

From the design example of the T-Beam consisting of UHPFRC material, designed in accordance with CSA Annex A8.1, the 1m wide and 1m deep T-Beam was analyzed to be able to resist the prescribed loads under SLS, ULS, and FLS. From this investigation, it was also reported that Annex A8.1 uses a constant value for tensile stress for layers of concrete with a strain less than the ultimate design strain. This was observed to overestimate the layer strength near the neutral axis where small amounts of strain exist, and also allows for no residual resistance to stress for strain values just beyond the design strains.

8.2.5 CPCI Girder Design

To develop design charts for the CPCI 900 girder geometries, a design methodology was developed which used the compression model prescribed by AFGC (2013) and a tensile model following CSA S6 Annex A8.1. The models were analyzed in an excel program and verified in SAP2000 for the moment-resistances. The models made consisted of a range of compressive strengths (100 MPa – 200 MPa), Tensile strengths (dependent of f_c'), and girder size (CPCI 900 vs CPCI 1200). From the analysis, it was concluded that the design charts developed using the design methodology, converge consistently to the correct values for all compressive strengths and girder sizes analyzed when the moment resistance was converted into a dimensionless parameter.

8.3 Recommendations

Recommendations for code revisions drawn from the study are summarized as follows:

- For specimens to be tested for Direct Tension Tests, the molds should be made on plastic or steel, as using wood molds can lead to inconsistent specimen dimensions, and poor testing results. The same is recommended for flexure molds, as wood molds are absorbent and degrade with repeated use. All molds should be covered with a flat glass plate to ensure the top surface is finished and does not contain inconsistencies; this material is very strong compared to the common concretes and the familiar methods of grinding and plastering either do not perform or introduce geometric uncertainties during the tests.
- The current tension tests which use the gripping devices of the universal testing machine tend to cause slip until cracking has propagated. As an alternative, the tension test proposed in Figure 35 is recommended as it uses inclined aluminum strips to tighten the specimen as it slips, where the instrumentation placed only at the center of the specimen is recommended. This is because the displacements obtained from the testing machine reports include slip. The instrumentation used the new setup alleviate slip and only consider the specimens' elongation.
- To ensure that dimensional inconsistencies in flexural prisms do not affect test response, it is recommended to rotate the prims 90 degrees with respect to the position at casting so that the surface in contact with the support and loading rollers are smooth.
- The salt-scaling specimen used was rather heavy; it is recommended to allow for specimens with half the height currently used in testing.
- The sulfate resistance test should be conducted with a control specimen made of concrete, with a data base that can be relied upon to ensure the resistance of the UHPFRC material can be compared with using the same concentration of sulfate solution.
- The abrasion test performed should be done on both the exterior surface and the core of the specimen, so that the difference in abrasion at different concrete depths can be better understood.

Recommendations for future research summarized as follows:

Further research should be conducted for the C.T.E test as the extreme temperatures used and the need to immerse the specimens in hot water are difficult in handling, and often damage the instrumentation. It is also recommended to further research the effects shear and bearing mechanisms on tension tests to better understand why such variation exists. Lastly, its also

recommended to further research how tests done in the lab and the tests done in the field change the results so that this material can be used confidently in the field for future designs of more sustainable structural elements.

References

Aarup, B., "CRC—A Special Fibre Reinforced High Performance Concrete," *Proceedings of the First International RILEM Symposium on Advances in Concrete Through Science and Engineering*, Publication pro048, March 21–24, 2004, Evanston, IL, Ed., Weiss, J. et al.

AASHTO (2015) 'Coefficient of Thermal Expansion of Hydraulic Cement Concrete.'

AASHTO (2018) 'T132-87: Standard Method of Test for Tensile Strength of Hydraulic Cement Mortars.'

AFGC (Association Francaise de Genie Civil-Service) (June, 2013 Revised Edition) 'Ultra-High-Performance Fibre-Reinforced Concretes'

AFGC-SETRA (Association Francaise de Genie Civil-Service d'etudes Techniques des Routes et Autoroutes) (2002) 'Ultra-High-Performance Fibre-Reinforced Concretes, Recommendations provisoires-interim recommendations', pp.98.

AFNOR NF EN 13670/CN (2013). 'Exécution des Structures en Béton-Complément National à la Norme NF EN 1367.'

Ahlborn, T.M. et al., "Durability and Strength Characterization of Ultra-High Performance Concrete Under Variable Curing Regimes," *Proceedings of the Second International Symposium on Ultra High Performance Concrete*, Ed., Fehling, E., Schmidt, M., and Stürwald, S., Kassel University Press, Kassel, Germany, 2008, pp. 197–204.

Alexander, Mark Gavin. "Service Life Design and Modelling of Concrete Structures – Background, Developments, and Implementation." *Revista ALCONPAT*, vol. 8, no. 3, 2018, pp. 224–245., https://doi.org/10.21041/ra.v8i3.325.

Almansour, H. & Lounis, Zoubir. (2010). Innovative precast bridge superstructure using ultra high performance concrete girders.

American Concrete Institute (2012) 'C1202: Standard Test Method for Electrical Indication of Concrete's Ability to Resist Chloride Ion Penetration, American Concrete Institute.

American Society for Testing and Materials (2002) 'C192/C192M: Standard Practice for Making and Curing Concrete Test Specimens in the Laboratory', The American Society for Testing and Materials.

American Society for Testing and Materials (2002) ‘C215: Standard Test Method for Fundamental Transverse, Longitudinal, and Torsional Resonant Frequencies of Concrete Specimens’, The American Society for Testing and Materials.

American Society for Testing and Materials (ASTM) (2005) ‘C39: Standard Test Method for Compressive Strength.’

American Society for Testing and Materials (2008) ‘C666/C666 M: Standard Test Method for Concrete to Rapid Freezing and Thawing’, The American Society for Testing and Materials.

American Society for Testing and Materials (2010) ‘C469/C469M: Standard Test Method for Static Modulus of Elasticity and Poisson’s Ratio of Concrete in Compression’, The American Society for Testing and Materials.

American Society for Testing and Materials (ASTM) (2012) ‘C1609: Standard Test Method for Flexural Strength.’

American Society for Testing and Materials (ASTM) (2015) ‘C512: Standard Test Method for Creep of Concrete in Compression.’

American Society for Testing and Materials (2017) ‘C157M: Standard Test Method for Length Change of Hardened Hydraulic-Cement Mortar and Concrete’, The American Society for Testing and Materials.

American Society for Testing and Materials (2017) ‘C1856/C1856M: Fabricating and Testing Specimens of Ultra-High-Performance Concrete’, The American Society for Testing and Materials.

Annex 8.1 of CSA-S6 (2018) ‘Canadian Highway Bridge Design Code – Annex 8.1 Fibre Reinforced Concrete (New Edition)’, Canadian Standards Association.

Annex U of CSA-A23.1 (2019) ‘Ultra-High-Performance Concrete (UHPC)’, Canadian Standards Association

Azmee, N.M., and N.Shafiq. “Ultra-High Performance Concrete: From Fundamental to Applications.” Case Studies in Construction Materials, vol. 9, 2019, https://doi.org/10.1016/j.cscm.2018.e00197.

Baby, F., Graybeal, B., Marchand, P., & Toutlemonde, F. (2012). Proposed Flexural Test Method Associated Inverse Analysis for Ultra High-Performance Fiber Reinforced Concrete. *ACI Materials Journal*, 109(5), 545-556

Banthia, N. (2012) 'FRC: Milestone in International Research and Development', Proceedings of FIBCON2012, ICI, pp.48.

Bétons Fibrés à Ultra-Hautes Performances, Recommandations Provisoires, (*Ultra High Performance Fibre-Reinforced Concretes)*, Interim Recommendations, SETRA-AFGC, Groupe de travail BFUP, Paris, France, January 2002. (in French and English). Available at http://www.afgc.asso.fr/statuts-de-lassociation-francaise-de-genie-civil.html

Behloul, M. et al., "Fire Resistance of Ductal® Ultra High Performance Concrete," *Proceedings of the First fib Congress*, Osaka, Japan, 2002, pp. 421–430

Bonneau, O. et al., "Mechanical Properties and Durability of Two Industrial Reactive Powder Concretes," *ACI Materials Journal*, Vol. 94, No. 4, July–August 1997, pp. 286–290.

Bouzoubaâ, N., et al. "Deicing Salt Scaling Resistance of Concrete Incorporating Supplementary Cementing Materials: Laboratory and Field Test Data." *Canadian Journal of Civil Engineering*, vol. 35, no. 11, 2008, pp. 1261–1275., https://doi.org/10.1139/l08-067.

Burkart, I. and Müller, H.S., "Creep and Shrinkage Characteristics of Ultra High Strength Concrete (UHPC)," *Proceedings of the Second International Symposium on Ultra High Performance Concrete*, Ed., Fehling, E., Schmidt, M., and Stürwald. S., Kassel University Press, Kassel, Germany, 2008, pp. 469–476.

Canadian Standards Association (2014) 'CSA A23.2: 'Concrete Materials and Methods of Concrete Construction', *Canadian Standards Association.*

Canadian Standards Association (2014) 'CSA A23.2-9C: 'Compressive Strength of Cylindrical Concrete Specimens', *Canadian Standards Association*.

Canadian Standards Association (2014) 'CSA A23.2-11C: 'Water content, density, absorption, and voids in hardened concrete, grout, or mortar', *Canadian Standards Association.*

Canadian Standards Association (2014) 'CSA A23.2-13C: Splitting Tensile Strength of Cylindrical Concrete Specimens', *Canadian Standards Association.*

Canadian Standards Association (2014) ‘CSA A23.2-21C: ‘Test Method for length change of hardened concrete’, *Canadian Standards Association.*

Canadian Standards Association (2014) ‘CSA A23.2-22C: ‘Electrical indication of concrete’s ability to resist chloride ion penetration’, *Canadian Standards Association.*

Canadian Standards Association (2014) ‘CSA A23.2-23C: ‘Scaling resistance of concrete surfaces exposed to deicing chemicals using mass loss’, *Canadian Standards Association.*

Chao, Shih-Ho, et al. “Toward a Non-Prestressed Precast Long-Span Bridge Girder Using UHP-FRC.” *Second International Interactive Symposium on UHPC*, 2019, https://doi.org/10.21838/uhpc.9661.

CPCI Design Manual: Precast and Prestressed Concrete. Canadian Precast/Prestressed Concrete Institute, 2017.

Dong, You. “Performance Assessment and Design of Ultra-High Performance Concrete (UHPC) Structures Incorporating Life-Cycle Cost and Environmental Impacts.” *Construction and Building Materials*, vol. 167, 2018, pp. 414–425., https://doi.org/10.1016/j.conbuildmat.2018.02.037.

Fehling, E., Bunje, K., and Leutbecher, T., "Design Relevant Properties of Hardened Ultra High Performance Concrete," *Proceedings of the International Symposium on Ultra High Performance Concrete*, Ed., Schmidt, M., Fehling, E., and Geisenhanslüke, C., Kassel University Press, Kassel, Germany, 2004, pp. 327–338.

FHWA-HRT-13-060 (2013) ‘Ultra-High Performance Concrete: A State-Of-The-Art Report for The Bridge Community’, U.S Department of Transportation.

FHWA-HRT-17-097 (2017) ‘Ultra-High-Performance Concrete for Bridge Deck Overlays’, U.S. Department of Transportation.

FHWA-HRT-18-036 (2018) ‘Properties and Behaviour of UHPC-Class Materials’, U.S. Department of Transportation.

Frettlohr, B., Reineck, K.-H. and Reinhardt, H.-W. (2012) ”Size and Shape Effect of UHPFRC Prism Tested under Axial Tension and Bending” In: Parra-Montesinos G.J., Reinhardt H.W., Naaman A.E. (eds) High Performance Fiber Reinforced Cement Composites 6.

RILEM State of the Art Reports, vol 2. Springer, Dordrecht doi https://doi.org/10.1007/978-94-007-2436-5_44

Gao, R., Stroeven, P., and Hendriks, C.F., "Mechanical Properties of Reactive Powder Concrete Beams," *Seventh International Symposium on the Utilization of High-Strength/High-Performance Concrete*, Vol. II, Publication No. SP-228, Ed., Russell, H.G., American Concrete Institute, Farmington Hills, MI, 2005, pp. 1,237–1,252.

Graybeal, B. A. (2005). *Characterization of the behavior of ultra-high performance concrete* (Order No. 3178565). Available from ProQuest Dissertations & Theses Global. (304992480).http://ezproxy.library.yorku.ca/login?url=https://www.proquest.com/dissertations-theses/characterization-behavior-ultra-high-performance/docview/304992480/se-2?accountid=15182

Graybeal, B. A. "Material Property Characterization of Ultra-High Performance Concrete" FHWA Report, August 2006.

Graybeal, B., "Structural Behavior of Ultra-High Performance Concrete Prestressed I-Girders," FHWA, U.S. Department of Transportation, Report No. FHWA-HRT-06-115, 2006. Available through National Technical Information Service at http://www.ntis.gov with Accession No. PB2007104386

Graybeal, B. A. "Flexural Behavior of an Ultrahigh-Performance Concrete I-Girder" *Journal of Bridge Engineering, ASCE*, November 2008.

Graybeal, B.A., "Simultaneous Structural and Environmental Loading of an Ultra-High Performance Concrete Component," FHWA, U.S. Department of Transportation, Report No. FHWA-HRT-10-054. Available through National Technical Information Service at http://www.ntis.gov with Accession No. PB2010110331.2008

Graybeal, B. and Stone, B., "Compression Response of a Rapid-Strengthening Ultra-High Performance Concrete Formulation," FHWA, U.S. Department of Transportation, Report No. FHWA-HRT-12-065, National Technical Information Service Accession No. PB2012-112545, 2012.

Graybeal, B. A. & El-Helou, R. G., (2019) "Development of an AASHTO Guide Specification for UHPC", *International Interactive Symposium on Ultra-High Performance Concrete* 2(1). doi: https://doi.org/10.21838/uhpc.9708

Graybeal, B. A. and Baby, F. "Tension testing of Ultra-High Performance Concrete" FHWA Report, February, 2019.

Granger, Sébastien & Loukili, Ahmed & Pijaudier-Cabot, G. & Chanvillard, Gilles. (2005). Mechanical Characterization of the Self-Healing Effect of Cracks in Ultra High Performance Concrete.

Groeneveld, Andrew B., et al. "Dynamic Strength and Ductility of Ultra-High Performance Concrete with Flow-Induced Fiber Alignment." *International Journal of Impact Engineering*, vol. 111, 2018, pp. 37–45., doi:10.1016/j.ijimpeng.2017.08.009.

Gu, Chunping, et al. "Simulation of the Flexural Response of Ultrahigh Performance Fiber-Reinforced Concrete with Lattice Fracture Model." *Advances in Civil Engineering*, vol. 2018, 2018, pp. 1–8., https://doi.org/10.1155/2018/7894192.

Habel, Katrin, et al. "Ultra-High Performance Fibre Reinforced Concrete Mix Design in Central Canada." *Canadian Journal of Civil Engineering*, vol. 35, no. 2, 2008, pp. 217–224., https://doi.org/10.1139/l07-114.

Hassan, A., Jones, S., and Mahmud, G. (2012) 'Experimental Test Methods to Determine the Uniaxial Tensile and Compressive Behaviour of Ultra-High-Performance Fiber Reinforced Concrete', Construction and Building Materials, pp.374-882.

Huang, Huanghuang, et al. "Numerical Simulation and Visualization of Motion and Orientation of Steel Fibers in UHPC under Controlling Flow Condition." *Construction and Building Materials*, vol. 199, 2019, pp. 624–636., doi:10.1016/j.conbuildmat.2018.12.055.

Huang, Huanghuang, et al. "Improvement Effect of Steel Fiber Orientation Control on Mechanical Performance of UHPC." *Construction and Building Materials*, vol. 188, 2018, pp. 709–721., doi:10.1016/j.conbuildmat.2018.08.146.

Huang, Huanghuang, et al. “Influence of Formwork Wall Effect on Fiber Orientation of UHPC with Two Casting Methods.” *Construction and Building Materials*, vol. 215, 2019, pp. 310–320., doi:10.1016/j.conbuildmat.2019.04.200.

Huang, Huanghuang, Xiaojian Gao, Le Teng, Fiber alignment and its effect on mechanical properties of UHPC: An overview, Construction and Building Materials, Volume 296, 2021, 123741,ISSN 0950-0618,https://doi.org/10.1016/j.conbuildmat.2021.123741.

Hussein, Luaay, and Lamya Amleh. “Size Effect of Ultra-High Performance Fiber Reinforced Concrete Composite Beams in Shear.” *Structural Concrete*, vol. 19, no. 1, 2018, pp. 141–151., doi:10.1002/suco.201700078.

Ichinomiya, T. et al., "Experimental Study on Mechanical Properties of Ultra-High-Strength Concrete with Low-Autogenous-Shrinkage," *Seventh International Symposium on the Utilization of High-Strength/High-Performance Concrete*, Vol. II, Publication No. SP-228, Ed., Russell, H.G., American Concrete Institute, Farmington Hills, MI, 2005, pp. 1,341–1,352.

Joh, C. et al., "Punching Shear Strength Estimation of UHPC Slabs," *Proceedings of the Second International Symposium on Ultra High Performance Concrete*, Ed., Fehling, E., Schmidt, M., and Stürwald. S., Kassel University Press, Kassel, Germany, 2008, pp. 719-726.

Juan Angel Lopez Martinez “Characterization of The Tensile Behaviour of UHPFRC By Means of Four-Point Bending Tests” A Ph.D Thesis Report , 2017

Kazemi, S., and Lubell, A. (2012) ‘Influence of Specimen Size and Fiber Content on Mechanical Properties of Ultra-High-Performance Fiber-Reinforced Concrete’, ACI Materials Journal 109(6), pp.675-684.

Kim, Jin-Keun & Yi, S.-T & Kim, Jang-Ho. (2001). Effect of specimen sizes on flexural compressive strength of concrete. ACI Structural Journal. 98. 416-424.

Larsen, I. L. and Thorstensen, R. T. “The influence of steel fibres on compressive and tensile strength of ultra-high performance concrete: A review” *Construction and Building Materials* (2020)

Lee, Bang-Yeon, et al. “Corrosion and Strength Behaviors in Prestressed Tendon under Various Tensile Stress and Impressed Current Conditions.” *Advances in Materials Science and Engineering*, vol. 2017, 2017, pp. 1–7., https://doi.org/10.1155/2017/8575816.

Maca, P., Zatloukal, J., and Konvalinka, P. (2012) ‘Development of Ultra-Higher-Performance FiberReinforced Concrete Mixture’, IEEE Symposium, pp.861-866.

Ma, J. et al., "Comparative Investigations on Ultra-High Performance Concrete With and Without Coarse Aggregates," *Proceedings of the International Symposium on Ultra High Performance Concrete*, Ed., Schmidt, M., Fehling, E., and Geisenhanslüke, C., Kassel University Press, Kassel, Germany, 2004, pp. 205–212.

Marijan, S., Dubravka, B., and Zeljana, S., "Acoustic Emission Response and Mechanical Characterization of Ultra High-Performance Concrete Types," *Seventh International Symposium on the Utilization of High-Strength/High-Performance Concrete*, Vol. II, Publication No. SP-228, Ed., Russell, H.G., American Concrete Institute, Farmington Hills, MI, 2005, pp. 1,207–1,220.

Mermigas, K., 2018. Evolution of Bridge Practices in Ontario, Canada. [online] Tac-atc.ca. Available at: [Accessed 10 March 2021].

Mohamadreza Shafieifar, Mahsa Farzad, Atorod Azizinamini, A comparison of existing analytical methods to predict the flexural capacity of Ultra High Performance Concrete (UHPC) beams, Construction and Building Materials, Volume 172, 2018, Pages 10-18, ISSN 0950-0618,https://doi.org/10.1016/j.conbuildmat.2018.03.229.

Mosaberpanah, Mohammad Ali, and Ozgur Eren. “Effect of Density on Compressive Strength of Ultra High Performance Fiber Reinforced Concrete (UHPFRC) Using Design of Experiment.” *Solid State Phenomena*, vol. 249, 2016, pp. 119–124., https://doi.org/10.4028/www.scientific.net/ssp.249.119.

Nakov, Darko. “Experimental and Analytical Analysis of Creep of Steel Fibre Reinforced Concrete.” *Periodica Polytechnica Civil Engineering*, 2017, https://doi.org/10.3311/ppci.11184.

Nguyen, Duy Liem, et al. “Size Effect on Flexural Behavior of Ultra-High-Performance Hybrid Fiber-Reinforced Concrete.” *Composites Part B: Engineering*, vol. 45, no. 1, 2013, pp. 1104–1116., doi:10.1016/j.compositesb.2012.07.012.

Nguyen, Duy Liem, et al. “Size and Geometry Dependent Tensile Behavior of Ultra-High-Performance Fiber-Reinforced Concrete.” *Composites Part B: Engineering*, vol. 58, 2014, pp. 279–292., doi:10.1016/j.compositesb.2013.10.072.

Nguyen, D. L., Ryu, G. S., Koh, K. T. and Jim, D. J. “Size and Geometry dependent tensile behavior of ultra-high-performance fiber-reinforced concrete” *Composites: Part B*, vol. 58, 2014, pp.:279-292

Orgass, M., and Klug, Y. (2004) ‘Fiber-Reinforced Ultra-High-Strength Concretes’, Proceedings of the International Symposium on UHPC, pp,637-648.

Ozyildirim, C., "Evaluation of Ultra-High-Performance Fiber-Reinforced Concrete," Virginia Center for Transportation Innovation and Research, Report No. FHWA/VCTIR 12-R1, Federal Highway Administration, McLean, VA, 2011.

Pfeifer, Donald W., et al. “The Rapid Chloride Permeability Test and Its Correlation to the 90-Day Chloride Ponding Test.” *PCI Journal*, vol. 39, no. 1, 1994, pp. 38–47., https://doi.org/10.15554/pcij.01011994.38.47.

Piérard, J., Dooms, B., and Cauberg, N., "Evaluation of Durability Parameters of UHPC Using Accelerated Lab Tests," *Proceedings of Hipermat 2012 3rd International Symposium on UHPC and Nanotechnology for High Performance Construction Materials*, Ed., Schmidt, M., Fehling, E., Glotzbach, C., Fröhlich, S., and Piotrowski, S., Kassel University Press, Kassel, Germany, 2012, pp. 371–376

Pyo, Sukhoon, et al. “Abrasion Resistance of Ultra High Performance Concrete Incorporating Coarser Aggregate.” *Construction and Building Materials*, vol. 165, 2018, pp. 11–16., https://doi.org/10.1016/j.conbuildmat.2018.01.036.

Qiu, M., Zhang, Y., Qu, S., Zhu, Y. and Shao, X. “Effect of reinforcement ratio, fiber orientation, and fiber chemical treatment on the direct tension behavior of rebar-reinforced UHPC” *Construction and Building Materials* vol. 256 (2020)

Ralli, Z. & Pantazopoulou, S. J. “Correlation Between Tensile Strength & Modulus of rupture for Ultra-High Performance Concrete “ *Proceedings of 2019 National Accelerated Bridge Construction Conference including Automation, Service Life and UHPC,* 11-13 December 2019, Miami, Florida, USA.

Rigaud, S., Chanvillar, G., and Chen, J. (2011). Characterization of Bending and Tensile Behavior of Ultra-High-Performance Concrete Containing Glass Fibers. *6th International Symposium on High Performance Fiber Reinforce Cement Composites*, 373-380

Rodrigues, Romain, et al. “Reinforced Concrete Structures: A Review of Corrosion Mechanisms and Advances in Electrical Methods for Corrosion Monitoring.” *Construction and Building Materials*, vol. 269, 2021, p. 121240., https://doi.org/10.1016/j.conbuildmat.2020.121240.

Roy, Manish, et al. “Influence of Volume Fraction and Orientation of Fibers on the Pullout Behavior of Reinforcement Bar Embedded in Ultra High Performance Concrete.” *Construction and Building Materials*, vol. 146, 2017, pp. 582–593., doi:10.1016/j.conbuildmat.2017.04.081.

Russel, H. G. and Graybeal, B. A. “Ultra-High Performance Concrete: A State-of-the-Art Report for the Bridge Community” FHWA Report, June 2013.

Schmidt, M. et al., "Durability of Ultra High Performance Concrete," *Proceedings of the 6th International Symposium on High Strength/High Performance Concrete*, Leipzig, Germany, June 2002, Ed., König, G., Dehn, F., and Faust, T., Vol. 2, pp. 1,367-1,376.

Shafieifar, Mohamadreza, et al. “A Comparison of Existing Analytical Methods to Predict the Flexural Capacity of Ultra High Performance Concrete (UHPC) Beams.” Construction and Building Materials, vol. 172, 2018, pp. 10–18., doi:10.1016/j.conbuildmat.2018.03.229.

Shehab El-Din, Hamdy K., et al. “Effect of Steel Fibers on Behavior of Ultra High Performance Concrete.” *First International Interactive Symposium on UHPC*, 2016, https://doi.org/10.21838/uhpc.2016.11.

Shen, X. and Bruhwiler, E. “TENSILE BEHAVIOR UNDER UNIAXIAL AND BIAXIAL STRESS CONDITIONS” *Proceedings of 2nd ACF Symposium Innovations for Sustainable Concrete Infrastructures*, 23-25 November 2017, Chiang Mai, Thailand.

SIA 2052 (2014) ‘Béton Fibré Ultra-Performant (BFUP): Matériaus, dimensionnement et exéctuion. Draft’

Simon, A., "Les Nouvelles Recommandations AFGC sur les BFUP CHAPITRE I—Comportement et Caractéristiques Mécaniques des BFUP," (Updated AFGC Recommendations: Chapter 1 Materials), *Proceedings of the International Workshop on Ultra High Performance Fibre Reinforced Concrete—Designing and Building with UHPFRC: State of the Art Development*, 17–19 November 2009, Marseille, France, AFGC/*fib*, Paper 6.1.2.

Skazlic, M, Bjegovic, D., and Serdar, M. (2008) ‘Influence of Test Specimens’ Geometry on Compressive Strength of Ultra-High-Performance Concrete’, Proceedings of the 2nd International Symposium on UHPC, pp.295- 301.

Sobuz, Md. Habibur & Oehlers, Deric & Visintin, Phillip & Hasan, Noor & Hoque, Md & Akid, Abu. (2017). Flow and Strength Characteristics of Ultra-high Performance Fiber Reinforced Concrete: Influence of Fiber Type and Volume-fraction. Journal of Civil Engineering and Construction. 6. 15-21.

Tadros, Maher K., et al. “Ultra-High-Performance Concrete.” *STRUCTURE Magazine*, April 2019, https://www.structuremag.org/?p=14370.

Tehmina Ayub, Sadaqat Ullah Khan, Fareed Ahmed Memon, "Mechanical Characteristics of Hardened Concrete with Different Mineral Admixtures: A Review", The Scientific World Journal, vol. 2014, Article ID 875082, 15 pages, 2014. https://doi.org/10.1155/2014/875082

Thomas, M. et al., "Marine Performance of UHPC at Treat Island," *Proceedings of Hipermat 2012 3rd International Symposium on UHPC and Nanotechnology for High Performance Construction Materials*, Ed., Schmidt, M., Fehling, E., Glotzbach, C., Fröhlich, S., and Piotrowski, S., Kassel University Press, Kassel, Germany, 2012, pp. 365–370.

Thomas, R.j., and Andrew D. Sorensen. “Review of Strain Rate Effects for UHPC in Tension.” *Construction and Building Materials*, vol. 153, 2017, pp. 846–856., doi:10.1016/j.conbuildmat.2017.07.168.

Wille, Kay, and Gustavo J. Parra-Montesinos. “Effect of Beam Size, Casting Method, and Support Conditions on Flexural Behavior of Ultra-High-Performance Fiber-Reinforced Concrete.” *ACI Materials Journal*, vol. 109, no. 3, 2013, doi:10.14359/51683829.

Wu, Zemei, et al. “Effects of Steel Fiber Content and Shape on Mechanical Properties of Ultra High Performance Concrete.” *Construction and Building Materials*, vol. 103, 2016, pp. 8–14., doi:10.1016/j.conbuildmat.2015.11.028.

Yang, In Hwan, et al. “Structural Behavior of Ultra High Performance Concrete Beams Subjected to Bending.” *Engineering Structures*, vol. 32, no. 11, 2010, pp. 3478–3487., doi:10.1016/j.engstruct.2010.07.017.

Ye, Y. et al. (2012) ‘Mechanical Behaviour of Ultra-High-Performance Concrete Reinforced with Hybrid Different Shapes of Steel Fibers’, In ASCE, CICTP, pp.3014-3028.

Yoo, Doo-Yeol, et al. “Material and Bond Properties of Ultra High Performance Fiber Reinforced Concrete with Micro Steel Fibers.” *Composites Part B: Engineering*, vol. 58, 2014, pp. 122–133., https://doi.org/10.1016/j.compositesb.2013.10.081.

Yoo, Doo-Yeol, and Young-Soo Yoon. “Structural Performance of Ultra-High-Performance Concrete Beams with Different Steel Fibers.” *Engineering Structures*, vol. 102, 2015, pp. 409–423., doi:10.1016/j.engstruct.2015.08.029.

Yoo, Doo-Yeol, et al. “Size Effect in Ultra-High-Performance Concrete Beams.” *Engineering Fracture Mechanics*, vol. 157, 2016, pp. 86–106., doi:10.1016/j.engfracmech.2016.02.009.

Yoo, Doo-Yeol, et al. “Enhancing the Flexural Performance of Ultra-High-Performance Concrete Using Long Steel Fibers.” *Composite Structures*, vol. 147, 2016, pp. 220–230., doi:10.1016/j.compstruct.2016.03.032.

Yoo, Doo-Yeol, et al. “Effect of Fiber Orientation on the Rate-Dependent Flexural Behavior of Ultra-High-Performance Fiber-Reinforced Concrete.” *Composite Structures*, vol. 157, 2016, pp. 62–70., doi:10.1016/j.compstruct.2016.08.023.

Yuechen Yang, Mohammed Ismail, S.J. Pantazopoulou, and Dan Palermo. Tensile behaviour of ultra-high-performance steel fiber reinforced concrete. *Canadian Journal of Civil Engineering*. 48(11): 1409-1421. https://doi.org/10.1139/cjce-2019-0592

Zhang, Y., Zhu, Y., Qu, S., Kumar, A. and Shao, X. “Improvement of flexural and tensile strength of layered-casting UHPC with aligned steel fibers” *Construction and Building Materials* vol. 251 (2020).

Zhou, F.p, et al. “Size Effect on Flexural, Splitting Tensile, and Torsional Strengths of High-Strength Concrete.” *Cement and Concrete Research*, vol. 28, no. 12, 1998, pp. 1725–1736., doi:10.1016/s0008-8846(98)00157-4.

Zhou, Z. and Qiao, P. “Tensile Behaviour of ultra-high performance concrete: Analytical model and experimental validation” *Construction and Building Materials,* vol. 201, 2019, pp.: 842-851.

Zhou Bo and Uchida Yuichi “Relationship between fiber orientation and distribution and post-cracking behaviour in Ultra-High Performance Fiber Reinforced Concrete (UHPFRC)” *Cement and Concrete Composites,* vol. 83, 2017, pp.66-75.

Appendices

Appendix 1: Dura Material Tests

Batch 1: Compression Test

A load-controlled compression-testing machine was used to test the cylinders under compression at a loading rate of 1 MPa/s in accordance with ASTM C1856 (2017). The nominal dimensions of the cylinder are 75 mm × 150 mm. The actual dimensions of each cylinder can be found in Table A-43. This batch of material contains 2% steel fibers by unit volume, and the straight fibers were 20 mm long with a diameter of 0.2 mm. Prior to testing, top and bottom surfaces of each cylinder were grinded. Amoug the ten cylinders tested under compression, three were tested at the age of 27 days, and all other were tested at the age of 28 days.

Table A-36: Batch 1 Compression result summary

Cylinder	Test Date	Age (Days)	Diameter × Height (mm)	Strength (MPa)
# 1	2/24/2020	28	76.1 × 148.5	148.58
# 2	2/24/2020	28	76.2 × 148.6	157.15
# 3	2/24/2020	28	75.6 × 150.8	145.98
# 4	2/24/2020	28	76.0× 149.9	138.31
# 5	2/23/2020	27	76.3 × 150.8	133.64
# 6	2/23/2020	27	76.5 × 149.3	142.83
# 7	2/24/2020	28	75.8 × 150.4	154.67
# 8	2/23/2020	27	76.2 × 149.0	141.50
# 9	2/24/2020	28	75.8 × 150.2	158.14
# 10	2/24/2020	28	76.0 × 147.3	146.03
Average				146.68

Batch 1: Flexural Tests

Prisms subjected to four-point loading were tested by using the universal testing machine at a stepwise loading rate. A loading rate of 0.15 mm/min was applied to the prisms before reaching 70% post-peak load. The loading rate was increased by 0.05 mm/min for the post-peak softening branch after the load dropped below 70% of the peak load. In addition, all the prisms were tested up until the post-peak residual strength had degraded to 20% of the peak load.

This batch of material contained 2% steel fibers by unit volume, and the straight fibers were 20 mm long with a diameter of 0.2 mm. The nominal dimensions of the prisms were 101.6 mm × 101.6 mm × 356.6 mm. The shear span from each side and the distance between loading rollers were 100 mm, and the distance between support rollers was 300 mm. As depicted in Figure A-84, to measure the net vertical deflection at midspan, a linear variable differential transducer (LVDT) was placed at midspan and mounted at the mid-height of the prism on the specimen chord using a fabricated instrumentation jig. Digital Image Correlation (DIC) was used to record the field of strains on one side of the deforming specimens during the tests. The actual dimensions and flexural strength of each prism can be found in Table A-44, where the nominal flexural strength was calculated with Equation 1. In this Equation, P_{max} is the experimental peak load, L is the total span between supports, and b and h are the cross-sectional width and depth near the failure plane measured after each test.

$$\sigma_f = P_{max}L/bh^2 \qquad (1)$$

Figure A-106. Experimental test setup of four-point bending test

Table A-37. Flexural strength results

Prism	Date of Testing	b (mm)	h (mm)	L (mm)	P_{max} (kN)	σ_f (MPa)
# 1	02/23/2020	101.4	100.6	300	79.07	23.12
# 2	02/24/2020	100.5	99.9	300	75.80	22.67
# 3	02/24/2020	100.3	100.0	300	112.39	33.72
# 4	02/24/2020	102.9	99.6	300	78.02	22.96
# 5	02/24/2020	99.0	100.6	300	81.57	24.42
# 6	02/24/2020	103.7	100.7	300	79.99	22.82
# 7	02/24/2020	101.4	100.3	300	71.39	20.99
# 8	02/24/2020	101.9	100.0	300	91.99	27.10
# 9	02/24/2020	101.2	100.1	300	88.35	26.14
# 10	02/24/2020	102.9	102.2	300	89.30	24.93
Average Flexural Strength (MPa)						**23.51**

**The results of prism #3 and prism #8 were not used to calculate the average flexural strength due to the obvious difference in results compared with other prisms and unexpected failure modes (i.e., the prisms failed in shear or torsion).*

The resistance curves of each prism are presented in Figure A-85. These were used to perform the inverse analysis procedures prescribed in Annex 8.1 of CSA-S6 (2018). As shown in Table A-45, the inverse analysis essentially relies on four characteristic points of the resistance curve, where point (P_o, δ_o)

determines the linearity limit and initial slope (s_o) of the resistance curve. The four characteristic points on the resistance curve are defined as follows: Points (P_1, δ_1) and (P_2, δ_2) lie on the secant lines drawn from the origin with a slope s_{75} and s_{40} equal to 75% and 40% of the initial slope, s_o, respectively. Point (P_3, δ_3) corresponds to 97% of peak load (P_{max}), whereas (P_4, δ_4) is in the post-peak range at 80% of P_3.

The tensile properties obtained from the inverse analysis can be found in Table A-43. In Table A-43, f_{cr} represents the cracking strength corresponding to the onset of crack formation, f_{Fu} represents the ultimate tensile strength corresponding to crack localization, ε_{cr} and ε_{tu} are the strains corresponding to f_{cr} and f_{Fu} respectively, and w_o represents the crack width after crack localization.

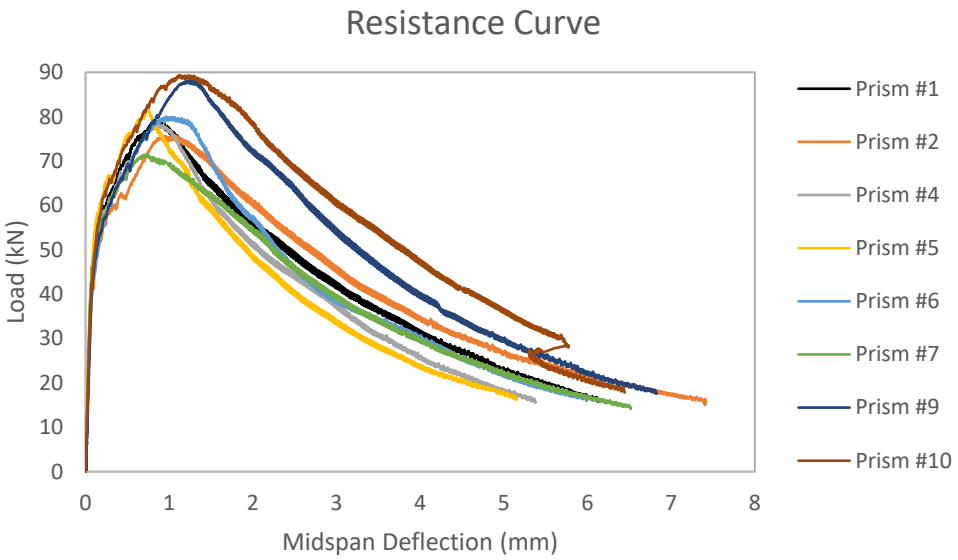

Figure A-107. Resistance curves of four-point bending tests

Table A-38. Characteristic points utilized for inverse analysis

Prism	E_{co} (GPa)	P_o (kN)	δ_o (mm)	P_1 (kN)	δ_1 (mm)	P_2 (kN)	δ_2 (mm)	P_3 (kN)	δ_3 (mm)	P_4 (kN)	δ_4 (mm)	P_{max} (kN)	δ_{max} (mm)
# 1	46.59	41.01	0.0625	47.21	0.0959	59.74	0.2259	76.70	0.7382	61.35	1.6673	79.07	0.8153
# 2	41.63	37.21	0.0640	42.15	0.0967	55.69	0.2410	73.52	0.7962	58.80	2.1304	75.80	1.0563
# 3	-	-	-	-	-	-	-	-	-	-	-	-	-
# 4	47.12	37.01	0.0550	46.95	0.0931	58.51	0.2166	75.66	0.7284	60.56	1.5166	78.02	0.8739
# 5	53.78	34.53	0.0467	50.96	0.0917	61.95	0.2096	79.12	0.6225	63.29	1.3355	81.56	0.7420

# 6	47.05	32.02	0.0473	42.59	0.0838	55.18	0.2034	77.59	0.7980	62.08	1.7294	79.99	0.9635
# 7	51.92	38.52	0.0527	45.36	0.0831	56.53	0.1932	69.25	0.5723	55.41	1.9497	71.39	0.7379
# 8	-	-	-	-	-	-	-	-	-	-	-	-	-
# 9	40.56	37.72	0.0662	47.98	0.1123	57.99	0.2540	85.70	1.0559	68.54	2.2242	88.35	1.2798
# 10	45.15	37.64	0.0583	46.68	0.0965	62.25	0.2416	86.60	0.9505	69.24	2.4201	89.30	1.2219

Table A-39. Linearized tensile stress-strain-crack width properties

Prism	**f_{crm} (MPa)**	**ε_{cr} (mm/mm)**	**f_{Fu}/f_{crm}**	**ε_{tu} (mm/mm)**	**w_o (mm)**
# 1	8.10	0.000174	1.112	0.008407	2.85
# 2	7.34	0.000176	1.241	0.009249	4.06
# 3	-	-	-	-	-
# 4	8.13	0.000173	1.093	0.008510	2.30
# 5	9.02	0.000168	1.054	0.006944	2.18
# 6	7.10	0.000151	1.293	0.009395	2.49
# 7	7.85	0.000151	1.018	0.006367	4.30
# 8	-	-	-	-	-
# 9	8.40	0.000207	1.255	0.012716	3.35
# 10	7.57	0.000168	1.324	0.010862	3.80
Average	**7.94**	**0.000171**	**1.17**	**0.009056**	**3.17**

Batch 1: Poisson's Ratio and Static Modulus of Elasticity

Ten 75 mm × 150 mm cylinders were subjected to compressive loading at the age of 27 days to determine the static modulus of elasticity and Poisson's ratio. This batch of material contains 2% steel fibers by unit volume, and the straight fibers were 20 mm long with a diameter of 0.2 mm. Prior to testing, both top and bottom surfaces of the cylinder were grinded smooth. Four foil strain gauges were installed along the two diametrically opposite lines near the mid-height of the cylinder: two strain gauges were placed vertically to measure longitudinal strains, and the other two strain gauges were placed horizontally to measure transverse strains. Each cylinder was loaded up to around 246 kN which corresponds to 40% of the compressive strength determined by testing another three 75 mm × 150 mm cylinders from the same batch at the age of 27 days. A loading rate of 0.0023 mm/s was employed, and each cylinder was tested consecutively three times.

Figure A-86 illustrates the response curve of a test, where the horizontal axis represents the applied load values, and the vertical axis represents strain values of the four strain gauges. The average static modulus of elasticity (E) was **45.89 GPa** and the average Poisson's ratio (ν) was **0.213**. Table A-47 presents the experimental results of each test, where σ_1 and σ_2 are the compressive stresses corresponding to a longitudinal strain of 50 μm/m and 40% of the compressive strength, respectively; ε_1 represents a longitudinal strain of 50 μm/m, and ε_2 is the longitudinal strain corresponding to σ_2; ε_{t1} and ε_{t2} are the transverse strains corresponding to σ_1 and σ_2, respectively; F_1 and F_2 are the compressive loads corresponding to σ_1 and σ_2, respectively; E was calculated with Equation 1, and ν was calculated with Equation 2.

$$\mathrm{E} = \frac{\sigma_2 - \sigma_1}{\varepsilon_2 - \varepsilon_1} \quad (1)$$

$$\nu = \frac{\varepsilon_{t2} - \varepsilon_{t1}}{\varepsilon_2 - \varepsilon_1} \quad (2)$$

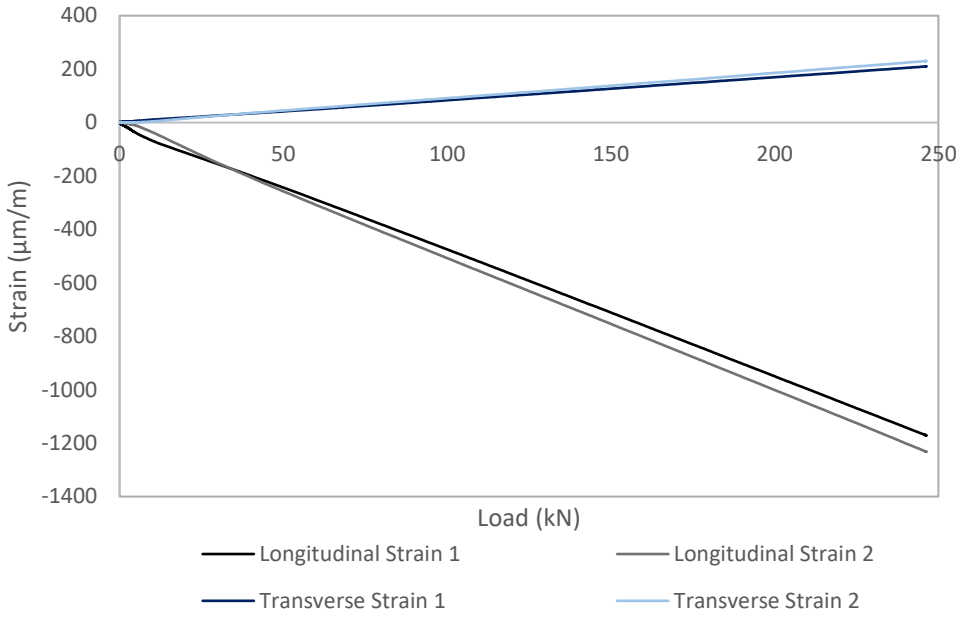

Figure A-108. Response curve of static modulus of elasticity and Poisson's ratio test

Table A-40. Results of static modulus of elasticity and Poisson's ratio

Cylinder	**Diameter (mm)**	**Test**	**ε_1 (µm/m)**	**ε_2 (µm/m)**	**ε_{t1} (µm/m)**	**ε_{t2} (µm/m)**	**F_1 (kN)**	**F_2 (kN)**	**σ_1 (MPa)**	**σ_2 (MPa)**	**E (GPa)**	***ν***
# 1	76.0	1	50.04	1269.74	9.66	285.70	10.05	245.88	2.22	54.20	42.62	0.226
		2	50.05	1264.04	7.39	275.25	10.30	245.26	2.27	54.06	42.66	0.221
		3	50.00	1264.00	7.26	277.98	10.75	245.55	2.37	54.13	42.63	0.223
Average											*42.65*	*0.222*
# 2	75.6	1	50.00	1314.85	7.47	244.13	8.04	245.63	1.79	54.79	41.90	0.187
		2	50.16	1299.97	6.43	246.15	8.25	245.78	1.84	54.83	42.39	0.192
		3	50.02	1292.58	7.65	247.03	8.40	245.88	1.87	54.85	42.63	0.193
Average											*42.51*	*0.192*
# 3	75.9	1	50.10	1151.10	10.78	234.62	12.41	246.01	2.74	54.37	46.89	0.203

		2	50.03	1155.17	9.64	238.43	12.48	245.78	2.76	54.32	46.66	0.207
		3	50.24	1157.91	9.48	239.51	12.16	246.05	2.69	54.38	46.67	0.208
Average											*46.66*	*0.207*
# 4	76.0	1	50.01	1150.79	13.08	272.24	10.80	246.26	2.38	54.28	47.15	0.235
		2	50.15	1135.49	12.79	268.67	11.98	245.52	2.64	54.12	47.43	0.236
		3	50.00	1140.46	15.28	273.13	12.31	245.93	2.71	54.21	47.23	0.236
Average											*47.33*	*0.236*
# 5	76.3	1	50.04	1135.96	12.34	232.51	14.93	245.59	3.27	53.78	46.52	0.203
		2	50.03	1258.39	7.37	241.91	7.22	245.52	1.58	53.77	43.19	0.194
		3	50.26	1262.52	7.10	244.26	7.33	245.97	1.60	53.87	43.11	0.196
Average											*43.15*	*0.195*
# 6	75.8	1	50.13	1170.35	12.40	228.90	13.27	245.99	2.94	54.51	46.04	0.193
		2	50.01	1197.18	10.50	230.93	11.57	245.68	2.56	54.44	45.22	0.192
		3	50.19	1182.50	10.06	229.76	11.97	245.81	2.65	54.47	45.76	0.194
Average											*45.49*	*0.193*
# 7	76.0	1	50.03	1227.00	7.54	214.15	9.24	246.11	2.04	54.25	44.36	0.176
		2	50.03	1200.29	7.02	220.01	9.61	245.96	2.12	54.22	45.30	0.185
		3	50.22	1197.29	7.71	222.37	9.58	246.52	2.11	54.34	45.53	0.187
Average											*45.41*	*0.186*
# 8	76.1	1	50.21	1191.33	9.07	248.04	8.94	245.80	1.97	54.11	45.70	0.209
		2	50.07	1168.15	4.85	242.04	10.58	246.00	2.33	54.16	46.35	0.212

		3	50.01	1166.47	4.90	241.36	11.13	246.28	2.45	54.22	46.37	0.212
Average											*46.36*	*0.212*
# 9	75.7	1	50.17	1283.35	12.51	298.70	10.05	246.06	2.23	54.67	42.52	0.232
		2	50.03	1229.07	10.06	279.66	9.61	245.28	2.14	54.50	44.41	0.229
		3	50.08	1229.55	8.68	280.46	9.55	245.87	2.12	54.63	44.52	0.230
Average											*44.46*	*0.230*
# 10	76.1	1	50.12	1023.38	8.45	248.57	11.02	245.67	2.42	54.01	53.01	0.247
		2	50.02	991.14	10.50	253.66	11.59	245.97	2.55	54.08	54.75	0.258
		3	50.22	989.37	10.59	254.36	11.59	246.27	2.55	54.14	54.94	0.260
Average											*54.85*	*0.259*
Overall Average											**45.89**	**0.213**

Batch 2: Compression Test

A load-controlled compression-testing machine was used to test the cylinders under compression at a loading rate of 1 MPa/s in accordance with ASTM C1856 (2017). The nominal dimensions of the cylinder are 75 mm × 150 mm. The actual dimensions of each cylinder can be found in Table A-48. This batch of material contains 2% steel fibers by unit volume, and the straight fibers were 20 mm long with a diameter of 0.2 mm. Prior to testing, top and bottom surfaces of each cylinder were grinded. All cylinders were tested on the 27th day.

Table A-41: Batch 2 Compression Test Summary

Cylinder	Test Date	Age (Days)	Diameter × Height (mm)	Strength (MPa)
# 1	7/20/2020	27	76.98 × 144.55	144.57
# 2	7/20/2020	27	76.9 × 147.45	142.81
# 3	7/20/2020	27	75.88 × 145.95	134.00
# 4	7/20/2020	27	77.0× 148.05	136.89
# 5	7/20/2020	27	77.5 × 144.95	135.44
# 6	7/20/2020	27	77.05 × 148.3	136.38
# 7	7/20/2020	27	76.55 × 147.5	143.83
# 8	7/20/2020	27	77.00 × 147.5	132.74
# 9	7/20/2020	27	76.8 × 148.80	136.24
# 10	7/20/2020	27	75.80 × 146.65	132.52
Average				137.54

Batch 2: Flexural Test

Prisms subjected to four-point loading were tested by using the universal testing machine at a stepwise loading rate. A loading rate of 0.15 mm/min was applied to the prisms before reaching 70% post-peak load. The loading rate was increased by 0.05 mm/min for the post-peak softening branch after the load dropped below 70% of the peak load. In addition, all the prisms were tested up until the post-peak residual strength had degraded to 20% of the peak load.

This batch of material contained 2% steel fibers by unit volume, and the straight fibers were 20 mm long with a diameter of 0.2 mm. The nominal dimensions of the prisms were 101.6 mm × 101.6 mm × 356.6 mm. The shear span from each side and the distance between loading rollers were 100 mm, and the distance between support rollers was 300 mm. As depicted in Figure A-87, to measure the net vertical deflection at midspan, a linear variable differential transducer (LVDT) was placed at midspan and mounted at the mid-height of the prism on the specimen chord using a fabricated instrumentation jig. Digital Image Correlation (DIC) was used to record the field of strains on one side of the deforming specimens during the tests. The actual dimensions and flexural strength of each prism can be found in Table A-49, where the nominal flexural strength was calculated with Equation 1. In this Equation, P_{max} is the experimental peak load, L is the total span between supports, and b and h are the cross-sectional width and depth near the failure plane measured after each test.

$$\sigma_f = P_{max}L/bh^2 \qquad (1)$$

Figure A-109. Experimental test setup of four-point bending test

Table A-42. Flexural strength results

Prism	**Date of Testing**	**b (mm)**	**h (mm)**	**L (mm)**	**Pmax (kN)**	**σf (MPa)**
# 1	7/21/2020	99.8	101.4	300	105.77	30.92
# 2	7/21/2020	101.2	99.9	300	90.42	26.86
# 3	7/21/2020	102.2	100.9	300	95.52	27.54
# 4	7/22/2020	99.7	102.4	300	116.72	33.49
# 5	7/22/2020	103.5	100.2	300	107.85	31.14
# 6	7/22/2020	103.5	100.5	300	102.26	29.35
# 7	7/22/2020	105.6	100	300	103.57	29.42
# 8	7/22/2020	101.5	100.1	300	119.95	35.38
# 9	7/22/2020	102.5	99.6	300	95.13	28.07
# 10	7/22/2020	101.5	100.6	300	95.49	27.89
Average Flexural Strength (MPa)						**28.58**

The resistance curves of each prism are presented in Figure A-88. These were used to perform the inverse analysis procedures prescribed in Annex 8.1 of CSA-S6 (2018). As shown in Table A-50, the inverse analysis essentially relies on four characteristic points of the resistance curve, where point (P_o, δ_o) determines the linearity limit and initial slope (s_o) of the resistance curve. The four characteristic points on the resistance curve are defined as follows: Points (P_1, δ_1) and (P_2, δ_2) lie on the secant lines drawn from

the origin with a slope s_{75} and s_{40} equal to 75% and 40% of the initial slope, s_o, respectively. Point (P_3, δ_3) corresponds to 97% of peak load (P_{max}), whereas (P_4, δ_4) is in the post-peak range at 80% of P_3.

The tensile properties obtained from the inverse analysis can be found in Table A-51. In Table A-51, f_{cr} represents the cracking strength corresponding to the onset of crack formation, f_{Fu} represents the ultimate tensile strength corresponding to crack localization, ε_{cr} and ε_{tu} are the strains corresponding to f_{cr} and f_{Fu} respectively, and w_o represents the crack width after crack localization.

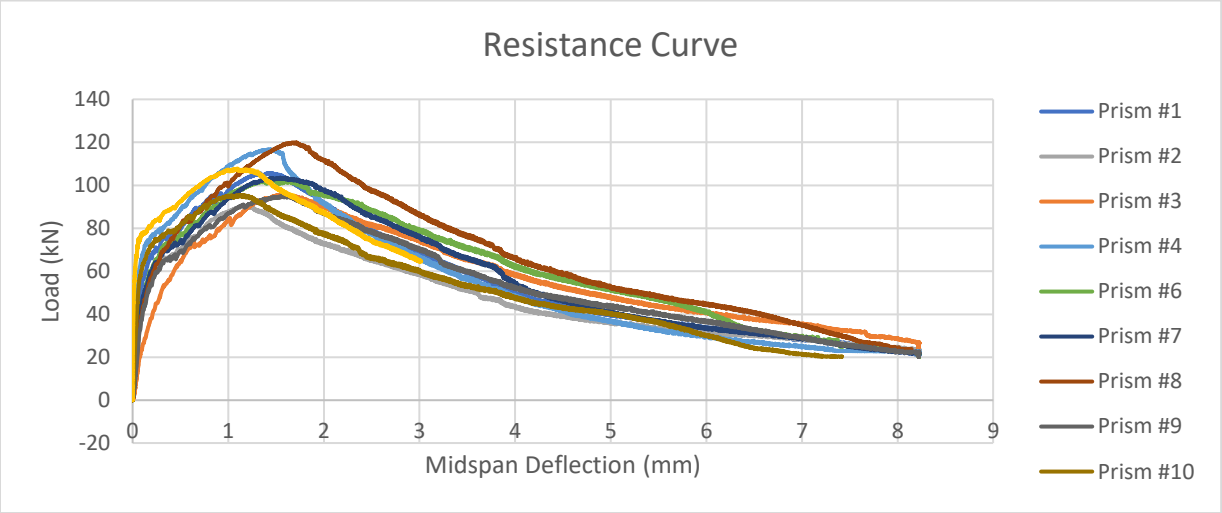

Figure A-110. Resistance curves of four-point bending tests

Table A-43. Characteristic points utilized for inverse analysis

Prism	E_{co} (GPa)	S_o (kN/mm)	P_o (kN)	δ_o (mm)	P_1 (kN)	δ_1 (mm)	P_2 (kN)	δ_2 (mm)	P_3 (kN)	δ_3 (mm)	P_4 (kN)	δ_4 (mm)	P_{max} (kN)	δ_{max} (mm)
# 1	52.14	724.156	7.06	0.0097	53.54	0.0987	70.31	0.2383	102.60	1.1635	82.04	2.3582	105.77	1.4385
# 2	75.13	1043.48	5.38	0.0051	20.81	0.0272	57.13	0.1377	87.61	0.8942	70.08	1.8838	90.42	1.1254
# 3	41.29	573.520	47.90	0.0835	55.65	0.1302	73.11	0.3114	92.65	0.9648	74.18	2.4584	95.52	1.2235
# 4	47.00	652.862	46.04	0.0705	72.67	0.1476	78.44	0.3046	112.62	1.1455	90.09	2.1145	116.72	1.4447
# 5	60.80	844.478	20.67	0.0243	51.91	0.0823	77.33	0.225	104.62	0.9024	83.69	2.2144	107.85	1.1368
# 6	47.466	659.254	43.09	0.0653	60.15	0.1365	72.64	0.2725	99.18	1.1104	79.33	2.6879	102.26	1.3829
# 7	52.52	729.450	37.90	0.0519	52.38	0.0998	69.73	0.2579	100.53	0.9996	80.46	2.1507	103.57	1.3385
# 8	51.88	720.572	41.48	0.0575	55.17	0.1021	78.59	0.2727	116.35	1.2256	92.96	2.3792	119.95	1.1412
# 9	49.59	688.850	43.29	0.0628	51.02	0.1011	66.03	0.2608	92.25	1.1667	73.01	2.544	95.13	1.4586

# 10	45.61	633.490	40.47	0.0639	53.72	0.1141	71.83	0.2802	92.59	0.9322	74.07	2.3849	95.49	1.1989

Table A-44: Batch 2 FPBT- Inverse analysis tensile properties

Prism	**f_{crm}**	**ε_{cr}**	**f_{Fu}/f_{crm}**	**ε_{tu}**	**w_o**
	(MPa)	**(mm/mm)**		**(mm/mm)**	**(mm)**
# 1	10.05	0.0002031	1.25	0.0142426	3.18
# 2	9.52	0.000181	1.09	0.0100935	2.89
# 3	11.61	0.0004138	1.00	0.0094187	4.74
# 4	13.44	0.0004443	1.03	0.0178788	4.10
# 5	9.63	0.0001808	1.37	0.010298	3.54
# 6	11.48	0.0003125	1.05	0.0127748	5.51
# 7	10.70	0.0002337	1.18	0.0107543	3.17
# 8	10.04	0.0002141	1.48	0.0149142	2.89
# 9	9.48	0.0002243	1.18	0.0137981	3.96
# 10	11.50	0.000356	1.02	0.009466	4.82
Average	**10.74**	**0.000276**	**1.16**	**0.0123639**	**3.88**

Batch 2: Poisson's Ratio and Static Modulus of Elasticity

Ten 75 mm × 150 mm cylinders were subjected to compressive loading at the age of 27 days to determine the static modulus of elasticity and Poisson's ratio. This batch of material contains 2% steel fibers by unit volume, and the straight fibers were 20 mm long with a diameter of 0.2 mm. Prior to testing, both top and bottom surfaces of the cylinder were grinded smooth. Four foil strain gauges were installed along the two diametrically opposite lines near the mid-height of the cylinder: two strain gauges were placed vertically to measure longitudinal strains, and the other two strain gauges were placed horizontally to measure transverse strains. Each cylinder was loaded up to around 246 kN which corresponds to 40% of the compressive strength determined by testing another three 75 mm × 150 mm cylinders from the same batch at the age of 27 days. A loading rate of 0.0023 mm/s was employed, and each cylinder was tested consecutively three times.

Figure A-89 illustrates the response curve of a test, where the horizontal axis represents the applied load values, and the vertical axis represents strain values of the four strain gauges. The average static modulus of elasticity (E) was **45.87 GPa** and the average Poisson's ratio (ν) was **0.200**. Table A-52 presents the experimental results of each test, where σ_1 and σ_2 are the compressive stresses corresponding to a longitudinal strain of 50 μm/m and 40% of the compressive strength, respectively; ε_1 represents a longitudinal strain of 50 μm/m, and ε_2 is the longitudinal strain corresponding to σ_2; ε_{t1} and ε_{t2} are the transverse strains corresponding to σ_1 and σ_2, respectively; F_1 and F_2 are the compressive loads corresponding to σ_1 and σ_2, respectively; E was calculated with Equation 1, and ν was calculated with Equation 2.

$$\mathrm{E} = \frac{\sigma_2 - \sigma_1}{\varepsilon_2 - \varepsilon_1} \quad (1)$$

$$\nu = \frac{\varepsilon_{t2} - \varepsilon_{t1}}{\varepsilon_2 - \varepsilon_1} \quad (2)$$

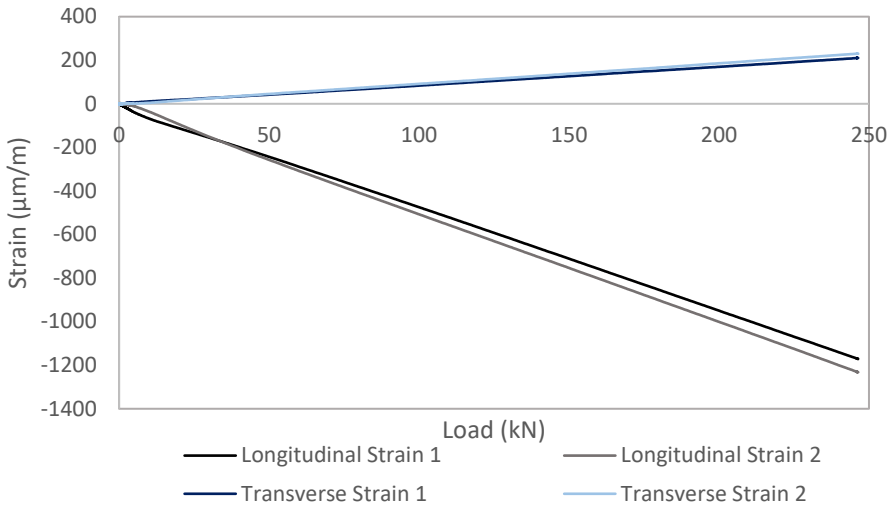

Figure A-111. Response curve of static modulus of elasticity and Poisson's ratio test

Table A-45. Results of static modulus of elasticity and Poisson's ratio

Cylinder	**Diameter (mm)**	**Test**	**ε_1 (µm/m)**	**ε_2 (µm/m)**	**ε_{t1} (µm/m)**	**ε_{t2} (µm/m)**	**F_1 (kN)**	**F_2 (kN)**	**σ_1 (MPa)**	**σ_2 (MPa)**	**E (GPa)**	**ν**
		1	50.0671	851.039	14.5472	201.903	17.6688	255.264	3.97	57.40	66.6987	0.234
# 1	75.25	2	50.3115	946.692	17.8918	216.472	32.8158	255.135	7.38	57.37	55.7677	0.222
		3	50.079	1070.42	13.0259	229.62	18.4859	255.249	4.16	57.39	52.1753	0.212
Average											*53.9715*	*0.217*
Cylinder	**Diameter (mm)**	**Test**	**ε_1 (µm/m)**	**ε_2 (µm/m)**	**ε_{t1} (µm/m)**	**ε_{t2} (µm/m)**	**F_1 (kN)**	**F_2 (kN)**	**σ_1 (MPa)**	**σ_2 (MPa)**	**E (GPa)**	**ν**
		1	50.1489	1224.53	10.8033	247.243	11.5047	254.996	2.42	53.57	43.5581	0.201
# 2	757.85	2	50.1414	1296.98	6.03462	229.105	10.5056	255.028	2.21	53.58	41.2002	0.179
		3	50.0316	1326.12	13.4267	255.699	12.5221	255.06	2.63	53.58	39.9294	0.190
Average											*41.5626*	*0.190*
Cylinder	**Diameter (mm)**	**Test**	**ε_1 (µm/m)**	**ε_2 (µm/m)**	**ε_{t1} (µm/m)**	**ε_{t2} (µm/m)**	**F_1 (kN)**	**F_2 (kN)**	**σ_1 (MPa)**	**σ_2 (MPa)**	**E (GPa)**	**ν**

		1	50.15 75	1477. 11	7.792 48	285.5 34	7.216 69	255.2 1	1.60	56.4 8	38.461 8	0.195
# 3	75.85	2	50.24 69	1291. 75	9.033 63	250.9 3	9.338 43	255.2 01	2.07	56.4 8	43.827 1	0.195
		3	50.01 76	1581. 53	6.902 25	293.1 67	7.181 06	255.1 85	1.59	56.4 7	35.837 4	0.187
Average											*39.375 4*	*0.1 92*

Cylinder	**Diameter (mm)**	**Test**	**ε_1 (μm/m)**	**ε_2 (μm/m)**	**ε_{t1} (μm/m)**	**ε_{t2} (μm/m)**	**F_1 (kN)**	**F_2 (kN)**	**σ_1 (MPa)**	**σ_2 (MPa)**	**E (GPa)**	**ν**
		1	50.29 53	1286. 95	3.399 45	139.9 98	8.951 5	255.0 5	1.98	56.4 4	44.041 3	0.110
# 4	75.85	2	50.01 76	1325. 83	1.171 19	171.4 63	8.883 19	255.1 39	1.97	56.4 6	42.716 7	0.133
		3	50.01 98	1249. 58	5.070 12	37.88 7	10.23 02	254.9 96	2.26	56.4 3	45.157 4	0.027
Average											*43.971 8*	*0.0 90*

Cylinder	**Diameter (mm)**	**Test**	**ε_1 (μm/m)**	**ε_2 (μm/m)**	**ε_{t1} (μm/m)**	**ε_{t2} (μm/m)**	**F_1 (kN)**	**F_2 (kN)**	**σ_1 (MPa)**	**σ_2 (MPa)**	**E (GPa)**	**ν**
		1	50.04 24	1018. 75	22.40 75	314.7 37	15.86 53	251.1 08	3.53	55.9 4	54.099 1	0.302
# 5	75.6	2	50.30 83	678.5 82	132.2 02	347.6 52	103.8 44	252.3 87	23.1 3	56.2 3	52.670 8	0.343
		3	49.35 45	863.1 47	37.84 93	320.1 58	26.99 28	251.5 96	6.01	56.0 5	61.485	0.347
Average											*56.085*	*0.3 31*

Cylinder	**Diameter (mm)**	**Test**	**ε_1 (μm/m)**	**ε_2 (μm/m)**	**ε_{t1} (μm/m)**	**ε_{t2} (μm/m)**	**F_1 (kN)**	**F_2 (kN)**	**σ_1 (MPa)**	**σ_2 (MPa)**	**E (GPa)**	**ν**
		1	50.07 04	1110. 54	32.99 02	322.2 87	22.28 52	254.8 85	4.75	54.3 5	46.767 3	0.273
# 6	75.275	2	50.01 55	1227. 02	21.56 04	302.7 21	14.42 02	254.7 3	3.07	54.3 1	43.533 9	0.239
		3	50.01 65	1235. 32	23.62 93	298.4 99	16.01 72	255.0 4	3.42	54.3 8	42.997 3	0.232
Average											*44.432 9*	*0.2 48*

Cylinder	**Diameter (mm)**	**Test**	**ε_1 (μm/m)**	**ε_2 (μm/m)**	**ε_{t1} (μm/m)**	**ε_{t2} (μm/m)**	**F_1 (kN)**	**F_2 (kN)**	**σ_1 (MPa)**	**σ_2 (MPa)**	**E (GPa)**	**ν**

		1	50.1048	1240.8	2.14002	158.51	11.1339	255.116	2.46	56.46	45.348	0.131
# 7	75.85	2	50.0962	1329.08	12.6581	68.0041	16.0583	254.579	3.55	56.34	41.2726	0.143
		3	50.0047	1267.39	3.42206	200.261	8.78137	255.062	1.94	56.45	44.7715	0.162
Average											*43.7974*	*0.147*
Cylinder	**Diameter (mm)**	**Test**	**ε_1 (μm/m)**	**ε_2 (μm/m)**	**ε_{t1} (μm/m)**	**ε_{t2} (μm/m)**	**F_1 (kN)**	**F_2 (kN)**	**σ_1 (MPa)**	**σ_2 (MPa)**	**E (GPa)**	**ν**
		1	50.079	1070.42	13.0259	229.62	18.4859	255.249	4.16	57.39	52.1753	0.212
# 8	76.45	2	50.08	819.132	26.8565	199.671	8.50433	251.949	1.85	54.82	68.8702	0.225
		3	50.2469	1291.75	9.03363	250.93	9.33843	255.201	2.07	56.48	43.8271	0.195
Average											*54.9575*	*0.211*
Cylinder	**Diameter (mm)**	**Test**	**ε_1 (μm/m)**	**ε_2 (μm/m)**	**ε_{t1} (μm/m)**	**ε_{t2} (μm/m)**	**F_1 (kN)**	**F_2 (kN)**	**σ_1 (MPa)**	**σ_2 (MPa)**	**E (GPa)**	**ν**
		1	50.1016	1502.8	5.31985	272.277	9.39273	255.073	2.08	56.49	37.4526	0.184
#9	75.825	2	50.1436	1568.18	5.85162	279.71	7.83612	255.142	1.74	56.50	36.0777	0.180
		3	50.0973	1540.31	5.52546	278.241	8.41566	255.131	1.86	56.50	36.6634	0.183
Average											*36.7312*	*0.182*
Cylinder	**Diameter (mm)**	**Test**	**ε_1 (μm/m)**	**ε_2 (μm/m)**	**ε_{t1} (μm/m)**	**ε_{t2} (μm/m)**	**F_1 (kN)**	**F_2 (kN)**	**σ_1 (MPa)**	**σ_2 (MPa)**	**E (GPa)**	**ν**
		1	50.0187	1286.1	1.2713	229.029	6.77843	241.111	1.50	53.50	42.0658	0.184
# 10	76.09	2	50.2587	1207.99	4.58571	235.783	6.98971	240.575	1.55	53.38	44.7694	0.200
		3	50.1555	1219.34	3.15823	235.575	5.63462	240.658	1.25	53.40	44.6038	0.199
Average											*43.813*	*0.194*
Overall Average											45.86983	0.200

Batch 3: Compression Test

A load-controlled compression-testing machine was used to test the cylinders under compression at a loading rate of 1 MPa/s in accordance with ASTM C1856 (2017). The nominal dimensions of the cylinder are 75 mm × 150 mm. The actual dimensions of each cylinder can be found in Table A-53. This batch of material contains 2% steel fibers by unit volume, and the straight fibers were 20 mm long with a diameter of 0.2 mm. Prior to testing, top and bottom surfaces of each cylinder were grinded. All cylinders were tested on the 28th day.

Table A-46: Batch 3 Compression Results

Cylinder	Test Date	Age (Days)	Diameter × Height (mm)	Strength (MPa)
# 1	9/15/2020	28	76.45 × 149.05	146.40
# 2	9/15/2021	28	76.76 × 149.30	141.22
# 3	9/15/2022	28	76.53 × 150.40	134.70
# 4	9/15/2023	28	76.35× 150.60	136.60
# 5	9/15/2024	28	76.40 × 149.30	138.89
# 6	9/15/2025	28	76.30 × 150.15	137.98
# 7	9/15/2026	28	76.28 × 149.15	138.79
# 8	9/15/2027	28	76.55 × 149.9	130.60
# 9	9/15/2028	28	76.35 × 150.06	136.01
# 10	9/15/2029	28	76.45 × 148.95	141.35
Average				138.25

Batch 3: Flexural Test

Prisms subjected to four-point loading were tested by using the universal testing machine at a stepwise loading rate. A loading rate of 0.15 mm/min was applied to the prisms before reaching 70% post-peak load. The loading rate was increased by 0.05 mm/min for the post-peak softening branch after the load dropped below 70% of the peak load. In addition, all the prisms were tested up until the post-peak residual strength had degraded to 20% of the peak load.

This batch of material contained 2% steel fibers by unit volume, and the straight fibers were 20 mm long with a diameter of 0.2 mm. The nominal dimensions of the prisms were 101.6 mm × 101.6 mm × 356.6 mm. The shear span from each side and the distance between loading rollers were 100 mm, and the distance between support rollers was 300 mm. As depicted in Figure A-90, to measure the net vertical deflection at midspan, a linear variable differential transducer (LVDT) was placed at midspan and mounted at the mid-height of the prism on the specimen chord using a fabricated instrumentation jig. Digital Image Correlation (DIC) was used to record the field of strains on one side of the deforming specimens during the tests. The actual dimensions and flexural strength of each prism can be found in Table A-54, where the nominal flexural strength was calculated with Equation 1. In this Equation, P_{max} is the experimental peak load, L is the total span between supports, and b and h are the cross-sectional width and depth near the failure plane measured after each test.

$$\sigma_f = P_{max}L/bh^2 \qquad (1)$$

Figure A-112. Experimental test setup of four-point bending test

Table A-47. Flexural strength results

Prism	Date of Testing	b (mm)	h (mm)	L (mm)	Pmax (kN)	σf (MPa)
# 1	9/18/2020	102.5	101.8	300	132.45	37.41
# 2	9/16/2020	101.5	100.1	300	86.299	25.46
# 3	9/16/2020	102.1	100.1	300	81.02	23.76
# 4	9/16/2020	100.8	99.98	300	85.87	25.57
# 5	9/17/2020	101.2	104.6	300	108.32	29.35
# 6	9/17/2020	102.1	100.3	300	102.6	29.97
# 7	9/17/2020	100.4	99.5	300	98.01	29.58
# 8	9/17/2020	100.96	100.7	300	79.58	23.32
# 9	9/17/2020	100.5	100.3	300	119.56	35.48
# 10	9/17/2020	100.5	100	300	103.61	30.93
Average Flexural Strength (MPa)						**23.57**

The resistance curves of each prism are presented in Figure A-91. These were used to perform the inverse analysis procedures prescribed in Annex 8.1 of CSA-S6 (2018). As shown in Table A-55, the inverse analysis essentially relies on four characteristic points of the resistance curve, where point (P_o, δ_o) determines the linearity limit and initial slope (s_o) of the resistance curve. The four characteristic points on the resistance curve are defined as follows: Points (P_1, δ_1) and (P_2, δ_2) lie on the secant lines drawn from

the origin with a slope s_{75} and s_{40} equal to 75% and 40% of the initial slope, s_o, respectively. Point (P_3, δ_3) corresponds to 97% of peak load (P_{max}), whereas (P_4, δ_4) is in the post-peak range at 80% of P_3.

The tensile properties obtained from the inverse analysis can be found in Table A-56. In Table A-56, f_{cr} represents the cracking strength corresponding to the onset of crack formation, f_{Fu} represents the ultimate tensile strength corresponding to crack localization, ε_{cr} and ε_{tu} are the strains corresponding to f_{cr} and f_{Fu} respectively, and w_o represents the crack width after crack localization.

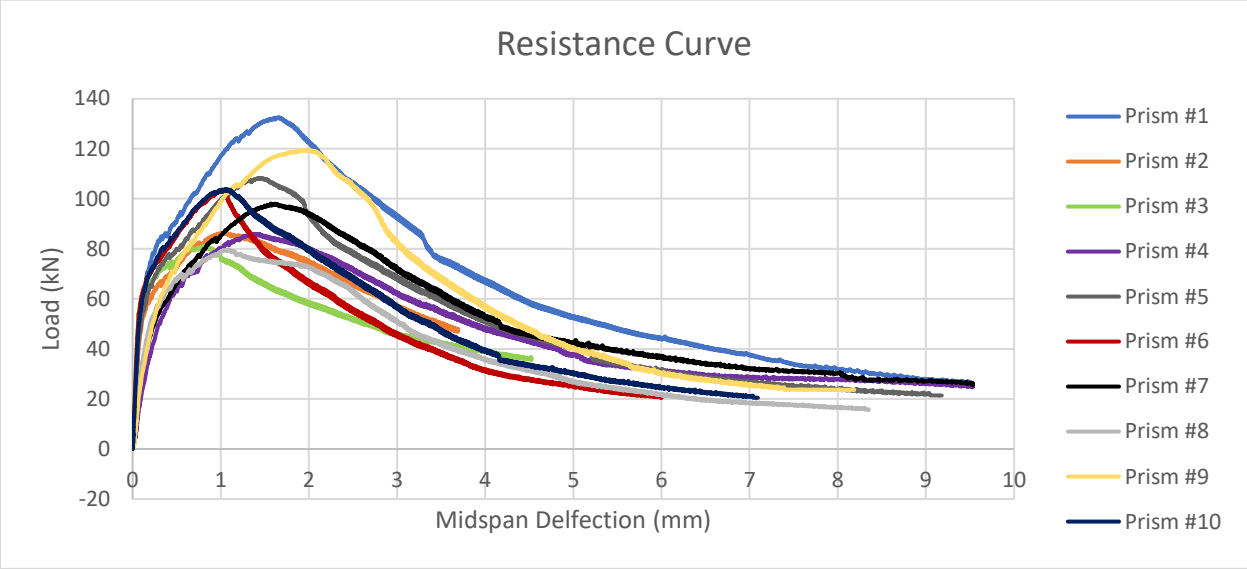

Figure A-113. Resistance curves of four-point bending tests

Table A-48. Characteristic points utilized for inverse analysis

Prism	E_{co} (GPa)	S_o (kN/mm)	P_o (kN)	δ_o (mm)	P_1 (kN)	δ_1 (mm)	P_2 (kN)	δ_2 (mm)	P_3 (kN)	δ_3 (mm)	P_4 (kN)	δ_4 (mm)	P_{max} (kN)
# 1	50.23	697.6909	29.79	0.0427	60.8	0.1178	82.65	0.2853	128.36	1.8504	102.68	2.6481	132.45
# 2	49.718	690.5225	30	0.0434	45.84	0.086	57.97	0.1906	83.75	1.5193	66.98	2.487	86.299
# 3	39.436	547.7197	40.95	0.0748	50.15	0.1229	62.26	0.2926	78.57	0.8243	62.83	2.2153	81.02
# 4	51.45	714.5382	35.75	0.05	44.71	0.0834	64.45	0.2242	83.28	0.8288	66.62	2.3735	85.87
# 5	39.8	552.8621	38.9	0.0703	54.41	0.1206	74.49	0.2758	105.07	1.173	84.06	2.2465	108.32

# 6	45.37	630.1177	10.16	0.0161	49.37	0.1048	67.62	0.2794	99.54	0.9979	79.63	1.7944	102.6
# 7	35.97	499.565	40.09	0.0802	52.83	0.1384	70.67	0.3519	95.08	1.112	76.07	2.6132	98.01
# 8	46.5	645.7008	32.29	0.05	47.57	0.0954	59.77	0.2255	77.2	0.8275	61.76	2.3287	79.58
# 9	50.88	706.7843	37.82	0.0535	56.2	0.1074	72.14	0.2529	115.97	1.2157	92.76	2.1611	119.56
# 10	44.18	613.7157	39.78	0.0648	53.93	0.1162	71.9	0.2937	100.55	0.9922	80.43	2.4149	103.61

Table A-49. Linearized tensile stress-strain-crack width properties

Prism	fcrm (MPa)	εcr (mm/mm)	fFu/fcrm	εtu (mm/mm)	wo (mm)
# 1	10.56	0.000210	1.47	0.02303	1.09
# 2	8.07	0.000162	1.15	0.02023	2.38
# 3	8.86	0.000225	1.07	0.00915	4.37
# 4	7.68	0.000149	1.33	0.00977	4.19
# 5	9.43	0.000236	1.41	0.01514	2.82
# 6	9.34	0.000228	1.38	0.12334	2.39
# 7	9.20	0.000256	1.31	0.01303	4.24
# 8	8.38	0.000180	1.08	0.01007	4.84
# 9	9.87	0.000193	1.52	0.01474	2.13
# 10	9.40	0.000213	1.37	0.01165	4.06
Average	8.70	0.000200	1.24	0.02818	3.78

Batch 3: Poisson's Ratio and Static Modulus of Elasticity

Ten 75 mm × 150 mm cylinders were subjected to compressive loading at the age of 27 days to determine the static modulus of elasticity and Poisson's ratio. This batch of material contains 2% steel fibers by unit volume, and the straight fibers were 20 mm long with a diameter of 0.2 mm. Prior to testing, both top and bottom surfaces of the cylinder were grinded smooth. Four foil strain gauges were installed along the two diametrically opposite lines near the mid-height of the cylinder: two strain gauges were placed vertically to measure longitudinal strains, and the other two strain gauges were placed horizontally to measure transverse strains. Each cylinder was loaded up to around 246 kN which corresponds to 40% of the compressive strength determined by testing another three 75 mm × 150 mm cylinders from the same batch at the age of 27 days. A loading rate of 0.0023 mm/s was employed, and each cylinder was tested consecutively three times.

Figure A-92 illustrates the response curve of a test, where the horizontal axis represents the applied load values, and the vertical axis represents strain values of the four strain gauges. The average static modulus of elasticity (E) was **48.03 GPa** and the average Poisson's ratio (ν) was **0.210**. Table A-57 presents the experimental results of each test, where σ_1 and σ_2 are the compressive stresses corresponding to a longitudinal strain of 50 μm/m and 40% of the compressive strength, respectively; ε_1 represents a longitudinal strain of 50 μm/m, and ε_2 is the longitudinal strain corresponding to σ_2; ε_{t1} and ε_{t2} are the transverse strains corresponding to σ_1 and σ_2, respectively; F_1 and F_2 are the compressive loads corresponding to σ_1 and σ_2, respectively; E was calculated with Equation 1, and ν was calculated with Equation 2.

$$\mathrm{E} = \frac{\sigma_2 - \sigma_1}{\varepsilon_2 - \varepsilon_1} \quad (1)$$

$$\nu = \frac{\varepsilon_{t2} - \varepsilon_{t1}}{\varepsilon_2 - \varepsilon_1} \quad (2)$$

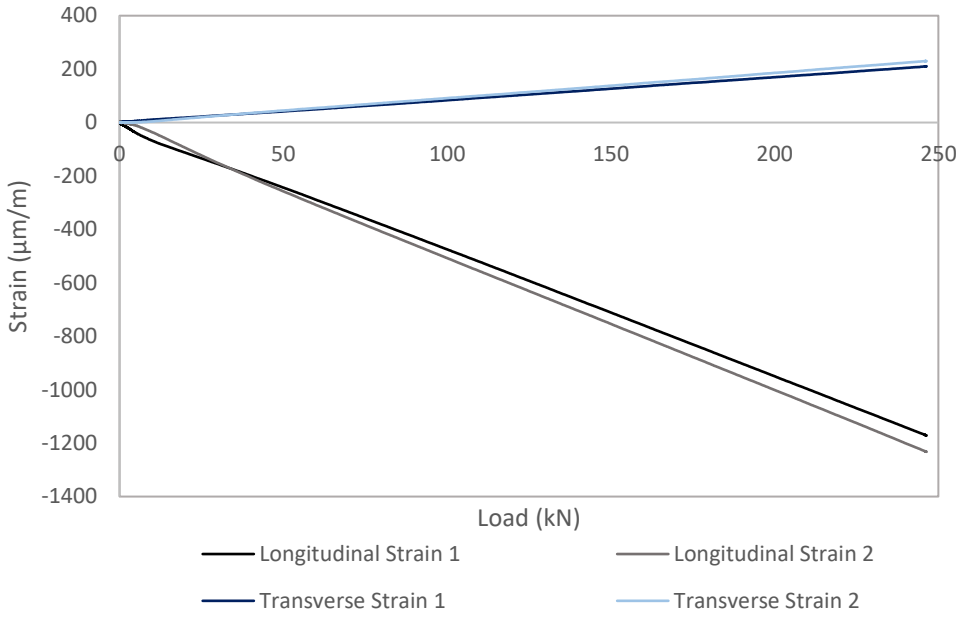

Figure A-114. Response curve of static modulus of elasticity and Poisson's ratio test

Table A-50. Results of static modulus of elasticity and Poisson's ratio

Cylinder	**Diameter (mm)**	**Test**	**ε_1 (µm/m)**	**ε_2 (µm/m)**	**ε_{t1} (µm/m)**	**ε_{t2} (µm/m)**	**F_1 (kN)**	**F_2 (kN)**	**σ_1 (MPa)**	**σ_2 (MPa)**	**E (GPa)**	**v**
# 1	76.375	1	50.0112	1039.41	16.7852	340.859	12.6931	255.21	2.77	55.71	53.5032	0.328
		2	50.1941	1130.93	20.6099	340.854	14.0685	255.192	3.07	55.70	48.7	0.296
		3	50.1662	1119.47	25.7693	339.109	18.2352	255.243	3.98	55.71	48.3806	0.293
Average											*50.1946*	*0.306*
Cylinder	**Diameter (mm)**	**Test**	**ε_1 (µm/m)**	**ε_2 (µm/m)**	**ε_{t1} (µm/m)**	**ε_{t2} (µm/m)**	**F_1 (kN)**	**F_2 (kN)**	**σ_1 (MPa)**	**σ_2 (MPa)**	**E (GPa)**	**v**
# 2	76.375	1	50.1522	1221.63	11.5644	301.376	14.01	255.244	3.06	55.71	44.9481	0.247
		2	50.3298	1216.48	12.1263	312.159	16.8958	255.218	3.69	55.71	44.6083	0.257
		3	50.093	1215.94	11.0994	311.063	17.3319	255.089	3.78	55.68	44.5142	0.257
Average											*44.6902*	*0.254*
Cylinder	**Diameter**	**Test**	**ε_1**	**ε_2**	**ε_{t1}**	**ε_{t2}**	**F_1**	**F_2**	**σ_1**	**σ_2**	**E**	**v**

	(mm)		(μm/m)	(μm/m)	(μm/m)	(μm/m)	(kN)	(kN)	(MPa)	(MPa)	(GPa)	
# 3	76.45	1	50.0112	1263.03	8.48895	239.029	8.65579	255.205	1.89	55.60	44.2784	0.190
		2	50.1026	1402.5	1.61361	218.788	5.13102	255.271	1.12	55.50	40.2146	0.161
		3	50.2092	1212.19	10.3771	265.748	12.3952	255.069	2.71	55.68	45.5859	0.220
Average											*43.3596*	*0.190*
Cylinder	**Diameter (mm)**	**Test**	**ε_1 (μm/m)**	**ε_2 (μm/m)**	**ε_{t1} (μm/m)**	**ε_{t2} (μm/m)**	**F_1 (kN)**	**F_2 (kN)**	**σ_1 (MPa)**	**σ_2 (MPa)**	**E (GPa)**	**ν**
# 4	76.275	1										
		2	50.347	882.798	19.0921	248.399	14.3337	255.239	3.14	55.86	63.3336	0.275
		3	50.1188	677.079	14.8164	215.725	16.9836	255.209	3.72	55.85	83.1561	0.320
Average											*73.2448*	*0.298*
Cylinder	**Diameter (mm)**	**Test**	**ε_1 (μm/m)**	**ε_2 (μm/m)**	**ε_{t1} (μm/m)**	**ε_{t2} (μm/m)**	**F_1 (kN)**	**F_2 (kN)**	**σ_1 (MPa)**	**σ_2 (MPa)**	**E (GPa)**	**ν**
# 5	76.525	1	50.1468	1139.2	31.5661	218.71	25.0187	255.204	5.44	55.49	45.9548	0.172
		2	50.3126	1437.54	2.22719	210.996	3.88624	255.198	0.84	55.49	39.3884	0.150
		3	50.1026	1402.5	1.61361	218.788	5.13102	255.271	1.12	55.50	40.2146	0.161
Average											*41.8526*	*0.161*
Cylinder	**Diameter (mm)**	**Test**	**ε_1 (μm/m)**	**ε_2 (μm/m)**	**ε_{t1} (μm/m)**	**ε_{t2} (μm/m)**	**F_1 (kN)**	**F_2 (kN)**	**σ_1 (MPa)**	**σ_2 (MPa)**	**E (GPa)**	**ν**
# 6	76.325	1	50.065	1564.6	2.8537	194.034	6.19847	255.114	1.35	55.76	35.921	0.126
		2	50.2071	1032.15	12.0348	222.525	10.5382	255.242	2.30	55.79	54.4668	0.214
		3	50.0973	1207.32	17.9736	230.394	15.5662	255.072	3.40	55.75	45.2352	0.184
Average											*45.2077*	*0.175*
Cylinder	**Diameter (mm)**	**Test**	**ε_1 (μm/m)**	**ε_2 (μm/m)**	**ε_{t1} (μm/m)**	**ε_{t2} (μm/m)**	**F_1 (kN)**	**F_2 (kN)**	**σ_1 (MPa)**	**σ_2 (MPa)**	**E (GPa)**	**ν**
		1	50.0564	1317.4	11.6645	218.359	7.83484	255.072	1.71	55.57	42.4986	0.163

# 7	76.45	2	50.206	1281.45	12.6268	218.955	9.21836	255.179	2.01	55.59	43.5189	0.168
		3	50.1759	1278.39	13.4288	219.695	9.21497	255.059	2.01	55.56	43.6055	0.168
Average											*43.2077*	*0.166*
Cylinder	**Diameter (mm)**	**Test**	**ε_1 (μm/m)**	**ε_2 (μm/m)**	**ε_{t1} (μm/m)**	**ε_{t2} (μm/m)**	**F_1 (kN)**	**F_2 (kN)**	**σ_1 (MPa)**	**σ_2 (MPa)**	**E (GPa)**	**ν**
# 8	76.45	1	50.2437	1563.31	16.0737	260.339	10.8849	255.173	2.37	55.59	35.1721	0.161
		2	52.0758	1962.47	10.9691	255.898	7.48186	255.193	1.63	55.59	28.2474	0.128
		3	50.0682	3570.63	21.7671	255.288	15.2234	255.192	3.32	55.59	14.849	0.066
Average											*26.0895*	*0.119*
Cylinder	**Diameter (mm)**	**Test**	**ε_1 (μm/m)**	**ε_2 (μm/m)**	**ε_{t1} (μm/m)**	**ε_{t2} (μm/m)**	**F_1 (kN)**	**F_2 (kN)**	**σ_1 (MPa)**	**σ_2 (MPa)**	**E (GPa)**	**ν**
#9	76.375	1	50.0887	1224.22	10.3641	264.894	11.1475	255.093	2.43	55.68	45.3508	0.217
		2	50.2092	1212.19	10.3771	265.748	12.3952	255.069	2.71	55.68	45.5859	0.220
		3	50.3029	1211.65	10.9024	266.08	12.5891	255.055	2.75	55.67	45.5717	0.220
Average											*45.5028*	*0.219*
Cylinder	**Diameter (mm)**	**Test**	**ε_1 (μm/m)**	**ε_2 (μm/m)**	**ε_{t1} (μm/m)**	**ε_{t2} (μm/m)**	**F_1 (kN)**	**F_2 (kN)**	**σ_1 (MPa)**	**σ_2 (MPa)**	**E (GPa)**	**ν**
# 10	76.45	1	50.0112	1263.03	8.48895	239.029	8.65579	255.205	1.89	55.60	44.2784	0.190
		2	50.3276	1229.48	8.31564	241.026	9.48013	255.257	2.07	55.61	45.4075	0.197
		3	50.3287	1226.14	8.04653	240.537	9.63796	255.247	2.10	55.61	45.5053	0.198
Average											*45.0637*	*0.195*
Overall Average											48.0359	0.210

Batch 4: Compression Test

A load-controlled compression-testing machine was used to test the cylinders under compression at a loading rate of 1 MPa/s in accordance with ASTM C1856 (2017). The nominal dimensions of the cylinder are 75 mm × 150 mm. The actual dimensions of each cylinder can be found in Table A-58. This batch of material contains 2% steel fibers by unit volume, and the straight fibers were 20 mm long with a diameter of 0.2 mm. Prior to testing, top and bottom surfaces of each cylinder were grinded. All cylinders were tested on the 28th day.

Table A-51: Batch 4 Compression Test Results

Cylinder	Test Date	Age (Days)	Diameter × Height (mm)	Strength (MPa)
# 1	10/08/2020	28	76.40 × 149.25	138.10
# 2	10/08/2021	28	76.41 × 149.10	131.90
# 3	10/08/2022	28	76.33 × 149.85	136.43
Average				135.48

Batch 5: Compression Results

A load-controlled compression-testing machine was used to test the cylinders under compression at a loading rate of 1 MPa/s in accordance with ASTM C1856 (2017). The nominal dimensions of the cylinder are 75 mm × 150 mm. The actual dimensions of each cylinder can be found in Table A-59. This batch of material contains 2% steel fibers by unit volume, and the straight fibers were 20 mm long with a diameter of 0.2 mm. Prior to testing, top and bottom surfaces of each cylinder were grinded. Among the ten cylinders tested under compression, three were tested at the age of 28 days.

Table A-52: Batch 5 Compression Results

Cylinder	Test Date	Age (Days)	Average Diameter (mm)	Average Height (mm)	Strength (MPa)
1	12/9/2020	28	76.78	143.31	143.30
2	12/9/2020	28	76.55	141.79	137.55
3	12/9/2020	28	79.03	146.92	130.84
				Average	137.23

Batch 5: Compression Test – Freeze Cured

A load-controlled compression-testing machine was used to test the cylinders under compression at a loading rate of 1 MPa/s in accordance with ASTM C1856 (2017). The nominal dimensions of the cylinder are 75 mm × 150 mm. The actual dimensions of each cylinder can be found in Table A-60. This batch of material contains 2% steel fibers by unit volume, and the straight fibers were 20 mm long with a diameter of 0.2 mm. Prior to testing, top and bottom surfaces of each cylinder were grinded. Among the ten cylinders tested under compression, three were tested at the age of 28 days.

This report contains 12 cylinders tested with 4 different curing conditions for 3 cylinders per curing condition. Specimen FC1 were cured by placing the specimens in a freezer after final setting time of 6 hours. FC2 were cured by placing the specimens outside for normal weather exposure, FC3 were cured by placing the specimens in the curing chamber for 24 hours and then transferred to the freezer. Note: a set of control specimens were also tested and are included in the Batch 5- Compression Test report, the control specimens were cured as per standard C1856/C39.

Table A-53: Batch 5 Compression Test for Freeze cured specimens

Compression Test-Freeze Curing				
Specimens	**Average Diameter (mm)**	**Average Length (mm)**	**Compressive Strength (MPa)**	**Average Strength (MPa)**
FC1-1	76.62	147.31	42.26	**40.77**
FC1-2	76.39	147.49	41.37	
FC1-3	76.62	147.85	38.68	
FC2-1	76.36	147.47	103.45	**106.93**
FC2-2	76.62	145.41	108.21	
FC2-3	76.10	145.45	109.15	
FC3-1	76.58	147.56	88.13	**91.84**
FC3-2	76.53	145.92	94.32	
FC3-3	76.71	147.19	93.08	

Batch 6: Compression Test

A load-controlled compression-testing machine was used to test the cylinders under compression at a loading rate of 1 MPa/s in accordance with ASTM C1856 (2017). The nominal dimensions of the cylinder are 75 mm × 150 mm. The actual dimensions of each cylinder can be found in Table A-61. This batch of material contains 2% steel fibers by unit volume, and the straight fibers were 20 mm long with a diameter of 0.2 mm. Prior to testing, top and bottom surfaces of each cylinder were grinded. All cylinders were tested on the 28th day.

Table A-54. Compressive Strength Results

Cylinder	Test Date	Age (Days)	Average Diameter (mm)	Average Height (mm)	Strength (MPa)
1	03/03/2020	28	76.4	145.2	144.28
2	03/03/2020	28	76.47	143.35	155.76
3	03/03/2020	28	79.03	141.95	140.28
4	03/03/2020	28	76.78	143.31	143.30
5	03/03/2020	28	76.55	141.79	137.55
				Average	144.23

Table A-55: Mean, Standard Deviation, Characteristic Value

	Mean	Standard Deviation	Characteristic Value
f_c	144.23	6.23	135.51

Batch 6: Absorption Test

A total of 4 concrete cylinders were used to perform the test. The specimens' nominal dimensions were 75mm × 150mm. This batch of material contains 2% steel fibers by unit volume, and the straight fibers were 20mm long with a diameter of 0.2mm. The specimens were cured for 28 days in a controlled humidity chamber. The CSA A23.2 -11C code for water content, density, absorption, and voids in hardened concrete, grout or mortar was used. A scale with a sensitivity of 0.01g was used to measure the mass at various stages. An oven capable of maintaining a temperature of 110 C was used.

Table A-56: Batch 6 Absorption Test results

Cylinder #	Water Content (%)	Absorption After Immersion (%)	Absorption after Immersion and Boiling (%)	Air-dry Density (kg/m^3)
C1	2.52	1.66	1.35	2605.01
C2	2.52	1.64	1.64	2605.07
C3	2.50	1.73	1.73	2587.77
C4	2.52	1.72	2.00	2589.57
Average	***2.52***	***1.69***	***1.68***	***2596.85***
Cylinder #	**Oven-dried Density (kg/m^3)**	**Density after immersion (kg/m^3)**	**Density after immersion and Boiling (kg/m^3)**	**Void (%)**
C1	2545.56	2587.73	2579.94	3.44
C2	2545.74	2587.61	2587.43	4.17
C3	2530.04	2573.69	2573.85	4.38
C4	2530.50	2574.07	2581.13	5.06
Average	**2537.96**	**2580.78**	**2580.59**	**4.26**

Batch 6: Absorption Test

A Drill press with a rotational speed of 130 rpm was used to perform the abrasion test with a load of 200 N on the rotating cutter configured as specified in ASTM C944. A total of 3 concrete cylinders were used to perform the test. The specimens' nominal dimensions were 100mm × 150mm. The surfaces to be abraded were cut then cleaned of all remaining dust with a dry towel and pressurized air. This batch of material contains 2% steel fibers by unit volume, and the straight fibers were 20 mm long with a diameter of 0.2 mm. The specimens were cured for 28 days. Table A-64 shows the results for the abrasion of three-2 min cycles at a normal load of 200 N on the rotating cutter. Note: The test method of ASTM C944 suggests using 100 rpm, but the equipment available was limited to a speed of 130 rpm as its slowest speed, the time tested per cycle was modified to 1.538 minutes to reflect the same total rotations per cycle.

Table A-57: Batch 6 Abrasion Test Masses

Specimens	Initial Mass (g)	Before 1st Abrasion (g)	After 1st Abrasion (g)	Before 2nd Abrasion (g)	After 2nd Abrasion (g)	Before 3rd Abrasion (g)	After 3rd Abrasion (g)
1	1606.30	1606.30	1603.96	1603.22	1601.82	1600.94	1599.54
2	1460.62	1430.50	1429.04	1426.44	1424.08	1423.84	1421.94
3	1538.28	1538.14	1535.93	1535.22	1533.98	1533.01	1531.27

Table A-58: Batch 6 Abrasion Test Results

Specimens	Mass Loss 1st abrasion (g)	Mass Loss 2nd abrasion (g)	Mass Loss 3rd abrasion (g)	Average Mass Loss (g)	Average of all 3 Specimens (g)
1	2.34	1.4	1.4	1.71	1.78
2	1.46	2.36	1.9	1.91	
3	2.21	1.24	1.74	1.73	

Batch 6: Chloride Ion Penetration Test

Perma2 software and test apparatus was used to perform the chloride ion penetration test. The test program was set to the standard testing procedure of ASTM C1202. The specimens did not include fibers to avoid short circuiting the testing apparatus. The specimens were cured for 56 days for an extended moist curing condition. The specimens were conditioned before the test was begun, the conditioning included of coating the side surface with a concrete sealer, once the coating was set, the specimens were placed in the vacuum desiccator for 3 hours, then distilled water was added into the desiccator for an additional hour, and lastly the vacuum was released, and the specimens were soaked under water for 18 hours. The test was conducted for 6hrs as described in ASTM C1202.

Table A-59. Chloride Ion Penetration Test

Chloride Ion Penetration	**Age (Days)**	**Length (mm)**	**Diameter (mm)**	**Charge Passed (Coulombs)**
Specimen 1	56	50.1	100.12	32
Specimen 2	56	51.4	101.5	37
Specimen 3	56	50.5	99.87	33
Average	56	50.66	100.50	34
Result	Charge <100 Negligible as per Table X1.1 (C1202-12)			

Batch 6: Coefficient of Thermal Expansion Test

A water tank capable of holding water with 4 cyclinders along with one controll specimen was used to perform the test for coefficient of thermal expansion. The cylinders were conditioned by submersion in limewater in a water storage tank at 23 ± 2°C (73 ± 4°F) until two successive weighings of the surface-dried sample at intervals of 24 h show an increase in weight of less than 0.5 percent. A total of 4 concrete cylinders were used to perform the test. The specimens' nominal dimensions were 75mm × 150mm. This batch of material contains 2% steel fibers by unit volume, and the straight fibers were 20 mm long with a diameter of 0.2 mm. The specimens were cured for 38 days. Table A-67 and A-68 shows the results for the CTE of the cylinders. For accuracy of the results and precision to obtain the true CTE values for the material, 4 gauge lines were used per cylinder, as opposed to two diametrically opposing gauge lines. The test performed follows the AASTHO T336 standard. Note: The standard suggests to use 50 degrees and 10 degrees for the change in temperature to measure the CTE values, where as the test performed has been done at 55 degrees and 15 degrees.

Table A-60. CTE Results

Cylinder	C1			C2			C3			C4		
Test #	1	2	3	1	2	3	1	2	3	1	2	3
Xº(C)	54.2	54.2	54.2	54.2	54.2	54.2	54.2	54.2	54.2	54.2	54.2	54.2
A-A (mm)	0.048	0.05	0.04	0.043	-	-	0.035	0.037	0.036	0.038	0.049	0.04
B-B (mm)	0.043	0.046	0.042	0.037	0.041	0.039	0.036	-	-	0.042	0.046	0.043
C-C (mm)	0.036	0.043	0.044	0.035	0.04	0.037	0.038	-	-	0.048	0.057	0.051
D-D (mm)	0.036	0.038	0.035	0.035	0.039	0.036	0.046	0.045	0.045	0.031	0.034	0.034
Y º(C)	15.4	15.4	15.5	15.4	15.4	15.4	15.4	15.4	15.4	15.4	15.4	15.4
A-A (mm)	-0.015	-0.012	-0.013	-0.016	-	-	-0.035	-0.028	-0.027	-0.018	-0.015	-0.016
B-B (mm)	-0.02	-0.018	-0.019	-0.028	-0.028	-0.028	-0.026	-	-	-0.024	-0.018	-0.02
C-C (mm)	-0.024	-0.02	-0.024	-0.029	-0.025	-0.028	-0.03	-	-	-0.018	-0.014	-0.015
D-D (mm)	-0.026	-0.023	-0.026	-0.031	-0.026	-0.026	-0.025	-0.018	-0.022	-0.032	-0.031	-0.031

CTE1	16.237	15.979	13.660	15.206	-	-	18.041	16.753	16.237	14.433	16.495	14.433
CTE2	16.237	16.495	15.722	16.753	17.784	17.268	15.979	-	-	17.010	16.495	16.237
CTE3	15.464	16.237	17.526	16.495	16.753	16.753	17.526	-	-	17.010	18.299	17.010
CTE4	15.979	15.722	15.722	17.010	16.753	15.979	18.299	16.237	17.268	16.237	16.753	16.753
Average	15.979	16.108	15.657	16.366	17.096	16.667	17.461	16.495	16.753	16.173	17.010	16.108
Z º(C)	54.2	54.2	54.1	54.2	54.2	54.2	54.2	54.2	54.2	54.2	54.2	54.2
A-A (mm)	0.05	0.04	0.05	-	-	-	0.037	0.037	0.0377	0.049	0.048	0.048
B-B (mm)	0.046	0.042	0.047	0.041	0.042	0.041	-	-	-	0.046	0.045	0.046
C-C (mm)	0.043	0.044	0.042	0.04	0.044	0.042	-	-	-	0.057	0.055	0.056
D-D (mm)	0.038	0.035	0.037	0.039	0.035	0.035	0.045	0.046	0.045	0.034	0.033	0.033
CTE1	16.753	13.402	16.321	-	-	-	18.557	16.753	16.675	17.268	16.237	16.495
CTE2	17.010	15.464	17.098	17.784	18.041	17.784	-	-	-	18.041	16.237	17.010
CTE3	17.268	16.495	17.098	17.784	17.784	18.041	-	-	-	19.330	17.784	18.299
CTE4	16.495	14.948	16.321	18.041	15.722	15.722	18.041	16.495	17.268	17.010	16.495	16.495
Average	16.881	15.077	16.710	17.869	17.182	17.182	18.299	16.624	16.972	17.912	16.688	17.075

Table A-61: CTE Average Values

Cylinder	C1			C2			C3			C4		
Test #	*1*	*2*	*3*	*1*	*2*	*3*	*1*	*2*	*3*	*1*	*2*	*3*
CTE 1	16.495	14.691	16.021	-	-	-	18.299	16.753	16.456	15.851	16.366	15.464
CTE 2	16.624	15.979	16.410	17.268	17.912	17.526	-	-	-	17.526	16.366	16.624
CTE 3	16.366	16.366	17.312	17.139	17.268	17.397	-	-	-	18.170	18.041	17.655
CTE 4	16.237	15.335	16.021	17.526	16.237	15.851	18.170	16.366	17.268	16.624	16.624	16.624
Average CTE	**16.155**			**17.125**			**17.219**			**16.828**		

A-A, B-B, C-C, D-D refers to the gauge line

gauge lines A-A, C-C are diametrically opposing, and B-B and D-D are diametrically opposing

Note: the dash line refers to the gauges destroyed during the test, these gauges had fallen off due to the high temperature in the tank during testing.

The following appendix contains the test results of the same specimens as tested in the above. These were tested in the temperature change of 21.2 ºC – 3.2 ºC. The specimens were first tested in this temperature change to obtain the C.T.E values as shown in table A-68.1 and A-68.2. This test was performed first due to the harsh temperatures as requested by AASTHO T336, which often destroy the gauges used in this test.

Table A-68.1: CTE Results

Cylinder	C1			C2			C3			C4		
Test #	*1*	*2*	*3*	*1*	*2*	*3*	*1*	*2*	*3*	*1*	*2*	*3*
X	21.2	21.2	21.2	21.2	21.2	21.2	21.2	21.2	21.2	21.2	21.2	21.2
A-A	-0.002	-0.001	-0.003	-0.013	-0.012	-0.012	-0.01	-0.011	-0.012	-0.005	-0.006	-0.007
B-B	-0.006	-0.006	-0.005	-0.013	-0.013	-0.013	-0.013	-0.014	-0.013	-0.005	-0.007	-0.006
C-C	-0.01	-0.011	-0.01	-0.011	-0.011	-0.012	-0.014	-0.013	-0.014	-0.004	-0.005	-0.008
D-D	-0.013	-0.012	-0.013	-0.015	-0.015	-0.016	-0.023	-0.021	-0.022	-0.022	-0.021	-0.019
Y	3.2	3.2	3.2	3.2	3.2	3.2	3.2	3.2	3.2	3.2	3.2	3.2
A-A	-0.031	-0.033	-0.032	-0.041	-0.042	-0.041	-0.043	-0.044	-0.044	-0.034	-0.035	-0.036
B-B	-0.037	-0.036	-0.036	-0.043	-0.044	-0.044	-0.046	-0.044	-0.045	-0.038	-0.041	-0.039
C-C	-0.041	-0.04	-0.041	-0.045	-0.045	-0.046	-0.044	-0.045	-0.044	-0.036	-0.038	-0.039
D-D	-0.047	-0.044	-0.045	-0.049	-0.05	-0.049	-0.053	-0.051	-0.052	-0.05	-0.052	-0.049
CTE1	16.111	17.778	16.111	15.556	16.667	16.111	18.333	18.333	17.778	16.111	16.111	16.111

CTE2	17.222	16.667	17.222	16.667	17.222	17.222	18.333	16.667	17.778	18.333	18.889	18.333
CTE3	17.222	16.111	17.222	18.889	18.889	18.889	16.667	17.778	16.667	17.778	18.333	17.222
CTE4	18.889	17.778	17.778	18.889	19.444	18.333	16.667	16.667	16.667	15.556	17.222	16.667
Average	17.361	17.083	17.083	17.500	18.056	17.639	17.500	17.361	17.222	16.944	17.639	17.083
Z	21.2	21.2	21.2	21.2	21.2	21.2	21.2	21.2	21.2	21.2	21.2	21.2
A-A	-0.001	-0.003	-0.002	-0.012	-0.011	-0.012	-0.011	-0.012	-0.012	-0.006	-0.005	-0.006
B-B	-0.005	-0.004	-0.006	-0.011	-0.011	-0.013	-0.014	-0.013	-0.014	-0.005	-0.005	-0.007
C-C	-0.011	-0.009	-0.009	-0.009	-0.012	-0.012	-0.014	-0.013	-0.014	-0.005	-0.006	-0.008
D-D	-0.015	-0.014	-0.011	-0.014	-0.015	-0.016	-0.02	-0.021	-0.02	-0.02	-0.021	-0.02
CTE1	16.667	16.667	16.667	16.111	17.222	16.111	17.778	17.778	17.778	15.556	16.667	16.667
CTE2	17.778	17.778	16.667	17.778	18.333	17.222	17.778	17.222	17.222	18.333	20.000	17.778
CTE3	16.667	17.222	17.778	20.000	18.333	18.889	16.667	17.778	16.667	17.222	17.778	17.222
CTE4	17.778	16.667	18.889	19.444	19.444	18.333	18.333	16.667	17.778	16.667	17.222	16.111
Average	17.222	17.083	17.500	18.333	18.333	17.639	17.639	17.361	17.361	16.944	17.917	16.944

Table A-68.2: Average CTE Values

Cylinder	C1			C2			C3			C4		
Test #	*1*	*2*	*3*	*1*	*2*	*3*	*1*	*2*	*3*	*1*	*2*	*3*
CTE 1	16.389	17.222	16.389	15.833	16.944	16.111	18.056	18.056	17.778	15.833	16.389	16.389
CTE 2	17.500	17.222	16.944	17.222	17.778	17.222	18.056	16.944	17.500	18.333	19.444	18.056
CTE 3	16.944	16.667	17.500	19.444	18.611	18.889	16.667	17.778	16.667	17.500	18.056	17.222
CTE 4	18.333	17.222	18.333	19.167	19.444	18.333	17.500	16.667	17.222	16.111	17.222	16.389

Average CTE	**17.222**	**17.917**	**17.407**	**17.245**

Batch 6: Creep Test

Six-cylinder specimens with a size of 75mm × 150mm were casted. The molds were filled using a one-way pour, this was done by taking a large scoop of the fresh mix in a trowel where the mold was filled to the top. The molds were consolidated with 30 taps due to the flow of the mix being over 200mm. As per CSA Annex U, the creep is tested in accordance with testing method ASTM C512, with testing conducted at a sustained load of 40% of the specified strength of UHPFRC. Upon arrival of the specimens at the age of 24 hours, the specimens were in a moist condition at a relative humidity of 95% until the age of 33 days. To read creep strains, a digital demec gauge is used. A total of 4-gauge lines are used so that if one gauge stud falls off, the other two diametrically opposing gauge lines can be used. To ensure all 4 lines are placed at equal lengths and are diametrically opposing, the specimens are grinded until the top and bottom ends of the cylinders are perfectly horizontal. Two cylinders were tested in compression at the age of 34 days and showed a compressive strength of 149 MPa and 148 MPa. The 40% load at which the creep specimens are to be loaded was calculated at 262 kN or 26.7 Tons. The results up to 7 months in the creep frame are summarized in Figure A-93 and Table A-69.

Table A-62: Creep Strain per unit stress

Creep Strain per unit stress	
0.1	574.0
0.3	651.0
1.0	598.1
3.0	653.8
7.0	669.2
21.0	753.8
35.0	794.2
64.0	836.5
80.0	879.8
107.0	891.3
135.0	877.0
167.0	885.3
201.0	932.7

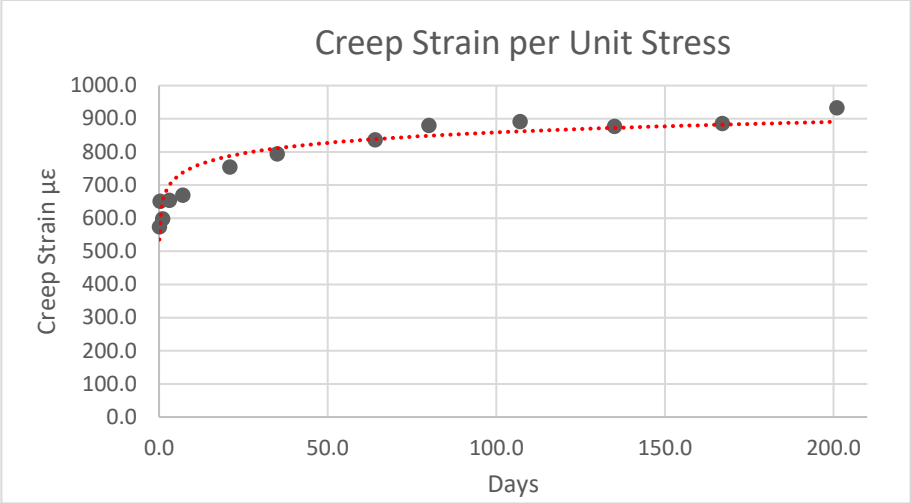

Figure 115: Creep strain per unit stress

Batch 6: Linear Shrinkage

A length comparator was used to measure the length change in the specimen for this test. The specimens were of the following nominal dimensions, 75mm × 75mm × 295mm. Upon arrival of the specimens, the specimens were placed in a lime water solution for 30 mintures and measured within 30 mintues to determine the original length. The specimens were placed in the lime water solution for an additional 6 d. The specimens were measured at 7d to determine the length, which is taken as 0 day drying age. These specimens were then placed into a humiditity chamber at 50% humidity for the rest of the 90 days. This batch of material contains 2% steel fibers by unit volume, and the straight fibers were 20 mm long with a diameter of 0.2 mm. This test was performed as per CSA A23.2-21C.

Table A-63: Linear Shrinkage Test Results (90 Days)

Age of Specimen (D)	**Drying Time (D)**		**Linear shrinkage (%)**			
		Prism 1	**Prism 2**	**Prism 3**	**Prism 4**	**Average**
7	1	0	0	0	0	0
11	4	0	0	0	0	0
14	7	0.006	0.004	0.006	0.004	0.005
21	14	0.007	0.005	0.009	0.004	0.006
28	21	0.009	0.008	0.008	0.005	0.006
35	28	0.011	0.012	0.011	0.009	0.011
63	56	0.012	0.014	0.011	0.009	0.012
97	90	0.011	0.015	0.012	0.009	0.012

Batch 6: Salt Scaling

A freezing chamber in which a control specimen of size 150mm × 150mm × 100mm was used with an embedded temperature probe to measue the temperature of the concrete core, the conrol specimen measured at -18°C at equalibirum. A humidiity chamber in which a humidity of 50% was used. An oven capable to maintain 110°C was also used. To ensure the oven can maintain an evaporation rate of at least 25 grams, a 1L griffin beaker was used with 500g of water placed at center and in the corners of the oven. After 4 hrs in the oven, the average evaporation rate was measured to be 34.32 grams per hour. The nominal dimensions of the speceimens were 300mm × 300mm × 75mm. The surface of the slabs was finished with a wood strike off board. The specimens were placed in a moist storage for 14 days, and in air storage for 14 days as per CSA A23.2-3C. The dykes were a height of 35mm. A total of 3 specimens were used, 2 with sodium chloride (CSA A23.2-22C) and 1 specimens with calcium chloride (ASTM C672). This batch of material contains 2% steel fibers by unit volume, and the straight fibers were 20 mm long with a diameter of 0.2 mm. This test was performed as per CSA A23.2-22C and ASTM C672.

Table A-64: Salt Scaling Test results.

Number of Cycles	**Specimen # 1 (CSA A23.2-22C)**	**Specimen # 2 (CSA A23.2-22C)**	**Specimen # 3 (ASTM C672)**	**Visual Rating**
5	0.05	0.08	0.15	0
15	0.19	0.23	0.25	0
30	0.46	0.57	0.59	0
50	0.64	0.79	0.96	0
Total (g)	1.34	1.67	1.95	-
Total (kg/m^2)	**0.015**	**0.019**	**0.022**	-
Durability Life (Annex U)	**DL200**	**DL200**	**DL200**	-

Batch 6: Sulfate Resistance

Six bars with the size of 25mm × 25mm × 285mm were casted to conduct the sulfate resistance test in accordance with CSA Annex U and testing method CSA A3004-C8A. The prisms were casted as one-way prisms and were consolidated by tapping 30 times due to the flow reading of over 200mm. The testing method included in CSA A3004-C8A is used to determine the sulphate resistance of mortar bars by measuring length change from exposure to a sulfate solution. Twenty cubes were also casted along with the six bars. Immediately after the bars are molded, the molds were kept in a sealed container at a temperature of 35 ± 3°C. After 24 hours the molds are removed from the curing tank and were transported to the laboratory. Upon arrival of the specimens, the cubes were tested in compression and showed a strength greater than 20 MPa at an age > 24 hours. Before every reading of the test prisms is taken, the reference invar bar is inserted, and the gauge is zeroed on the reference bar. The invar bar is then taken out and the prisms to be measured are wiped surface dry. Special care was given to the ends of the bars on the gauge studs and their seating caps on the length comparator as dust can accumulate and give poor readings. Before noting the length of the bar, each bar was rotated while inserted in the length comparator to ensure no prisms showed signs of bending. Bars which showed a change in length whilst rotating in the length comparator were taken out and the seating cups were inspected of dust or particles which may affect the results.

These bars were then re-inserted into the length comparator. A difference of less than 0.006mm is noted as an average of length change whilst rotating the bar in the length comparator. After all bars are measured, the invar reference bar is measured, and its reading is again recorded. The lengths of the bars were recorded at 1,3,4,14,15 weeks, and at 4,6,9,12,13 months. The sulfate solution was made using sodium sulfate at a concentration of 50g/L of solution. The total solution made is 4 volumes of solution to 1 volume of mortar bar. Each bar consisted of a volume of 0.178L, to make enough solution for one bar 4 x 0.178L = 0.7125 L, for a total of 6 bars the total volume of sulfate solution needed is 4.275L. The total volume of solution made after every reading is taken is 4.3L of sulfate solution. To ensure the solution is conforming with ASTM C1012, the pH reading of the distilled water before the addition of sulfate solution and the pH reading of the solution after addition of the sodium sulfate is taken, the distilled water used varied within a range of 6.7-7.2 pH, and a range of 7.2-7.6 pH respectively as is shown in Figures A-94 to A-96. The bars were placed in a container and the lid was closed so that the solution does not evaporate. The container used for storage is shown in Figure A-116: Storage Container, Figure A-117: pH reading with Distilled water, Figure A-118: pH reading with sodium sulfate solution. The results are summarized in Table A-65: Results Obtained until 12 Months

Figure A-116: Storage Container, Figure A-117: pH reading with Distilled water, Figure A-118: pH reading with sodium sulfate solution

Table A-65: Results Obtained until 12 Months

Sample ID	1	2	3	4	5	6	Average	Standard Deviation
Age	Length Change %							
Initial	-	-	-	-	-	-	-	-
3 weeks	-0.004	0.001	0.001	0.004	0.004	-0.001	0.00	0.003
4 weeks	0.058	0.060	0.062	0.063	0.064	0.059	0.06	0.002
13 weeks	0.091	0.067	0.073	0.067	0.068	0.061	0.07	0.009
15 weeks	0.081	0.083	0.086	0.084	0.087	0.082	0.08	0.002
4 months	0.106	0.106	0.112	0.109	0.110	0.104	0.11	0.003
6 months	0.109	0.112	0.116	0.116	0.114	0.109	0.11	0.003
9 months	0.108	0.106	0.109	0.112	0.110	0.112	0.11	0.002
12 months	0.108	0.109	0.112	0.111	0.111	0.139	0.11	0.011

Appendix 1-A: Inverse Analysis Parameters for batches 1-3

Batch 1			
S_0			
Prism #	Min	Max	% Difference
1	565.047	667.581523	16.637
2	530.380	634.520	17.880
3	-	-	-
4	416.958	480.139	14.085
5	619.164	1038.577	50.601
6	628.839	728.802	14.726
7	669.287	759.813	12.669
8	-	-	-
9	477.277	573.003	18.229
10	652.802	740.849	12.635
Average	**569.969**	**702.911**	**19.683**

Batch 1			
f_{fu}			
Prism #	Min	Max	% Difference
1	9.254	9.240	0.144
2	8.841	8.950	1.232
3	-	-	-
4	9.767	9.904	1.394
5	9.317	9.510	2.046
6	9.661	9.764	1.063
7	8.074	8.078	0.052
8	-	-	-
9	10.759	10.690	0.650
10	10.873	10.777	0.878
Average	**9.568**	**9.614**	**0.932**

Batch 1			
ε_{fu}			
Prism #	Min	Max	% Difference
1	0.009886	0.008313	17.28
2	0.012510	0.009779	24.51
3	-	-	-
4	0.008361	0.007363	12.70
5	0.006595	0.007150	8.08
6	0.009245	0.009598	3.75
7	0.006159	0.006478	5.03
8	-	-	-
9	0.012048	0.012746	5.63
10	0.010641	0.010704	0.58
Average	**0.009431**	**0.009016**	**9.70**

Batch 2			
S_0			
Prism #	Min	Max	% Difference
1	687.142	724.156	5.245
2	730.487	1043.482	35.288
3	389.711	573.521	38.165
4	567.041	652.863	14.070
5	740.032	844.478	13.183
6	510.199	659.254	25.491
7	635.721	729.451	13.731
8	651.078	720.573	10.133
9	587.064	688.851	15.955
10	394.650	633.490	46.461
Average	**589.313**	**727.012**	**21.772**

Batch 2			
f_{fu}			
Prism #	Min	Max	% Difference
1	12.565	12.485	0.641
2	10.360	10.126	2.278
3	11.625	11.395	1.997
4	13.788	13.438	2.571
5	13.185	13.074	0.844
6	12.071	12.057	0.118
7	12.678	12.718	0.317
8	14.831	14.744	0.592
9	11.202	10.980	2.004
10	11.711	11.396	2.724
Average	**12.402**	**12.241**	**1.409**

Batch 2			
ε_{fu}			
Prism #	Min	Max	% Difference
1	0.014243	0.014328	0.59
2	0.010093	0.010145	0.51
3	0.009419	0.010871	14.32
4	0.017879	0.013693	26.52
5	0.010298	0.010682	3.66
6	0.012775	0.011628	9.40
7	0.010754	0.011483	6.56
8	0.014914	0.014885	0.20
9	0.013798	0.014015	1.56
10	0.009466	0.010658	11.85
Average	**0.012364**	**0.012239**	**7.52**

Batch 3			
S_0			
Prism #	Min	Max	% Difference
1	591.104	697.691	16.540
2	591.297	690.522	15.482
3	394.984	547.720	32.404
4	601.711	714.538	17.144
5	437.512	552.862	23.294
6	569.703	630.118	10.071
7	369.114	499.565	30.034
8	600.120	645.701	7.317
9	561.218	706.784	22.960
10	462.866	613.716	28.024
Average	**517.963**	**629.922**	**20.327**

Batch 3			
f_{fu}			
Prism #	Min	Max	% Difference
1	17.250	15.562	10.289
2	9.214	9.255	0.450
3	9.520	9.518	0.015
4	10.208	10.205	0.030
5	13.379	13.348	0.232
6	12.910	13.018	0.837
7	12.207	12.094	0.929
8	8.898	9.071	1.931
9	15.011	14.999	0.077
10	12.929	12.922	0.053
Average	**12.153**	**11.999**	**1.484**

Batch 3			
ε_{fu}			
Prism #	Min	Max	% Difference
1	0.023126	0.023033	0.40
2	0.022077	0.020238	8.69
3	0.007690	0.009158	17.42
4	0.011240	0.009774	13.95
5	0.012792	0.015142	16.83
6	0.012334	0.011754	4.82
7	0.011738	0.013032	10.44
8	0.009895	0.010072	1.78
9	0.014220	0.014746	3.63
10	0.015611	0.011651	29.06
Average	**0.012941**	**0.012240**	**10.70**

Batch 1			
ε_{cr}			
Prism #	Min	Max	% Difference
1	0.000204	0.000174	15.84
2	0.000193	0.000160	18.71
3	-	-	-
4	0.000240	0.000211	12.70
5	0.000223	0.000043	135.73
6	0.000174	0.000123	34.09
7	0.000176	0.000148	17.43
8	-	-	-
9	0.000266	0.000206	25.18
10	0.000172	0.000140	20.44
Average	**0.000206**	**0.000151**	**35.01**

Batch 1			
f_{crm}			
Prism #	Min	Max	% Difference
1	8.32	8.38	0.80
2	7.37	7.31	0.84
3	-	-	-
4	7.21	7.31	1.39
5	9.95	3.20	102.77
6	7.87	6.46	19.61
7	8.50	8.10	4.79
8	-	-	-
9	9.14	8.51	7.03
10	8.10	7.48	7.86
Average	**8.31**	**7.09**	**18.14**

Batch 2			
ε_{cr}			
Prism #	Min	Max	% Difference
1	0.000203	0.000188	7.72
2	0.000181	0.000042	124.52
3	0.000414	0.000236	54.90
4	0.000444	0.000280	45.22
5	0.000181	0.000146	21.51
6	0.000313	0.000225	32.55
7	0.000234	0.000174	29.38
8	0.000214	0.000183	15.66
9	0.000224	0.000180	21.76
10	0.000356	0.000205	53.82
Average	**0.000276**	**0.000186**	**40.70**

Batch 2			
f_{crm}			
Prism #	Min	Max	% Difference
1	10.05	9.68	3.73
2	9.52	3.16	100.24
3	11.61	9.73	17.67
4	13.44	13.18	1.94
5	9.63	8.86	8.39
6	11.48	10.68	7.21
7	10.70	9.13	15.81
8	10.04	9.49	5.55
9	9.48	8.94	5.86
10	11.50	9.36	20.56
Average	**10.74**	**9.22**	**18.70**

Batch 3			
ε_{cr}			
Prism #	Min	Max	% Difference
1	0.000275	0.000210	26.69
2	0.000196	0.000162	18.97
3	0.000366	0.000225	47.80
4	0.000166	0.000149	10.57
5	0.000365	0.000237	42.51
6	0.000228	0.000189	18.74
7	0.000397	0.000256	43.30
8	0.000204	0.000180	12.22
9	0.000281	0.000194	36.79
10	0.000278	0.000213	26.69
Average	**0.000262**	**0.000196**	**28.43**

Batch 3			
f_{crm}			
Prism #	Min	Max	% Difference
1	11.70	10.56	10.29
2	8.36	8.07	3.51
3	10.40	8.86	16.01
4	7.54	7.68	1.79
5	11.50	9.43	19.70
6	9.34	8.56	8.72
7	10.55	9.20	13.71
8	8.80	8.38	4.91
9	11.37	9.87	14.13
10	9.27	9.40	1.36
Average	**9.18**	**8.59**	**9.41**

Batch 1			
	w_0		
Prism #	**Min**	**Max**	**% Difference**
1	3.267	2.768664	16.527
2	5.378	4.208	24.415
3			-
4	3.072	2.705	12.698
5	2.189	0.755	97.382
6	2.619	2.234	15.847
7	4.320	4.290	0.686
8			-
9	3.448	3.294	4.573
10	4.087	3.816	6.850
Average	**3.547**	**3.009**	**22.372**

Batch 2			
	w_0		
Prism #	**Min**	**Max**	**% Difference**
1	3.184	3.086	3.134
2	2.888	0.980	98.655
3	4.735	4.451	6.191
4	4.105	2.946	32.868
5	3.540	3.360	5.219
6	5.515	4.647	17.077
7	3.168	2.870	9.869
8	2.890	2.689	7.221
9	3.963	3.753	5.446
10	4.816	4.341	10.383
Average	**3.880**	**3.312**	**19.606**

Batch 3			
	w_0		
Prism #	**Min**	**Max**	**% Difference**
1	1.423	1.087	26.801
2	2.763	2.380	14.863
3	4.434	4.365	1.562
4	4.751	4.193	12.483
5	3.098	2.819	9.423
6	2.391	2.074	14.185
7	4.545	4.240	6.947
8	5.022	4.836	3.774
9	2.524	2.126	17.112
10	5.376	4.059	27.912
Average	**4.183**	**3.735**	**13.506**

Average Tensile Stress-Strain and Stress-Crack Width plots. Batches (1-3)

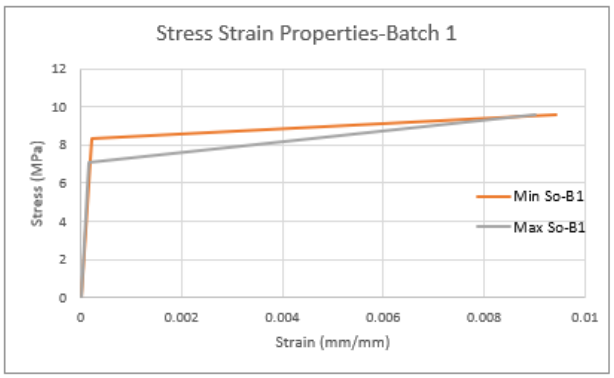

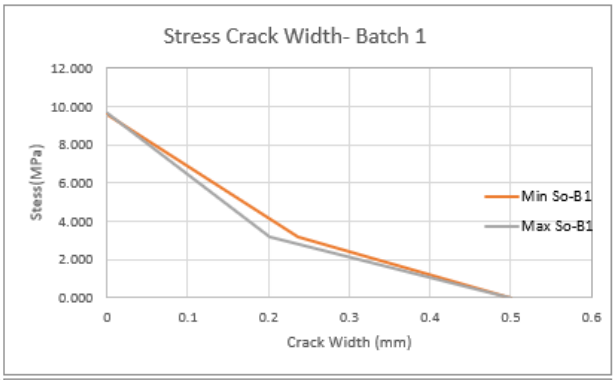

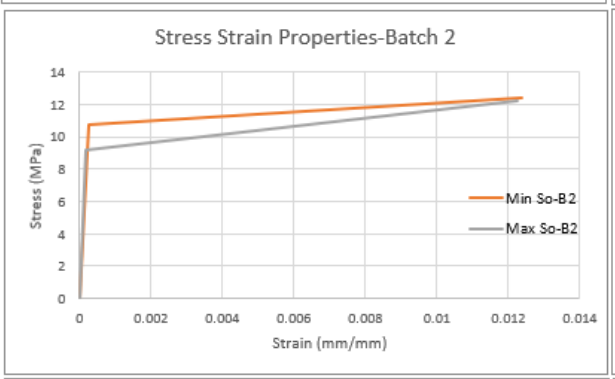

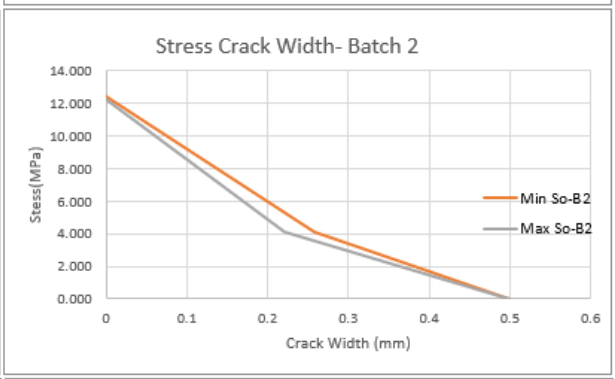

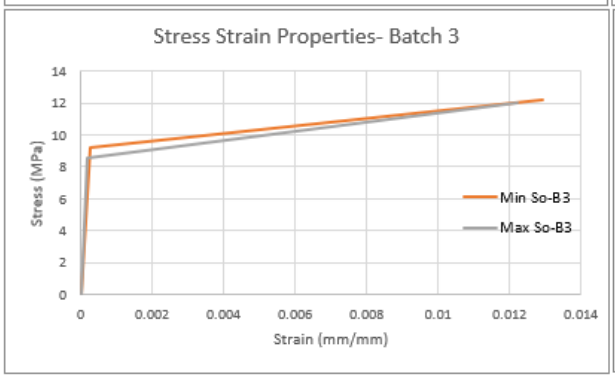

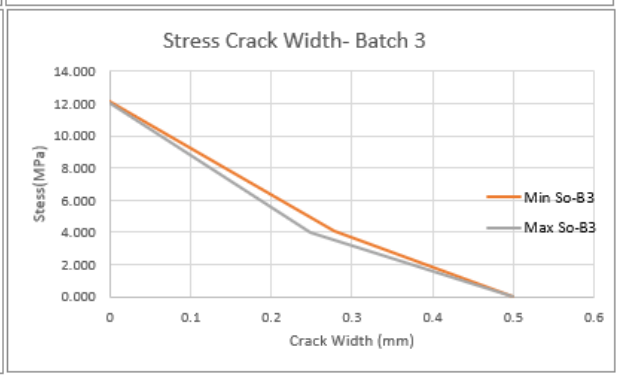

Average Stress-Strain and Stress-Crack width plots from bathes (1-3)

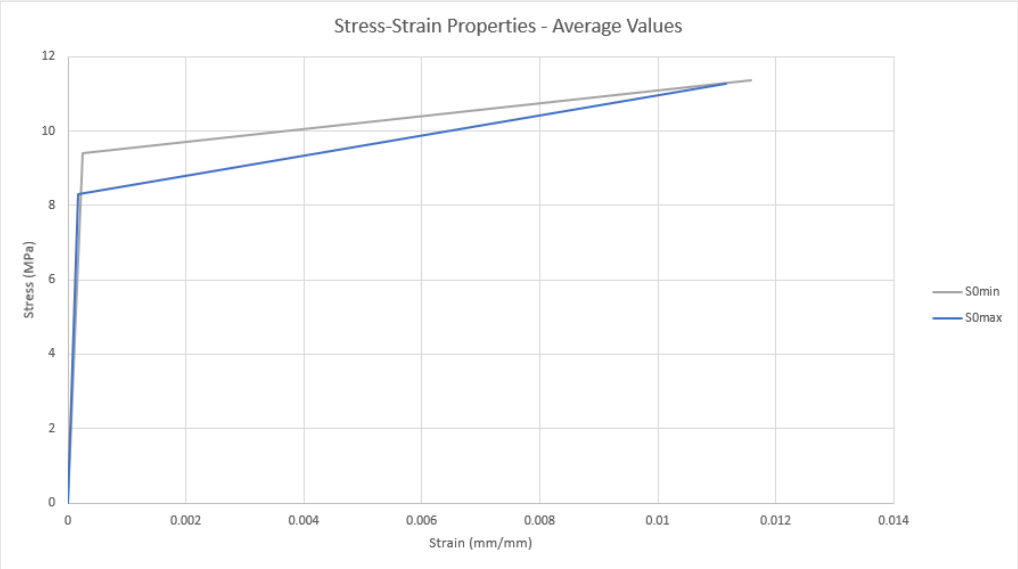

Tensile properties from a minimum S0 and maximum S0 from batches 1-3

S_{0min}	ffu	S_{0max}	ffu
565.05	9.25	667.58	9.24
530.38	8.84	634.52	8.95
416.96	9.77	480.14	9.90
619.16	9.32	1038.58	9.51
628.84	9.66	728.80	9.76
669.29	8.07	759.81	8.08
477.28	10.76	573.00	10.69
652.80	10.87	740.85	10.78
687.14	12.57	724.16	12.48
730.49	10.36	1043.48	10.13
389.71	11.62	573.52	11.39
567.04	13.79	652.86	13.44
740.03	13.18	844.48	13.07
510.20	12.07	659.25	12.06
635.72	12.68	729.45	12.72
651.08	14.83	720.57	14.74
587.06	11.20	688.85	10.98
394.65	11.71	633.49	11.40
591.10	17.25	697.69	15.56
591.30	9.21	690.52	9.26
394.98	9.52	547.72	9.52
601.71	10.21	714.54	10.20
437.51	13.38	552.86	13.35
569.70	12.91	630.12	13.02
369.11	12.21	499.56	12.09
600.12	8.90	645.70	9.07
561.22	15.01	706.78	15.00
462.87	12.93	613.72	12.92

S_{0min}	ε_{tu}	S_{0max}	ε_{tu}
565.05	0.009886	667.58	0.008313
530.38	0.012510	634.52	0.009779
416.96	0.008361	480.14	0.007363
619.16	0.006595	1038.58	0.007150
628.84	0.009245	728.80	0.009598
669.29	0.006159	759.81	0.006478
477.28	0.012048	573.00	0.012746
652.80	0.010641	740.85	0.010704
687.14	0.014243	724.16	0.014328
730.49	0.010093	1043.48	0.010145
389.71	0.009419	573.52	0.010871
567.04	0.017879	652.86	0.013693
740.03	0.010298	844.48	0.010682
510.20	0.012775	659.25	0.011628
635.72	0.010754	729.45	0.011483
651.08	0.014914	720.57	0.014885
587.06	0.013798	688.85	0.014015
394.65	0.009466	633.49	0.010658
591.10	0.023126	697.69	0.023033
591.30	0.022077	690.52	0.020238
394.98	0.007690	547.72	0.009158
601.71	0.011240	714.54	0.009774
437.51	0.012792	552.86	0.015142
569.70	0.012334	630.12	0.011754
369.11	0.011738	499.56	0.013032
600.12	0.009895	645.70	0.010072
561.22	0.014220	706.78	0.014746
462.87	0.015611	613.72	0.011651

S_{0min}	w_0	S_{0max}	w_0
565.05	3.27	667.58	2.77
530.38	5.38	634.52	4.21
416.96	3.07	480.14	2.71
619.16	2.19	1038.58	0.76
628.84	2.62	728.80	2.23
669.29	4.32	759.81	4.29
477.28	3.45	573.00	3.29
652.80	4.09	740.85	3.82
687.14	3.18	724.16	3.09
730.49	2.89	1043.48	0.98
389.71	4.74	573.52	4.45
567.04	4.10	652.86	2.95
740.03	3.54	844.48	3.36
510.20	5.51	659.25	4.65
635.72	3.17	729.45	2.87
651.08	2.89	720.57	2.69
587.06	3.96	688.85	3.75
394.65	4.82	633.49	4.34
591.10	1.42	697.69	1.09
591.30	2.76	690.52	2.38
394.98	4.43	547.72	4.37
601.71	4.75	714.54	4.19
437.51	3.10	552.86	2.82
569.70	2.39	630.12	2.07
369.11	4.54	499.56	4.24
600.12	5.02	645.70	4.84
561.22	2.52	706.78	2.13
462.87	5.38	613.72	4.06

S_{0min}	ε_{cr}	S_{0max}	ε_{cr}
565.05	0.000204	667.58	0.000174
530.38	0.000193	634.52	0.000160
416.96	0.000240	480.14	0.000211
619.16	0.000223	1038.6	0.000043
628.84	0.000174	728.8	0.000123
669.29	0.000176	759.81	0.000148
477.28	0.000266	573	0.000206
652.80	0.000172	740.85	0.000140
687.14	0.000203	724.16	0.000188
730.49	0.000181	1043.5	0.000042
389.71	0.000414	573.52	0.000236
567.04	0.000444	652.86	0.000280
740.03	0.000181	844.48	0.000146
510.20	0.000313	659.25	0.000225
635.72	0.000234	729.45	0.000174
651.08	0.000214	720.57	0.000183
587.06	0.000224	688.85	0.000180
394.65	0.000356	633.49	0.000205
591.10	0.000275	697.69	0.000210
591.30	0.000196	690.52	0.000162
394.98	0.000366	547.72	0.000225
601.71	0.000166	714.54	0.000149
437.51	0.000365	552.86	0.000237
569.70	0.000228	630.12	0.000189
369.11	0.000397	499.56	0.000256
600.12	0.000204	645.7	0.000180
561.22	0.000281	706.78	0.000194
462.87	0.000278	613.72	0.000213

S_{0min}	f_{crm}	S_{0max}	f_{crm}
565.05	8.32	667.58	8.38
530.38	7.37	634.52	7.31
416.96	7.21	480.14	7.31
619.16	9.95	1038.58	3.20
628.84	7.87	728.80	6.46
669.29	8.50	759.81	8.10
477.28	9.14	573.00	8.51
652.80	8.10	740.85	7.48
687.14	10.05	724.16	9.68
730.49	9.52	1043.48	3.16
389.71	11.61	573.52	9.73
567.04	13.44	652.86	13.18
740.03	9.63	844.48	8.86
510.20	11.48	659.25	10.68
635.72	10.70	729.45	9.13
651.08	10.04	720.57	9.49
587.06	9.48	688.85	8.94
394.65	11.50	633.49	9.36
591.10	11.70	697.69	10.56
591.30	8.36	690.52	8.07
394.98	10.40	547.72	8.86
601.71	7.54	714.54	7.68
437.51	11.50	552.86	9.43
569.70	9.34	630.12	8.56
369.11	10.55	499.56	9.20
600.12	8.80	645.70	8.38
561.22	11.37	706.78	9.87
462.87	9.27	613.72	9.40

S_{0min}	E_{c0}	S_{0max}	E_{c0}
565.05	48.07	667.58	40.68
530.38	45.69	634.52	38.19
416.96	34.57	480.14	30.02
619.16	74.78	1038.58	44.58
628.84	52.47	728.80	45.28
669.29	54.71	759.81	48.19
477.28	41.26	573.00	34.36
652.80	53.34	740.85	47.00
687.14	49.47	724.16	52.14
730.49	52.59	1043.48	75.13
389.71	28.06	573.52	41.29
567.04	40.83	652.86	47.00
740.03	53.28	844.48	60.80
510.20	36.73	659.25	47.47
635.72	45.77	729.45	52.52
651.08	46.87	720.57	51.88
587.06	42.27	688.85	49.59
394.65	28.42	633.49	45.61
591.10	42.56	697.69	50.23
591.30	42.57	690.52	49.72
394.98	28.44	547.72	39.44
601.71	38.11	714.54	51.45
437.51	31.50	552.86	39.80
569.70	41.02	630.12	45.37
369.11	26.57	499.56	35.97
600.12	43.21	645.70	46.50
561.22	40.41	706.78	50.88
462.87	33.32	613.72	44.18

Inverse analysis parameters from additional Flexure Tests on prisms size of 150mm x 150mm x 500mm

DSM - MTO - Beams 150mm x 150mm x 500mm (450mm shear span)

$S_{\Omega min}$	ffu	$S_{\Omega max}$	ffu
1209.41	5.95	1444.88	5.67
1144.59	8.36	1260.83	8.09
1054.56	5.95	1172.63	6.33
1153.60	3.40	1310.56	3.45
1208.87	8.51	1339.08	8.43
1110.73	8.80	1264.38	8.44
1075.82	10.56	1161.72	10.41
1026.16	8.57	1106.45	8.48

$S_{\Omega min}$	εtu	$S_{\Omega max}$	εtu
1209.41	0.001799	1444.88	0.001862
1144.59	0.000641	1260.83	0.000891
1054.56	0.001073	1172.63	0.001431
1153.60	0.007345	1310.56	0.007565
1208.87	0.004913	1339.08	0.004978
1110.73	0.00437	1264.38	0.004811
1075.82	0.005866	1161.72	0.005976
1026.16	0.005308	1106.45	0.005278

$S_{\Omega min}$	w_Ω	$S_{\Omega max}$	w_Ω
1209.41	2.54	1444.88	2.65
1144.59	1.63	1260.83	2.08
1054.56	1.68	1172.63	1.84
1153.60	0.24	1310.56	0.17
1208.87	3.19	1339.08	3.07
1110.73	3.62	1264.38	3.94
1075.82	3.80	1161.72	3.82
1026.16	2.61	1106.45	2.47

$S_{\Omega min}$	$\varepsilon_{,,}$	$S_{\Omega max}$	$\varepsilon_{,,}$
1209.41	0.000196	1444.88	0.000184
1144.59	0.00018	1260.83	0.00016
1054.56	0.000139	1172.63	0.000102
1153.60	0.000155	1310.56	0.000135
1208.87	0.000156	1339.08	0.000131
1110.73	0.000183	1264.38	0.000167
1075.82	0.000199	1161.72	0.000181
1026.16	0.000152	1106.45	0.000123

$S_{\Omega min}$	f_{crm}	$S_{\Omega max}$	f_{crm}
1209.41	9.65	1444.88	9.78
1144.59	9.30	1260.83	8.94
1054.56	7.42	1172.63	6.18
1153.60	8.97	1310.56	8.67
1208.87	8.64	1339.08	8.27
1110.73	9.29	1264.38	9.40
1075.82	10.91	1161.72	10.94
1026.16	8.80	1106.45	8.54

$S_{\Omega min}$	$E_{c\Omega}$	$S_{\Omega max}$	$E_{c\Omega}$
1209.41	58.05	1444.88	69.35
1144.59	54.94	1260.83	60.52
1054.56	50.62	1172.63	56.29
1153.60	55.37	1310.56	62.91
1208.87	58.03	1339.08	64.28
1110.73	53.32	1264.38	60.69
1075.82	51.64	1161.72	55.76
1026.16	49.26	1106.45	53.11

Inverse analysis parameters from additional Flexure Tests on prisms size of 100mm x 50mm x 300mm

Afnor Specimens, w x h x span , 100mm x 50mm x 300 mm

$S_{\Omega min}$	ffu	$S_{\Omega max}$	ffu
72.07	10.63	84.17	10.84
117.94	8.97	127.00	8.88
128.54	12.19	140.70	11.91

$S_{\Omega min}$	εtu	$S_{\Omega max}$	εtu
72.07	0.048361	84.17	0.053982
117.94	0.039304	127.00	0.038504
128.54	0.024519	140.70	0.025825

$S_{\Omega min}$	$\varepsilon_{,,}$	$S_{\Omega max}$	$\varepsilon_{,,}$
72.07	0.00	84.17	0.00
117.94	0.00	127.00	0.00
128.54	0.00	140.70	0.00

$S_{\Omega min}$	f_{crm}	$S_{\Omega max}$	f_{crm}
72.07	11.93	84.17	10.81
117.94	8.08	127.00	7.90
128.54	11.08	140.70	11.33

Appendix 2: Pictures of Tests performed

Batch 1: Flexural Tests

Table A-66: Batch 1 Flexure failure modes summary

Specimen ID #	Failure Type
1	Flexure
2	Flexure
3	Shear
4	Flexure /Torsion
5	Flexure/Torsion
6	Flexure
7	Flexure
8	Flexure/Torsion
9	Flexure
10	Flexure

Specimen #1

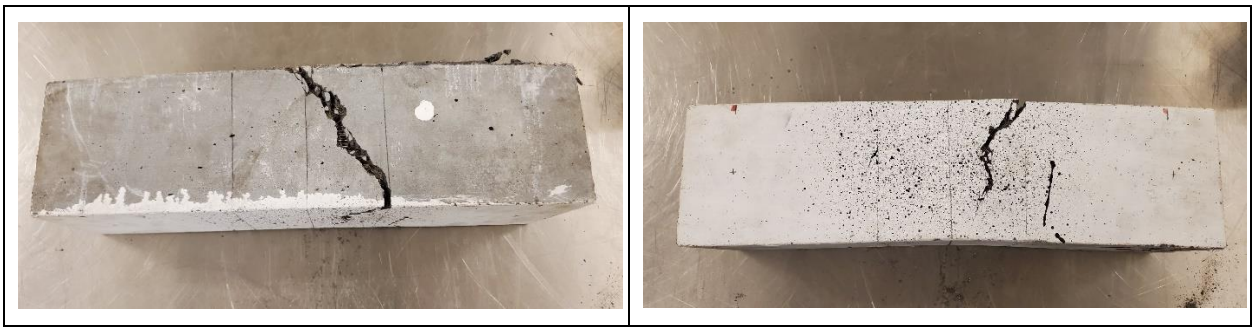

Specimen #2

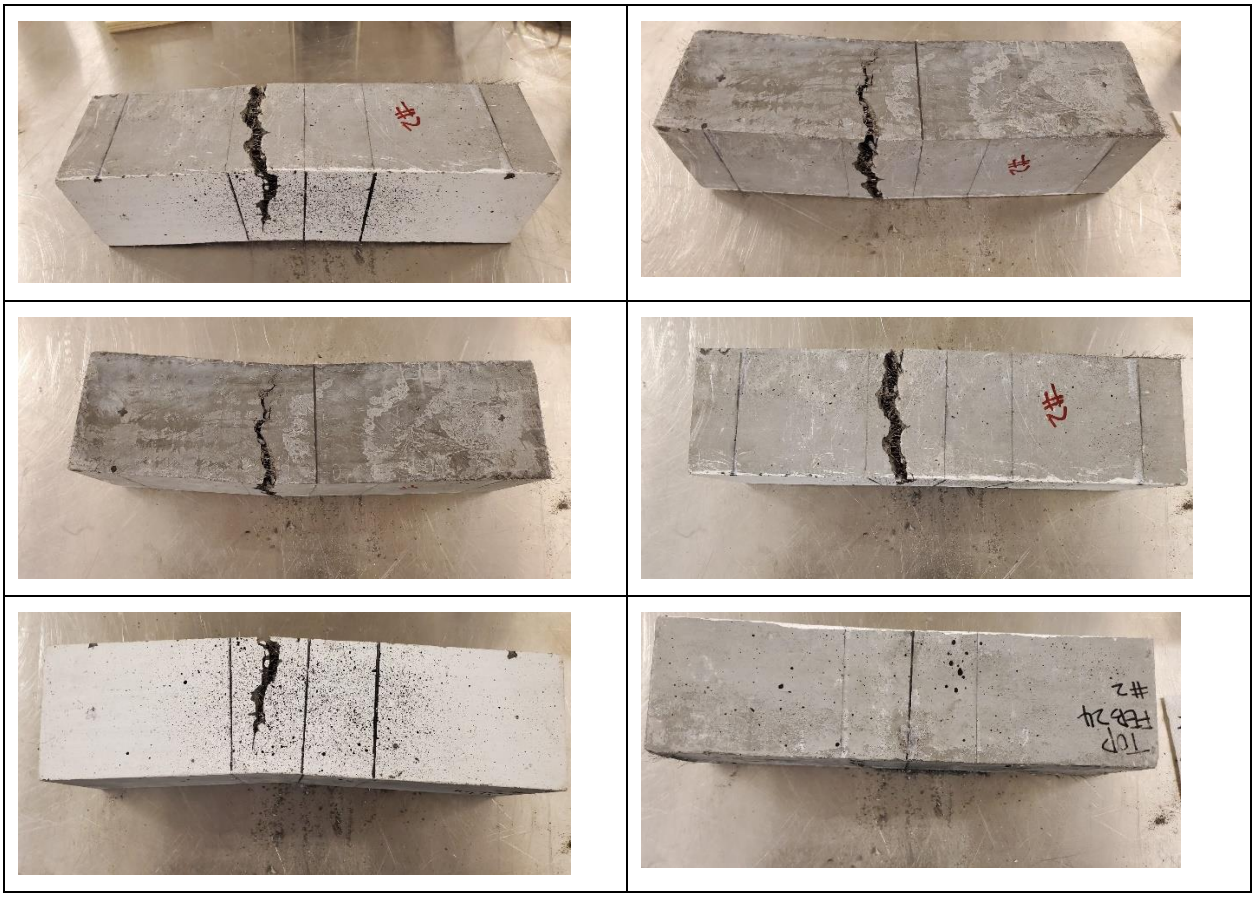

Specimen #3

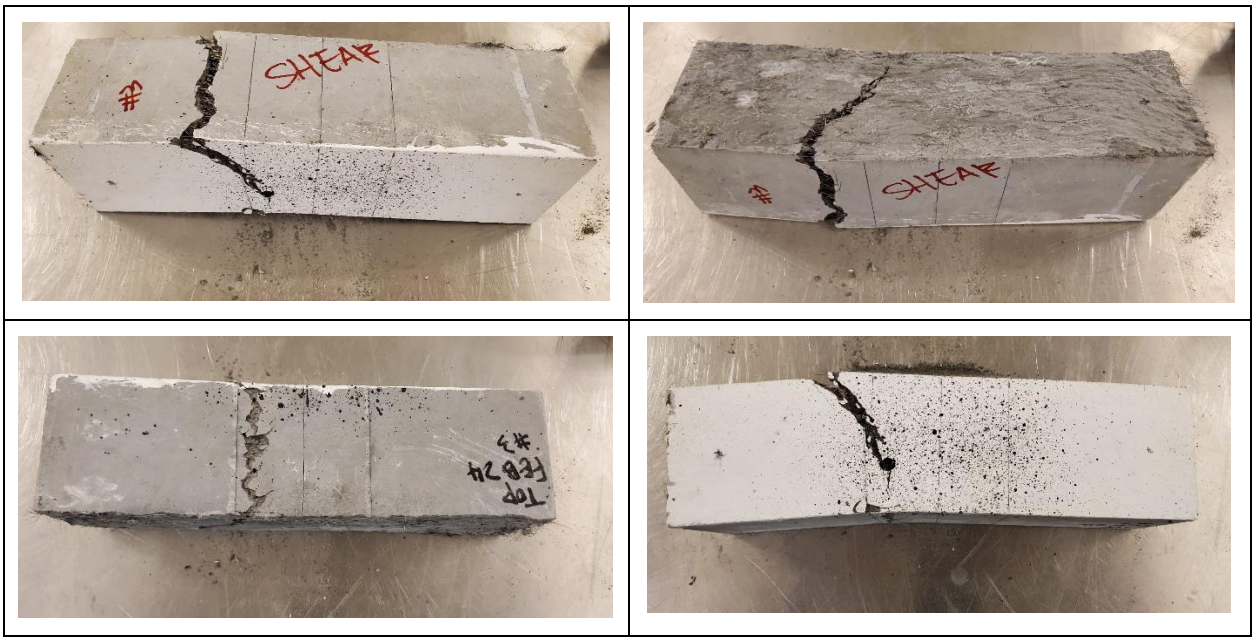

Specimen #4

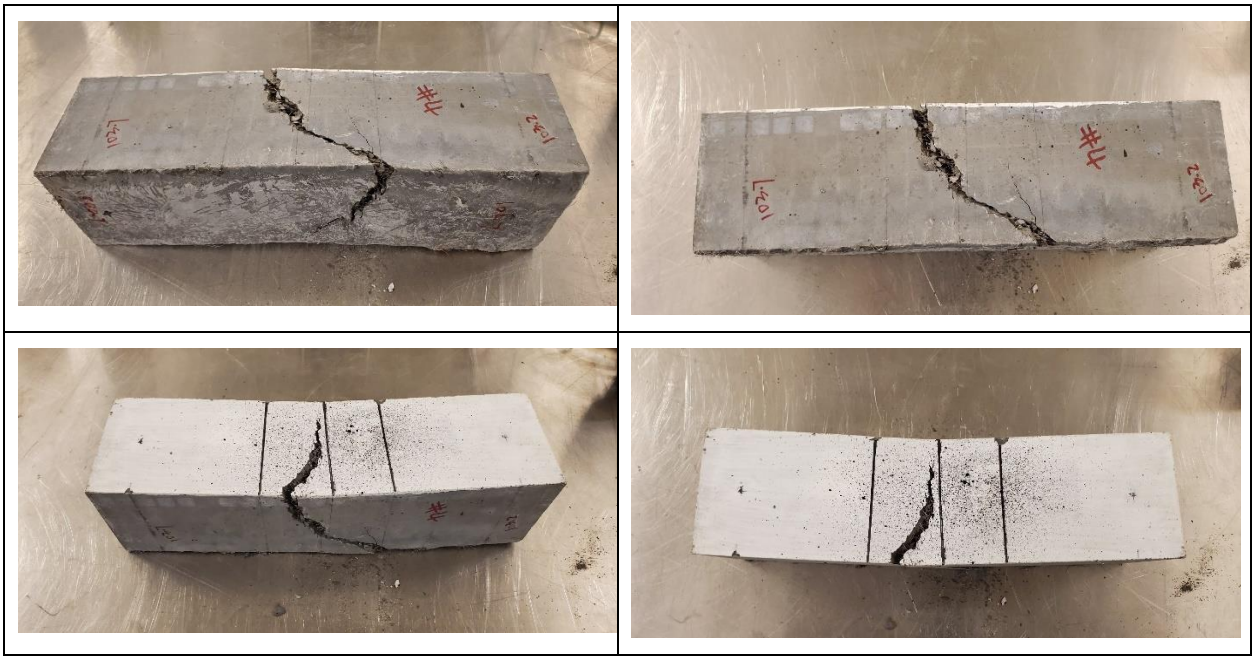

Specimen #5

Specimen #6

Specimen #7

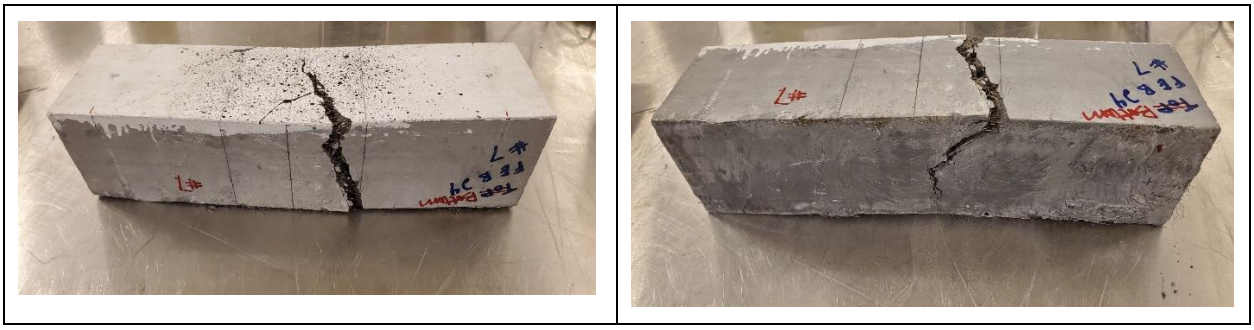

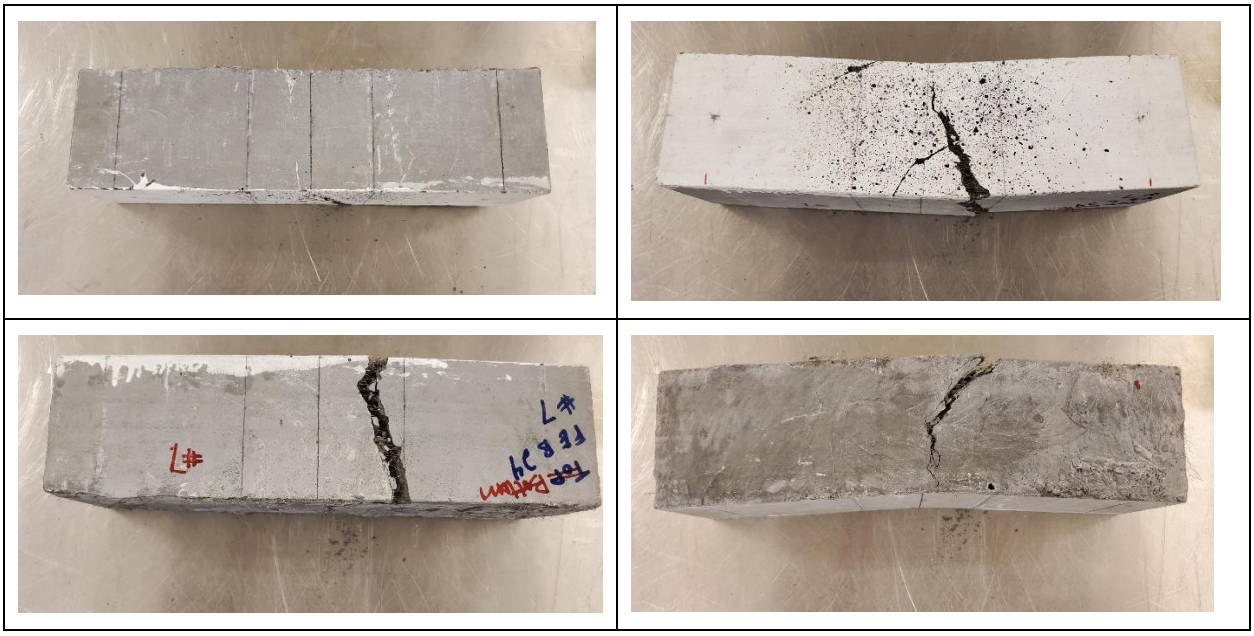

Specimen #8

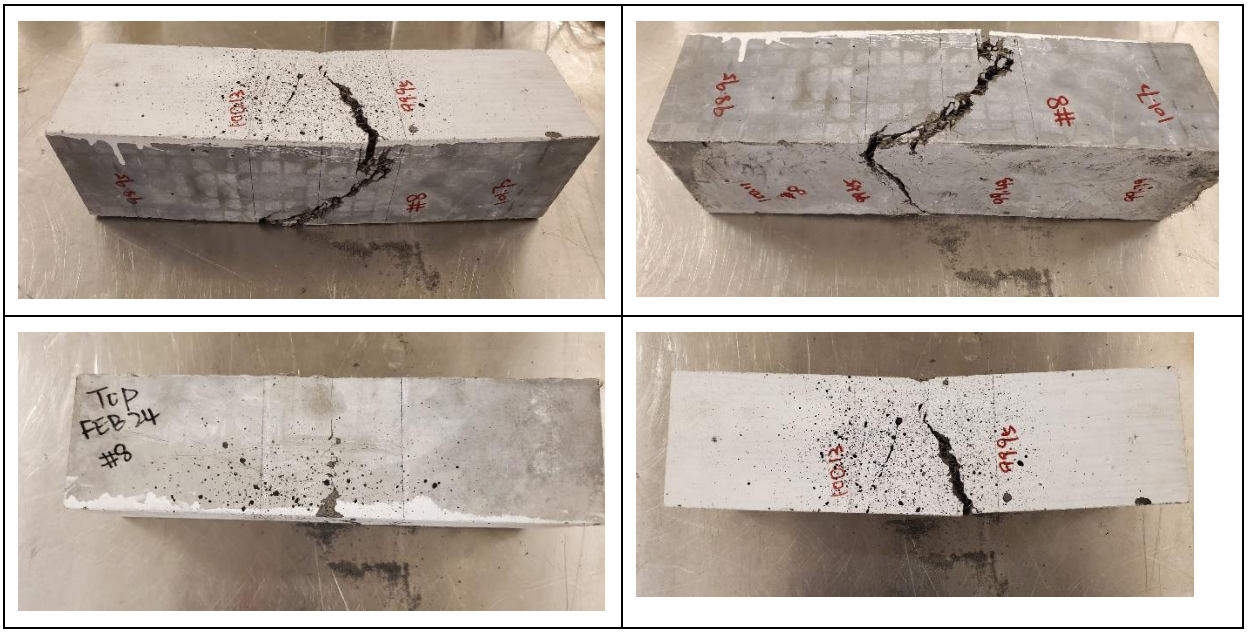

Specimen #9

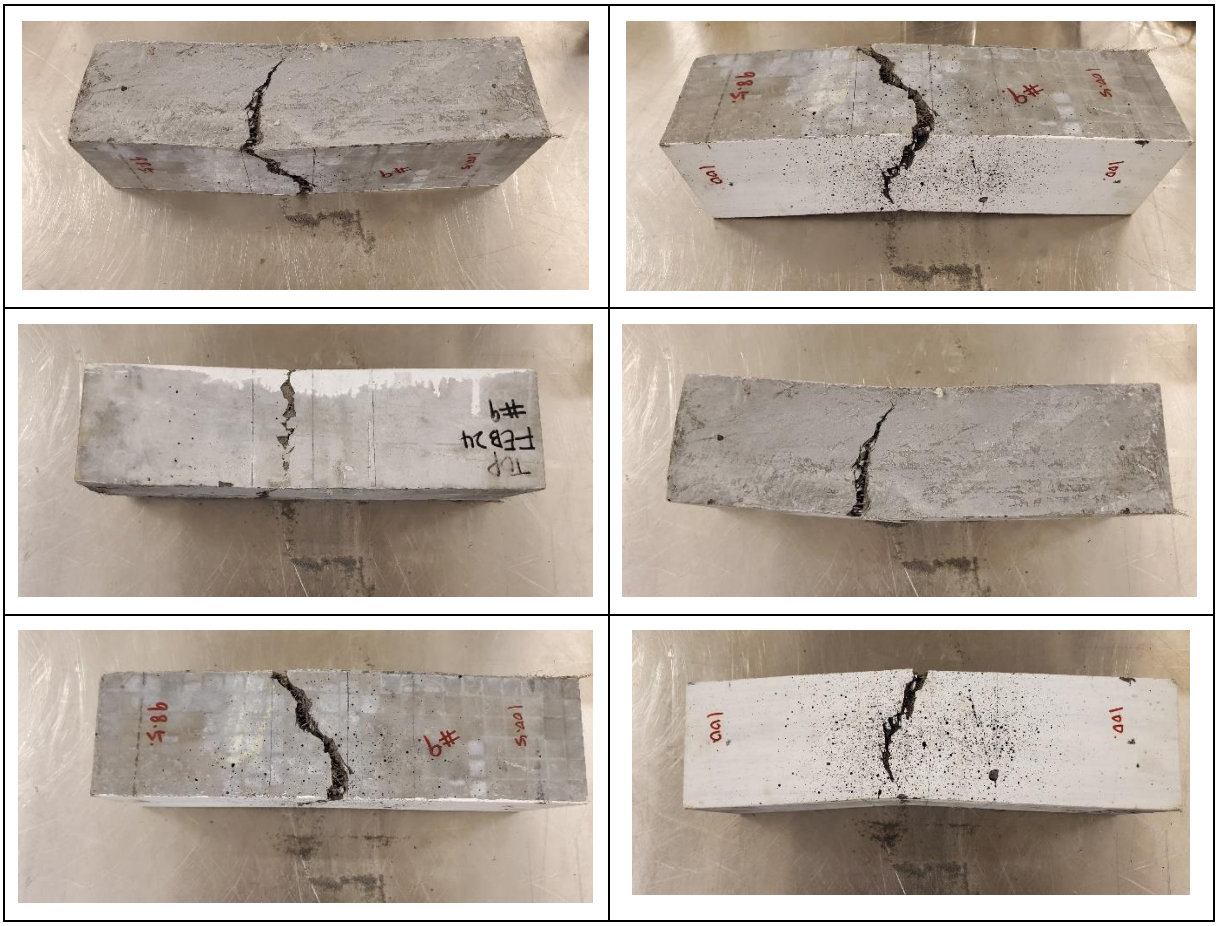

Specimen #10

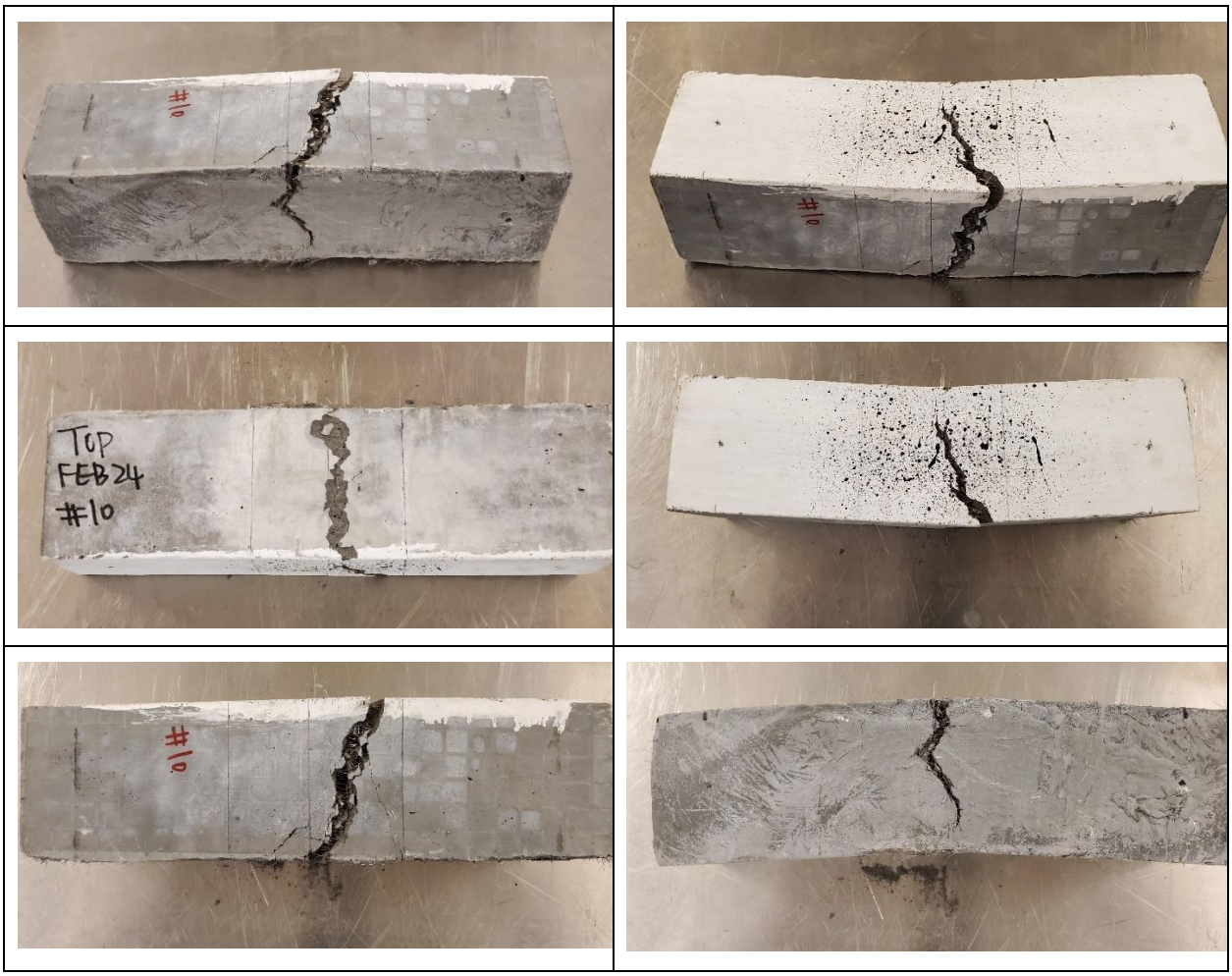

Flexural Test Setup with instrumentation

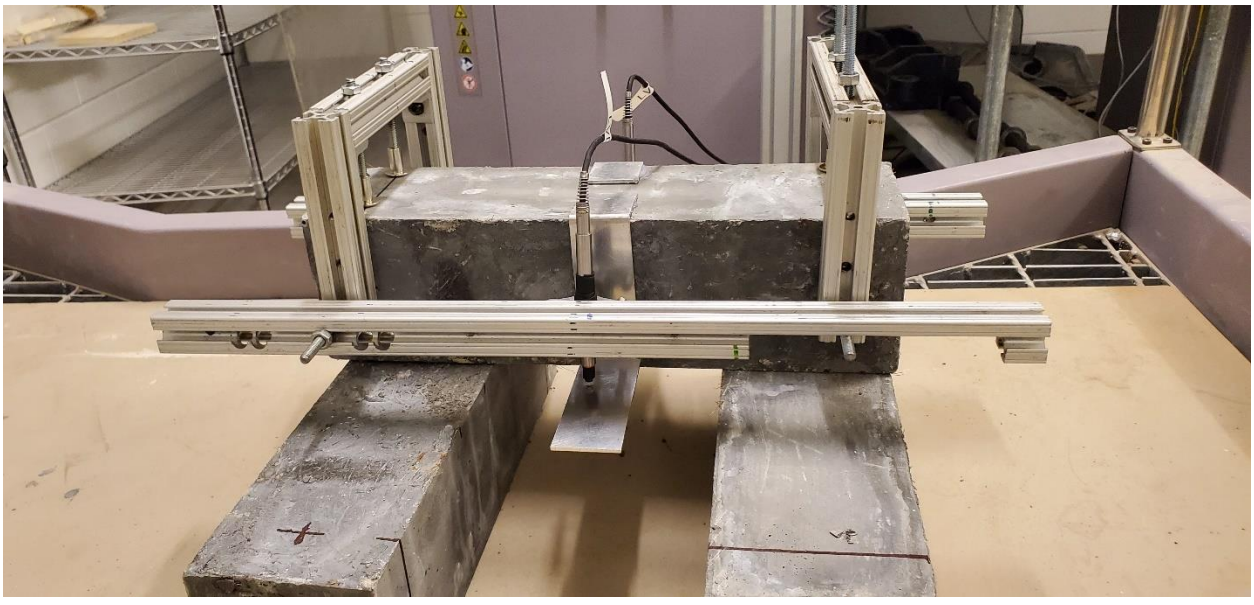

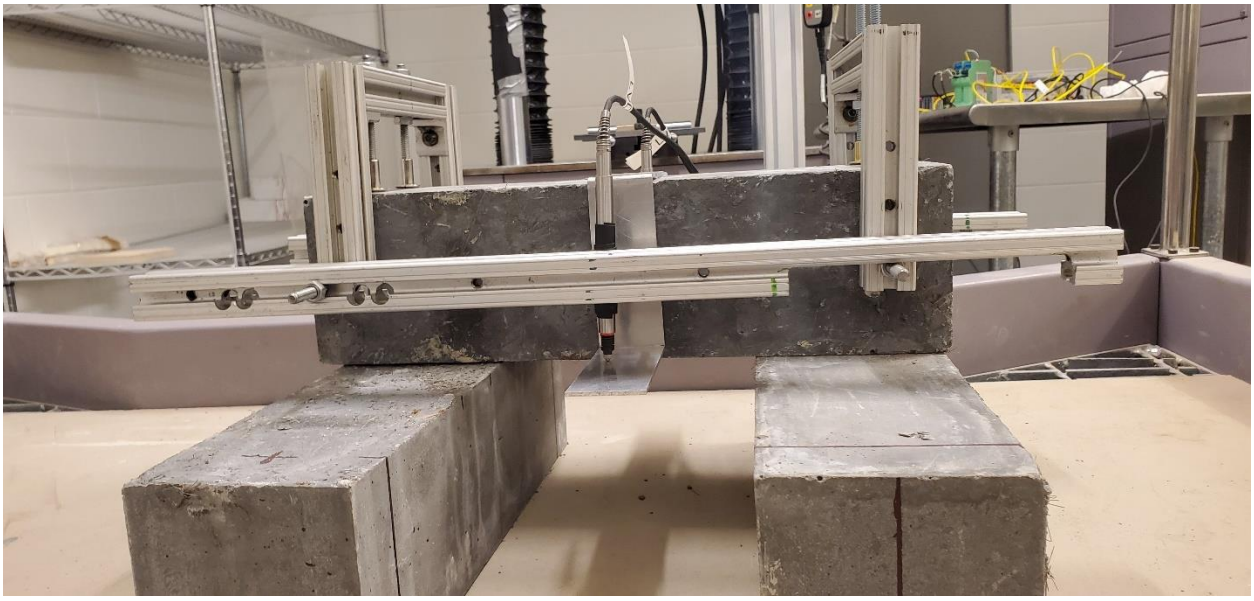

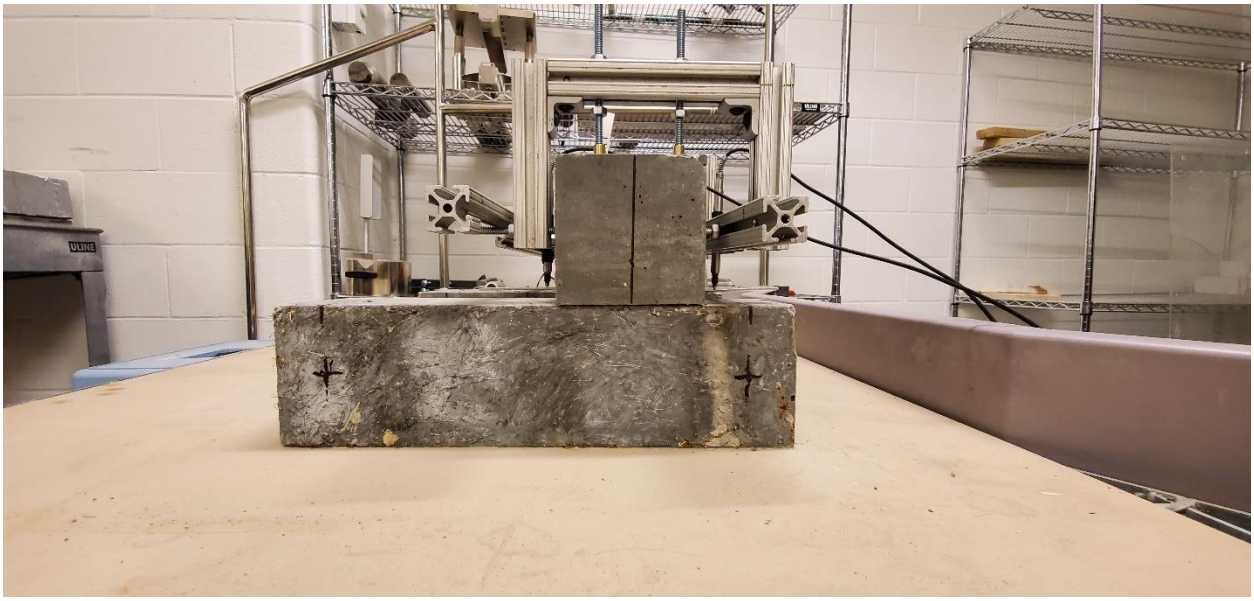

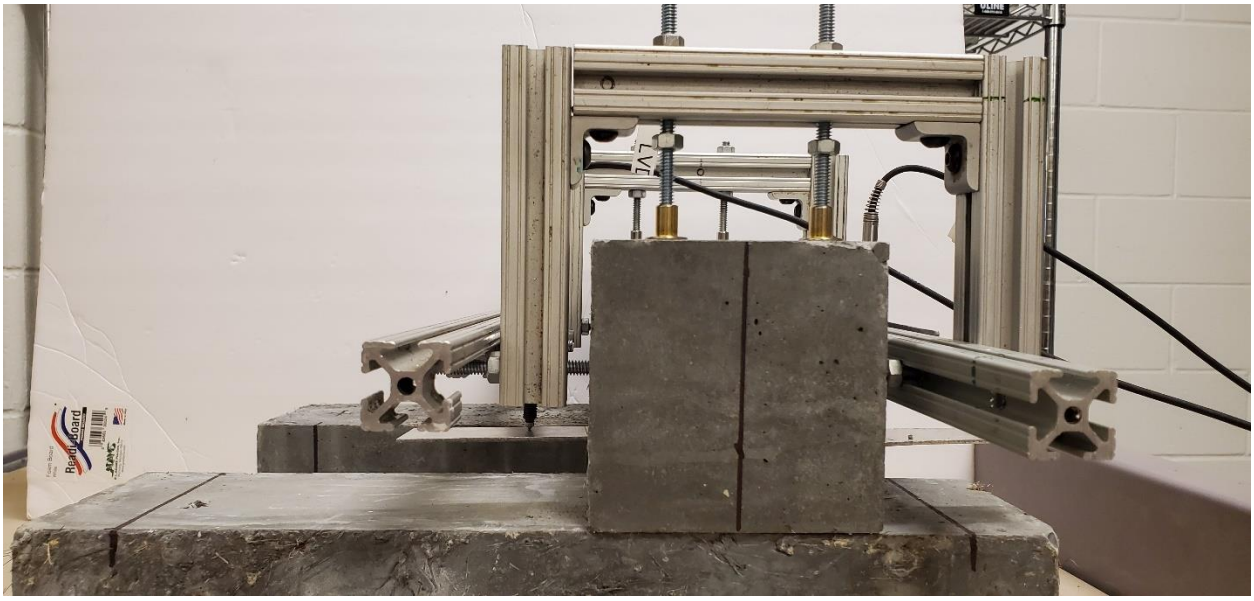
LVT

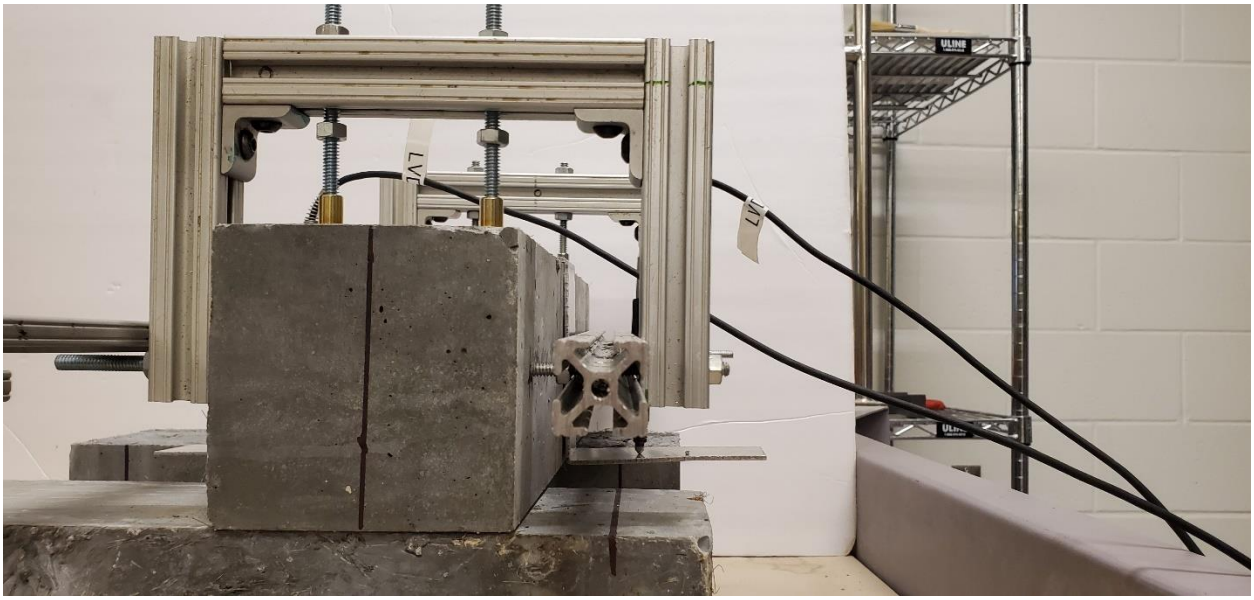
LVT
LVT
ULINE

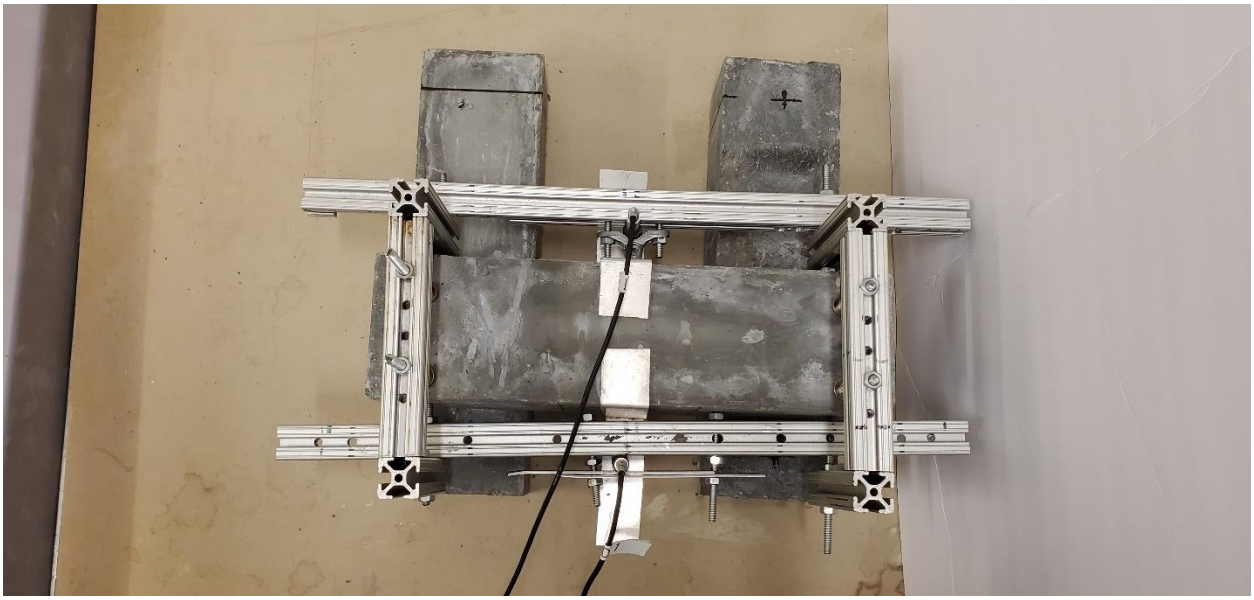

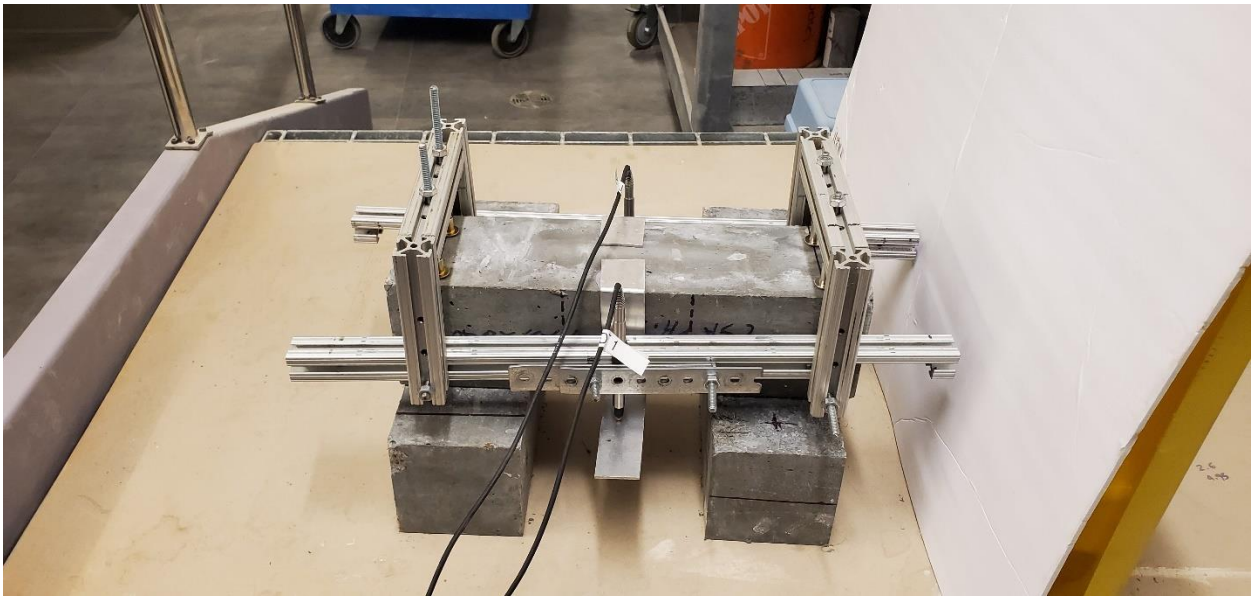

Batch 2: Static Modulus of Elasticity

Specimen # 1			
Specimen # 2	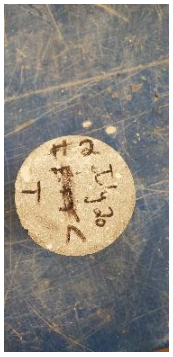		

Specimen # 3			
Specimen # 4			

Specimen # 5			
Specimen # 6			

Specimen # 7			
Specimen # 8			

Specimen # 9			
Specimen # 10			

Batch 2: Compression Test

Table A-67: Batch 2 Compression failure type summary

Specimen ID #	Failure Type
1	Type 1/ Type 2
2	Type 1/ Type 2
3	Type 2/ Type 6
4	Type 2/ Type 6
5	Type 1/ Type 2
6	Type 2
7	Type 2
8	Type 2
9	Type 2
10	Type 1/ Type 2

Specimen # 1	

Specimen # 2	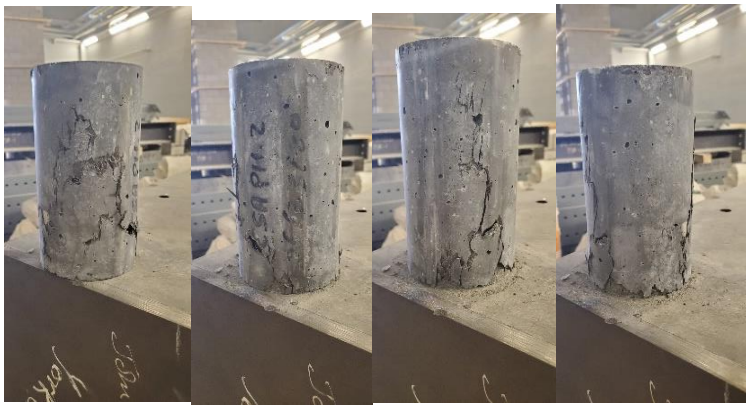
Specimen # 3	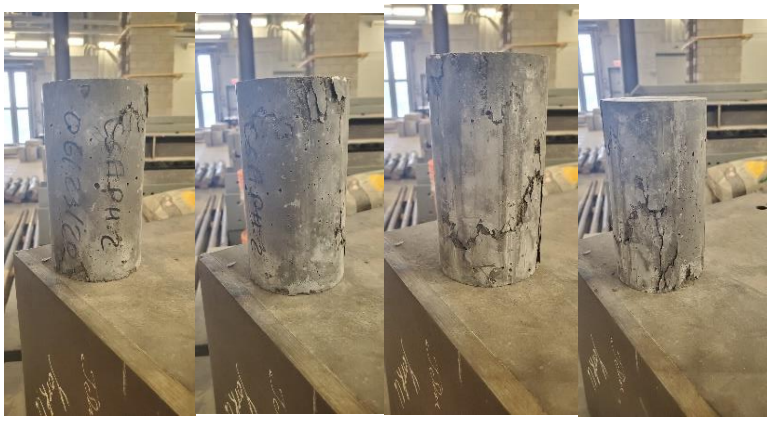

Specimen # 4	
Specimen # 5	

Specimen # 6	
Specimen # 7	

Specimen # 8	
Specimen # 9	

Specimen # 10	 

Batch 3: Compression Test

Specimen ID #	Failure Type
1	Type 2/ Type 3
2	Type 2
3	Type 2
4	Type 1 / Type 6
5	Type 2
6	Type 2
7	Type 2
8	Type 2
9	Type 2
10	Type 2

Figure A-119: Batch 3, Compression failure type summary

Specimen #1

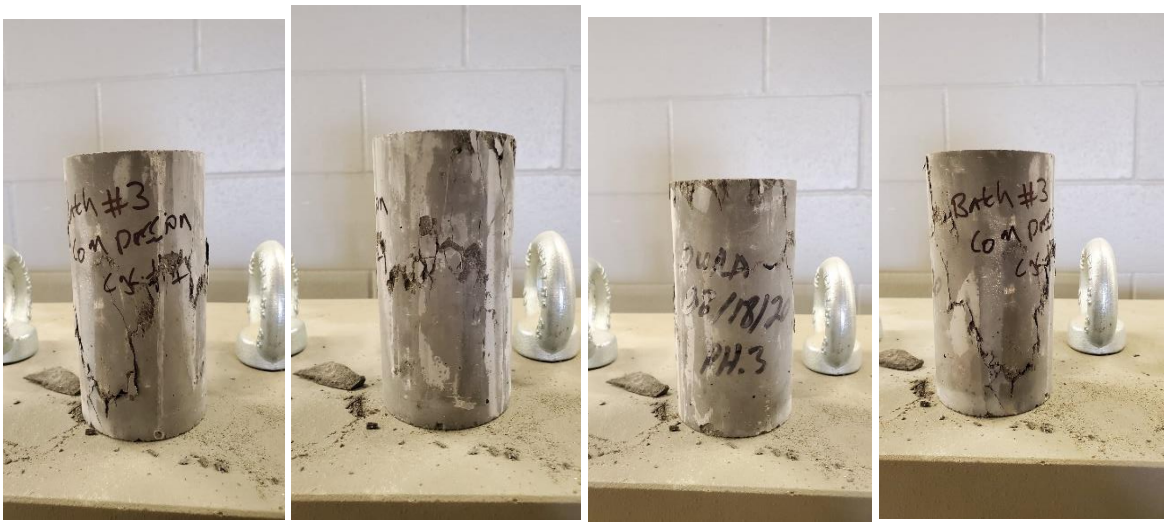

Specimen #2

Specimen #3

Specimen #4

Specimen #5

Specimen #6

Specimen #7

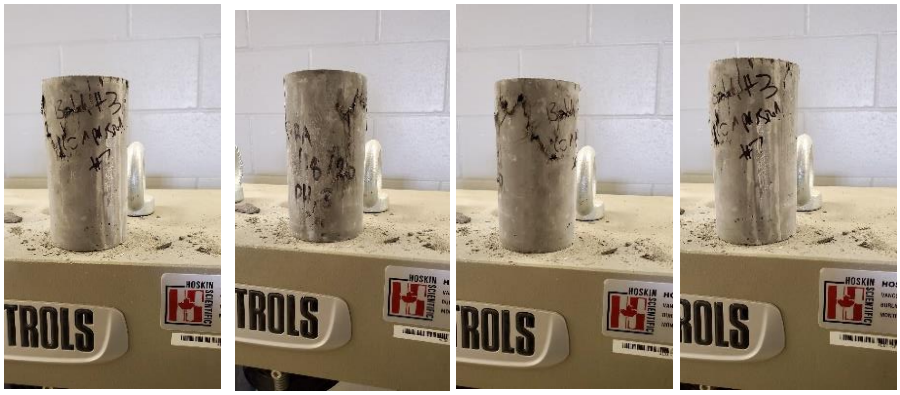

Specimen #8

Specimen #9

Specimen #10

Batch 3: Flexure Prisms

Specimen ID #	Failure Type
1	Flexure / shear
2	Flexure
3	Shear
4	Flexure
5	Flexure/Torsion
6	Flexure
7	Flexure
8	Flexure
9	Flexure
10	Flexure

Specimen # 1

Specimen # 2

Specimen # 3

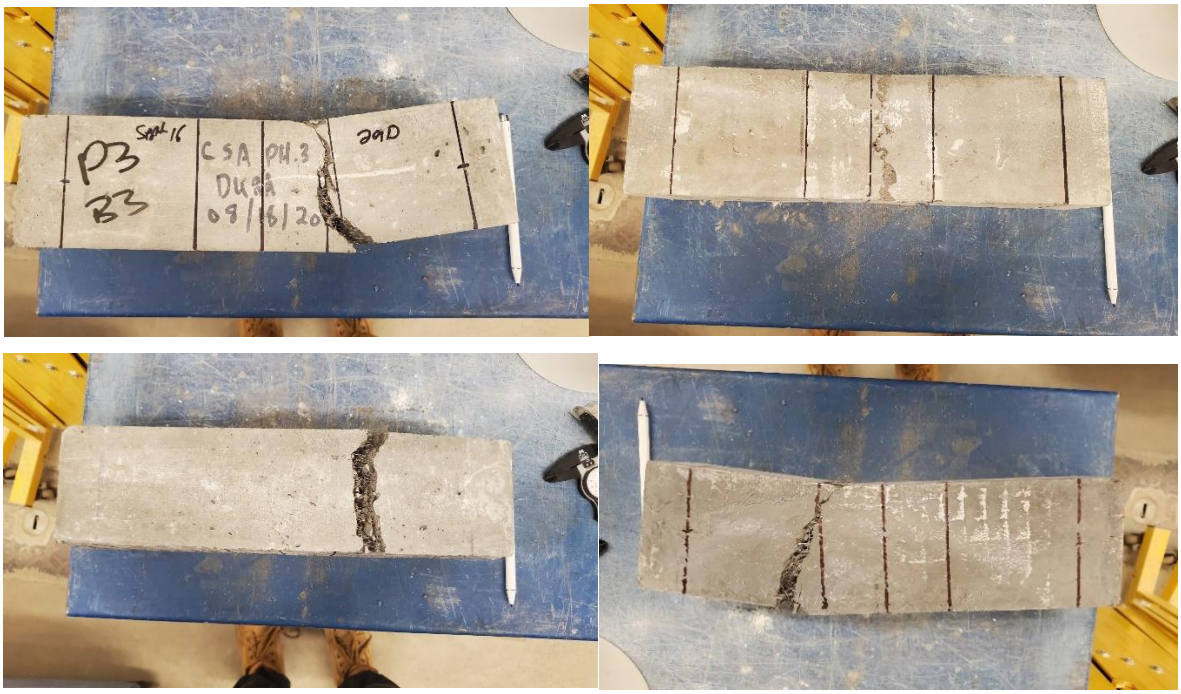

Specimen # 4


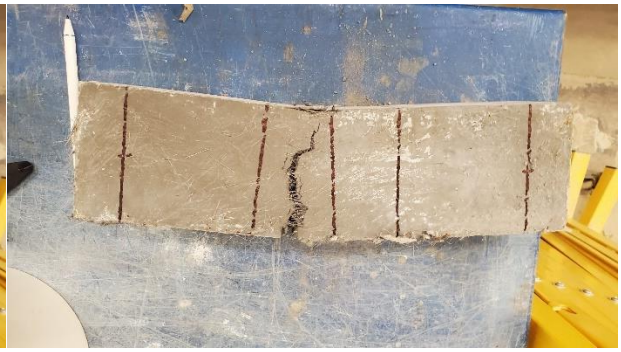
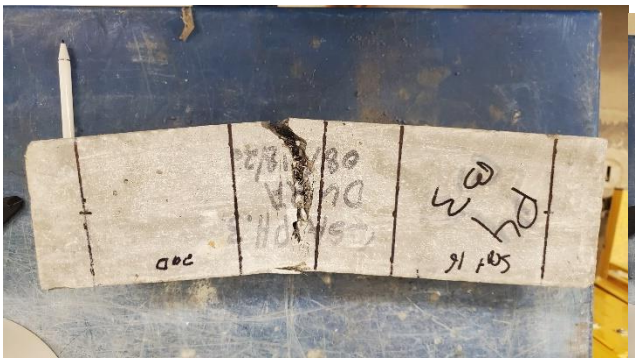


Specimen # 5

Specimen # 6

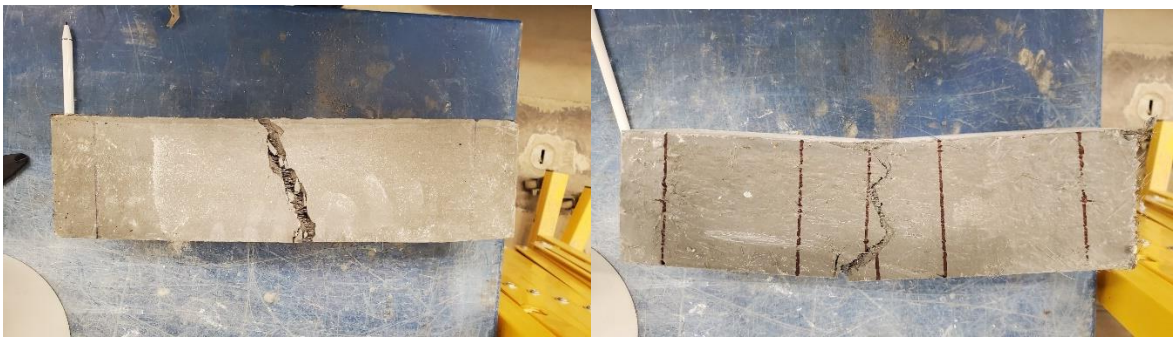

Specimen # 7

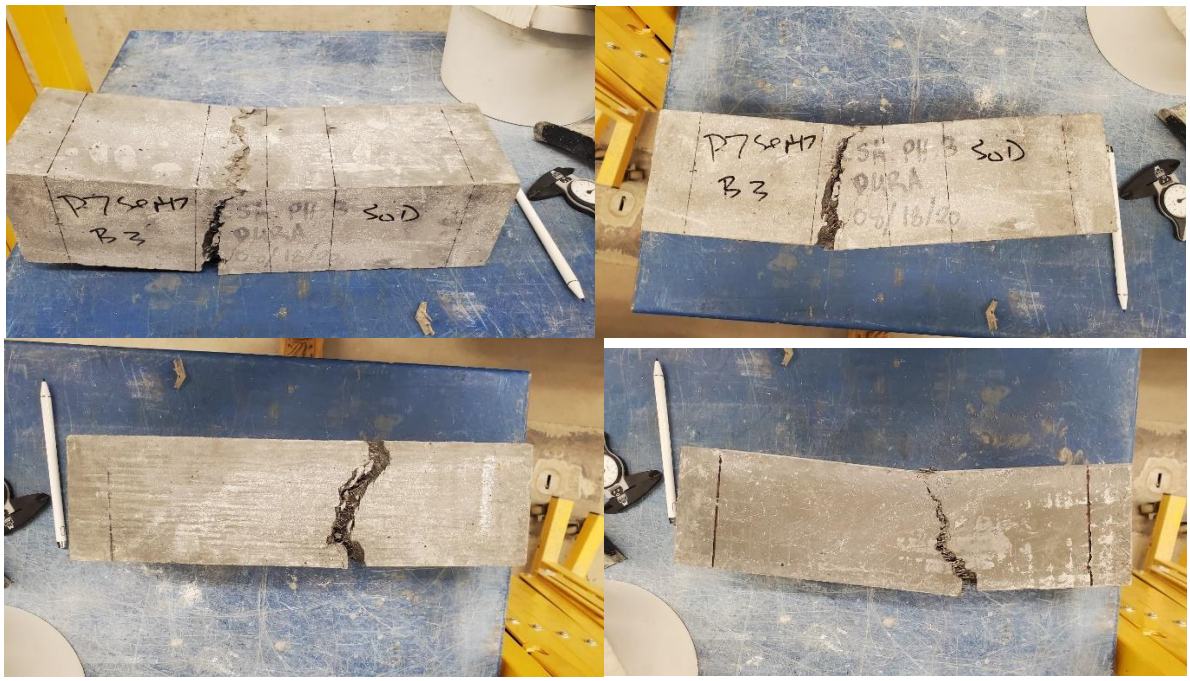

Specimen # 8

Specimen # 9

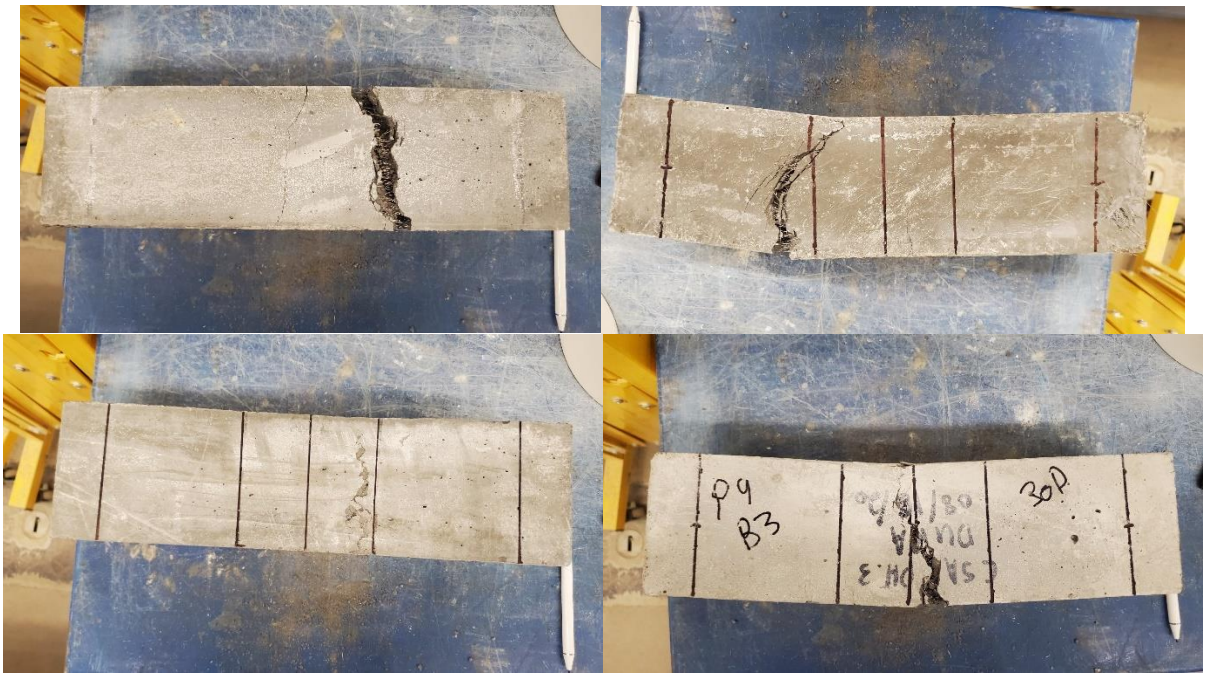

Specimen # 10

Flexure Testing instrumentation with 2 LVDT's